TOYOTA
Technical Review

The Battery Technologies of the Future
- Fuel Cells and Storage Batteries

VOL.65

Cover design:

As the automotive industry stands on the verge of a once-in-a-century period of profound change, the theme of this cover is Toyota's transformation from a car-making company into a mobility company, as represented by the Japanese character " 革 " (pronounced "kaku"), which means "to rebuild" or "renew" and is used in the Japanese words 変革 (*henkaku*: change and improvement) and 革新 (*kakushin*: innovation). The character is emphasized using a red color motif to symbolize Toyota's strong resolve to implement this transformation.

Contents

▷ **Special Feature: The Battery Technologies of the Future - Fuel Cells and Storage Batteries**

▷ **Technical Papers/Technical Articles**

▷ **Technical Award News**

From a Car-Making Company into a Mobility Company
- The Electrification Technologies Supporting Toyota's Transformation -

Shigeki Terashi,
Executive Vice President
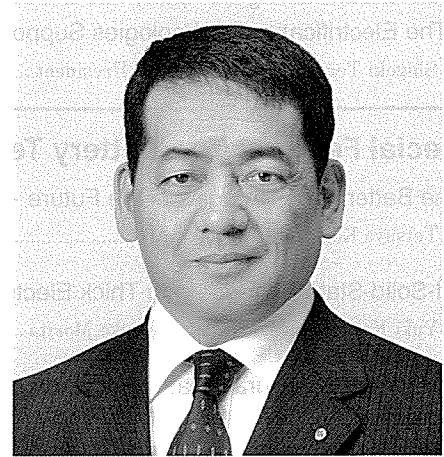
Throughout our history, we have dedicated ourselves to contributing to local communities and becoming the most admired company in town through vehicle manufacturing. Now, we are faced with the urgent task of broadening our focus away from our home towns and countries to encompass our entire home planet. So, when we regard the whole planet as our home across all national boundaries, we have to answer the questions of what Toyota and the automotive industry can do to contribute on this massive scale.

The automotive industry has entered a once-in-a-century period of profound transformation. As Toyota transforms itself from a car-making company into a mobility company, its role is also changing. In addition to working to resolve social issues, such as those related to the environment and traffic congestion, we are facing the challenge of working hand-in-hand with everyone around us to build an even more intelligent and productive mobility society.

The keyword at the root of this transformation is CASE, an acronym that stands for "connected, autonomous, shared/service, electric." Progress in these four technological fields is generating immense changes in product lineups and business models.

Toyota is also a worldwide partner of the Olympic and Paralympic Games. We have established three key themes ahead of the Tokyo summer games in 2020: (1) mobility for all, (2) sustainability, centering on the realization of a hydrogen-based society, with the environment and safety as core principles, and (3) transportation support for staff, media, and athletes between venues based on the Toyota Production System (TPS). We want to use the Games as an opportunity to propose the way ahead for our future mobility society, including the evolution of CASE technologies.

The development of innovative electrification technologies (i.e., the "E" of CASE) is the foundation for progress in all these fields.

In 1997, Toyota launched the Prius hybrid vehicle (HV) as the car of the 21st century. Twenty years have passed since then, and the fourth generation of the Prius is currently on the road all around the world. Toyota also launched the world's first mass-production fuel cell vehicle (FCV) in 2014. We will start the full-scale roll out of electric vehicles (EVs) in 2020 and have set various challenging targets for the future. For example, by 2030, we want to raise our rate of electrification to above 50%, achieve a 10% EV/FCV model mix, and boost annual sales of electrified vehicles to at least 5.5 million units. To encourage the widespread use of electrified vehicles, which are an essential part of measures to reduce CO_2 emissions, it will be important to satisfy a wide range of requirements created by the energy situation and policies of countries and regions around the world, as well as customer preferences.

Currently, commercial EVs have a battery capacity approximately 50 times greater than HVs. To achieve our objective of annual electrified vehicle sales of 5.5 million units, we will need to establish a far more extensive battery supply network. We must work with our partner companies to further accelerate the pace of this process.

We must also think of what to do with this massive amount of batteries once their service life has expired. We are working on solutions encompassing reuse by other industries, in addition to reuse within the automotive industry.

Another issue of mass battery production is the question of resource risks. We need to reduce the use of scarce resources in new technologies and work to lower costs.

Intelligent, information, and connected technologies, such as advanced safety and autonomous driving, are becoming intertwined with the electrification of vehicles. As these trends prompt Toyota to redefine its concept of transportation to encompass the boundless possibilities of mobility, we are proposing and providing new value as a mobility company beyond the boundaries of traditional car making. For example, the use of electrified vehicles to supply large amounts of power and various related services in the right locations after a natural disaster demonstrates the possibilities of mobility as a member of society in a different way than before. Our goal is to propose the wide-reaching possibilities of mobility to all those that need it, and to help realize an ever-better mobility society, with the whole world as our home.

The Battery Technologies of the Future – Fuel Cells and Storage Batteries

Tetsuya Kohigashi[1]
Machiko Abe[1]

1. Introduction

Electrified vehicles are attracting attention around the world in reaction to growing concerns about air pollution from emissions, global warming due to CO_2, and the depletion of fossil fuels. However, despite a long history of practical adoption, electrified vehicle development has proceeded in fits and starts.

In 1769, Nicolas-Joseph Cugnot, a Captain in the French Army, manufactured a wooden three-wheeled steam-powered cart that is recognized as the world's first self-propelled automobile. Cugnot chose steam as the first automotive power source and created a powertrain that used pressure from a boiler to operate a piston and drive the front wheel.

Subsequently, various attempts were made in the first half of the 19th century to develop electric vehicles. However, these efforts did not have any practical results. Finally, in 1873, the British inventor Robert Davidson is said to have manufactured the world's first electric vehicle (EV). Subsequently, in 1886, German engineer Karl Benz was granted a patent for a three-wheeled gasoline-powered vehicle, which is now recognized as the world's first practical automobile. The first four-wheeled gasoline-powered automobile appeared in 1893.

In this period of the 1800s, steam-powered vehicles were as competitive as EVs, and no one was sure which powertrain was most suitable for automobiles. The Ford Model T, a compact and robust gasoline-powered vehicle manufactured under the leadership of American industrialist Henry Ford, debuted in this environment in 1908. By 1915, more than 1 million Model Ts had been sold, gaining it a dominant position in the market. **Fig. 1** shows an example of a Model T in use during this period. The advent of the Ford Model T ushered in the age of gasoline-powered vehicles, and steam-powered vehicles and EVs were gradually pushed out of the market.

In the 1900s, although gasoline-powered vehicles developed in leaps and bounds, this progress was accompanied by issues such as air pollution, global warming, and fossil fuel depletion. These issues came to be studied around the world.

Fig. 1 Ford Model T Carrying Hay (1921)[1]

Since its foundation, Toyota Motor Corporation has recognized the importance of energy sources that do not rely on fossil fuels. This sense of urgency has been passed down to succeeding generations. In 1925, Sakichi Toyoda donated prize money to the Imperial Institute of Invention to be awarded for storage battery invention. In 1935, the same Institute held a contest for secondary battery invention based on the Ideal Battery Million Yen Contest proposed by Sakichi. Subsequently, the Imperial Institute of Invention established a dedicated laboratory to pursue research into storage batteries.

In 1939, following in the footsteps of Sakichi, Kiichiro Toyoda set up a storage battery research laboratory in Shibaura, Tokyo. This step inaugurated studies into batteries for EVs, and encouraged future research and development efforts. Realizing that the continued popularization of gasoline-powered vehicles would lead to a future of worsening environmental issues, the Toyota group continued its research into battery-powered vehicles. As a result, Toyota launched the TownAce EV in 1993 and the RAV4 EV in 1996.

In 1997, Toyota launched the Prius hybrid vehicle (HV), lifting the curtain on the hybrid era. Since then, the Prius has become the global pioneer for environmentally friendly vehicles, with a growing number of models following its example. This was followed up by the launch of the Mirai fuel cell vehicle (FCV) in 2014.

Then, in 2017, Toyota announced that it was taking up the challenge of popularizing electrified vehicles. **Fig. 2** shows a projected scenario for the future growth of electrified vehicles.

By 2030, Toyota is aiming to increase the proportion of

*1 R&D and Engineering Management Div., Advanced R&D and Engineering Company

electrified vehicles in its total sales to at least 50%. It also wants to raise the proportion of EV and FCV sales to at least 10%. To achieve these targets, the development of core electrified vehicle technologies, namely the motor, battery, and power control unit (PCU) is of critical importance. This article focuses on batteries and provides a broad overview of fuel cell and storage battery development.[2]-[4]
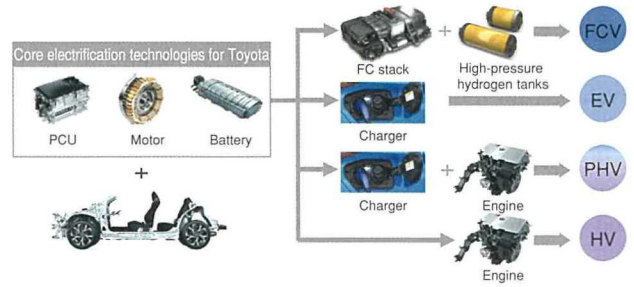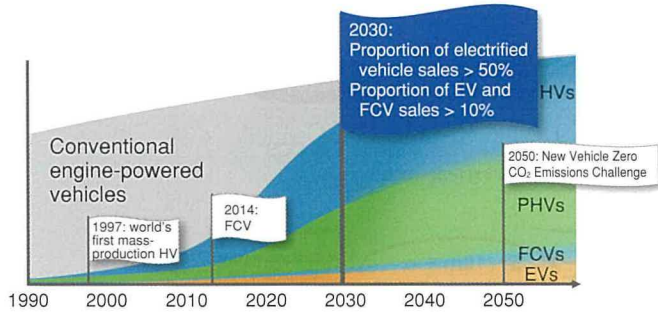

Fig. 2 Projected Scenario for Future Popularization of Electrified Vehicles

2. Relationship between Electrified Vehicles, Fuel Cells, and Storage Batteries

Fig. 3 depicts a definition of vehicles based on customer requirements, with the driving distance on the horizontal axis and vehicle size on the vertical axis. To encourage the widespread use of electrified vehicles, it will be important to satisfy a wide range of requirements created by the energy situation and policies of countries and regions around the world, as well as customer preferences. For this reason, Toyota is developing a strong lineup of electrified vehicles, including EVs, HVs, FCVs, and plug-in hybrid vehicles (PHVs). **Fig. 4** compares the characteristics of each type of electrified vehicle. By developing both storage batteries and fuel cells, Toyota is aiming to broaden the bounds of mobility and increase customer choice.

The characteristics and future direction of each type of battery are described below, starting from Section 3.
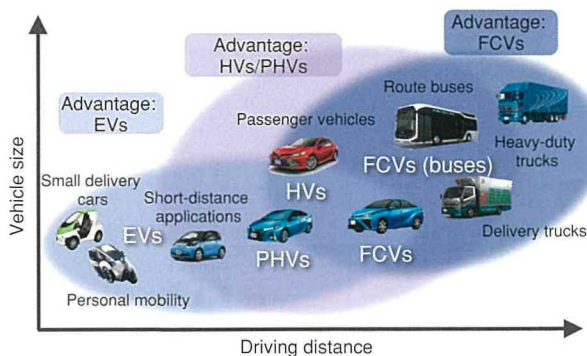

Fig. 3 Relationship between Driving Distance and Vehicle Size

Fig. 4 Comparison of Electrified Vehicles

3. What is a Fuel Cell?

A fuel cell generates electricity from the chemical reaction between hydrogen and oxygen. This chemical reaction can be expressed as follows.

$$2H_2 + O_2 \rightarrow 2H_2O + 4e^- \tag{1}$$

Since water is the only by-product of this reaction, fuel cells generate no CO_2 emissions.

Additionally, since hydrogen can be produced from a wide range of primary energy sources, supplies can be secured without the concern of fossil fuel depletion.

As a result, countries around the world have begun to adopt hydrogen energy as a promising environmentally friendly energy source with a stable supply.

4. Fuel Cell Development Initiatives

Fuel cell research has a long history and began in Europe in the 19th century. Fuel cell technology was eventually practically adopted by the US space program in the 1960s, and incorporated into both the Gemini 5 and Apollo spaceship programs.

Growing momentum for the development of fuel cells for ground-based applications led Ballard Power Systems Inc. to invent the polymer electrolyte fuel cell (PEFC), which uses a fluorinated ion exchange resin as an electrolyte membrane, in 1987.

The development of FCVs as well as fuel cell and control system technologies for mobility is now advancing around the world.

Currently, the Japanese Ministry of Economy, Trade and Industry (METI) is promoting the development of technologies to encourage the adoption of hydrogen energy, with the aim of realizing a hydrogen-based society. For this purpose, it has formulated a Basic Hydrogen Strategy to create a more strategic and effective approach (**Fig. 5**). With the objective of achieving a dramatic expansion in hydrogen use, targets have been set for

the popularization of stationary fuel cells (for homes, businesses, and industry), FCVs, and means of mobility.

Toyota also has a long history of FCV development. In 1996, it developed the FCEV-1, which was equipped with a fuel cell and hydrogen-absorbing alloy tanks. In December 2002, Toyota took the first step toward the practical adoption of FCVs by offering the Toyota FCHV for sale in Japan and the U.S. on a limited lease basis. This vehicle was equipped with the Toyota FC stack, a fuel cell developed in-house by Toyota. In 2005, Toyota was the first automaker to obtain vehicle type certification for an FCV. Subsequently, Toyota launched the Mirai FCV in 2014 as an ideal environmentally friendly vehicle. The Mirai runs using motors powered by electricity generated through chemical reactions between hydrogen stored in on-board tanks and oxygen in the air. **Fig. 6** illustrates how an FCV operates. The fuel cell system is at the heart of every FCV, and
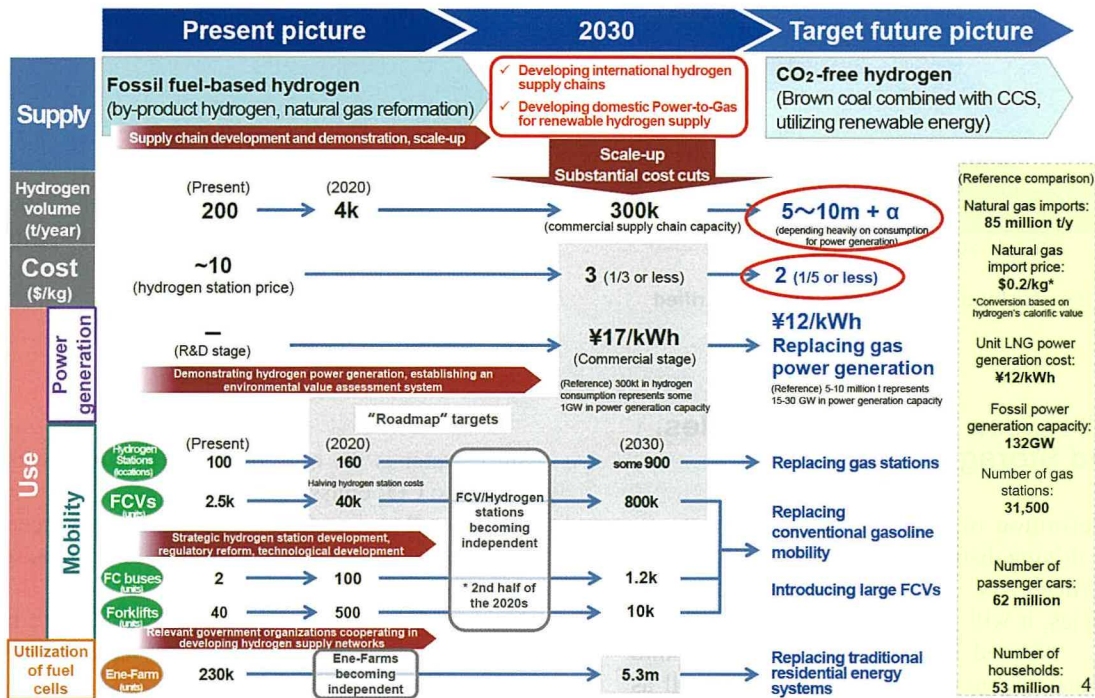

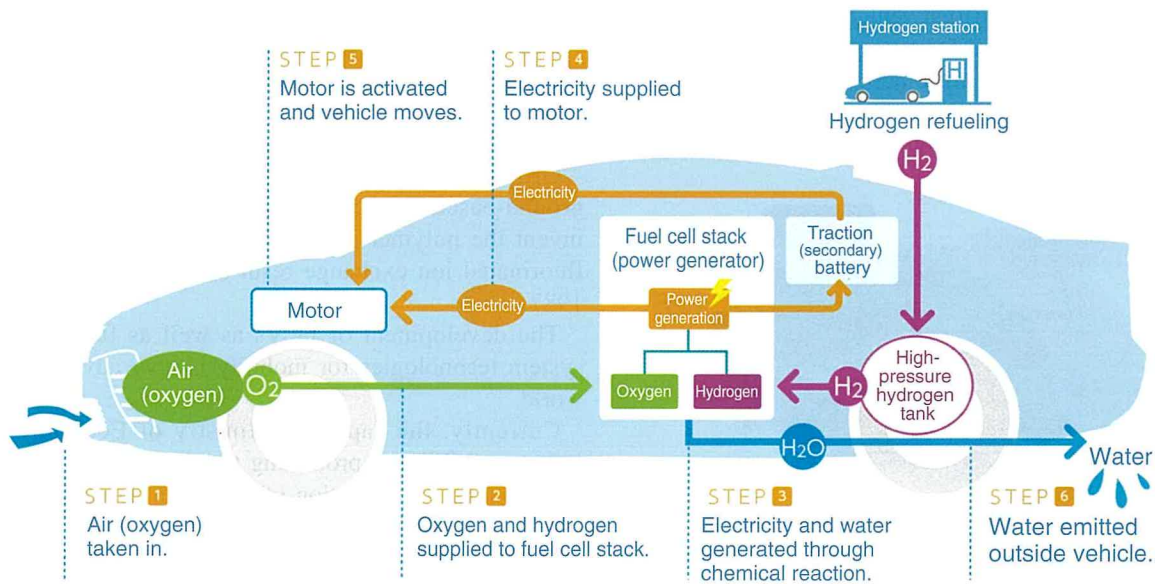Fig. 5 Basic Hydrogen Strategy[(5)]

Fig. 6 Outline of FCV Operation

Toyota is developing this system in-house, including the FC stack and high-pressure hydrogen tanks. At its launch, the FC stack in the Mirai achieved world-leading performance. It is also compact enough to be installed under the vehicle's seats. In addition, with the objectives of stimulating hydrogen demand and encouraging the establishment of the necessary infrastructure, Toyota is also working to apply fuel cell technology from popular passenger vehicle models to commercial vehicles. Some examples are as follows.

In 2017, Toyota introduced two FC forklifts, which were developed by Toyota Industries Corporation, to the Motomachi Plant, followed by twenty more in 2018. A dedicated hydrogen refueling station was also established inside the plant.

In 2017, Toyota conducted field tests of heavy-duty FC trucks in California and began studying the feasibility of introducing a new heavy-duty FC truck in 2018. It also launched the Sora FC bus in the Tokyo Metropolitan area in the same year.

In September 2018, to facilitate initiatives encouraging the widespread utilization of hydrogen (such as the establishment of hydrogen refueling stations, introduction of FCVs and FC buses for local transportation, the adoption of FC technology for railroad vehicles, and so on), Toyota and the East Japan Railway Company signed a basic agreement for a comprehensive business partnership centered on a hydrogen-based mobility partnership between railways and automobiles.

Although the marketplace for FCVs is growing steadily, issues standing in the way of the full-scale popularization of this technology include reducing the cost of FCVs and establishing the necessary hydrogen refueling stations.

5. Fuel Cell Popularization

This section describes various initiatives related to reducing costs and establishing hydrogen refueling stations to help achieve full-scale popularization of FCVs.

Cost reduction was a major issue for achieving widespread acceptance of HVs, and Toyota has played a leading global role in reducing the size, weight, and cost of hybrid systems. FCVs combine technologies related to both fuel cells and HVs. Toyota is accelerating its efforts to reduce the cost of FCVs by both lowering the costs of dedicated FC parts and by adopting HV technologies in FCVs.

Key elements for increasing the number of hydrogen refueling stations include forming and following a strategic approach to station establishment, facilitating efficient station management, and so on. In February 2018, a partnership including Toyota set up a new company called Japan H_2 Mobility, LLC (JHyM) to promote the establishment of hydrogen refueling stations across

Japan. This is the world's first such partnership and it encompasses infrastructure business operators, automotive companies, financial institutions and the like. The objective of this type of nationwide initiative is to accelerate FCV popularization and the self-reliance of hydrogen refueling stations, while also helping to realize a hydrogen-based society in Japan.

Toyota intends to continue working toward achieving the full-scale acceptance of FCVs in the market by addressing the issues of FCVs and hydrogen refueling stations, and creating a virtuous circle.

6. What is a Storage Battery?

Batteries can be separated into two broad categories: primary batteries that are used and discarded, and secondary batteries that can be repeatedly recharged and reused. Storage batteries fall into the second category. In 1800, Alessandro Volta developed the voltaic pile. This, the world's first true battery, has been continually improved and has evolved into the convenient form of the portable rechargeable dry battery. Typical examples of storage batteries than can be charged and discharged include the nickel-cadmium battery, nickel-metal hydride battery, and lithium-ion battery.

The nickel-cadmium battery was developed as early as 1899 and evolved rapidly from the 1970s. These batteries are mass-produced today in large numbers as power sources for compact cordless consumer products such as electric razors. However compared with more modern nickel-metal hydride or lithium-ion batteries, nickel-cadmium batteries have drawbacks such as high weight per unit of capacity.

The energy density of nickel-metal hydride batteries is 1.5 times higher than nickel-cadmium. From the 1990s, these batteries started to replace nickel-cadmium in high-capacity applications.

Lithium ion batteries were commercialized in 1991 for use in mobile telephones. These batteries are now widely used as power sources for mobile telephones and computers. Furthermore, various efforts are being made to increase the energy density and input/output density properties of these batteries. Recent developments have seen the adoption of large-scale high-capacity lithium-ion batteries as stationary power sources and in EVs. These trends are the result of progress in compact battery technology development, which has enabled the practical adoption of large-scale batteries, and has been greatly stimulated by rising social consciousness of environmental and energy issues.[6]-[10]

7. Storage Battery Development Initiatives

Research and development into storage batteries has naturally focused on battery materials and structures. At the same time, further progress has been achieved into developing evaluation methods and control systems for electrified vehicle storage batteries. Currently, storage batteries are being developed with particular performance attributes for specific applications.

This section focuses on storage batteries for HVs, PHVs, and EVs. Although the future performance requirements of storage batteries will differ depending on the application, the future popularization of electrified vehicles depends on developing lower cost batteries with greater output. For EV batteries in particular, increasing battery capacity to extend cruising range is a key ongoing issue.

7.1 Storage batteries for HVs

The 2015 Prius lineup includes models with two different battery types: nickel-metal hydride and lithium-ion. Compared with the previous generation, the charging performance of the nickel-metal hydride battery was enhanced through the adoption of a newly developed electrode material and a new battery case structure. In contrast, models equipped with the lithium-ion battery include a newly developed electrode material that lowers cell resistance and greatly boosts output performance.

Lithium-ion batteries have a higher energy density (i.e., the amount of energy that can be stored per unit of weight or capacity) than nickel-metal hydride batteries, which feature particularly stable performance at low temperatures.

Toyota has adopted both battery types reflecting customer requirements and regional characteristics.

7.2 Storage batteries for PHVs

To realize smooth and powerful driving in EV mode, the Prius PHV is equipped with compact, lightweight, and high-capacity lithium-ion batteries.

The second-generation Prius PHV, which was launched in the U.S. in 2016 as the Prius Prime, was awarded the 2017 World Green Car of the Year as the most environmentally friendly new model to debut between the autumn of 2015 and the autumn of 2016.

7.3 Storage batteries for EVs

EVs require batteries with even greater capacity than PHVs. In addition to further lithium-ion battery development to boost performance, EVs will also require the development of next-generation batteries.

8. Future Direction of Storage Battery Development

Toyota recognizes the need for innovative battery development to achieve wider acceptance of electrified vehicles. It is currently researching and developing various types of next-generation storage batteries with higher outputs and capacities, including all-solid-state batteries, metal-air batteries, sodium-ion batteries, and magnesium batteries. All-solid-state batteries are currently considered to be closest to the level of practical application for adoption in mass-production vehicles. Toyota is continuing to work on research and development of these batteries, including production engineering.

Generally, lithium-ion batteries use a transition metal oxide containing lithium as the cathode active material, a carbon material as the anode active material, and a liquid electrolyte consisting of a lithium salt dissolved in an organic solvent.

In contrast, all-solid-state batteries replace this liquid electrolyte with a solid electrolyte (**Fig. 7**). Since solid electrolytes contain a higher amount of lithium than liquid electrolytes and can transport a larger amount of lithium in the same time, it should be feasible to reduce battery size. The development of smaller batteries may enable more batteries to be installed in a given space, thereby increasing the total battery capacity of the EV.
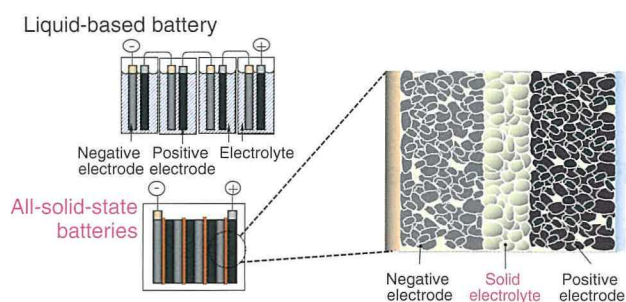

Fig. 7 Outline of all-solid-state batteries

9. Conclusion

The development of fuel cells and storage batteries, which are fundamental technologies for the diversification of mobility, is of the utmost importance. The popularization of electrified vehicles cannot proceed without progress in these fields.

In contrast, this goal cannot be achieved by progress in the fields of fuel cells and storage batteries alone. Other key items include the establishment of infrastructure and the development of control systems capable of maximizing the performance of fuel cells and storage batteries installed in vehicles.

As global electrified vehicle development becomes increasingly active, Toyota intends to make every effort in its own development initiatives and to work closely with its group companies, suppliers, business partners, and research institutions to promote the further popularization of electrified vehicles around the world.

References

(1) F. Clymer. _Henry's Wonderful Model T_, 1908-1927. Bonanza Books (1955).

(2) _A Quick History of Cars_ (in Japanese). Gazoo. https://gazoo.com/article/carhistory/150327_1.html

(3) _75 Years of Toyota_. Toyota Motor Corporation. http://www.toyota-global.com/company/history_of_toyota/75years/

(4) _Inheriting Sakichi's Aspiration – Our Life, With the Toyota Group_. Explanatory Panel at the Special Event to Commemorate the 150th Birthday of Sakichi Toyoda, Toyota Commemorative Museum of Industry and Technology (2017).

(5) _Basic Hydrogen Strategy_. Ministry of Economy, Trade and Industry (METI), Japan (2017). http://www.meti.go.jp/press/2017/12/20171226002/20171226002-1.pdf

(6) Z. Ogumi et al. _Secondary Battery Technology for Beginners_ (in Japanese). Kogyo Chosakai Publishing Co., Ltd. Tokyo (2001).

(7) K. Mizushima et al. "Li$_x$CoO$_2$ (0<x<-1): A New Cathode Material for Batteries of High Energy Density." _Materials Research Bulletin_ 5 (1980) pp. 783-789.

(8) R. Kanno et al. "Carbon as Negative Electrodes in Lithium Secondary Cells." _Journal of Power Sources_ 26 (1989) pp. 535-543.

(9) M. Mohri et al. "Rechargeable Lithium Battery Based on Pyrolytic Carbon as a Negative Electrode." _Journal of Power Sources_ 26 (1989) pp. 545-551.

(10) J. Dahn et al. "Rechargeable LiNiO$_2$/Carbon Cells." _Journal of the Electrochemical Society_ 138 (1991) pp. 2207-2211.

Authors

T. KOHIGASHI   **M. ABE**

Special Feature

All-Solid-State Batteries with Thick Electrode Configurations

Yuki Kato[*1]
Shinya Shiotani[*2]
Keisuke Morita[*1]

Abstract

This article describes the preparation of thick electrode all-solid-state lithium-ion cells in which a large geometric capacity of 15.7 mAh cm^{-2} was achieved at room temperature using a 600 μm-thick cathode layer. The effect of ionic conductivity on the discharge performance was then examined using two different materials for the solid electrolyte. Furthermore, important morphological information regarding the tortuosity factor was electrochemically extracted from the capacity-current data. The effect of tortuosity on cell performance was also quantitatively discussed.

Keywords: *all-solid-state battery, thick electrode, ion transfer, tortuosity*

1. Background

Increasing the thickness of an electrode is an attractive option for improving the energy densities of batteries, as it minimizes the relative volume of inactive components, such as the current collector and separator.[1]-[5] However, this creates challenges in terms of power characteristics due to the ion or electron transfer limitations of thick electrodes. To date, the power capabilities of lithium-ion batteries containing thick electrodes have been improved by the incorporation of three-dimensional structured substrates, such as aligned carbon, metal foil, and porous carbon.[2]-[4] However, in the high current density region, the rate capabilities of thick electrode systems remain limited by ion diffusion in the liquid electrolyte.[4][5] Indeed, the low number of lithium ions transferred ($t_{Li+}<0.4$) results in a concentration gradient of lithium ions across the system during charge/discharge.[6][7]

As such, all-solid-state batteries can be considered an alternative option for thick electrode systems because the number of lithium ions transferred in inorganic solid electrolytes is almost unity. In addition, some solid electrolytes exhibit higher ionic conductivity than liquid electrolytes, allowing the production of high-power all-solid-state batteries with higher rate capabilities than liquid electrolyte-based lithium-ion batteries.[8] Although all-solid-state batteries with thick electrode configurations have been reported,[8][9] a quantitative analysis of ion transfer, including the effects of ionic conductivity and morphology, has yet to be carried out. This article describes the details of all-solid-state batteries with higher surface capacities than previously reported systems.[8][10]-[12] It also details a systematic investigation of the effects of ionic conductivity and electrode morphology on the discharge performances of such systems.

Table 1 Details of Adopted Solid Electrolytes

Solid electrolyte	Composition	Ionic conductivity (κ/mS cm^{-1})
SE1	$Li_{10}GeP_2S_{12}$	3.2
SE2	$75Li_2S$-$25P_2S_5$	0.28
SE3	$30LiI$-$70(0.75Li_2S$-$0.25P_2S_5)$	1.2

*1 Advanced Material Engineering Div., Advanced R&D and Engineering Company
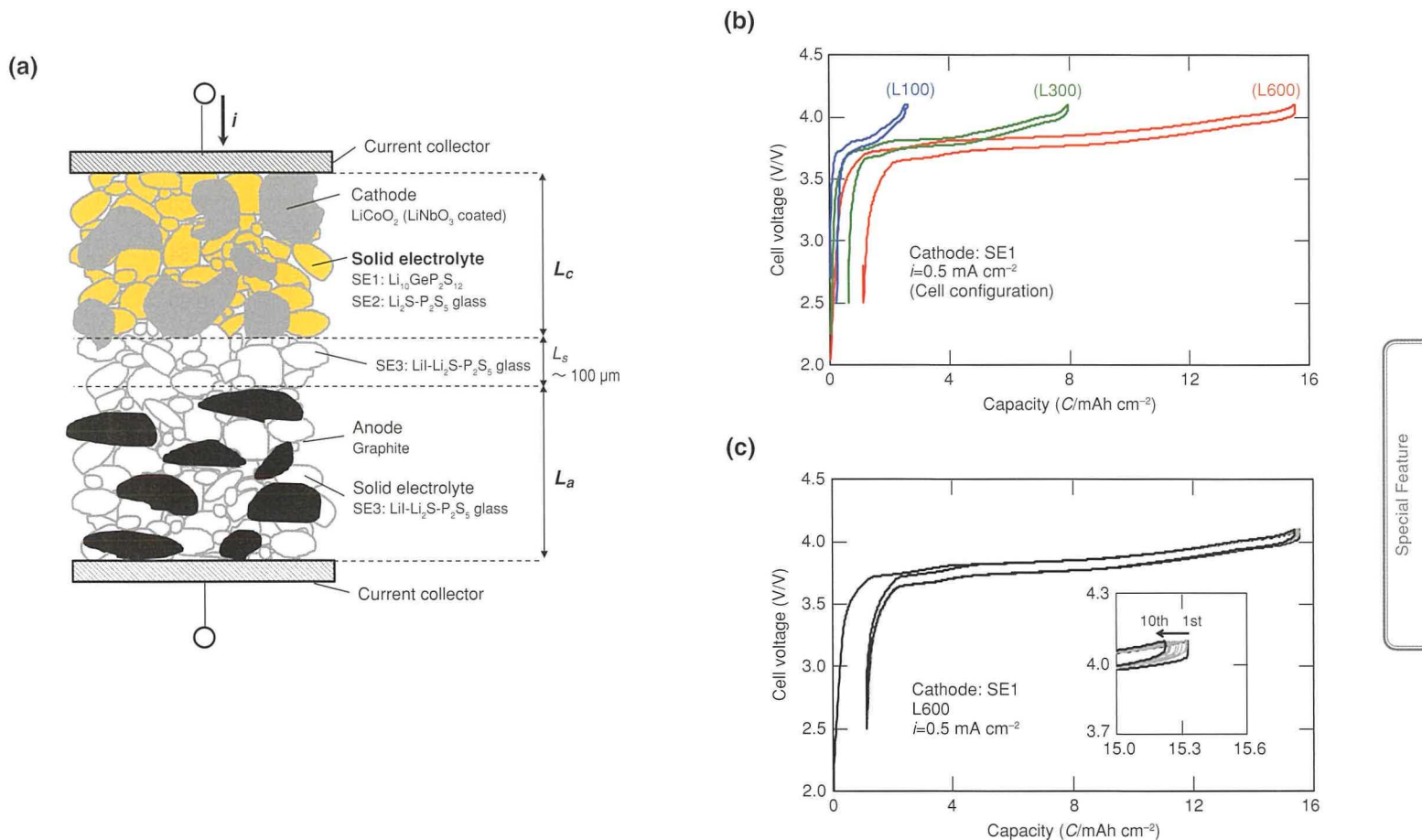*2 Battery Material Engineering & Research Div., Powertrain Company

Fig. 1 (a) Schematic Representation of Experimental Setup, (b) Charge/Discharge Capability of Thick Electrode Configuration, (c) Cycling Performance of L600 Configuration

Table 2 Powder Mixtures Employed for Preparation of Cathode and Anode Layers

Material	Density (ρ/g cm^{-3})	Mass fraction in electrode (wt%)		Volume fraction in electrode (vol%)	
		Cathode layer	Anode layer	Cathode layer	Anode layer
LiCoO$_2$ (LiNbO$_3$ coated)	5.05	61	–	38.1	–
Acetylene black	2.00	3	–	4.8	–
Solid electrolyte	2.00	36	54	57.1 (ε=0.57)	57 (ε=0.57)
Graphite	2.27	–	46	–	43

2. Results and Discussion

Fig. 1 shows a schematic representation of the adopted cell, and **Table 1** lists the details of the prepared solid electrolytes that exhibit different ionic conductivities.[13]–[15] LiNbO$_3$-coated

LiCoO$_2$[16] and graphite were selected for the cathode and the anode, respectively. As indicated in **Tables 2** and **3**, several types of all-solid-state batteries were prepared by systematically changing the electrode layer thickness. The separator layer (Ls) thickness was set to a constant value of 100 μm.

Table 3 Properties of Prepared Cathode and Anode Layers

Configuration	Cathode layer		Anode layer		Capacity $(C/\text{mAh cm}^{-2})$
	Thickness $(L_c/\mu\text{m})$	LCO loading $(M_{\text{LCO}}/\text{mg cm}^{-2})$	Thickness $(L_a/\mu\text{m})$	Graphite loading $(M_c/\text{mg cm}^{-2})$	
L75	~75	14.5	~66	6.4	2.00
L100	~100	19.3	~88	8.6	2.64
L125	~125	24.1	~109	10.7	3.30
L150	~150	28.9	~131	12.8	3.96
L200	~200	38.6	~174	17.1	5.29
L250	~250	48.2	~219	21.4	6.60
L300	~300	57.7	~262	25.6	7.93
L600	~600	115.4	~524	51.3	15.7
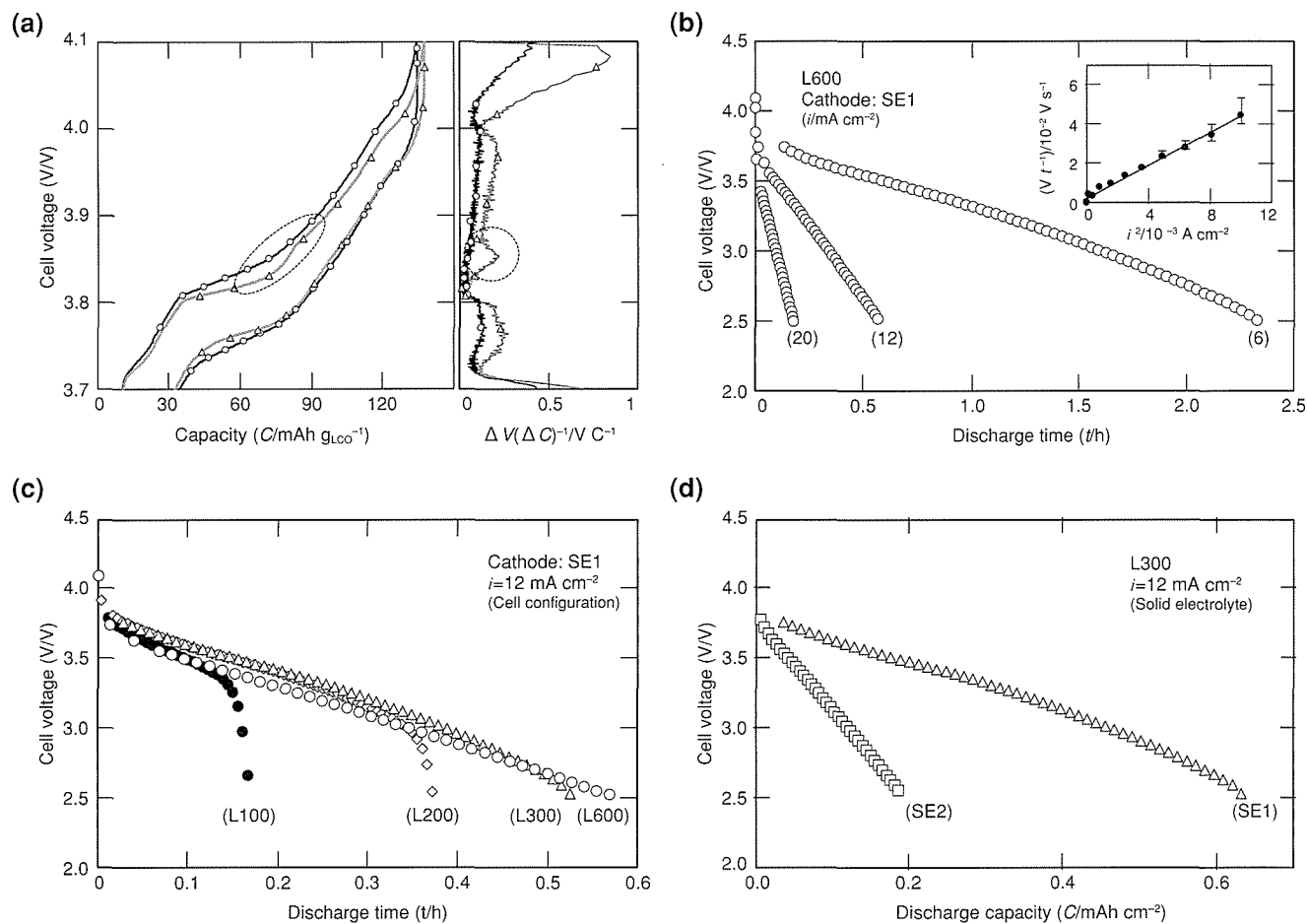
Fig. 2 Charge/Discharge Curves of All-Solid-State Cells: (a) Charge/Discharge Capability of Thick Electrode Configuration (Discharge Behavior was Investigated by Varying (b) Current Density, (c) Electrode Thickness, and (d) the Ionic Conductivity of the Cathode Layer

Fig. 1(b) shows the charge-discharge curves obtained at 0.5 mA cm^{-2} using SE1 as the solid electrolyte. It is apparent that the theoretical capacity was successfully cycled at this current density even for the L600 thick electrode configuration (active material mass per electrode area LiCoO$_2$=115.4 mg cm^{-2}). In addition, in the constant current mode, the charge capacity reached in excess of 95% of the theoretical capacity and the discharge capacity reached 93%, thereby indicating the potential of this system. Fig. 1(c) shows the cycling test of the L600 configuration at 0.5 mA cm^{-2}. Good cyclability (greater than 99% of capacity after 10 cycles with a charge/discharge efficiency of approximately 100%) was exhibited under these conditions, thereby indicating that the change in volume was accommodated over a minimum of 10 cycles.

Fig. 2(a) shows the variation in the charge-discharge characteristics of the L600 and L300 configurations at 0.5 mA cm^{-2} relative to the specific capacity of LiCoO$_2$. Evolution of the overpotential was also observed when the electrode thickness was increased, thereby indicating energy loss due to ion transfer in the electrolyte. Although a plateau in the potential was observed for the L300 configuration, which corresponds to the stage structure of graphite, a smoother slope was observed for the L600 configuration, with the differential constant ($\Delta V/\Delta C$) at around 3.8 V being a good indication of this (see the right-hand panel of Fig. 2(a)). Indeed, this difference between the two configurations reflects the particle distributions at different states of charge across the electrodes due to the required overpotential for mass transfer.

Fig. 2(b) shows the discharge curves of the L600 cell prepared using SE1 at different discharge current densities (i). Below i=6 mA cm^{-2}, the cell exhibited almost theoretical capacity, while a discharge capacity of 13.9 mAh cm^{-2}, which is 88% of the theoretical capacity, was obtained at i=6 mA cm^{-2}. In addition, the relatively straight discharge curves observed where i>6 mA cm^{-2} indicate that the reaction of this cell is limited by an ohmic potential drop in the electrolyte layer, which can be said to have reached the ohmic limit. This phenomenon is seen when the effect of ion transfer is greater than the diffusion in the active materials in terms of cell reactions. The operation of a LiCoO$_2$/graphite system at current densities greater than 50 mA cm^{-2} with a thin electrode layer (i.e., a thickness of 25 μm)[8] indicates that the active material particles can respond rapidly at these current densities. Indeed, in the case of a thick electrode system, this is feasible, as the current density per particle decreases as the thickness increases. As such, the reaction of batteries that have reached the ohmic limit can be understood using the reaction zone model proposed by Newman et al.[18] Since the effective electron conductivity (σ_{eff_c}=0.3 S cm^{-1}, σ_{eff_a}=0.7 S cm^{-1}) was significantly larger than the ionic conductivity of a solid electrolyte (κ), the potential drop is considered to originate mainly from ion transfer in this system. The voltage profile of the half-cell at the ohmic limit can therefore be expressed as indicated in Equation 1.

$$V = U^0 - R_o i - \frac{t}{q \, \kappa_{eff}} \, i^2 \tag{1}$$

where,

U^0: open circuit potential of the active material in the charged state

R_o: high frequency resistance

q: capacity density of the composite electrode

κ_{eff}: effective ionic conductivity of the composite electrode

t: time

Incorporation of the volume fraction of the electrolyte ε and the tortuosity factor τ gives the effective conductivity of the composite electrode as follows.

$$\kappa_{eff} = \frac{\varepsilon}{\tau} \, \kappa \tag{2}$$

As both Equations 1 and 2 incorporate the morphological parameter of the tortuosity factor, this parameter can be estimated by analyzing the discharge curves. At the ohmic limit, the slope of the discharge curves includes direct information regarding the morphology of the all-solid-state cell. Equation 1 can therefore be modified to give a full cell model, and upon considering the direction of current, the voltage behavior of the full cell at the ohmic limit can be expressed as Equation 3.

$$V = U_c^0 - U_a^0 - R_o i - \left(\frac{1}{q_c \, \kappa_{eff_c}} + \frac{1}{q_a \, \kappa_{eff_a}} \right) i^2 \times t \tag{3}$$

where,

c: values corresponding to the cathode

a: values corresponding to the anode

Therefore, Equation 3 indicates that the slope of the discharge curve is proportional to the square of the applied current density. The slope of the discharge curve shown in Fig. 2(b) corresponds with the ratios of the squared currents (i.e., slopes = -0.52, -2.07, and -6.22 at i=6, 12, and 20 mA cm^{-2}, respectively). In addition, the insert of Fig. 2(b) shows the relationship between the slope of the discharge curve and the squared current, indicating that the cells are at the ohmic limit. Furthermore, the slope shown in the inset of Fig. 2(b) corresponds with the value of

$\left(\dfrac{1}{q_c \, \kappa_{eff_c}} + \dfrac{1}{q_a \, \kappa_{eff_a}} \right)$ for the SE1 system.

Moreover, Fig. 2(c) shows the discharge curves at i=12 mA cm^{-2} for different electrode thicknesses (i.e., L100, L200, and L600). In the case of the thinnest electrode configuration (L100), more than 80% of the capacity was discharged, indicating that at this current density, the active materials can be

almost fully (de-)lithiated. This shows that the diffusion in the active material under this current is sufficiently fast and can respond to the applied current. In other words, the battery performance may be considered to be limited by lithium transfer within the electrolyte. Therefore, as shown in Expression 3, the slopes of the discharge curve are not dependent on the electrode thickness and are approximately constant. Furthermore, consistent with the reaction zone model, the slopes of the discharge curves are independent of the electrode thickness, but are strongly dependent on the ionic conductivity of the electrolyte. This can be clearly observed when cathode layers with different conductivities are used (**Fig. 2**(d)).
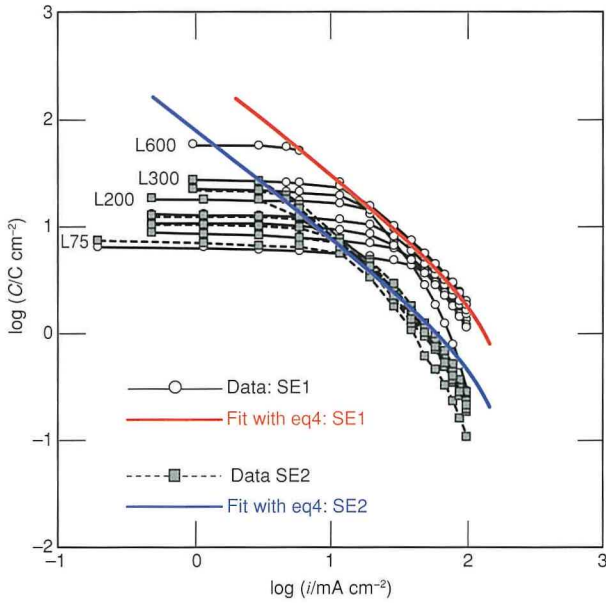
Fig. 3 Capacity-Rate Plots for All-Solid-State Cells for Electrodes L75 to L600 at Applied Current Range of 0.1 to 100 mA cm⁻²

The rate capability tests were then merged in the current-capacity plot shown in **Fig. 3**. Although the theoretical capacity based on the electrode thickness can be discharged at a low current density, it was found that the dischargeable capacity was both thickness-independent and current-dependent, forming a straight line with a slope of -1 at large current densities. Indeed, this is typical behavior of an ohmic-limited electrode system.[18][19]

Using the cut-off voltage V_{cutoff}, the capacity at the ohmic limit condition is defined as follows.

$$C = t_d i = \frac{1}{i} \times \left(\frac{1}{q_c \kappa_{eff\_cj}} + \frac{1}{q_a \kappa_{eff\_a}} \right)^{-1} (U_c^\theta - U_a^\theta - V_{cutoff} - R_o i) \qquad (4)$$

where,

       t_d: time at which the cell voltage reaches V_{cutoff}
       j: SE1 (j=1) or SE2 (j=2)

Table 4 lists the values of the various constants. Information regarding the electrode morphology was then extracted from **Fig. 3**. At a current of $i \ll (U_c^\theta - U_a^\theta - V_{cutoff})/R_s$, the capacity is inversely proportional to the current density, and it is favorable to use a small current density in addition to a thick electrode to minimize the effect of diffusion in the electrode particles.

Therefore, the value of $\left(\frac{1}{q_c \kappa_{eff\_cj}} + \frac{1}{q_a \kappa_{eff\_a}} \right)^{-1}$ can be extracted for each electrolyte system by fitting with the experimental data (**Fig. 3**), where the deviation observed at large current densities is caused by the effect of diffusion in the electrode particles.

Table 4 Cell Parameters for Prepared All-Solid-State Batteries

q_c/C cm⁻³	953
q_d/C cm⁻³	1298
U_c^θ/V (vs Li/Li⁺)	4.1
U_a^θ/V (vs Li/Li⁺)	0.1
V_c/V	2.5
R_o/Ω cm²	8

Table 5 Obtained Values for Ion Transfer in Electrode Layers

κ_{eff_c1}/mS cm⁻¹	0.73
κ_{eff_c2}/mS cm⁻¹	0.065
κ_{eff_a}/mS cm⁻¹	0.21
τ_{c1} ($=\tau_{c2}$)	2.47
τ_a	3.32

Considering that the cathode layer morphologies are comparable for SE1 and SE2 (i.e., $\tau_{c1}=\tau_{c2}$), the effective conductivities κ_{eff_c1}, κ_{eff_c2}, and κ_{eff_a} can be determined and the tortuosity factor τ can be estimated, as indicated in **Table 5**. It should be noted that, although estimation of the tortuosity tends to be challenging due to the complex battery reactions taking place,[20]-[22] a simplified electrochemical treatment of the all-solid-state cells due to the absence of a concentration gradient allows this value to be determined relatively easily. The obtained effective ion conductivity and tortuosity are as shown in **Table 5**.

Voids and cracks were observed in the solid electrolyte regions of both the cathode and the anode, which also interfere with ion transfer and increase the tortuosity factor. Such interference is a fundamental characteristic of all-solid-state batteries, and its effect on tortuosity should be analyzed carefully. Furthermore, an improved understanding and control of crack evolution is desirable when considering the application of such systems, thereby indicating the importance of electrode processing and pressure control during operation.

14

The effect of the tortuosity factor or the ionic conductivity on the performance of all-solid-state cells can be quantitatively discussed using Equation 4. Tortuosity has an impact on battery performance. For example, a doubling of the capacity can be achieved using SE1 at i=20 mA cm^{-2} for a homogeneously mixed system, again indicating the importance of electrode processing. More specifically, battery performance can be significantly improved by altering the adopted mixture conditions and by suppressing void formation in the electrode through sintering or hot pressing, although the occurrence of undesired side-reactions must be considered during such processes. Considering the cycle life, pressure control would also be required to suppress crack and void formation during operation.

Conductivity also has a significant influence on battery performance, with an increase in conductivity at the anode enhancing battery performance. In theory, the full capacity of the L600 configuration (15.8 mAh cm^{-2}) can be discharged at 30 mA cm^{-2} with an electrolyte of 10 mS cm^{-1}. Although some materials exhibiting values greater than 10 mS cm^{-1} have been reported,[8][13] these materials demonstrate exceptional conductivities at densified conditions achieved either by sintering or hot pressing, thereby suggesting that materials with high conductivity in the compressed state are desirable for thick electrode all-solid-state battery systems.

3. Summary

In summary, a thick electrode all-solid-state lithium-ion battery containing a 600 μm-thick cathode was successfully prepared and operated at room temperature. It was found that this system can be accurately described in the context of ohmic limits. In addition, following systematic capacity-current experiments and analysis, key morphologic parameters were extracted for the tortuosity factor, a value that is normally difficult to estimate. Furthermore, the effects of the ionic conductivity and tortuosity factor on battery performance were analyzed quantitatively. The results of this study should be capable of providing guidance in the context of electrode design for developing high performance all-solid-state batteries.

Lastly, the authors would like to express their gratitude to Professor Kota Suzuki, Professor Masaaki Hirayama, and Professor Ryoji Kanno of the Tokyo Institute of Technology for their valuable input.

This article was previously published under the title "All-solid-state batteries with thick electrode configurations" in *J. Phys. Chem. Lett.* Vol. 9 (2018), pp. 607-613 as approved by the American Chemical Society.

References
(1) R. Moshtev et al. "State of the Art of Commercial Li Ion Batteries." *J. Power Sources* Vol. 91 (2000) pp. 86-91.
(2) L. Hu et al. "Lithium-Ion Textile Batteries with Large Areal Mass Loading." *Adv. Energy Mater.* Vol. 1 (2011) pp. 1012-1017.
(3) K. Evanoff et al. "Towards Ultrathick Battery Electrodes: Aligned Carbon Nanotube-Enabled Architecture." *Adv. Mater.* Vol. 24 (2012) pp. 533-537.
(4) M. Singh et al. "Thick Electrodes for High Energy Lithium Ion Batteries." *J. Electrochem. Soc.* Vol. 162 (2015) pp. A1196-A1201.
(5) K. Gallagher et al. "Optimizing Areal Capacities through Understanding the Limitations of Lithium-Ion Electrodes." *J. Electrochem. Soc.* Vol. 163 (2016) A138-A149.
(6) T. Fuller et al. "Simulation and Optimization of the Dual Lithium Ion Insertion Cell." *J. Electrochem. Soc.* Vol. 141 (1994) pp. 1-10.
(7) P. Arora et al. "Comparison between Computer Simulations and Experimental Data for High-Rate Discharges of Plastic Lithium-Ion Batteries." *J. Power Sources* Vol. 88 (2000) pp. 219-231.
(8) Y. Kato et al. "High-Power All-Solid-State Batteries Using Sulfide Superionic Conductors." *Nat. Energy* Vol. 1 (2016).
(9) A. Kubanska et al. "Effect of Composite Electrode Thickness on the Electrochemical Performances of All-Solid-State Li-Ion Batteries." *J. Electroceram.* Vol. 38 (2017) pp. 189-196.
(10) W. Zhang et al. "The Detrimental Effects of Carbon Additives in Li$_{10}$GeP$_2$S$_{12}$-Based Solid-State Batteries." *ACS Appl. Mater. Interfaces* Vol. 9 (2017) pp. 35888-35896.
(11) A. Sakuda et al. "Interfacial Observation between LiCoO$_2$ Electrode and Li$_2$S-P$_2$S$_5$ Solid Electrolytes of All-Solid-State Lithium Secondary Batteries Using Transmission Electron Microscopy." *Chem. Mater.* Vol. 22 (2010) pp. 949-956.
(12) T. Otomo et al. "All-Solid-State Lithium Secondary Batteries Using the 75Li$_2$S·25P$_2$S$_5$ Glass and the 70Li$_2$S·30P$_2$S$_5$ Glass-Ceramic as Solid Electrolytes." *J. Power Sources* Vol. 233 (2013) pp. 231-235.
(13) N. Kamaya et al. "A Lithium Superionic Conductor." *Nat. Mater.* Vol. 10 (2011) pp. 682-686.
(14) F. Mizuno et al. "High Lithium Ion Conducting Glass-Ceramics in the System Li$_2$S-P$_2$S$_5$." *Solid State Ionics* Vol. 177 (2005) pp. 2721-2725.
(15) K. Takada et al. "Solid-State Lithium Battery with Graphite Anode." *Solid State Ionics* Vol. 158 (2003) pp. 269-274.
(16) N. Ota et al. "LiNbO$_3$-Coated LiCoO$_2$ as Cathode Material for All Solid-State Lithium Secondary Batteries." *Electrochem. Commun.* Vol. 9 (2007) pp. 1486-1490.
(17) G. Oh et al. "Bulk-Type All Solid-State Batteries with 5 V Class LiNi$_{0.5}$Mn$_{1.5}$O$_4$ Cathode and Li$_{10}$GeP$_2$S$_{12}$ Solid Electrolyte." *Chem. Mater.* Vol. 28 (2016) pp. 2634-2640.

Special Feature

(18) M. Doyle et al. "Modeling the Performance of Rechargeable Lithium-Based Cells: Design Correlations for Limiting Cases." *J. Power Sources* Vol. 54 (1995) pp. 46-51.

(19) M. Doyle et al. "Analysis of Capacity-Rate Data for Lithium Batteries Using Simplified Models of the Discharge Process." *J. Appl. Electrochem.* Vol. 27 (1997) pp. 846-856.

(20) C. Fongy et al. "Electronic and Ionic Wirings Versus the Insertion Reaction Contributions to the Polarization in $LiFePO_4$ Composite Electrodes." *J. Electrochem. Soc.* Vol. 157 (2010) pp. A1347-A1353.

(21) C. Fongy et al. "Ionic vs Electronic Power Limitations and Analysis of the Fraction of Wired Grains in $LiFePO_4$ Composite Electrodes." *J. Electrochem. Soc.* Vol. 157 (2010) pp. A885-A891.

(22) C. Fongy et al. "Carbon Nanofibers Improve Both the Electronic and Ionic Contributions of the Electrochemical Performance of Composite Electrodes." *J. Power Sources* Vol. 196 (2011) pp. 8494-8499.

Authors

Y. KATO **S. SHIOTANI** **K. MORITA**

Analysis of Structural Phase Transition of Storage Battery Carbon Negative Electrodes Using Synchrotron Radiation and Neutrons

Shigeharu Takagi[*1]

Abstract

This study used synchrotron radiation and neutron diffraction to carry out operando structural analysis of carbon (graphite) negative electrodes of storage batteries during the charge/discharge process. Low-temperature operando measurement using synchrotron radiation diffraction and neutron diffraction was enabled by the development of a new single-cell measurement tool capable of temperature control. When dQ/dV analysis was performed in accordance with the diffraction pattern, it was found that, at low-temperature, high-rate discharge, structural phase transition of the graphite (i.e., stage structure changes) is inhibited and that transition in multiple phases is facilitated. As a result, it was inferred that this structural transition affects battery low-temperature performance and high-rate discharge performance. In addition, X-ray diffraction (the fundamental parameter method) was used to analyze the crystallite size distribution and quantify the carbon structure, thereby identifying the relationship with battery performance. Furthermore, analysis of the effects on phase transition due to the crystallinity of graphite during charge and discharge found that the multi-phase transition phenomena differed due to the crystallinity of the graphite. This analysis also identified the graphite crystallinity and structural phase transition during charge and discharge, as well as the relationship between these parameters and battery performance.

Keywords: *synchrotron radiation diffraction, neutron diffraction, X-ray diffraction, fundamental parameter method, graphite, crystallite size*

Special Feature

1. Introduction

A number of issues related to storage batteries must be resolved to encourage the widespread adoption of electric vehicles (EVs). These include further increasing capacity, as well as enhancing both low-temperature and high rate charge-discharge characteristics. Understanding the lithium (Li) intercalation and de-intercalation mechanism at the carbon negative electrode of the storage battery is a critical step toward improving these battery performance attributes. To accomplish this objective, it is important to examine structural phase transition states using operando analysis during charge-discharge. Since the structural phase transitions that occur due to temperature change must be analyzed, temperature-controlling tools that can be utilized with synchrotron radiation diffraction and neutron diffraction measurement methodologies are under development. In addition, since recent research has found that the type of carbon used for the storage battery negative electrode causes differences in battery performance, researchers are also working to quantify the physical properties of storage battery carbon negative electrodes. Analysis is focusing on carbon crystallinity as a physical property of carbon that affects battery performance from the standpoint of Li diffusivity.

This article describes the development of new tools capable of low-temperature control (from -10 to 50°C), which enabled operando structural analysis with synchrotron radiation diffraction and neutron diffraction.[1]-[4] This research then applied these developments to identifying how the following factors affected phase transition: the differences under low- and room-temperature conditions, the effects of the charge-discharge rate, and different degrees of carbon crystallinity. Additionally, X-ray diffraction (the fundamental parameter (FP) method[5]) was used to quantify the crystallite size and distribution, and to analyze the relationship between these factors and lithium-ion battery low-temperature performance.[6]

Finally, these results enabled the effects on battery performance at low temperatures and during high rate charge-discharge to be analyzed. This helped to form useful guidelines for the development of next-generation storage battery materials.

*1 Material Engineering Div. No. 2, Advanced R&D and Engineering Company

2. Experimental Methodology

2.1 Phase transition analysis at low temperature (operando structural analysis by neutron diffraction)

For the neutron diffraction measurement, this research used the special environment neutron powder diffractometer (SPICA), located at the BL09 beam port of the Materials and Life Science Experimental Facility (MLF), which is part of the Japan Proton Accelerator Research Complex (J-PARC) in Ibaraki prefecture (**Fig. 1**),[3] and measured neutron diffraction patterns at the QA-bank.
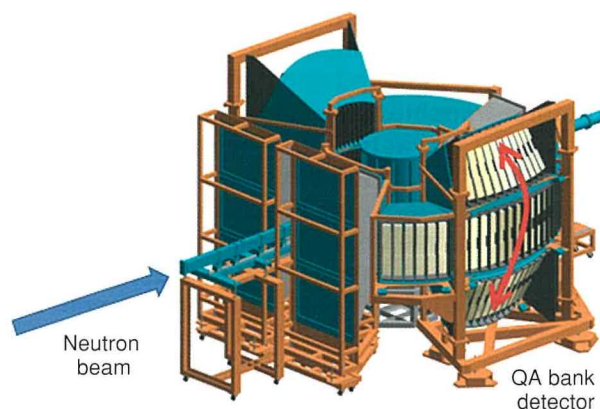
Fig. 1 TOF-Type Neutron Diffractometer (SPICA)

This research utilized polychlorotrifluoroethylene (PCTFE) for the external coating of individual cells. This is a thermoplastic chlorofluoropolymer that contains no hydrogen atoms. This material allowed the analysis to proceed without the use of a deuterium-substituted electrolyte and thoroughly reduced the background noise (reduction rate: 72%). As a result, the signal/noise (S/N) ratio increased and enabled the acquisition of high-quality neutron diffraction data.

The individual cells (four-layer cells) consisted of the following materials. Natural graphite was used for the carbon material, which was coated onto a copper collector foil to create the graphite electrode. Li was used for the counter electrode, and an EC/EMC-system electrolyte (proportion: 3/7 vol%) containing 1 mol/l of $LiPF_6$ in solution was adopted.

The individual cells were subjected to two cycles of pretreatment (aging) at room temperature (RT). After charging (Li intercalation) at a constant current (CC, 0.1C) and constant voltage (-CV, 0.05 V), the discharge (Li de-intercalation) reactions at 0.05C were analyzed at RT and 0°C. Additionally, the dQ/dv curve was calculated from the charge-discharge curve and the correspondence with the dQ/dV peaks was analyzed.

2.2 Phase transition analysis at low temperature and high-rate discharge (operando structural analysis by synchrotron radiation diffraction)

For the synchrotron radiation diffraction measurement, this research used the BL28XU beamline at the large SPring-8 synchrotron radiation facility under the Research and Development Initiative for Scientific Innovation of New Generation Batteries 2 (RISING 2) initiative.

The individual cells used natural graphite for the carbon material, which was coated onto a copper collector foil to create the graphite electrode, and Li for the counter electrode. An EC/EMC-system electrolyte (proportion: 3/7 vol%) containing 1 mol/l of $LiPF_6$ in solution was adopted in the cells.

The energy of the synchrotron radiation diffraction was set to 25 keV, and a two-dimensional detector (the Pilatus 300K-W manufactured by Rigaku Corporation) was used.

The camera length of the Pilatus 300K-W two-dimensional detector was set to 830 mm. This setting expanded the measurable angular range and improved the angular resolution, enabling the acquisition of X-ray diffraction data containing other than the graphite (002) peak (the main peak).

The individual cells were subjected to two cycles of pretreatment (aging) at RT. After charging (Li intercalation) at a CC of 0.1C and a -CV of 0.05 V, the discharge (Li de-intercalation) reactions at 0.2C were analyzed at RT and 0°C. Additionally, the dQ/dv curve was calculated from the charge-discharge curve and the correspondence with the dQ/dV peaks was analyzed. The discharge (Li de-intercalation) reactions at 1C were also analyzed at RT.

2.3 Relationship between quantification of carbon structure and battery performance (analysis of crystallite size distribution by X-ray diffraction)

The crystallite sizes and distributions of various carbon (graphite) materials were analyzed using the FP method. Six types of natural carbon (graphite) and four types of artificial graphite were analyzed.

In the FP method, a powder X-ray diffraction pattern simulation is carried out by convoluting machine-derived (i.e., using measurement conditions such as the slit width and sample thickness) profiles with profile shapes derived from the crystallite size and lattice distortion and profile shapes created by the X-ray emission profile. This simulation is used to optimize the crystallite size and lattice distortion parameters, and is capable of obtaining a precise value for the crystallite size distribution by approximation using lognormal distribution or similar techniques. The X-ray diffraction measurement used Cu K(alpha) radiation (0.154 nm).

Coil cells (full cells) were fabricated using the various carbon (graphite) materials described above as the negative electrode active material and a ternary system (NMC) cathode active material. The battery low-temperature and high-rate charge-discharge characteristics were then analyzed using these cells.

The relationship between the physical properties of carbon (graphite) and battery performance was analyzed based on the acquired results.

2.4 Analysis of effect of changes in carbon structure (crystallinity) on phase transition during charge-discharge

Individual cells (aluminum laminated) were fabricated using sample A (natural graphite, high crystallinity) and sample B (artificial graphite, low crystallinity) and the same Li counter electrode as described above. Operando analysis of charge-discharge was also carried out using the same synchrotron radiation diffraction methodology as described above. The energy of the synchrotron radiation diffraction was set to 25 keV, and a two-dimensional detector (the Pilatus 100K manufactured by Rigaku Corporation) was used.

The coin cells and aluminum laminated cells were aged at a predetermined charge-discharge current, and then analyzed at predetermined temperatures and charge-discharge currents.

3. Results and Discussion

3.1 Phase transition analysis at low temperature (operando structural analysis by neutron diffraction)

Fig. 2 shows the developed tool capable of low-temperature control. This tool can control the temperature from low temperatures to RT.
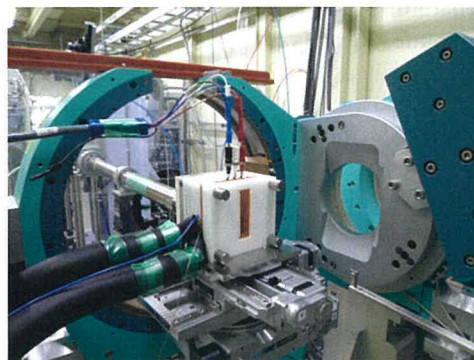

Fig. 2 Developed Temperature-Controlling Tool for Neutron Diffraction

Fig. 3 shows the neutron diffraction results during discharge (i.e., the Li de-intercalation process) with the graphite negative electrode at RT. In the Li de-intercalation process, a clear change can be observed through LiC_6 (d value: around 3.7Å) and LiC_{12} (d value: around 3.5Å) to C (d value: around 3.35 Å). As a result, it was possible to clearly identify the phase transition (i.e., the changes in stage structures) of graphite.
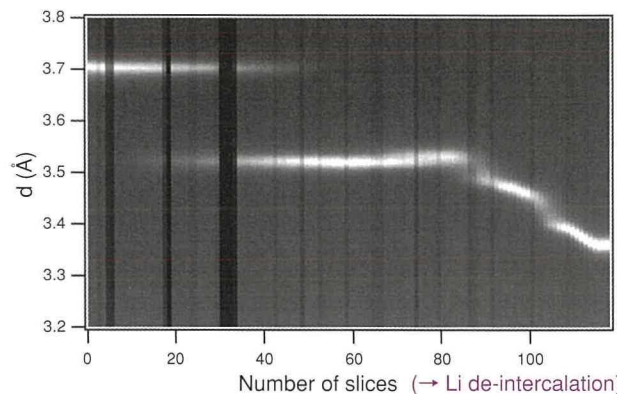
Fig. 3 Neutron Diffraction Pattern in Li De-Intercalation Process (RT, 0.05C)

Fig. 4 shows the dQ/dV curve calculated from the charge-discharge curve. The curve indicates that the phase transition differs at RT and 0°C from stage 2 onward. These results also confirm that operando structural analysis during charge-discharge can be carried out incorporating dQ/dV analysis.
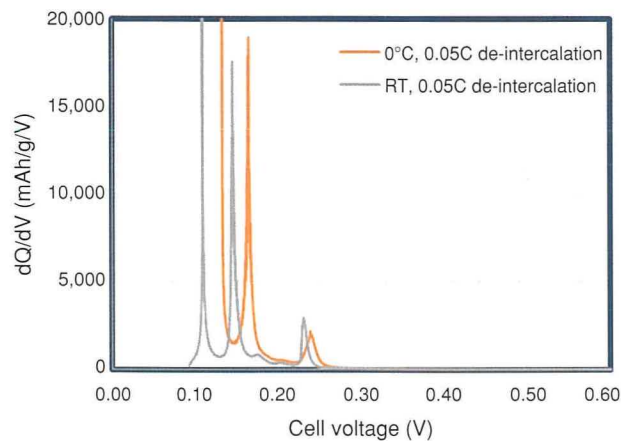
Fig. 4 dQ/dV Curve in Li De-Intercalation Process

Fig. 5 shows an example of the results after isolating the neutron diffraction pattern peaks. The peaks could be clearly isolated even for neutron diffraction patterns expressing multiple phases that include shoulder peaks.
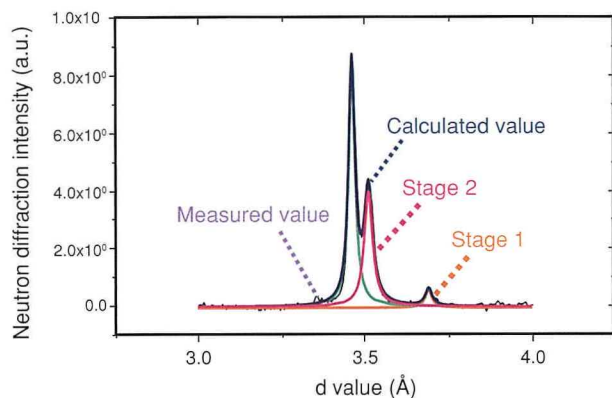
Fig. 5 Peaks Isolated from Neutron Diffraction Pattern (Example)

Neutron diffraction pattern peaks were isolated at state of charge (SOC) intervals of 5% in the Li de-intercalation process. **Figs. 6** and **7** show the state coexistence results of the phases, based on the peak area ratio. In contrast to RT, at which stage structure transition occurred in a single phase, it was found that stage structure transition occurred over multiple phases at 0°C.

These results confirmed the feasibility of operando structural analysis using the developed device configuration for analyzing the phase transition state due to differences in temperature.
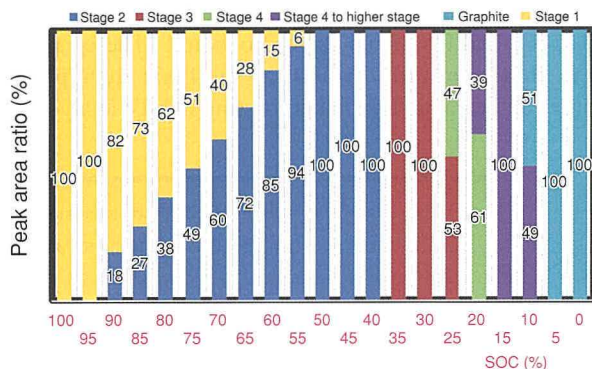
Fig. 6 State of Phase Coexistence in Li De-Intercalation Process (RT, 0.05C)
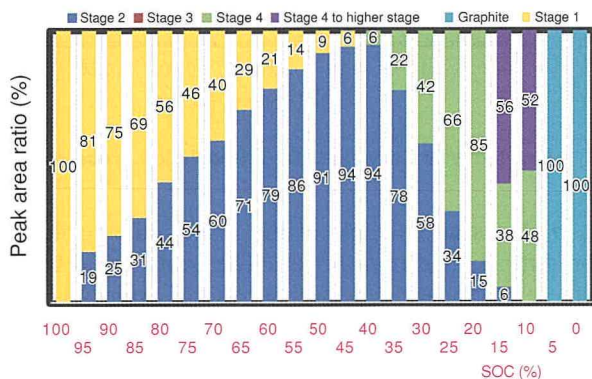
Fig. 7 State of Phase Coexistence in Li De-Intercalation Process (0°C, 0.05C)

From the results described above, it was estimated that structural phase transitions occur over multiple phases during discharge (i.e., the Li de-intercalation process) at low temperatures, and that this phenomenon affects battery low-temperature performance.

3.2 Phase transition analysis at low temperature and high-rate discharge (operando structural analysis by synchrotron radiation diffraction)

Fig. 8 shows the developed tool capable of low-temperature control. This tool can control the temperature from low temperatures to RT.

Fig. 8 Developed Temperature-Controlling Tool for Synchrotron Radiation Diffraction

Fig. 9 shows the synchrotron radiation diffraction results during discharge (i.e., the Li de-intercalation process) with the graphite negative electrode at RT and 0.2C. In the Li de-intercalation process, a clear change can be observed through LiC_6 (2θ: around 7.7°) and LiC_{12} (around 8.1°) to C (around 8.5°). As a result, it was possible to clearly identify the phase transition of graphite.
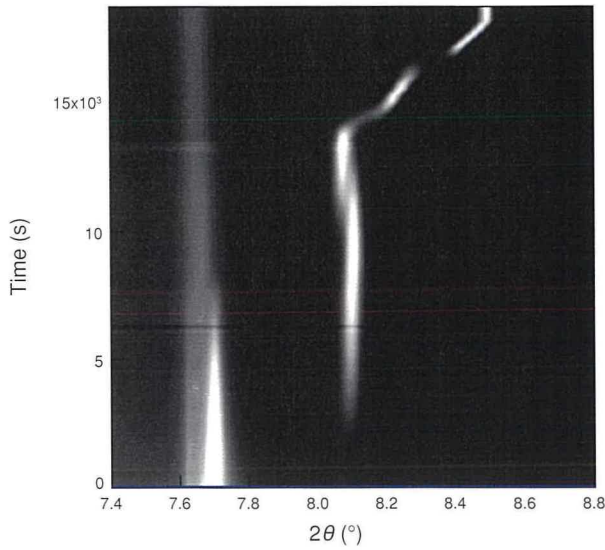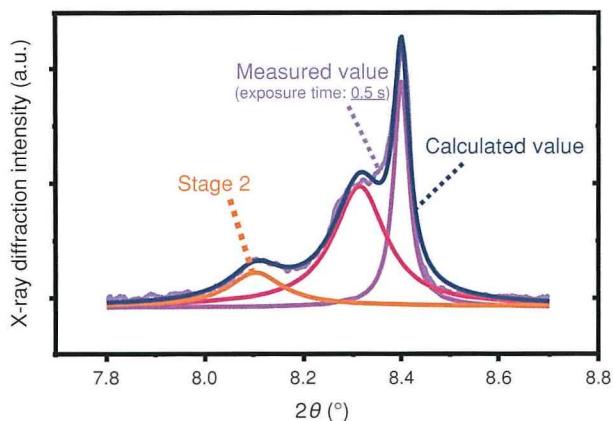
Fig. 9 Synchrotron Radiation Diffraction Pattern in Li De-Intercalation Process (RT, 0.2C)

Fig. 11 State of Phase Coexistence in Li De-Intercalation Process (0°C, 0.2C)

In the same way as the neutron diffraction analysis, synchrotron radiation diffraction pattern peaks were isolated at SOC intervals of 5% in the Li de-intercalation process. **Figs. 10** and **11** show the state coexistence results of the phases, based on the peak area ratio. Even when the discharge rate was set to 0.2C, stage structure transition occurred in a single phase at RT, but occurred over multiple phases at 0°C.

Fig. 12 shows the synchrotron radiation diffraction results during discharge (i.e., the Li de-intercalation process) with the graphite negative electrode at RT and 1C. Differences in LiC_{12} (2θ: around 8.1°) behavior can be seen compared with 0.2C and 1C.

Fig. 10 State of Phase Coexistence in Li De-Intercalation Process (RT, 0.2C)
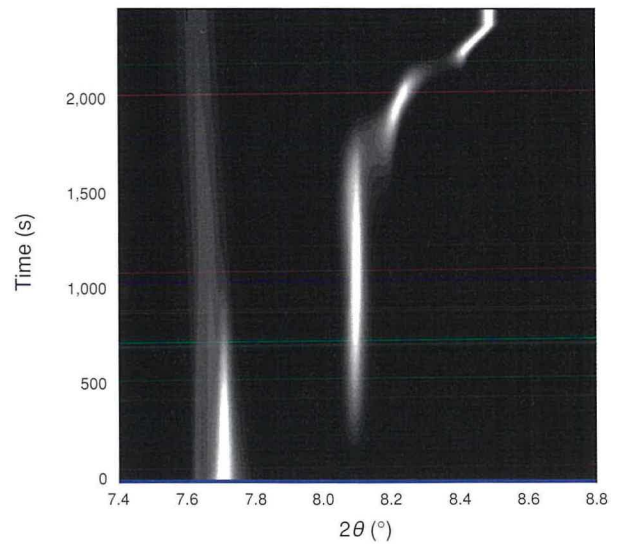
Fig. 12 Synchrotron Radiation Diffraction Pattern in Li De-Intercalation Process (RT, 1C)

Fig. 13 shows an example of the results after isolating the synchrotron radiation diffraction pattern peaks. Analysis was carried out with the exposure time of the detector set to 0.5 s (detection time at 1C). The peaks could be clearly isolated even for synchrotron radiation diffraction patterns expressing multiple phases that include shoulder peaks.

Fig. 13 Peaks Isolated from Synchrotron Radiation Diffraction Pattern (Example)

In the same way as described above, synchrotron radiation diffraction pattern peaks were isolated at SOC intervals of 5% in the Li de-intercalation process at RT and 1C. **Fig. 14** shows the state coexistence results of the phases, based on the peak area ratio. At 0.2C, stage structure transition occurred almost completely in a single phase. However, it was found that stage structure transition occurred over multiple phases at 1C.

These results confirmed the feasibility of operando structural analysis using the developed device configuration for analyzing the phase transition state due to differences in the charge-discharge rate and temperature.
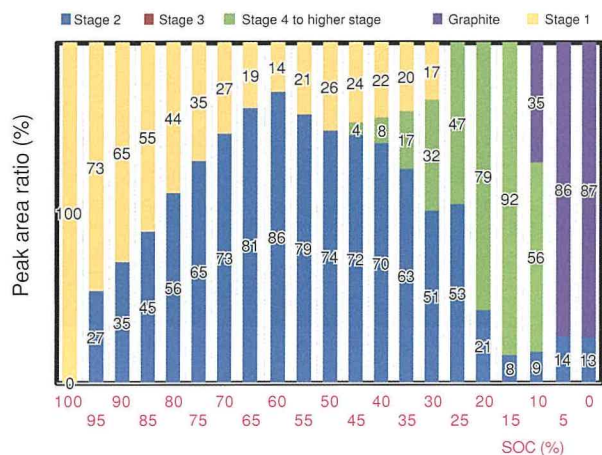
Fig. 14 State of Phase Coexistence in Li De-Intercalation Process (RT, 1C)

From the results described above, it was estimated that stage structure phase transitions occur over multiple phases during discharge (i.e., the Li de-intercalation process) at low temperatures and high discharge rates, and that this phenomenon affects battery performance under these conditions.

3.3 Relationship between quantification of carbon structure and battery performance (analysis of crystallite size distribution by X-ray diffraction)

The carbon crystallite size and distribution were analyzed using the FP method. **Fig. 15** shows an example of the analysis results for crystallite size distribution using the FP method, which were obtained from the X pattern. There is little difference (residual) between the measured and calculated values, indicating the high quality of the calculated results. **Fig. 16** shows the analysis results for crystallite size distribution in these calculations. The crystallite size distribution can be analyzed well at each graphite plane.
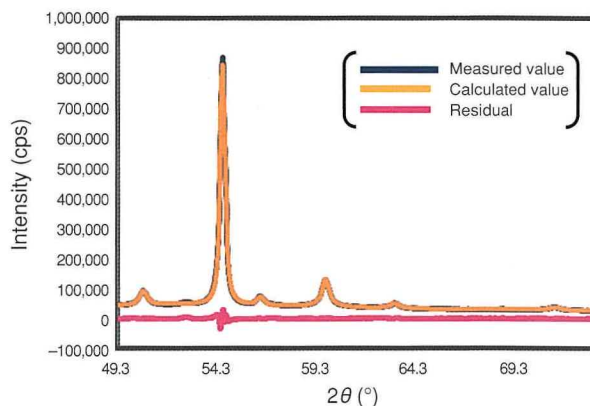
Fig. 15 X-Ray Diffraction Pattern of Carbon
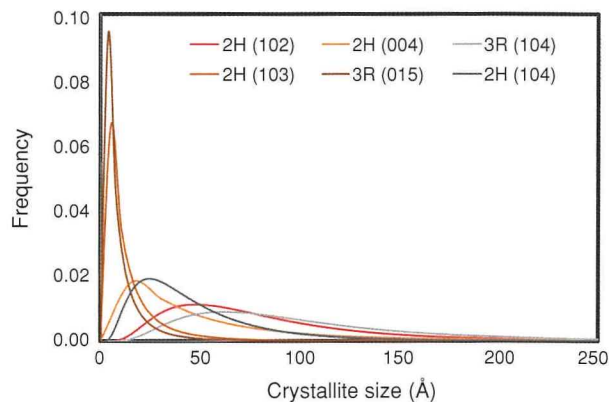
Fig. 16 Crystallite Size Distribution of Graphite

Fig. 17 shows the relationship between the crystallite size distribution of the graphite (102) plane and battery low-temperature characteristics. The discharge capacity (i.e., the specific capacity with respect to the amount of cathode active material) of the full cell at 0°C and 0.5C after charging at 0°C and 0.5C is shown as the low-temperature characteristics. The results indicate that the low-temperature characteristics improve

as the crystallite size and distribution of the graphite (102) plane decreases. The same results were also obtained for the relationship between the crystallite size distribution of the graphite (102) plane and the high-rate discharge characteristics of the battery. The crystallite size distribution of the graphite (102) plane is thought to express the Li diffusivity, considering the diffusion paths of the Li.
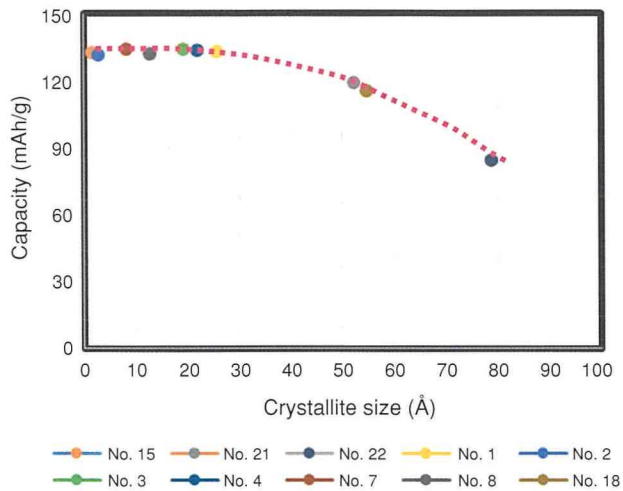

Fig. 17 Relationship between Crystallite Size (Distribution) and Battery Low-Temperature

These results suggest that analyzing the crystallite size and distribution of carbon (graphite) is a feasible way of inferring the low-temperature and high-rate discharge characteristics of a battery.

3.4 Analysis of effect of changes in carbon structure (crystallinity) on phase transition during charge-discharge

Differences in the phase transition during charge-discharge were investigated using sample A (high crystallinity) and sample B (low crystallinity). **Fig. 18** shows the dQ/dV curve in the Li de-intercalation process calculated from the charge-discharge curve. The curve indicates that the phase transition differs between the samples, which have different crystalline properties (i.e., different crystal sizes), from stage 2 onward.
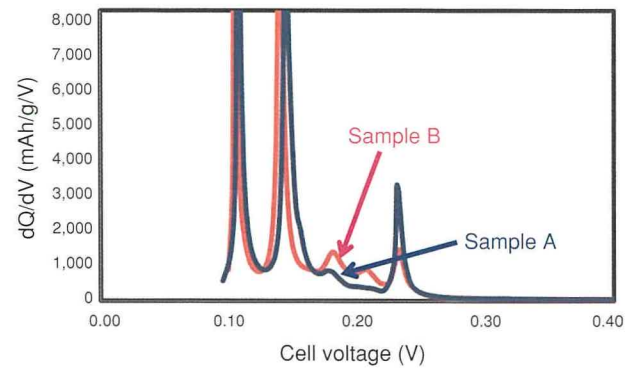
Fig. 18 dQ/dV Curve in Li De-Intercalation Process

In addition, **Figs. 19** and **20** show the phase transition states as analyzed by synchrotron radiation diffraction using sample A (high crystallinity) and sample B (low crystallinity). Here, the transition process to stage 3 is analyzed in detail. The results show that the structure when transitioning to stage 3 differs in accordance with the crystallinity (i.e., the crystallite size). As shown in **Fig. 19**, sample A (high crystallinity) has shoulder peaks and transitions to stage 3 over multiple phases. In contrast, sample B (low crystallinity) has no shoulder peaks in the transition process to stage 3, and the phase transition occurs almost completely in a single phase.
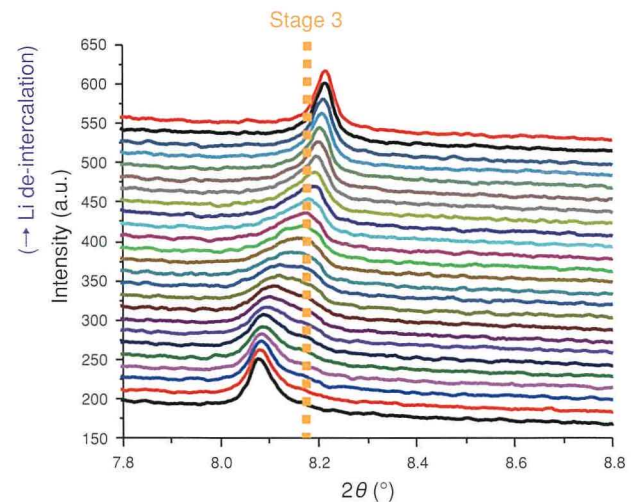
Fig. 19 X-Ray Diffraction Pattern in Stage 3 Transition Process (Sample A, Crystallite Size: Large)
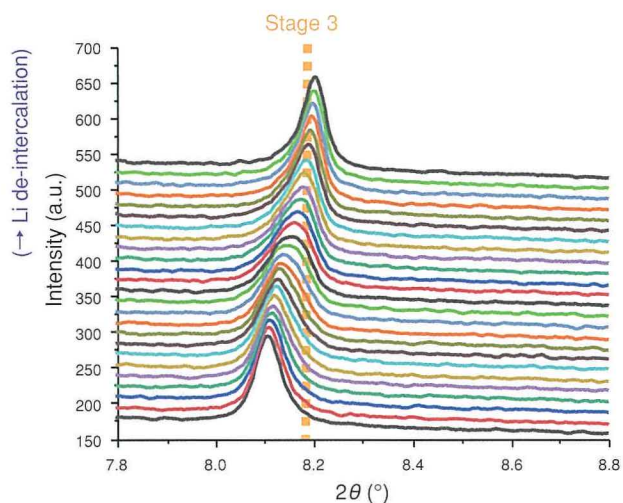
Fig. 20 X-Ray Diffraction Pattern in Stage 3 Transition Process (Sample B, Crystallite Size: Small)

These results suggest that reducing the crystallinity of carbon (graphite) (i.e., reducing the crystallite size) increases the area of edge planes and lattice defects. This facilitates inter-layer transition and the like and boosts Li diffusivity, thereby making transition more likely to occur in a single phase.

4. Conclusions

(1) Synchrotron radiation diffraction and neutron diffraction enabled low-temperature operando structural analysis incorporating dQ/dV to be applied to storage batteries (control is possible from -10 to 50°C).

(2) It was found that transition in multiple phases is more likely to occur at low temperatures than at RT, and at high discharge rates rather than low discharge rates.

(3) The results of the analysis also found that the crystallinity of the carbon (graphite) affects the low-temperature and high-rate discharge characteristics of a battery.

(4) A phenomenon was identified in which differences in carbon (graphite) crystallinity caused differences in phase transition during charge-discharge. A battery reaction mechanism was then identified through which this phenomenon affects low-temperature and high-rate charge-discharge characteristics, thereby facilitating the formation of development guidelines for new materials.

An objective for the future is to use these guidelines in the development of next-generation storage battery materials.

Finally, these research results were obtained as part of the RISING 2 initiative carried out under the auspices of the New Energy and Industrial Technology Development Organization (NEDO). The authors would like to extend their sincere gratitude to everyone involved.

References

(1) S. Takagi et al. "Identification of Physical Properties of Carbon that Affect Battery Performance and Estimation of Performance-Improvement Mechanism Using In-Situ Crystalline Structural Analysis" (in Japanese). *Abstracts of the 58th Battery Symposium in Japan* (2017) p. 1B02.

(2) S. Takagi et al. "Operando Structural Analysis of Graphite Negative Electrode by Synchrotron Radiation Diffraction" (in Japanese). *Abstracts of the 59th Battery Symposium in Japan* (2018) p. 2E14.

(3) M. Yonemura et al. "Development of SPICA, New Dedicated Neutron Powder Diffractometer for Battery Studies." *Journal of Physics: Conference Series* Vol. 502 (2014).

(4) S. Takagi et al. "Operando Structural Analysis of Graphite Negative Electrode by Neutron Diffraction" (in Japanese). *Abstracts of the 2018 Fall Meeting of the Electrochemical Society of Japan* (2018) p. 1E04.

(5) T. Ida et al. "Diffraction Peak Profiles from Spherical Crystallites with Lognormal Size Distribution." *Journal of Applied Crystallography* Vol. 36 (2003) pp. 1107-1115.

(6) S. Takagi et al. "Analysis of Carbon Crystallite Size Distribution and its Effects on Battery Low-Temperature Performance" (in Japanese). *Abstracts of the 45th Annual Meeting of the Carbon Society of Japan* (2018) p. 1A06.

Author

S. TAKAGI

Self-Forming Interface of LiFePO$_4$ Cathode in Sulfide All-Solid-State Battery

Mayuko Osaki[*1]
Manabu Imano[*2]
Hideyuki Koga[*2]
Yukinari Kotani[*1]
Shinji Nakanishi[*1]
Hideki Iba[*1]

Abstract

All-solid-state batteries are regarded as a promising next-generation storage battery with a high energy density that cannot be surpassed by conventional lithium-ion batteries. Cathode material design is an important factor in achieving a high energy density. Since resistance layers form due to side reactions at the interface between the cathode active material and solid electrolyte in sulfide all-solid-state batteries, the active materials adopted in these batteries are generally coated with a buffer layer comprising an oxide or the like. This research applied lithium iron phosphate (LiFePO$_4$), which is already adopted in conventional lithium-ion batteries, to an all-solid-state battery. A new phenomenon was discovered in which a stable and low-resistance phase self-formed at the interface between the LiFePO$_4$ active material and sulfide solid electrolyte. As a result, an all-solid-state battery that exhibits the theoretical capacity of the LiFePO$_4$ active material was successfully achieved without a coating layer.

Keywords: *electric vehicle, lithium battery, all-solid-state battery, lithium iron phosphate (LiFePO$_4$), sulfide solid electrolyte, cathode, solid interface, phase interface, coating-free, interface reaction, self-forming, film*

Special Feature

1. Introduction

1.1 Background

The automotive industry is undergoing a dramatic transformation prompted by the entry of IT companies and electronic appliance manufacturers into the market and the rapid economic growth of developing countries. These changes are leading toward the realization of a new mobility society. Vehicle electrification has become an inescapable trend and competition in the field of battery development is growing increasingly intense by each passing year. Electric vehicles (EVs), which run purely on battery power and therefore use a larger number of batteries than hybrid vehicles (HVs), require safe, low-cost batteries with a high energy density.

All-solid-state lithium batteries are one type of next-generation storage battery. Due to their high degree of design flexibility and excellent safety performance, these high-energy density batteries are being increasingly regarded as a practical successor to conventional lithium-ion (Li-ion) batteries. Of the different varieties of all-solid-state batteries, research has focused on those that use a sulfide solid electrolyte. This solid electrolyte has good formability and an ion conductivity as high as conventional liquid electrolytes.

1.2 Issues of sulfide all-solid-state battery cathodes

It has been reported that, in sulfide all-solid-state batteries, the transition metal and sulfur generates mutual diffusion at the interface between the cathode active material and the sulfide solid electrolyte, and that repeated charging and discharging of the battery has a negative effect on battery characteristics.[1] This mutual diffusion is usually suppressed by coating a thin oxide layer (Li$_2$SiO$_3$, LiNbO$_5$, or the like) on the cathode active material surface.[1][2]

Since lithium iron phosphate (LiFePO$_4$) contains PO$_4$ tetrahedral polyanions, which contribute to the highly stable crystalline structure, it has excellent durability and safety performance, as well as high energy density. For these reasons, it is used as a cathode active material in conventional liquid-type Li-ion batteries.[3] However, there are very few applications of LiFePO$_4$ in all-solid-state batteries,[4] and the theoretical capacity of a LiFePO$_4$ cathode has not been exhibited in an all-solid-state battery. Since the electron conductivity of LiFePO$_4$ is lower than general layered oxides used as cathode active materials, it is desirable to form a surface coating on microscopic particles using carbon. However, issues of applying this material to an all-solid-state battery include the coating method to form a uniform nano-level oxide film and the blending with the electrolyte.

Since it is difficult to create a uniform nano-level oxide coating on microscopic LiFePO$_4$ particles, this research studied how to electrochemically control the interface structure with the aim of creating a low-resistance interface. This research also studied the details of the interface states using various analysis methods and a model electrode to identify the mechanism of this low-resistance interface.

*1 Advanced Material Engineering Div., Advanced R&D and Engineering Company
*2 Battery Material Engineering & Research Div., Powertrain Company

2. Experimental Methodology

2.1 Synthesis of LiFePO$_4$ powder

First, sub-μm LiFePO$_4$ particles were synthesized using the standard hydrothermal technique.[5] The LiCl, H$_3$PO$_4$, and FeSO$_4$/H$_2$O precursors were dissolved in water with the Na$_2$SO$_3$ reductant, and placed in a hydrothermal vessel. The vessel was filled with N$_2$ gas and sealed, and then heated at 200°C to generate the hydrothermal reaction. The resulting LiFePO$_4$ sediment was further dispersed into a mixed solution of water and polyethylene glycol using a ball mill. This suspension was then spray-dried under a 180°C atmosphere to form a granulate coated with a carbon precursor. This granulate was sintered for one hour at 750°C to obtain secondary particles with a size of approximately 10 μm and coated in a thin carbon layer with a thickness of several nm.

Since the contact interface with the solid electrolyte cannot be sufficiently ensured by these particles in an all-solid-state battery, the secondary particles were further broken down to an average size of 0.9 μm using a jet mill. This process facilitates mixing with the solid electrolyte at a primary particle level, and allows carbon to be partially coated on the surface.

2.2 Fabrication of battery cell and electrochemical measurement

The sulfide solid electrolyte at the cathode used amorphous Li$_2$S-P$_2$S5-LiI[6] (σ_{ion} = 3.0 mS/cm) that was atomized to match the size of the LiFePO$_4$ particles. The LiFePO$_4$ and Li$_2$S-P$_2$S$_5$-LiI solid electrolyte were mixed with a vapor-grown carbon nano-fiber (VGCF) conductive additive at a volume ratio of 10:10:1 to form the cathode mixture. The counter electrode was prepared by mixing lithium titanate (Li$_4$Ti$_5$O$_{12}$)[7] with the same solid electrolyte and VGCF at a volume ratio of 30:20:1. The cathode/anode molar ratio was set to 2.4 to utilize the stable operating range of Li$_4$Ti$_5$O$_{12}$ around 1.5 V vs. Li/Li$^+$. A triple-layer pellet, consisting of a cathode mixture layer, Li$_2$S-P$_2$S$_5$-LiI solid electrolyte separator layer, and counter electrode layer, was prepared by pressing at 400 MPa.

The galvanostatic charge-discharge measurements were performed under C/10 conditions (current density: 0.40 mAcm^{-2}) at 60°C. The charge cut-off voltage was fixed at 2.5 V (4.1 V vs. Li/Li$^+$) and three discharge cut-off voltage levels were set: 0.7, 0.5, and 0 V. Each of these batteries was then evaluated.

3. Results and Discussion

3.1 Electrochemical characteristics

Fig. 1 shows the specific capacitance of LiFePO$_4$/Li$_4$Ti$_5$O$_{12}$ sulfide all-solid-state batteries during repeated charge-discharge cycles with different discharge cut-off voltages. Although the LiFePO$_4$ was not coated with an oxide, the discharge capacity of

the battery that discharged down to a cut-off voltage of 0 V (1.6 V vs. Li/Li$^+$) increased after several charge-discharge cycles. This battery realized the theoretical capacity of LiFePO$_4$ (approximately 170 mAh/g). In contrast, the capacity of the battery with the 0.7 V cut-off voltage (2.3 V vs. Li/Li$^+$) fell over several charge-discharge cycles, and the capacity of the battery with the 0.5 V cut-off voltage (2.1 V vs. Li/Li$^+$) fell by a large amount before increasing slightly.

Fig. 2 shows the charge-discharge curves of the battery with the 0 V discharge cut-off voltage. In the profiles of the first and second cycles, large polarization appears between charge and discharge. In particular, a discharge plateau occurred close to 2.6 V vs. Li/Li$^+$, which is substantially different from the theoretical potential of LiFePO$_4$ (3.4 V vs. Li/Li$^+$). Subsequently, from the third cycle, repeated charging and discharging resulted in a simultaneous increase in discharge voltage and capacity, and the polarization became smaller.
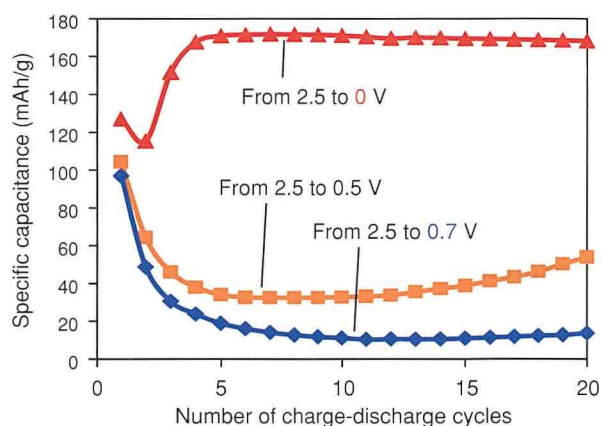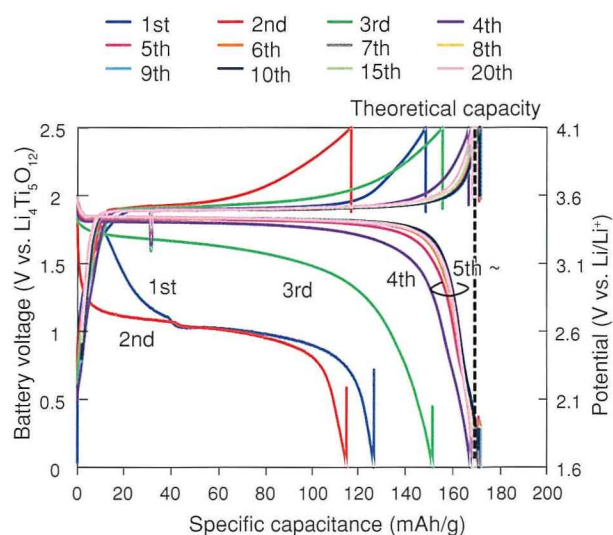

Fig. 1 Charge-Discharge Cycling Performance of LiFePO$_4$/Li$_4$Ti$_5$O$_{12}$ Batteries

Fig. 2 Charge-Discharge Curves of LiFePO$_4$/Li$_4$Ti$_5$O$_{12}$ Battery

As a large shift in the polarization was observed during the first few charge-discharge cycles, the electrical resistance of the battery was analyzed. An LiAl reference electrode was placed in the separator layer and the alternating current (AC) impedance between the cathode and the LiAl reference electrode was measured during the charge-discharge cycle process of the battery with the 0 V discharge cut-off voltage. **Fig. 3** shows the results. The resistance/capacitance caused by the charge transfer reactions of the cathode active material/electrolyte interface increased for the first two or three cycles. The resistance then continued to decrease from the fourth to the 100th cycle. This behavior is a new phenomenon unreported in previous literature.

electron beam diffraction pattern of these bright portions identified diffraction spots corresponding to 2.67 Å (red), 2.16 Å (blue), and 1.77 Å (green) in real space. These results correspond to the diffraction planes of FeS (hexagonal) and FeS_2 (cubic) (bottom left of **Fig. 4**). These results suggest that iron sulfide is formed at the interface in the initial charge-discharge cycles. This means that chemical reactions are occurring between the LiFePO₄ and solid electrolyte close to the interface. Since the ion conductivity of iron sulfide is low ($\sigma_{ion} < 10^{-7}$ mS/cm), these iron sulfide side reaction products seem to have an effect on the resistance of the cathode active material/electrolyte interface.

Fig. 3 Nyquist Plot between LiFePO₄ Cathode and Reference Electrode (SOC 40, 1 M to 10 mHz)
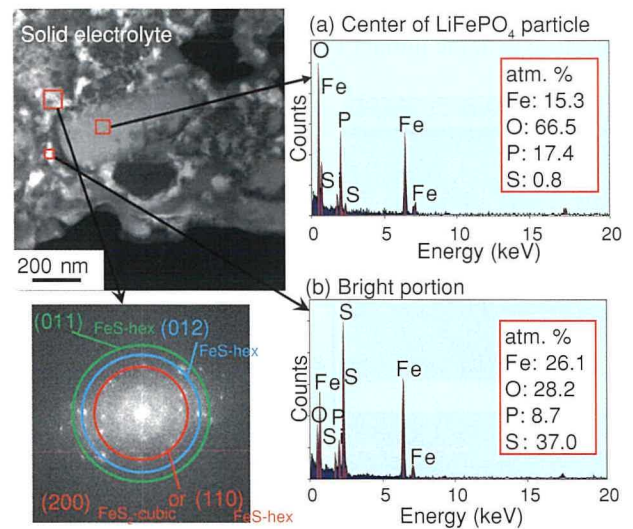
Fig. 4 Cross-Section of LiFePO₄ Cathode and Elemental Analysis after Two Charge-Discharge Cycles (Si Derives from the Focused Ion Beam (FIB) Grid)

3.2 Analysis of cathode active material/solid electrolyte interface state

The chemical phenomena, in which the charge transfer resistance of the cathode exhibits large shifts over the charge-discharge cycles, were investigated using a battery that was charged and discharged with a 0 V discharge cut-off voltage. Cross-sections of the cathode mixture were observed and elemental analysis carried out using scanning transmission electron microscopy with energy dispersive X-ray spectroscopy (STEM-EDS). A JEOL JEM-ARM200F transmission electron microscope was used and the accelerating voltage was set to 200 kV. **Fig. 4** shows the analysis results of the cathode after two charge-discharge cycles at a cut-off voltage of 0 V. In the high-angle annular dark field (HAADF) image at the top left, bright portions (b) (indicating the existence of a heavy element) were present at the outside of the LiFePO₄ particle (a) at the interface with the sulfide solid electrolyte. In contrast, the image also shows a comparatively darker layer to the inside of the particle. Elemental analysis of the bright portions found strong evidence of iron (Fe) and sulfur (S), indicating that Fe from the LiFePO₄ particles are diffused throughout the solid electrolyte. The

Similarly, **Fig. 5** shows a HAADF-STEM image of the cathode cross-section after twenty charge-discharge cycles. The bright portions observed after two cycles in **Fig. 4** (iron sulfide) have almost disappeared. These results suggest that the drop in cathode active material/electrolyte interface resistance from the fourth cycle may be caused by reactions that change the iron sulfide due to the discharge voltage being lowered to 0 V.
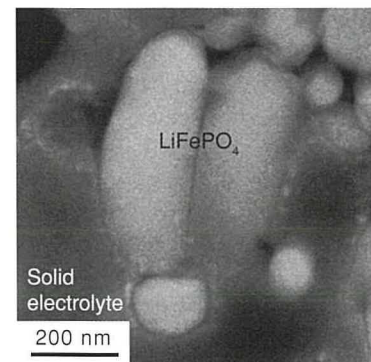

Fig. 5 Cross-Section of LiFePO₄ Cathode after Twenty Charge-Discharge Cycles

Next, the details of the LiFePO$_4$/sulfide solid electrolyte interface structure were investigated after twenty charge-discharge cycles (**Fig. 5**) and before charge-discharge. **Fig. 6** shows bright-field STEM (BF-STEM) images of each interface at a high resolution, as well as EDS elemental analysis results. Compared to the initial state before charge-discharge, a different phase with a thickness between several and ten nm formed at the interface between the LiFePO$_4$ particle and solid electrolyte after twenty cycles. This different phase is mainly non-crystalline (amorphous). Local elemental analysis of the phase using EDS found a lower Fe concentration than inside the LiFePO$_4$ particle, and that the phase contains phosphorous (P), oxygen (O), and S. This phase is likely to be a stable residual surface layer with less Fe after the Fe diffused from the LiFePO$_4$ particle surface to the solid electrolyte in the initial cycles.
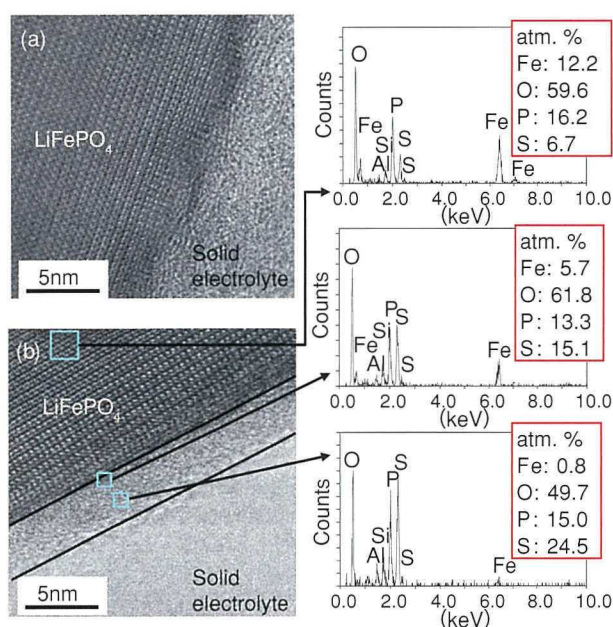
Fig. 6 LiFePO$_4$/Sulfide Solid Electrolyte Interface: (a) Before Charge-Discharge, (b) After Twenty Charge-Discharge Cycles (Al Derives from the Sample Holder)

3.3 Analysis of model interface using thin film

In the battery with a discharge cut-off voltage of 0 V, to analyze the mechanism by which the iron sulfide disappeared and to chemically identify the amorphous interface phase that formed, a sulfide all-solid-state battery with a LiFePO$_4$ thin film was fabricated and verified. The LiFePO$_4$ thin film was created using sputter deposition to form a 500 nm-thick layer on platinum (Pt) foil and sintered at 600°C in a reducing atmosphere. The LiFePO$_4$ thin film was adopted as the cathode after confirming its crystalline structure by X-ray diffraction (XRD). Amorphous Li$_2$SP$_2$S$_5$-LiI was used as the separator layer, and a Li-In alloy was utilized for the counter electrode.

First, the cyclic voltammetry of a battery with the LiFePO$_4$ thin film and the Li-In alloy counter electrode was measured

(**Fig. 7**). In the same way as the galvanostatic measurement, the reduction side sweep of the initial cycles created a peak close to a potential of 2.4 V vs. Li/Li$^+$, after which, the potential increased in the subsequent cycles (**Fig. 7** (1)). This peak is thought to correspond with the discharge plateau around 2.6 V vs. Li/Li$^+$ that occurred in the first and second cycles of the galvanostatic measurement in **Fig. 2**. In addition, a further smaller peak appeared close to 1.85 V vs. Li/Li$^+$. As the number of cycles increased, the peak position remained virtually unchanged, but became gradually smaller (**Fig. 7** (2)). According to the charge-discharge cycle characteristics shown in **Fig. 1**, a discharge cut-off voltage of 0.5 V (2.1 V vs. Li/Li$^+$) or less results in an increase in capacity in accordance with the number of cycles. The reduction reaction derived at this peak close to 1.85 V vs. Li/Li$^+$ is thought to indicate the decomposition of the iron sulfide resistance layer.
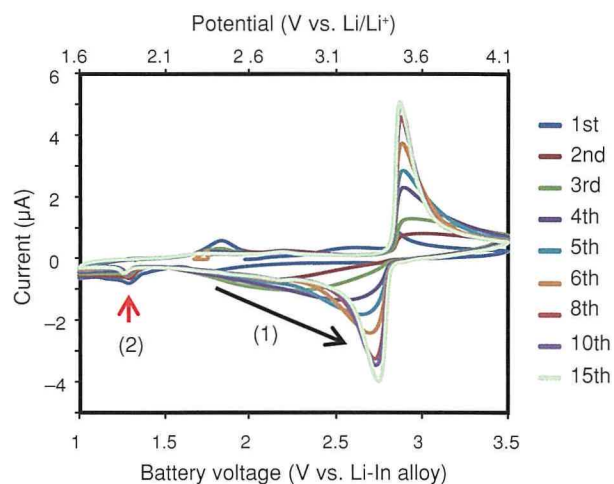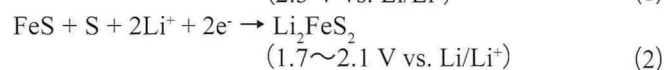

Fig. 7 Cyclic Voltammogram of LiFePO$_4$ Thin Film/Li-In Alloy Battery

Iron sulfide is used as an electrode material, and is known to react with Li ions. The literature shows that, in addition to the Li ion insertion reactions expressed by Equations (1) and (2), the conversion reactions expressed by Equations (3) and (4) occur at lower potentials.[8][9] Although the reactions that insert Li ions are reversible, the conversion reactions result in the decomposition of iron sulfide, and are not reversible. Therefore, the peak close to 1.85 V vs. Li/Li$^+$ is assumed to represent conversion-like reactions that decompose the iron sulfide of a resistance layer.
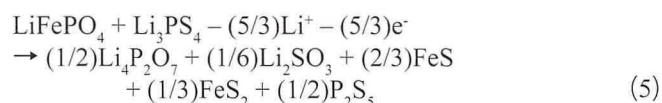
$$FeS_2 + 2Li^+ + 2e^- \rightarrow Li_2FeS_2$$
$$(2.3 \text{ V vs. Li/Li}^+) \qquad (1)$$

$$FeS + S + 2Li^+ + 2e^- \rightarrow Li_2FeS_2$$
$$(1.7\sim2.1 \text{ V vs. Li/Li}^+) \qquad (2)$$

$$Li_2FeS_2 + 2Li^+ + 2e^- \rightarrow Fe + 2Li_2S$$
$$(1.6 \text{ V vs. Li/Li}^+) \qquad (3)$$

$$FeS + 2Li^+ + 2e^- \rightarrow Fe + 2S + Li_2S$$
$$(1.75 \text{ V vs. Li/Li}^+) \qquad (4)$$
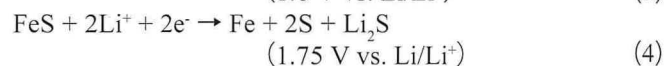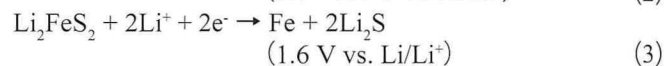
Next, X-ray absorption spectroscopy (XAS) was applied to the LiFePO$_4$ thin film/sulfide solid electrolyte interface. In the same way as a powder battery, the thin cathode film was peeled from the separator after galvanostatic charge-discharge (1.6 to 4.1 V vs. Li/Li$^+$) at a current density of 0.8 µAcm^{-2} equivalent to 0.1C. The thin cathode film/solid electrolyte interface phase was then analyzed. This phase was detected using a surface-sensitive technique called the total electron yield (TEY). **Fig. 8** shows the X-ray absorption near edge structure (XANES) spectra of the L absorption edge of P and K absorption edge of S at the interface on the cathode side. At the L absorption edge of P, the a/c peak ratio after forty cycles increases from 0.55 to 0.95. This indicates an increase in phosphate chains in the crystalline structure (O-mediated links between PO$_4$ tetrahedrons centered on the P with neighboring PO$_4$ tetrahedrons). In other words, the chemical composition of the LiFePO$_4$ changes into one with less O, such as pyrophosphoric acid or a metaphosphate.[10] In contrast, after forty cycles, the K absorption edge of S shows strong peaks at 2,478 eV, which is derived from SO$_3^-$ ions, and at 2,482 eV that corresponds to SO$_4^{2-}$. These results demonstrate that the different phase at the interface phase is an amorphous substance that can be chemically expressed as xLi$_2$O-(100-x) P$_2$O$_5$-Li$_2$SO$_y$ (x ≤ 67, y = 3 to 4). This phase is thought to be stable since S is present as sulfuric acid in a high state of oxidation as well as containing virtually no Fe in the interface. Consequently, this phase functions to suppress further chemical reactions due to diffusion of the transition metal and sulfur between the LiFePO$_4$ and sulfide solid electrolyte.

This amorphous Li$_2$O-P$_2$O5 substance also has Li ion conductivity. Furthermore, it has also been reported that Li ion conductivity increases when Li$_2$SO$_3$ and Li$_2$SO$_4$ is mixed.[11] Therefore, the reduction in resistance as the number of cycles increases is thought to be caused by the disappearance of iron sulfide and the increase in Li ion conductivity at the interface phase.

3.4 Summary of reaction mechanism of LiFePO₄ cathode interface

To summarize the results described above, **Fig. 9** shows an outline of the phenomena that are assumed to occur. In the first few cycles, during charging, Fe ions are extracted and diffuse to the solid electrolyte side from the surface of the LiFePO$_4$ particles. The chemical reaction shown in Equation (5) then occur at the LiFePO$_4$/sulfide solid electrolyte interface and an iron sulfide resistance layer forms.

$$\text{LiFePO}_4 + \text{Li}_3\text{PS}_4 - (5/3)\text{Li}^+ - (5/3)\text{e}^-$$
$$\rightarrow (1/2)\text{Li}_4\text{P}_2\text{O}_7 + (1/6)\text{Li}_2\text{SO}_3 + (2/3)\text{FeS}$$
$$+ (1/3)\text{FeS}_2 + (1/2)\text{P}_2\text{S}_5 \qquad (5)$$

During discharging, this iron sulfide reacts with Li ions at a lower potential than LiFePO$_4$. Therefore, the Li ions that had been conducted through the solid electrolyte are inserted by the discharge potential of the iron sulfide. When the voltage drops even lower, the iron sulfide resistance layer is decomposed by a reduction reaction at close to 1.85 V vs. Li/Li$^+$. When this cycle is repeated, the Fe ions activated by decomposition diffuse throughout the solid electrolyte and, concurrently, the voltage increases to the potential of the LiFePO$_4$.

At the interface, a phase with less Fe and that has a thickness between several and ten nm, which can be expressed as xLi$_2$O-(100-x)P$_2$O$_5$-Li$_2$SO$_y$ (x ≤ 67, y = 3 to 4), forms on the surface of the LiFePO$_4$ particles. Since this interface phase is stable and has Li ion conductivity, it suppresses further chemical reactions between the LiFePO$_4$ and sulfide solid electrolyte. This type of reaction process does not occur in layered oxide cathodes or other oxide active materials, and is thought to be particular to polyanions, including LiFePO$_4$.
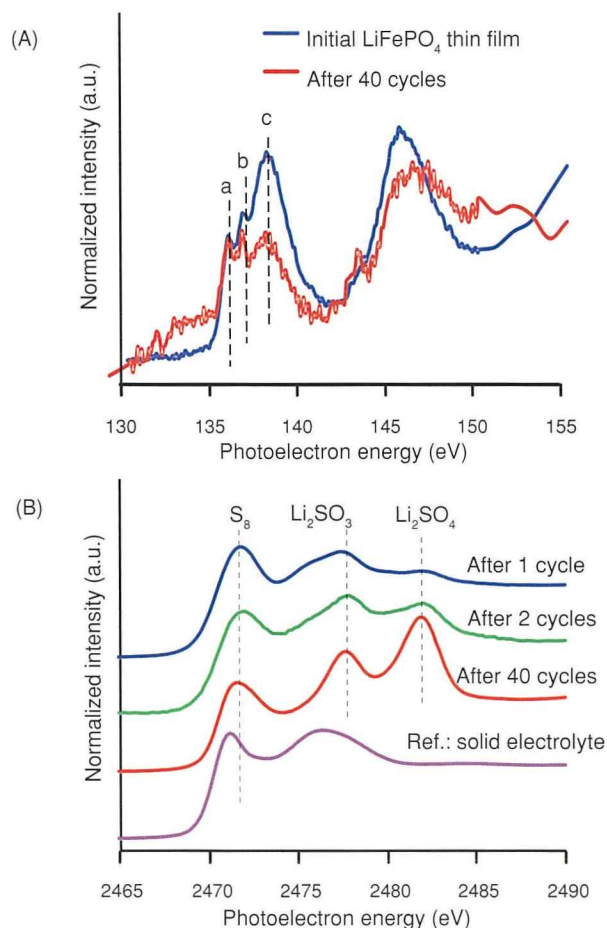
(A) Initial LiFePO₄ thin film / After 40 cycles

(B) S₈, Li₂SO₃, Li₂SO₄ — After 1 cycle / After 2 cycles / After 40 cycles / Ref.: solid electrolyte

Fig. 8 XANES Spectra of LiFePO₄ Thin Film Interface: (A) L Absorption Edge of P, (B) K Absorption Edge of S

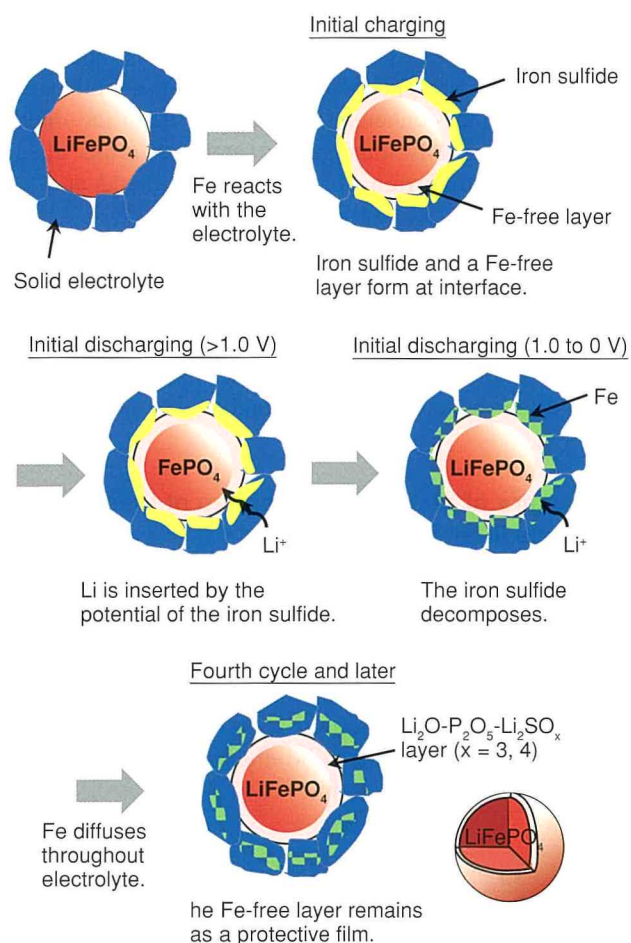Fig. 9 Outline Diagram of Reactions at LiFePO$_4$ Cathode Interface

Initial charging

LiFePO$_4$

Solid electrolyte

Fe reacts with the electrolyte.

Iron sulfide

LiFePO$_4$

Fe-free layer

Iron sulfide and a Fe-free layer form at interface.

Initial discharging (>1.0 V)

FePO$_4$

Li$^+$

Li is inserted by the potential of the iron sulfide.

Initial discharging (1.0 to 0 V)

Fe

LiFePO$_4$

Li$^+$

The iron sulfide decomposes.

Fourth cycle and later

Fe diffuses throughout electrolyte.

LiFePO$_4$

Li$_2$O-P$_2$O$_5$-Li$_2$SO$_x$ layer (x = 3, 4)

LiFePO$_4$

he Fe-free layer remains as a protective film.

References

(1) A. Sakuda et al. *Chemistry of Materials* Vol. 22 (2010) pp. 949-956.
(2) N. Ota et al. *Electrochemistry Communications* Vol. 9 (2007) pp. 1486-1490.
(3) S. Chung et al. *Nature Materials* Vol. 1 (2002) pp. 123-128.
(4) A. Sakuda et al. *Chemistry Letters* Vol. 41 (2012) pp. 260-261.
(5) Y. Maeyoshi et al. *J. Power Sources* Vol. 337 (2017) pp. 92-99.
(6) S. Ujie et al. *J. Solid State Electrochemistry* Vol. 17 (2013) pp. 675-680.
(7) H. Kitaura et al. *J. Material Research* Vol. 25 No. 8 (2010) pp. 1548-1553.
(8) K. Takada et al. *J. Electrochemical Society* Vol. 148 No.10 (2001) pp. A1085-A1090.
(9) T. Yersak et al. *J. Electrochemical Society* Vol. 160 No. 8 (2013) pp. A1009-A1015.
(10) Z. Yin et al. *Wear* Vol. 202 (1997) pp. 172-191.
(11) M. Ganguli et al. *Solid State Ionics* Vol. 122 (1999) pp. 23-33.

Authors

M. OSAKI

M. IMANO

H. KOGA

Y. KOTANI

S. NAKANISHI

H. IBA

4. Conclusion

The application of an LiFePO$_4$ cathode active material to a sulfur all-solid-state battery was studied. A phenomenon was discovered in which a low-resistance LiFePO$_4$/sulfide solid electrolyte interface can be formed by charge-discharge control. Detailed investigations of this interface identified the self-formation of a stable phase with Li ion conductivity. This phase creates a low-resistance cathode interface even on microscopic particles, without the need for an oxide coat. In addition, this self-formation function may be an effective means of maintaining durability through the self re-formation of this layer, even if the coating layer degrades and cracks due to the volume expansion and contraction of the active material during charging and discharging.

This research is the first practical demonstration of excellent battery characteristics at the level of the theoretical capacity of a sulfide all-solid-state battery using an olivine cathode. An LiFePO$_4$ cathode is highly reliable in terms of durability and safety, and has the potential to accelerate the practical adoption of all-solid-state batteries.

Development of Test Methodology for Internal Short-Circuits Caused by Foreign Matter in Lithium-Ion Batteries

Shinichi Hamasaki[*1]
Yuya Ishihara[*1]
Kensaku Miyazawa[*1]
Tetsuya Kaneko[*1]

Abstract

This article describes a safety test methodology that assumes the occurrence of an internal short-circuit in a lithium-ion battery installed in an electrified vehicle. For lithium-ion batteries, the ability to properly test states arising from short-circuits generated by foreign matter inside the battery is extremely important. In previous internal short-circuit test methods, the battery was disassembled, minute metal particles inserted inside the battery, and pressure applied to generate an internal short-circuit. This test could not be carried out without a high level of specialist knowledge and technology. Therefore, a simpler methodology was developed that generates small short circuits inside the battery by an external mechanical means, thereby eliminating the need to disassemble the battery. Efforts are currently under way to incorporate this methodology into global standards.

Keywords: *electrified vehicle, lithium-ion battery, internal short-circuit test, IEC*

Special Feature

1. Introduction

As the automotive industry stands on the verge of a once-in-a-century period of profound transformation, the progress of vehicle electrification and automation is increasing at a rapid pace. At the same time, with greater expectations being placed on vehicle electrification from the standpoint of the environment, Toyota Motor Corporation is working to reduce CO_2 emissions through its New Vehicle Zero CO_2 Emissions Challenge, which is a part of the Toyota Environmental Challenge 2050. **Fig. 1** shows historical and predicted milestones for the electrification of Toyota's vehicle lineup. Toyota is aiming to reduce the tailpipe CO_2 emissions of new cars by 90% in 2050 compared to 2010 by expanding the proportion of electrified vehicles.

Fig. 1 Vehicle Electrification Milestones

Fig. 2 shows the sales and CO_2 emissions savings achieved by Toyota's HVs. Compared with gasoline-powered vehicles in the same class, Toyota's HVs have saved the equivalent of 77 million tons of CO_2 emissions. Toyota intends to expand its lineup of electrified vehicles to achieve the targets laid out in the New Vehicle Zero CO_2 Emissions Challenge.[(1)]
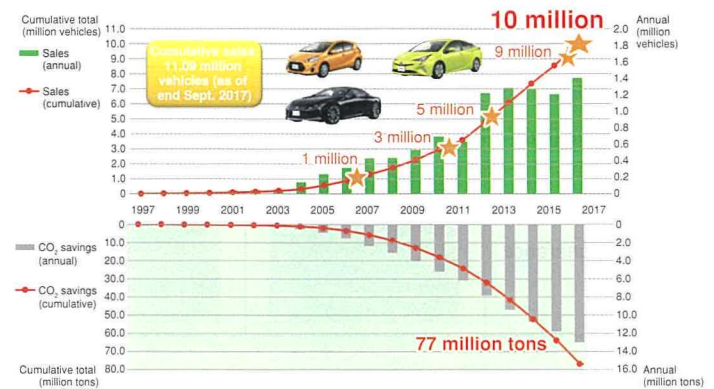
Fig. 2 HV Sales and CO_2 Emissions Savings

2. Lithium-Ion Batteries for Electrified Vehicles

After launching the first-generation Prius in the 1990s, most of Toyota's HVs have been equipped with nickel-metal hydride batteries. More recently, the company has also launched HVs and PHVs installed with lithium-ion batteries, which have a higher energy density than nickel-metal hydride.

*1 Battery Material Engineering & Research Div., Powertrain Company

Toyota's first HV equipped with a lithium-ion battery was the Prius Alpha in 2011. Since then, the fourth-generation Prius, which was launched in 2015, and other vehicles have also used lithium-ion batteries. The first- and second-generation Prius PHVs launched in 2012 and 2017, respectively, also used lithium-ion batteries. **Tables 1** and **2** show the specifications of the lithium-ion batteries installed in these HVs and PHVs. The lithium-ion batteries for HVs feature higher power density, which helps to improve vehicle fuel economy. In contrast, the lithium-ion batteries for PHVs feature higher capacity to help extend EV mode range.

Table 1 Specifications of Lithium-Ion Batteries for HVs
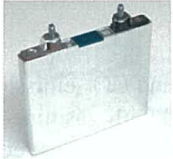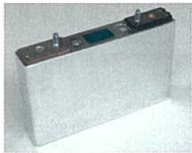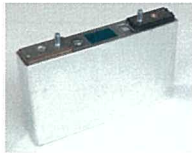
Vehicle	Prius Alpha	Fourth-generation Prius
Capacity (Ah)	5.0	3.6
Power density (W/kg)	2,950	3,920
Weight (g)	245	204
Dimensions (mm)	W: 111 × t: 14.1 × h: 91.8	W: 137 × t: 13.3 × h: 63.3
Battery appearance		

Table 2 Specifications of Lithium-Ion Batteries for PHVs

Vehicle	First-generation Prius PHV	Second-generation Prius PHV
Capacity (Ah)	21.5	25.0
Weight (g)	726	720
Dimensions (mm)	W: 148 × t: 26.5 × h: 91	W: 148 × t: 26.5 × h: 91
Battery appearance		

The improvements that have been achieved in aspects of the electrical performance of lithium-ion batteries, such as power and energy density, are the cumulative result of a wide range of development initiatives. Examples include improvements to the actual battery materials, as well as the development of manufacturing methods to increase the material packing density. However, the development of sufficient electrical characteristics is not the only precondition to be satisfied before a battery can be released onto the market. Since a battery stores energy within predetermined volumetric restrictions, the safety and reliability of the battery are just as important as excellent electrical characteristics when deciding whether it is suitable for release. The following section discusses how a lithium-ion battery is designed to ensure safety.

3. Ensuring Lithium-Ion Battery Safety in the Design

In general terms, lithium-ion batteries are used as battery packs that combine a number of individual cells. A battery pack also contains several controller units for battery voltage, temperature, and the like. Therefore, a three-phase design process is adopted to ensure battery safety: the design of the individual cells, the design of the battery controls, and the design of the battery pack. **Table 3** lists how a lithium-ion battery is designed to ensure safety based on this process.

Table 3 Ensuring Lithium-Ion Battery Safety in the Design

	Cell design	Battery control design	Battery pack design
Overcharging	Separator shutdown when abnormal heat generation occurs	Protection by multiple detection processes - Voltage monitoring of each cell - Voltage monitoring of each block - Voltage monitoring of the battery pack	–
External short circuits	Current shut-off by CID.	–	Over-current protection using fuses
Impacts	–	–	Higher strength Installation position
Internal short-circuits caused by foreign matter	Short-circuit resistance increased by HRL	Countermeasures based on battery control or pack design are not possible.	

Typical issues that might affect vehicle safety include overcharging, external short-circuits, impacts, and internal short-circuits caused by foreign matter.

Overcharging is addressed at the cell design phase by incorporating a function that shuts down the current inside the battery. This is accomplished using a polyolefin separator provided between the cathode and anode that melts when the temperature inside the battery rises. Overcharging is also addressed using a current interrupt device (CID) that shuts off the current when the pressure inside the battery rises. In addition, multiple detection processes are incorporated at the battery control design phase (such as cell voltage monitoring) to restrict the possibility of overcharging.

External short-circuits are addressed at the cell design phase in the same way as overcharging. Additionally, fuses are adopted at the battery pack design phase to prevent the flow of large currents.

Measures to address battery impacts caused by vehicle collisions include increasing the strength of the battery pack and installing the battery in a position protected from impacts at the battery pack design phase.

In the case of internal short-circuits caused by foreign matter, the risk of thermal runaway is reduced at the cell design phase by providing a heat resistant layer (HRL) between the cathode and anode, which restricts the heat generated when a short-circuit occurs inside the battery. The issue of foreign matter intrusion into the battery is also addressed by thoroughly controlling the generation of foreign objects during the battery manufacturing process. A system is used that detects batteries contaminated with foreign matter at the shipment inspection phase. However, unlike overcharging and other issues, it is not possible to protect against internal short-circuits caused by foreign matter at the battery control and battery pack design phases. As a result, the ability to properly assess safety due to foreign matter intrusion at the cell design phase is extremely important. The following section describes the current methodology used to test safety when the battery is contaminated with foreign matter.

4. Current Test Methodology for Internal Short-Circuits Caused by Foreign Matter

The international standard IEC 62660-3, which was drawn up by the International Electrotechnical Commission (IEC), includes the Forced Internal Short Circuit (FISC) test for internal short-circuits caused by foreign matter. The procedure of this test is as follows. First, the electrode assembly is removed from the outer battery case, and minute metal particles are inserted into the assembly. The electrode assembly is then returned to the case and external force is applied to forcibly generate an internal short-circuit. The test then confirms the safety of the battery when this short-circuit occurs (**Fig. 3**).
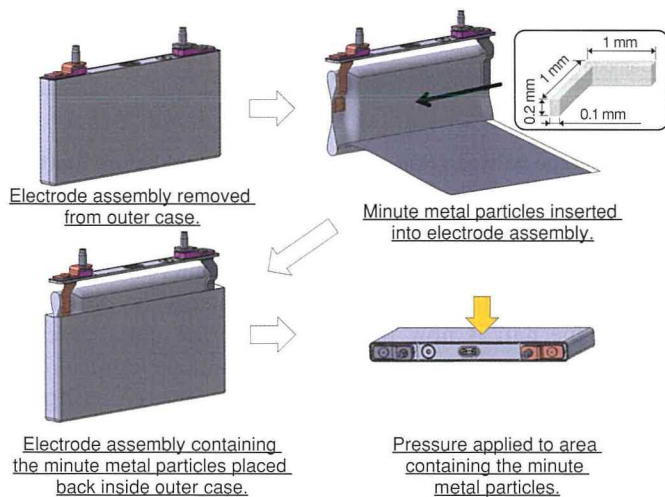
Fig. 3 Outline of FISC test

The FISC test is an extremely effective method of simulating the occurrence of an internal short-circuit caused by foreign matter. However, this test cannot be carried out without a high level of specialist knowledge and technology to disassemble the

battery and handle the minute metal particles properly. Therefore, different countries have proposed various alternative methods, including the Brandt rod test, Brandt nail test, and ceramic nail test (**Fig. 4**).
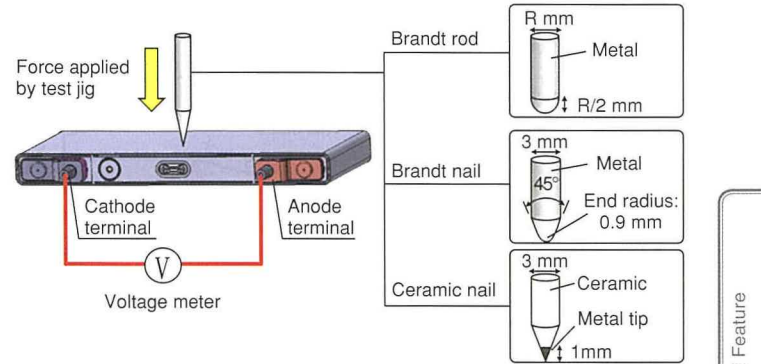
Fig. 4 List of Proposed Alternatives to FISC Test

In these alternative proposals, force is applied to the outside of the battery using a test jig to generate a local short-circuit. These are more simple methodologies that do not require disassembly of the battery.

However, unlike the FISC test, which generates a short circuit in only one of the several tens of cathode/anode layers in the battery, these alternative proposals generate short-circuits in multiple layers. This means that the alternative proposals diverge somewhat from the purpose of the FISC test, which simulates a short-circuit in one layer, assuming the intrusion of foreign matter inside the battery. Furthermore, in high-capacity batteries like those used in PHVs and EVs, the alternative proposals tend to increase the number of layers in which a short-circuit is generated (**Fig. 5**).
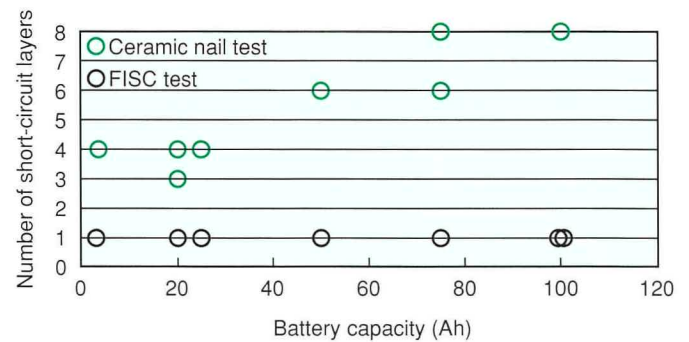
Fig. 5 Battery Capacity and Number of Short-Circuit Layers

The alternative proposals generate short-circuits in multiple layers for the following reason. In these tests, force is continually applied to the outside of the battery using a test jig. The test is completed when the battery voltage falls below a set value. Because a delay occurs between the occurrence of the short-circuit and the drop in battery voltage, short-circuits have

already occurred in multiple layers by the time the voltage conditions for ending the test are detected. Since this delay is particularly long with a high-capacity battery, the number of short-circuit layers increases (**Fig. 6**).
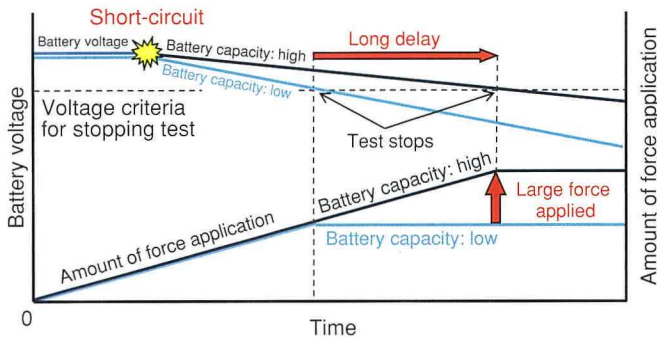
Fig. 6 Outline of Factors behind Increase in Number of Short-Circuit Layers

For these reasons, various studies were carried out to derive a new test methodology that is simple and capable of generating a short-circuit in a single layer. The following section describes the details of this new test methodology.

5. New Alternative Methodology for Testing Internal Short-Circuits Caused by Foreign Matter[2]

5.1 Principles of new test methodology

The new test measuring method is called the Directly Detected Internal Short Circuit (DISC) test. As shown in **Fig. 7**, it involves inserting a metal nail into the battery from the outside. Unlike the other proposals, it is simple and generates a short-circuit in only one layer because the nail also functions as a voltage measurement terminal.
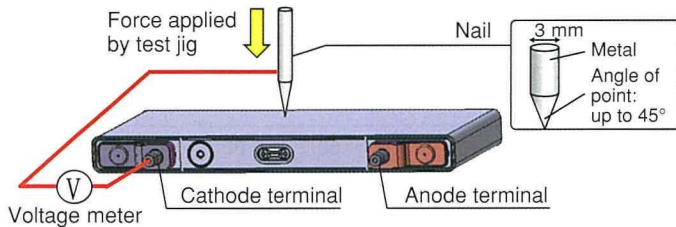
Fig. 7 Outline of DISC test

The workability of the DISC test can be described as follows. The DISC test resembles the other proposals in that an internal short-circuit is generated by inserting the metal nail into the battery. It is also a simple test methodology since there is no need to disassemble the battery or insert any minute metal particles. Unlike the ceramic nail test, since the DISC test does not require a special high-cost test jig that is difficult to procure, it is easier to carry out than the alternative proposals.

The number of short-circuit layers generated by the DISC test is as follows. In the alternative proposals, the average voltage of the entire battery is used to determine whether the test completion conditions have been achieved. This causes a delay between the occurrence of the short-circuit and the drop in voltage, resulting in short-circuits occurring in multiple layers. In contrast, in the DISC test, the nail also functions as the voltage measurement terminal. This means that the change in voltage at the location of the short-circuit can be measured directly and the minute changes in voltage that occur immediately after a short-circuit can be identified. Therefore, the test can be stopped after a short-circuit occurs in one layer.

5.2 Voltage behavior in DISC test

Although the methodology of the DISC test is extremely simple, the voltage between the nail and cathode terminal behaves in a complex manner. This can be described in sequence as follows.

(1) Before start of test
    The cathode terminal and nail are connected to the voltage meter. Since the nail is not in contact with the battery, the indicated voltage between the nail and cathode terminal is 0 V (**Fig. 8**).
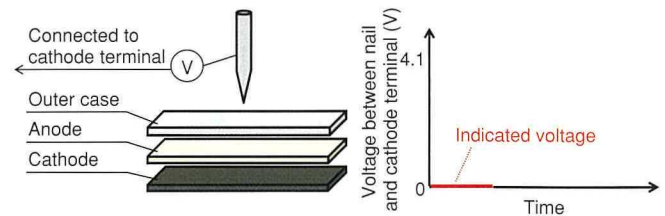
Fig. 8 Voltage between Nail and Cathode Terminal before Start of Test

(2) Start of nail application and contact with outer case
    When the nail is applied, it first contacts the outer case. Since the nail is now in contact with the outer case, the indicated voltage between the nail and cathode terminal is the voltage between the cathode terminal and outer case (**Fig. 9**).
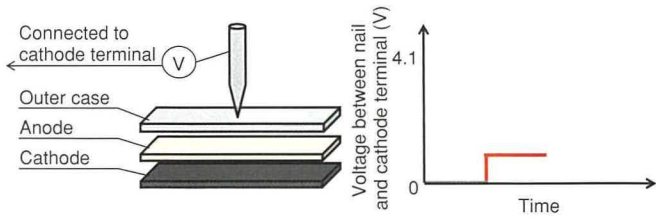
Fig. 9 Voltage between Nail and Cathode Terminal when Nail Contacts Case

(3) Contact with anode

When the nail is forced further in, it pierces through the battery case and the end of the nail contacts the anode. Since the nail is in contact with the anode, the indicated voltage between the nail and cathode terminal is the battery voltage (**Fig. 10**).
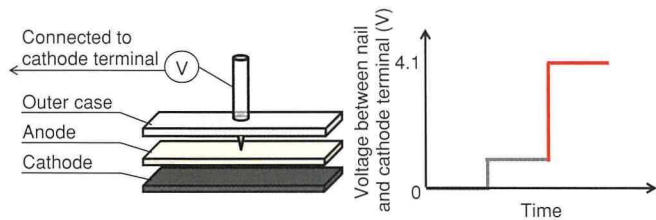
Fig. 10 Voltage between Nail and Cathode Terminal when Nail Contacts Anode

(4) Contact with cathode (short-circuit)

After the nail passes through the anode, the end of the nail contacts the cathode. The voltage between the nail and cathode terminal will drop due to the short-circuit between the cathode and the anode at the moment that the nail contacts the cathode. This drop in voltage can be detected as soon as a short-circuit occurs in one layer (**Fig. 11**).
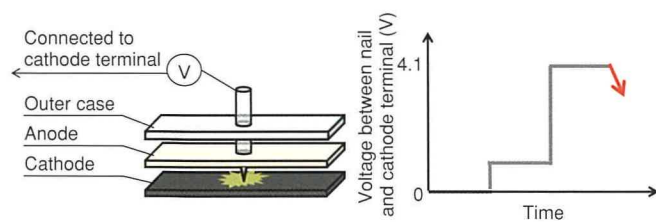
Fig. 11 Voltage between Nail and Cathode Terminal when Nail Contacts Cathode

6. Results of DISC Test and Discussion

6.1 Actual test methodology

Table 4 shows the conditions for an actual test conducted following the procedure described above. After the test, the battery was disassembled and the number of short-circuit layers counted.

Table 4 DISC Test Conditions

Nail specifications	Diameter	3 mm
	Angle of point	45°
	Material	SUS440
Test conditions	Test temperature	Room temperature
	Start voltage	4.1 V (fully charged state)
	Nail insertion speed	0.01 mm/s
End conditions	Amount of drop in voltage between nail and cathode terminal	0.2 V min.

6.2 Test results

The test used 3.6 and 25.0 Ah batteries. In addition, to simulate a high-capacity battery, four 25.0 Ah batteries were connected in parallel and used as a 100 Ah battery. The test results are shown in **Fig. 12**.
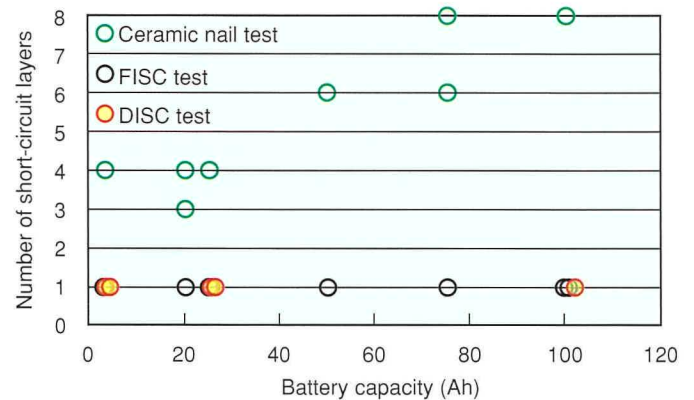
Fig. 12 Battery Capacity and Number of Short-Circuit Layers

At all the battery capacities, the DISC test generated a short-circuit in only one layer. As these results demonstrate, the DISC test is simple and can be stopped when a short-circuit occurs in one layer in the same way as the FISC test. This is an effective methodology for internal short-circuits caused by foreign matter.

7. Activities toward Global Standardization

Previous sections have described the background and details of this newly developed test methodology. This final section discusses the activities that are under way to turn the DISC test into a global standard.

In Japan, these activities are being administered by the Japan Automobile Research Institute (JARI). Relevant companies and organizations inside Japan are participating in the JARI Battery

Special Feature

Standardization Working Group, which hosts the discussions related to electrified vehicle lithium-ion battery standards. Part of its role is to consult about standards drawn up by the IEC and International Organization for Standardization (ISO). It collates proposals from Japan, consults with other countries participating in the standardization activities, and converts them into international standards. Particularly in the case of IEC 62660, which covers lithium-ion batteries for electrified vehicles, Japan is taking the lead role toward international standardization as the chair country.[3] Toyota is also a member of the JARI Battery Standardization Working Group. It takes part in the discussions and makes proposals related to IEC standards.

Although the FISC test was proposed as a part of IEC 62660-3, the high degree of technical difficulty of this test prompted several countries to suggest the necessity for an alternative methodology during consultations on international standardization. It is thought that the DISC test described above meets these requirements. Therefore, the effectiveness of the DISC test has been raised at meetings of the JARI Battery Standardization Working Group and international meetings of the IEC attended by the member countries. The international standardization of the DISC test is being targeted through these activities.

Authors

S. HAMASAKI　　**Y. ISHIHARA**　　**K. MIYAZAWA**

T. KANEKO

8. Conclusions

This article has described a simple and appropriate test method capable of performing an internal short-circuit test, which is an extremely important part of verifying the safety of lithium-ion batteries. This methodology should help to enhance the safety of electrified vehicles equipped with lithium-ion batteries, which is of particular importance to automotive engineers. Toyota intends to continue making every effort to practically implement this methodology.

Finally, the authors would like to extend their sincere gratitude to everyone that supported this development.

References

(1) K. Sato. "Toward the Electrification of Automobiles – Development and Perspective of High-Performance Li-ion Batteries in Toyota –." *Technical Review of the Society of Automotive Engineers of Japan* (2018).
(2) Y. Ishihara et al. "A New Method for Safety Test of Internal Short Circuit." *Advanced Automotive Battery Conference (AABC)* (2018).
(3) M. Takahashi. "International Standardization for Electric Vehicle Battery and Charging." *JARI Research Journal* 2014-12-01 (2014).

Development of Lithium-Ion Cells and Battery Pack for Redesigned Camry HV

Takanori Soejima[*1]
Shuta Ito[*2]

Abstract
The redesigned Camry HV that was launched in 2017 features a wide range of newly developed components. This development aimed to maximize the performance of the Toyota Hybrid System (THS II) installed in the redesigned Prius, which was the first vehicle based on the Toyota New Global Architecture for hybrid vehicles (HV-TNGA). The lithium-ion cells and battery pack used in the redesigned Camry HV were reduced in size and weight while maintaining high performance and safety. This article describes the technology of these lithium-ion cells and battery pack.

Keywords: *Camry HV, lithium-ion cell, battery pack, battery stack*

Special Feature

1. Introduction

Faced with increasingly stringent environmental regulations around the world, the automotive industry must develop and popularize vehicles with an even greater focus on environmental performance. Further expanding the availability of hybrid vehicles (HVs) is an essential part of satisfying this demand. However, to achieve this, it is necessary to enhance the comfort and fun-to-drive characteristics of HVs, as well as to simply focus on environmental performance. The traction battery installed in HVs is an extremely important component with a direct relationship to the appeal of the vehicle. This article describes the components and functions of the traction battery developed for the redesigned Camry HV that was launched in 2017.

2. Development Aims

The redesigned Camry HV achieves better handling than the previous model due to its lower height and center of gravity. Reflecting these changes, the traction battery development also aimed to further enhance the appeal of the vehicle (for example, by improving fuel efficiency, reducing the size and weight of the battery, expanding the available luggage compartment space, and so on). These aims were achieved by developing a new traction battery for the Camry HV with substantially higher performance than the previous battery, while making optimum use of component parts developed for the redesigned Prius that was launched in 2015.

3. Cell Design

3.1 Size of battery cells

Tables 1 and **2** compare the developed second-generation lithium-ion cell with the previous first-generation cell. The second-generation battery pack is smaller and lighter than the first-generation pack due to smaller and lighter cells that also feature a lower capacity optimized for use with HVs.

Table 1 First-Generation Lithium-Ion Cell
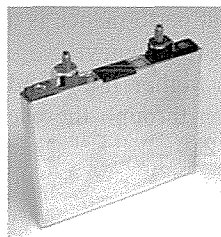
Voltage (V)	3.6
Capacity (Ah)	5.0
Weight (g)	276
Dimensions (mm)	Width: 110 Depth: 13.5 Height: 91.8

Table 2 Second-Generation Lithium-Ion Cell
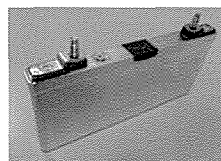
Voltage (V)	3.7
Capacity (Ah)	4.0
Weight (g)	217
Dimensions (mm)	Width: 137 Depth: 13.3 Height: 63.3

[*1] Battery Material Engineering & Research Div., Powertrain Company
[*2] EHV Battery Design Div., Powertrain Company

3.2 Safety

Safety is an essential requirement when using lithium-ion cells. The developed cell satisfied all the requirements laid out in Section 38.3 of the sixth edition of the UN Recommendations on the Transport of Dangerous Goods (UN 38.3), the applicable regulations in China (GB/T31485), as well as the requirements described in the IEC62660 standard determined by the International Electrotechnical Commission (IEC) (**Table 3**).

Table 3 Safety Test Results

Item	Result
Impact/crush	Requirements satisfied
Drop	Requirements satisfied
Nail penetration	Requirements satisfied
External short circuit	Requirements satisfied
Overcharge	Requirements satisfied
Forced discharge	Requirements satisfied
Forced internal short circuit	Requirements satisfied
Seawater immersion	Requirements satisfied

In addition, as a countermeasure against overcharging, the control adopted for nickel-metal hydride batteries was supplemented by a function that monitors the voltage of every cell in the battery. An upper limit voltage threshold is set for each cell as a decisive measure to prevent overcharging.

3.3 Output performance

To ensure the required levels of dynamic performance as well as energy regeneration during braking, an HV battery must have excellent input and output performance. Input performance is a particularly important aspect for enhancing fuel efficiency.

The second-generation battery achieves higher input and output performance than the first generation through the use smaller active material particles (**Figs. 1** and **2**).
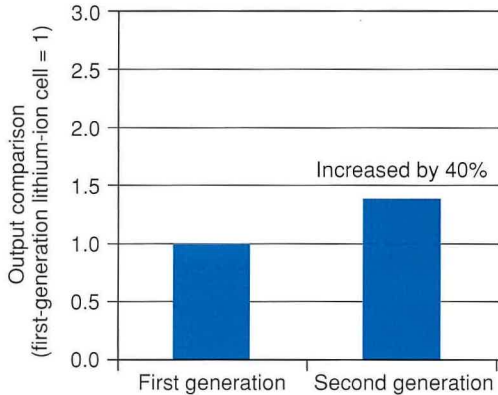
Fig. 1 Comparison of First- and Second-Generation Lithium-Ion Cell Output Performance
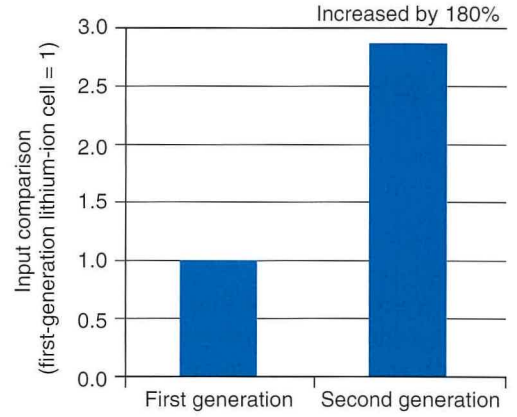
Fig. 2 Comparison of First- and Second-Generation Lithium-Ion Cell Input Performance

3.4 Performance lifetime prediction

For durability, the resistance of this lithium-ion cell briefly drops under low-temperature and low state of charge (SOC) conditions, before increasing once those conditions no longer apply.

The resistance transition of the cell was divided into a decreasing term and an increasing term, which enabled the resistance transition to be predicted more accurately.

In addition, a new lifetime prediction methodology was adopted to help make full use of the battery performance (**Fig. 3** and Equation 1).
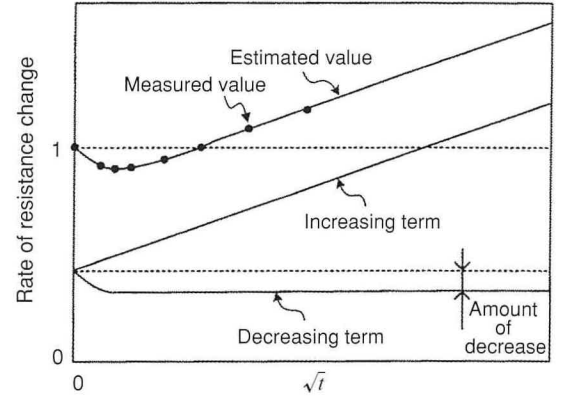
Fig. 3 Lifetime Estimation Method

$$R\% = \left\{ \underbrace{\frac{(1-x)(1+(1-h)kt)}{1+kt}}_{\text{Decreasing term}} + \underbrace{x(1+a0\sqrt{t})}_{\text{Increasing term}} \right\} \times 100 \qquad (1)$$

where,

$a0$: increasing term
k: decreasing term
h: amount of decrease
x: ratio of cathode and anode resistance
t: time

4. Traction Battery Pack

4.1 Outline and installation

The traction battery pack (abbreviated to "battery pack" below) is installed under the rear seats of the vehicle to expand the available luggage compartment space and to help achieve excellent handling by ensuring a lower center of gravity. The battery pack developed for the redesigned Camry HV is 11.5 liters smaller and 15.2 kg lighter than the battery pack in the previous generation Camry HV (**Fig. 4**). Moving the battery pack from behind to under the rear seats helped to substantially increase the capacity of the luggage compartment (by 84 liters compared to the previous generation Camry HV) (**Fig. 5**).
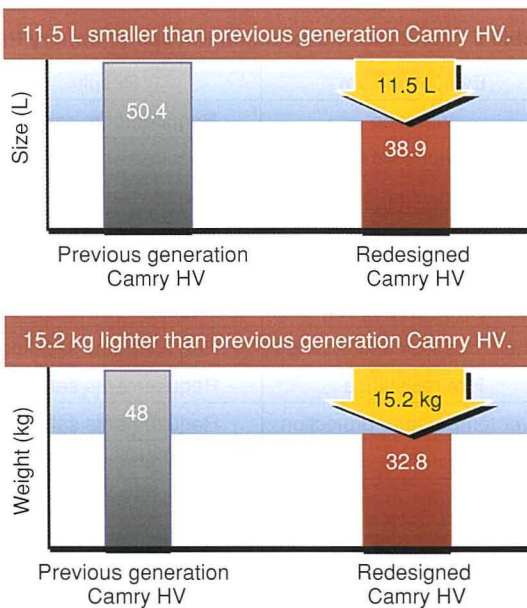
Fig. 4 Size and Weight Comparison
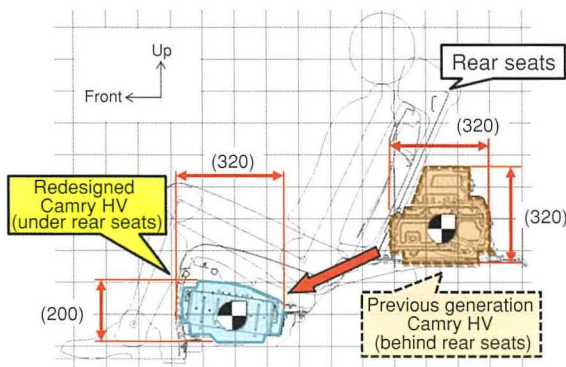
Fig. 5 Installation Position of Battery Pack

4.2 Specifications

Table 4 and **Fig. 6** show the specifications and appearance of the battery pack. The battery pack includes 70 of the lithium-ion cells described above, and has an energy capacity of 1.0 kWh. It features two battery stacks of 35 lithium-ion cells apiece, connected in series in the longitudinal direction of the vehicle.

Table 4 Battery Pack Specifications

Number of cells	70 (35 × 2)
Rated voltage (V)	259
Weight (kg)	32.8
Energy (kWh)	1.0
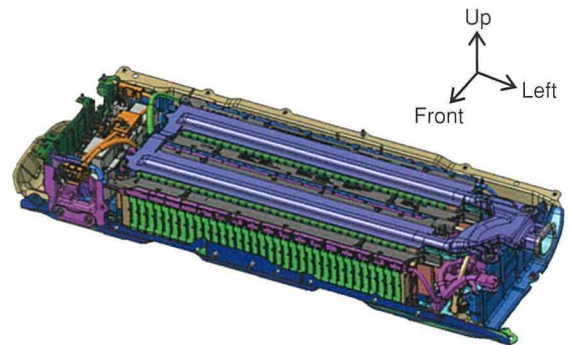
Fig. 6 Appearance of Battery Pack (Top Cover Removed)

4.3 Configuration of battery stacks

Fig. 7 shows the battery stack structure. Each stack features 35 lithium-ion cells layered together using plastic holders. The plastic holders act as insulation between the lithium-ion cells and create paths for the cooling air. Each stack is held at both ends using restraining plates and four steel bands arranged at the top and bottom of the stacks.
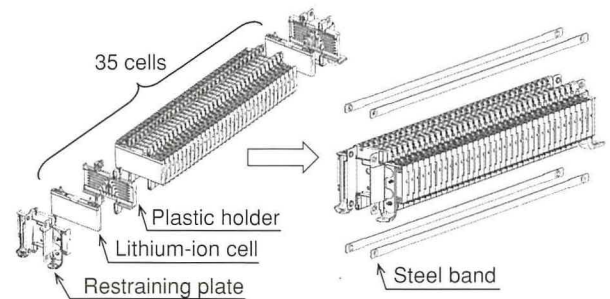
Fig. 7 Battery Stack Configuration

4.4 Cooling structure

The battery stacks are cooled via cooling air inlets under the rear seats. The performance of the cooling structure was enhanced to obtain the necessary amount of cooling air and to reduce the temperature of the cooling air by a sufficient amount.

Cooling air flows between the lithium-ion cells from underneath to both sides. The air cools the cells before being vented to the space under the rear seats and the luggage compartment. This configuration separates the intake (air from inside the occupant compartment before cooling) from the exhaust (air after cooling) to suppress the effects of heat on the lithium-ion cells (**Figs. 8** and **9**).
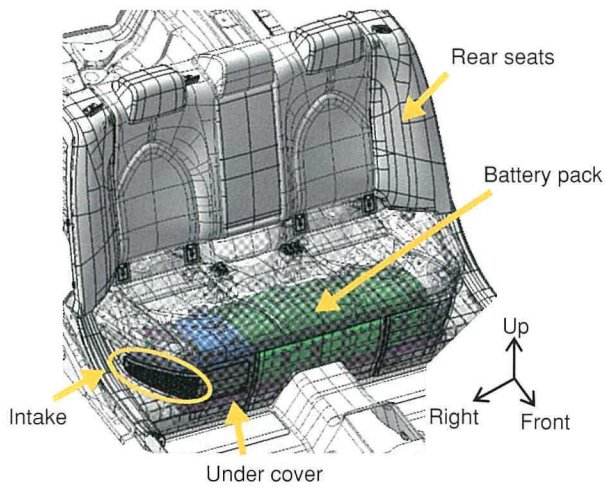
Fig. 8 Installation State under Rear Seats
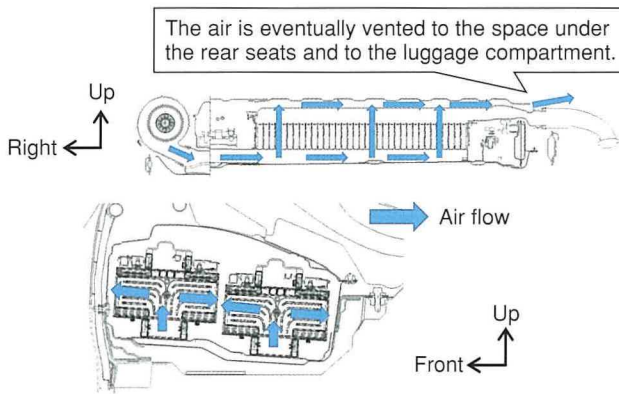
Fig. 9 Flow of Cooling Air inside Battery Pack

4.5 Safety evaluations

In addition to compliance with regulatory requirements, the battery pack was subjected to Toyota's stringent in-house safety evaluations. The developed battery pack satisfied all the stand-alone requirements for a battery pack, as well as the requirements after installation into the vehicle (**Tables 5** and **6**).

5. Conclusion

This development successfully enhanced the environmental performance of the battery pack installed in the redesigned Camry HV (see the fuel efficiency comparison in **Table 7**) and reduced its size and weight. This was achieved by increasing the input and output performance of the lithium-ion cells while also reducing the cell size. In addition, installing the traction battery pack under the rear seat helped to enhance vehicle handling, thereby contributing to the development of fun-to-drive vehicle performance.

Finally, the authors would like to extend their sincere gratitude for the invaluable support of all the companies that participated in the development of these lithium-ion cells and traction battery pack.

Table 5 Stand-Alone Evaluation Results of Battery Pack

Evaluation item	Result
Vibration	Requirements satisfied
High-altitude simulation	Requirements satisfied
Impact/crush	Requirements satisfied
Mechanical shock	Requirements satisfied
Drop	Requirements satisfied
Thermal propagation	Requirements satisfied
Thermal shock and cycling	Requirements satisfied
Fire resistance	Requirements satisfied
Over temperature protection	Requirements satisfied
External short circuit	Requirements satisfied
Overcharge protection	Requirements satisfied
Over-discharge protection	Requirements satisfied
Salt water immersion	Requirements satisfied
Humidity/moisture exposure	Requirements satisfied
Smoke exhaust performance	Requirements satisfied

Table 6 Vehicle Evaluation Results

Evaluation item	Result
Frontal impact	Requirements satisfied
Rear impact	Requirements satisfied
Side impact	Requirements satisfied
Water exposure	Requirements satisfied
Force resistance	Requirements satisfied
High-voltage safety	Requirements satisfied
Flooded road	Requirements satisfied

Table 7 Comparison of Fuel Efficiency of Redesigned and Previous Generation Camry HVs

Test cycle	Previous generation Camry HV	Redesigned Camry HV
Fuel efficiency (Japanese JC08 test cycle) (km/l)	25.4	33.4

Reference

(1) T. Soejima et al. "Battery Development for the new Camry HV." *AABC Asia* (2018).

Authors

T. SOEJIMA   **S. ITO**

Special Feature
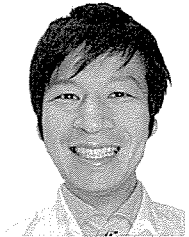
Introduction to the Toyota Fuel Cell System (TFCS)

Mikio Kizaki[*1]

Abstract

In December 2014, Toyota Motor Corporation launched the Mirai, a pioneering first step toward the general sale of fuel cell vehicles (FCVs). This was accomplished through the adoption of the newly developed Toyota Fuel Cell System (TFCS). The TFCS further enhances the established advantages of an FCV and substantially reduces the cost of the FC system, which had been a major challenge for FCV commercialization.

Keywords: *EV/HV system, fuel cell, hydrogen tank, system technology*

1. Introduction

The use of electricity and hydrogen (H_2) is regarded as a promising way of helping to resolve environmental and energy related issues. In particular, H_2-powered fuel cell vehicles (FCVs) are attracting attention as a type of alternative energy vehicle with strong market appeal. In addition to clean and highly efficient environmental performance, FCVs also combine driving enjoyment and user-friendliness through smooth and quiet dynamic performance using motors and a similar cruising range and refueling time as conventional gasoline vehicles.

Toyota Motor Corporation began the development of H_2-powered fuel cell (FC) systems in 1992 and was the first automaker in the world to start sales of an FCV on a limited lease basis in December 2002. Subsequently, after incorporating a number of incremental advances and making progress toward the resolution of the main technical issues of cruising range and cold start capability, lease sales of the Toyota FCHV-adv (**Fig. 1**) began in 2008. Over this period, Toyota verified the strong potential of the FCV as an alternative energy vehicle.

2. Development of the Toyota Fuel Cell System

In December 2014, Toyota launched the mass-production Mirai sedan, a pioneering first step toward the general sale of FCVs (**Fig. 2**). The development of the Toyota Fuel Cell System (TFCS) used in the Mirai was started with the aim of realizing the world's first truly practical FCV, which would be capable of demonstrating the potential of this type of vehicle and encouraging full-scale popularization in the future. The TFCS lowered the cost of the FC system, which is one of the largest obstacles to the commercialization of FCVs, while further

refining the dynamic performance and silent operation established by Toyota's previous FCVs. This article describes the overall development of the TFCS and its components, focusing on the approaches taken to reduce cost.

Fig. 1 Toyota FCHV-adv

Fig. 2 Mirai FCV

3. Cost Reduction Approach for FC System

The biggest cost drivers for an FC system may be categorized as follows: the high cost of special materials for FCs, the complexity of dedicated FCV systems (including the large numbers of parts), and the small production scale (**Table 1**). The details and countermeasures for these factors are described below.

*1 Fuel Cell Products Development Div., Powertrain Company

Table 1 FC System Cost Analysis

Factor	Countermeasures
1. High cost of special FC materials	- Reduce material amounts - Use or develop alternative materials
2. Complexity of dedicated FCV systems	- Consolidate parts - Optimize part requirement specifications (market feedback, regulations, etc.) - Revise part configurations
3. Small production scale	- Carry over mass-production parts from other vehicles - Carry over the production line from other vehicles - Unify mass-production specifications between automakers

3.1 Reducing the cost of special FC materials

An FC system uses large amounts of high-cost materials, such as a precious metal platinum (Pt) catalyst and carbon fiber high-pressure hydrogen tanks. As shown in **Fig. 3**, the FC system in the Toyota FCHV-adv used a significant proportion of special materials.

The TFCS lowered material cost by adopting compact, lightweight, and high-performance components that use less materials, and by replacing high-cost materials with general-purpose alternatives.
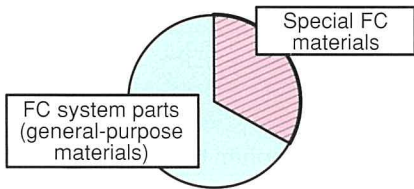
Fig. 3 Cost Breakdown

3.1.1 Cost reduction of materials in FC stack

(1) Innovative cell flow field structure: Conventional cell flow field structures in FC stacks generally use straight channels. This structure is susceptible to water accumulation underneath the flow field ribs that contact the electrode, which adversely affects oxygen (O_2) diffusion and causes non-uniform power generation (**Fig. 4**). To help resolve this issue, porous metal flow fields such as foamed sintered compacts that remove the generated water from the electrode by capillary force through minute holes have been studied as a way of ensuring O_2 diffusion and enhancing performance. However, issues caused by these porous metal flow fields include high pressure loss, large amounts of residual water left inside the pores, product quality, and cost.

To increase the current density and ensure the voltage stability of the newly developed FC stack, an innovative three-dimensional (3D) fine-mesh air flow field was developed

(**Fig. 5**). This 3D fine-mesh flow field is a 3D micro-lattice that promotes O_2 diffusion to the catalyst layer by flowing turbulent air toward the electrode. The front and back shapes and surface wettability of the flow field were also optimized to quickly draw water generated from the electrode to the back surface of the flow field. These measures help to prevent the inhibition of gas flows due to flooding of the flow field, enable uniform power generation within each cell surface, and reduce voltage variations between stack cells. Furthermore, the mesh flow field pattern within the cell surface can be modified to alleviate turbulence at the air inlet to help prevent drying of the electrode when the external humidifier is removed from the system.
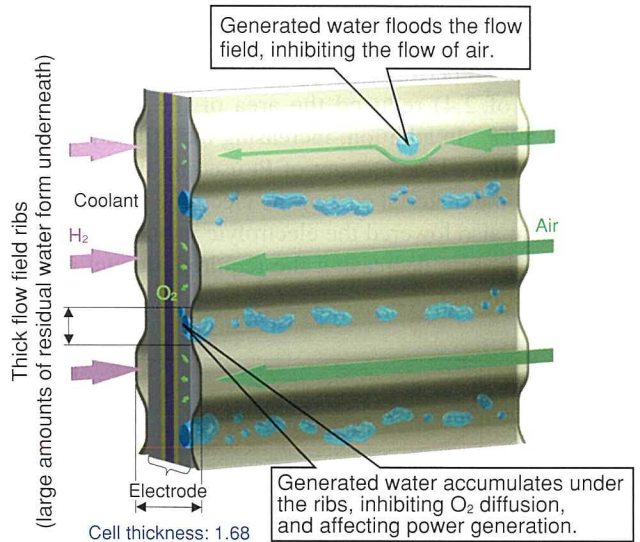
Fig. 4 Conventional Straight Channel Structure
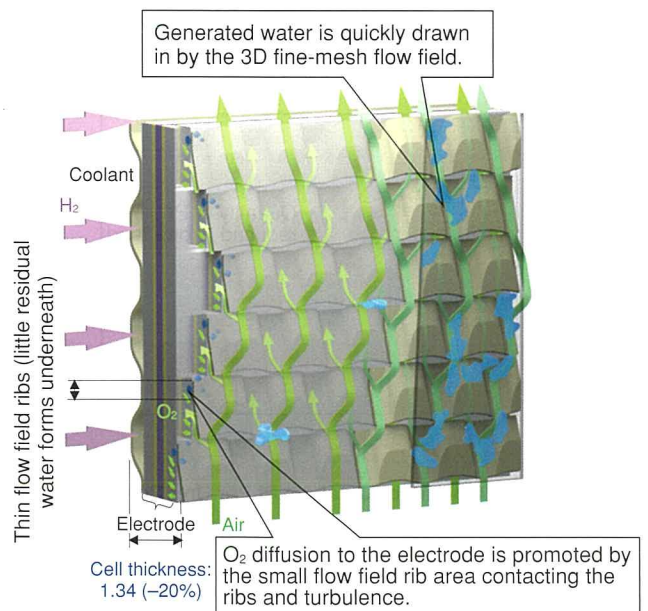
Fig. 5 New 3D Fine-Mesh Flow Field Structure

(2) Innovative electrode: The activity of the catalyst in the new cell structure was boosted by a factor of 1.8 by optimizing the Pt/cobalt (Co) alloy ratio. The carbon support was also changed from a hollow to a solid type. As a result, the Pt catalyst, which was functionally difficult to utilize effectively inside the support, could be reduced, thereby increasing the effective utilization rate of Pt by a factor of approximately 2.

The innovations that were applied to the cell flow field structure and electrode had the following effects: lower concentration overvoltage due to improved gas diffusion, lower resistance overvoltage due to improved proton conductivity, and lower active overvoltage due to improved catalytic activity. As a result, the generation current per unit area increased substantially, increasing the current density by a factor of 2.4 compared to the previous configuration (**Fig. 6**).

This increased performance (i.e., increasing the current density by a factor of 2.4) reduced the area of the electrode per unit power by 59%. In addition, increasing the utilization rate of the Pt catalyst reduced the amount of Pt used by two-thirds (**Fig. 7**) and lowered the material cost of the electrode per unit area. This development also lowered the electrolyte membrane thickness by two-thirds, thereby decreasing the required amount of high-cost electrolyte polymer.
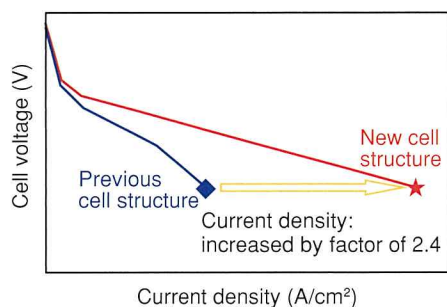
Fig. 6 Current-Voltage (I-V) Characteristics of New Cell Structure (Current Density)
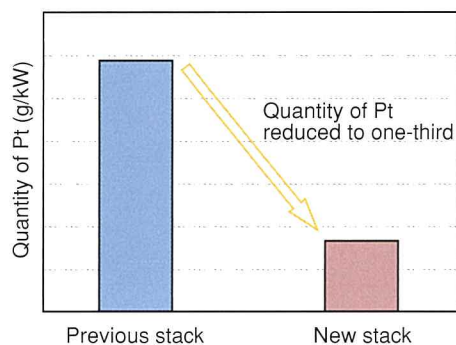
Fig. 7 Amount of Catalytic Pt Per Unit Power

(3) Cost reduction of separator and other components: The previous separator consisted of a stainless steel base material (SUS316L) coated with a high-cost gold (Au) surface treatment to reduce contact resistance and ensure anti-corrosion performance. Changing the base material to corrosion-resistant titanium allowed the required surface treatment function to be simplified to the reduction of contact resistance. As a result, the conventional Au plating treatment was replaced by a newly developed carbon nano-coating called Pi conjugated amorphous carbon (PAC). Eliminating the precious metal usage in the design enabled substantial cost reductions (**Fig. 8**). In addition, simplifying the FC stack tightening structure by integrating the functions of the structure also reduced the number of tightening parts and helped to reduce cost.
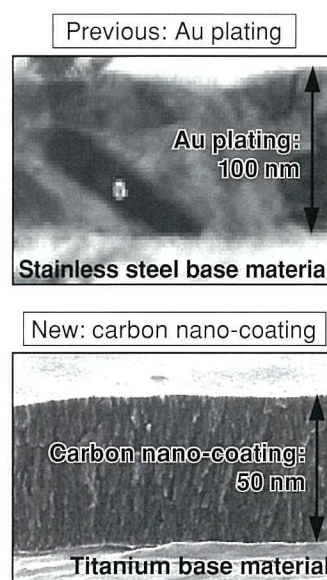
Fig. 8 Separator Surface Treatment.

These developments enabled the new FC stack to achieve a volumetric power density of 3.1 kW/L, which is more than twice as high as the previous stack (**Fig. 9**). The maximum power of the new stack was increased by 27% from 90 to 114 kW (a per cell increase of 36%). At the same time, the volume of the cells was reduced by 24% as a result of the higher current density (increased by a factor of 2.4) and the use of thinner cells (thickness reduced by 20%). Furthermore, changing the separator flow field material from stainless steel to titanium, which has a lower specific gravity, reduced cell weight by 39%.
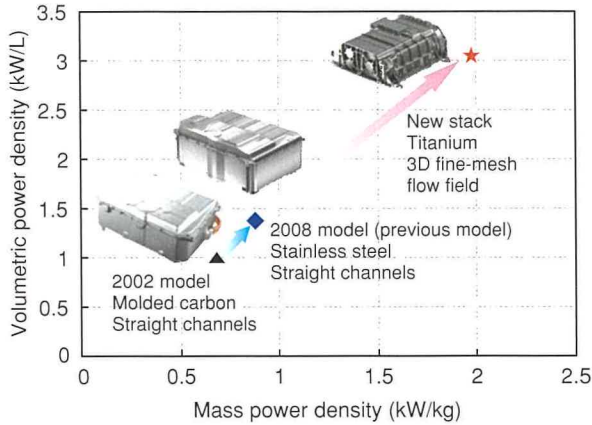
Fig. 9 FC Stack Volumetric and Mass Power Density

3.1.2 Cost reduction of materials in high-pressure hydrogen tanks

(1) Low-cost carbon fiber: a large proportion of the cost of the high-pressure hydrogen tanks is accounted for by the carbon fiber used. Consequently, reducing the cost and amount of the carbon fiber were both important aspects of the TFCS development. The previous model adopted high-grade aviation carbon fiber for the tanks. For the TFCS, with the cooperation of carbon fiber manufacturers, the properties of general-purpose carbon fiber were strengthened to the same level as aviation-grade carbon fiber, thereby lowering the cost of the carbon fiber.

(2) Reduction of amount of carbon fiber used: **Fig. 10** shows the structure of the high-pressure hydrogen tanks. The high-pressure hydrogen tanks are composed of a resin liner at the innermost layer that functions to seal in the hydrogen gas, surrounded by a strong carbon fiber reinforced plastic (CFRP) layer. Aluminum bosses are provided at both ends. To lower cost and weight, the development focused on the CFRP lamination and aimed to substantially reduce the amount of CFRP used.
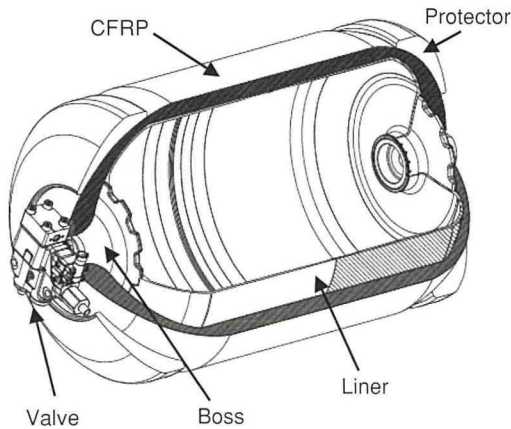
Fig. 10 Structure of High-Pressure Hydrogen Tanks

The CFRP lamination pattern of the high-pressure hydrogen tanks consists of a combination of three types of winding methods: hoop winding to strengthen the central region of the tank (in the circumferential direction), helical winding to strengthen the dome regions (in the axial direction), and high-angle helical winding to reinforce the boundary regions (**Fig. 11**).

Of these winding methods, the high-angle helical winding is wound around the tank at an angle of approximately 70° and also has to be wound around the dome regions. However, as shown in **Fig. 12**, the stress distribution in the circumferential direction is low, and this winding does not make a major contribution to tank strength.
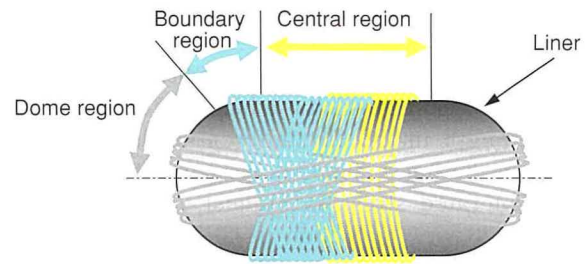
Fig. 11 Lamination Pattern of High-Pressure Hydrogen Tanks
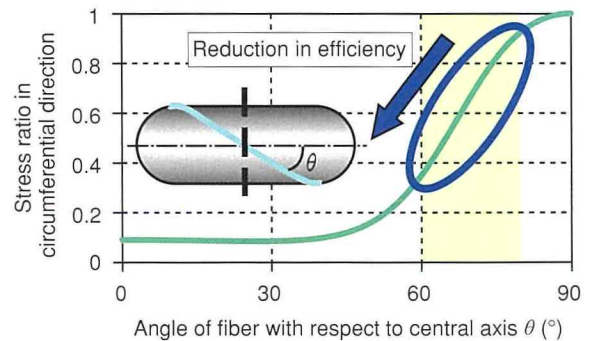
Fig. 12 Relationship between Fiber Angle and Strength Efficiency

Focusing on the fact that high-angle helical winding accounted for approximately 25% of the total laminated CFRP structure in the previous model, a new lamination method was developed to strengthen the boundary regions (**Fig. 13**).

Specifically, the following three changes were made to the lamination method.

(1) The shape of the liner was changed, flattening the boundary regions and allowing lamination by hoop winding.

(2) At the flat parts described in (1), the boundary regions were strengthened while forming the conventional liner shape by hoop winding.

(3) Hoop winding lamination was concentrated in the inner layers.

Special Feature
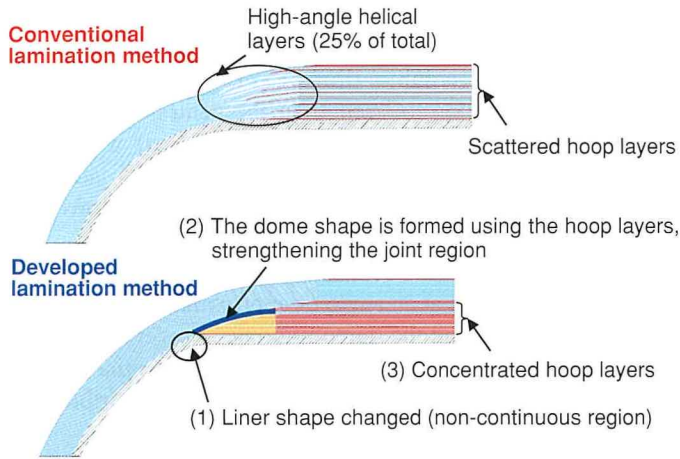
Fig. 13 Comparison of Conventional and New Lamination Methods

These changes eliminated the high-angle helical winding, and allowed the hoop winding, which is a highly effective method of increasing strength in the circumferential direction, to be concentrated in the inner layers of the laminated structure at which the generated stress is highest. This enabled an approximately 20 wt% reduction in CFRP compared to the previous lamination method. In addition, optimizing the boss shape and reducing the amount of CFRP used helped to achieve a storage performance (storable hydrogen weight / tank system weight) of 5.7 wt%, one of the highest in the world, thereby substantially lowering the cost of the high-pressure hydrogen tanks (**Fig. 14**).

* Tank storage performance (wt%) = hydrogen storage amount (kg) / tank weight (kg) × 100
* Source of competitors' data: Toyota
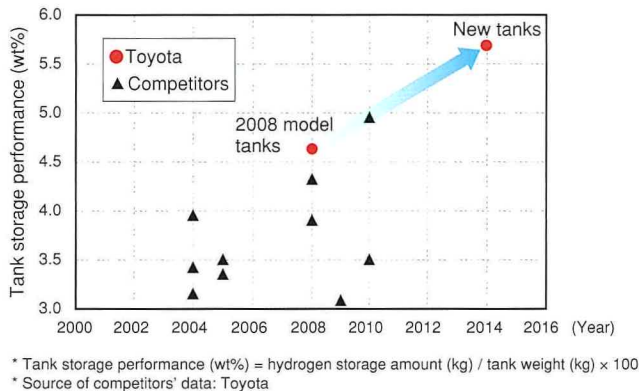
Fig. 14 Comparison of High-Pressure Tank Storage Performance

3.2 FC system simplification

Eliminating or consolidating parts is an indispensable aspect of FC system simplification. **Figs. 15** and **16** show the structures of the previous FC system and TFCS, respectively. To highlight the progress between the two, the parts that were carried over are shown in yellow, and the parts that were consolidated are shown in blue.
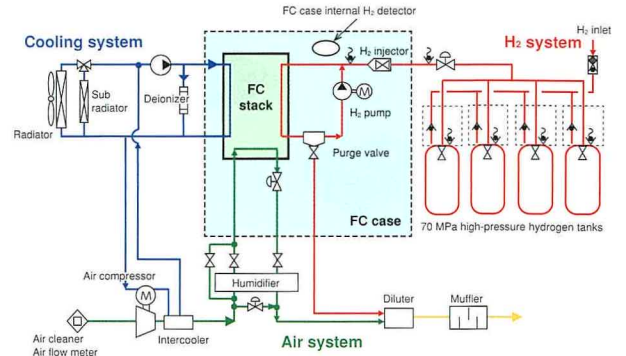
Fig. 15 Structure of Previous FC System
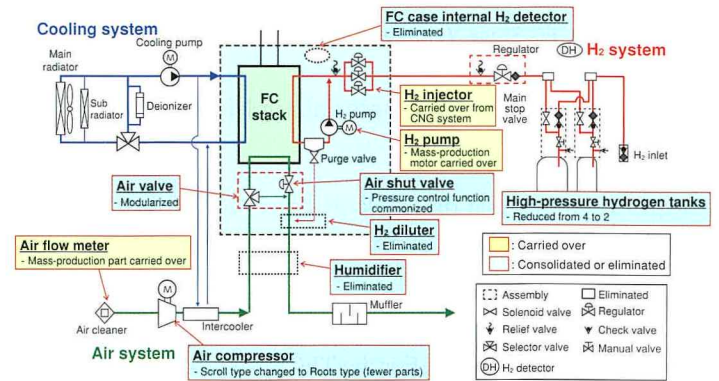
Fig. 16 Structure of TFCS

3.2.1 Elimination of humidifier

As part of the approach to simplify the FC system, the TFCS is the first FC system in the world without an external humidifier. Ionic conduction in the electrolyte membrane of an FC requires the membrane to contain an appropriate amount of water. However, by improving the FC stack and system control, it was possible to realize the humidifier-free concept by internally circulating water generated downstream of the air system (cathode) to the upstream side of the air inlet through the H_2 system (anode) (**Fig. 17**).

The H_2 and air flow paths of the new cell are macroscopically configured to run in counter directions on either side of the electrode (**Fig. 18**). This structure uses the water generated downstream of the air flow field in the cell by back diffusion to humidify the upstream portion of the H_2 flow field. The flow of H_2 transports water vapor to the H_2 outlet, achieves back diffusion of water through the electrolyte membrane, and humidifies the air flow field, which is susceptible to the drying action of the electrode. In addition, the electrolyte membrane thickness was reduced by two-thirds, thereby promoting the generation of water by back diffusion and increasing the proton conductivity by a factor of at least 3. Consequently, this configuration enables self-humidification by circulating generated water within each cell, thereby maintaining the required high-temperature performance even without a humidifier.
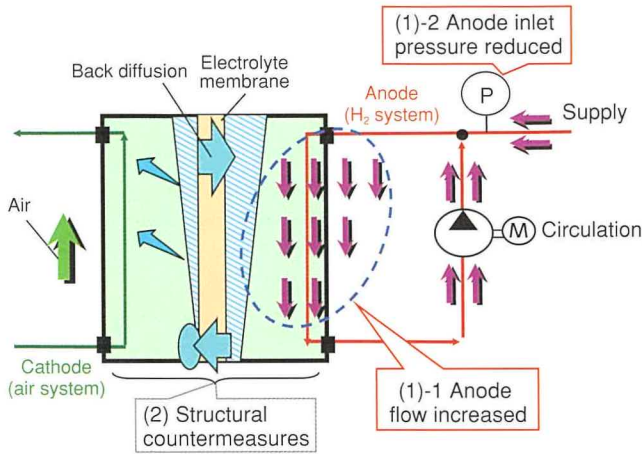
Fig. 17 Elimination of Humidifier by Self-Humidification
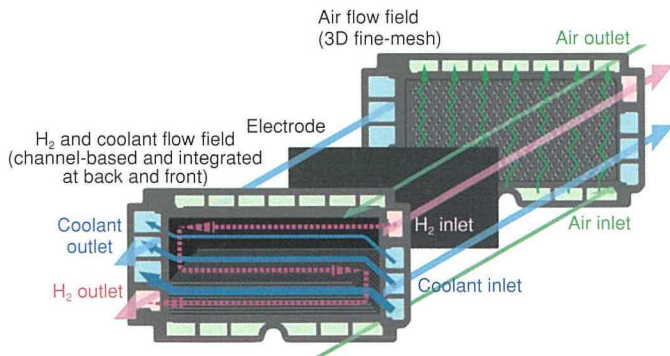
Fig. 18 New Cell Flow Field Structure

3.2.2 Reduction of number of high-pressure hydrogen tanks

The previous model used four high-pressure hydrogen tanks installed under the floor. However, it was necessary to reduce the number of tanks because the valves attached to each tank are a major cost driver of the system. In addition, a large number of tanks would also be an impediment to installing the system in a sedan package.

To reduce the number of tanks, it was important to minimize the required H_2 storage capacity of the vehicle by improving fuel efficiency, and to design an efficient way of packaging the high-pressure tanks to maximize the H_2 capacity within a limited space. In the Mirai, the number of tanks was reduced to two by improving fuel efficiency by approximately 20% compared to the previous model, and by newly developing two differently shaped tanks to store the required amount of H_2 without wasting cabin space in a sedan.

3.3 Utilization of mass-production parts

During the initial launch phase of FCVs, the size of the market will not be comparable to that of conventional gasoline-powered vehicles. As a result, it will be difficult to obtain the normal cost reductions by mass production and economies of scale. Therefore, efforts were made to reduce cost by carrying over existing mass-production parts in the motor system and the systems for operating the FC.

To maximize the adoption of motor system parts used in Toyota's mass-produced hybrid vehicles (HVs), the specifications of the FC system were adjusted in line with the specifications of those parts. However, in the previous model, it had been necessary to design a dedicated motor and inverter for the FCV motor system (**Fig. 19**) to match the unique characteristics of an FC (i.e., low voltage and high current) since the FC stack and inverter were directly connected and used the same voltage. Therefore, the TFCS features a new FC boost converter (FDC) that converts the FC voltage and enables the adoption of a mass-production HV motor and inverter (i.e., high voltage and low current). This measure helped to reduce the size and cost of the motor system.

The component parts of the FDC also feature a high proportion of components adopted in mass-production HVs, such as the intelligent power module (IPM) and inductor, helping to lower cost.
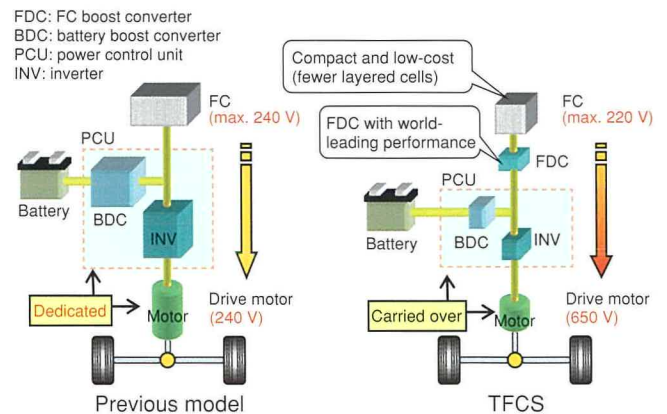
Fig. 19 Structure of Motor System

4. Conclusions

The mass-production and commercialization of the Mirai FCV is the result of a long and arduous journey by a large number of people at Toyota and its partner companies. Furthermore, the launch of this FCV signals only the start of a lengthy struggle toward achieving widespread popularization.

The name of the Mirai is derived from the Japanese word meaning "future" and Toyota has decided to use the same name in every market in which the Mirai is sold around the world. The name reflects the significance of the Mirai as a vehicle for the

next generation that will open the way to the future.

Toyota is continuing the development of FCVs as one of the most promising technologies for achieving sustainable mobility and energy diversification. At the same time, it will carry on actively working with governments and related fields toward the realization of a hydrogen-based society, for the sake of the Earth and future generations.

Note: this article is based on the following published technical paper.

M. Kizaki. "Introduction of Toyota Fuel Cell System "TFCS"." *Journal of Society of Automotive Engineers of Japan* Vol. 69 No. 5 (2015) pp. 51-56.

Author

M. KIZAKI

Development of High Performance and Low Cost Fuel Cell Stack

Seiji Mizuno[*1]
Norishige Konno[*1]
Kenji Tsubosaka[*1]
Hiroaki Nishiumi[*1]
Hideki Kubo[*1]
Toshiyuki Tonuma[*1]

Abstract

Greatly enhancing the performance and reducing the size and cost of the fuel cell (FC) stack is an important part of measures aimed at facilitating the widespread adoption of fuel cell vehicles (FCVs). The new FC stack installed in the Mirai, the pioneering mass-production FCV that was launched in December 2014, adopted an innovative cell flow-field structure and electrodes to realize the world's first humidifier-less system. Compared to the previous FC stack, these innovations improved performance by increasing current density by a factor of 2.4, and reduced size and weight by decreasing the external volume of the stack by 42%. As a result, this FC stack achieved a power density of 3.1 kW/L and 2.0 kW/kg, one of the highest in the world. These figures are more than twice as high as the previous model and allowed the FC stack to be installed under the floor of a sedan-type FCV. Furthermore, the durability of the electrodes was improved by a factor of 3 compared to the previous stack, and the reliability of the FC stack against impacts, water exposure, and corrosion was ensured. The cost of the FC stack was also greatly reduced by simplifying the stack tightening structure, cutting the amount of platinum (Pt) in the electrocatalyst by 72%, and replacing the gold (Au) plating of the separator surface treatment with a newly developed carbon nano-coating.

Keywords: *FC stack, cell, power density, humidifier-free design, flow field structure, electrode, impact resistance, durability and reliability, cost*

Special Feature

1. Introduction

A fuel cell (FC) generates power by electrochemical reactions through an electrocatalyst using hydrogen (H_2) as fuel and oxygen (O_2) in the air. Since these reactions generate only water as a by-product, FCs are regarded as an extremely clean and efficient means of generating power, with the potential to help resolve energy and environmental issues in the future. Fuel cell vehicles (FCVs) use polymer electrolyte fuel cells (PEFCs) that can start up and generate power at low temperatures, and that achieve fast reaction speeds and high current densities (**Fig. 1**).
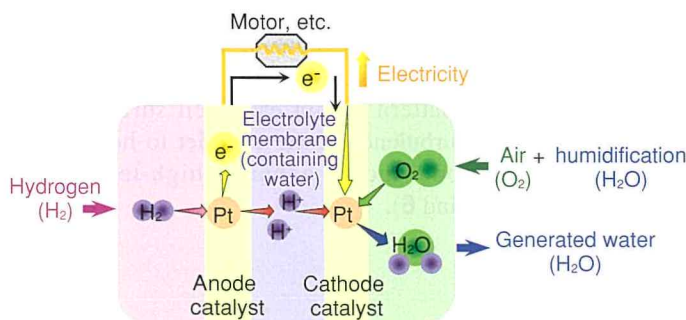
Fig. 1 Generation Principle of PEFCs

To achieve the required performance with a PEFC, it is necessary to reduce the proton conductivity resistance by maintaining the humidity of the ionomers of the electrolyte membrane and catalyst layer (CL). In a conventional FC system, air is passed through a humidifier and supplied to the FC stack (**Fig. 2**).
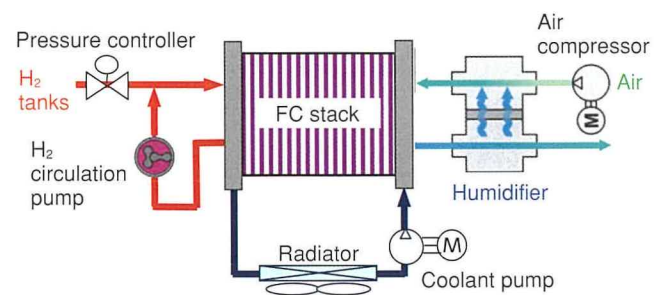
Fig. 2 Conventional FC System

For its mass-production FCV, Toyota aimed to develop a simpler FC system that would be smaller, lower cost, and more reliable. This was achieved by developing the world's first FC stack without a humidifier. As a result of these efforts, the developed FC stack achieves a world-leading power density of 3.1 kW/L and is compact enough to be installed under the floor in an FCV sedan. Furthermore, the durability of the electrodes and the reliability of the stack against impacts, water exposure,

and corrosion in the particular under-floor installation environment were ensured. The cost of the FC stack was reduced by adopting a simpler tightening structure with fewer parts, and by substantially lowering the amount of precious metals used through reducing the amount of platinum (Pt) in the electrocatalyst by 72% and eliminating the gold (Au) plating surface treatment of the separator.

This article describes the innovative cell flow field structure and electrodes, which are the key technologies for enhancing the performance of the FC stack, as well as the technologies for reducing size, enhancing aspects of reliability such as resistance against impacts, water exposure, and corrosion, and lowering cost.

2. Enhancing FC Stack Performance

Water management in each cell plays a key role in enhancing the power generation performance of the FC through ensuring sufficient diffusion of O_2 to the CL and maintaining proton conductivity. The newly developed FC stack features an innovative cell flow field structure and electrodes that achieve the required performance by self-humidification using only generated water.

2.1 Innovative cell flow field structure

Conventional cell flow field structures in FC stacks generally use straight channels. This structure is susceptible to water accumulation underneath the flow field ribs that contact the electrode, which adversely affects O_2 diffusion and causes non-uniform power generation.[1] In addition, straight channels are susceptible to flooding by generated water, which inhibits gas flows and affects voltage stability (**Figs. 3** and **4**).

Fig. 3 Conventional Straight Channel Structure
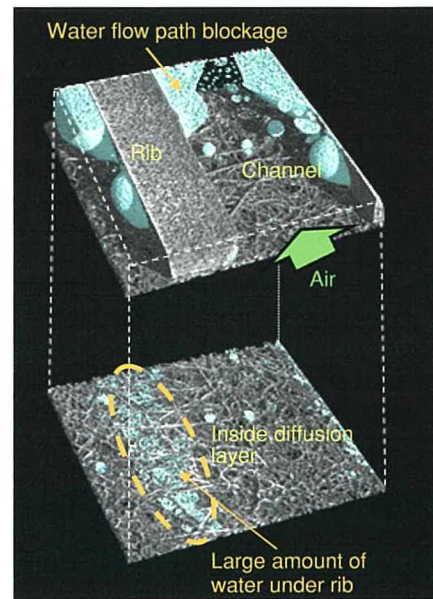
Fig. 4 State of Residual Water in Straight Flow Field

In contrast, porous metal flow fields such as foamed sintered compacts that remove the generated water from the electrode by capillary force through minute holes have been studied as a way of ensuring O_2 diffusion and enhancing performance. However, issues with porous metal flow fields include high pressure loss, large amounts of residual water left inside the pores, manufacturing quality, and cost.[2]

To increase the current density and ensure the voltage stability of the new stack, an innovative three-dimensional (3D) fine-mesh air flow field was developed. This 3D fine-mesh flow field is a 3D micro-lattice that promotes O_2 diffusion to the catalyst layer by flowing turbulent air toward the electrode. The front and back shapes of the 3D fine-mesh flow field were also optimized and the flow field surface given hydrophilic properties to quickly draw water generated from the electrode to the back surface of the flow field (called "inducted water"). These measures help to prevent the inhibition of gas flows due to blockage of the flow field, and also help to achieve uniform power generation within each cell surface and reduce voltage variations between stack cells by reducing the residual water in the diffusion layer to ensure gas diffusivity. Furthermore, the 3D fine-mesh flow field pattern within each cell surface can be modified to alleviate turbulence at the air inlet to help prevent drying of the electrode and to enhance high-temperature performance (**Figs. 5** and **6**).
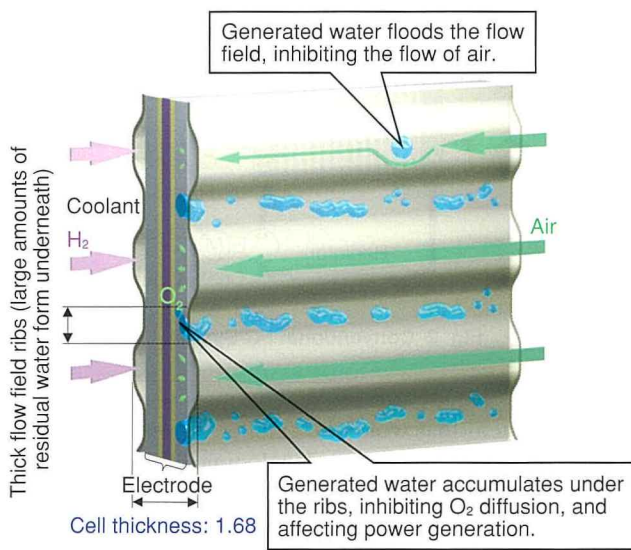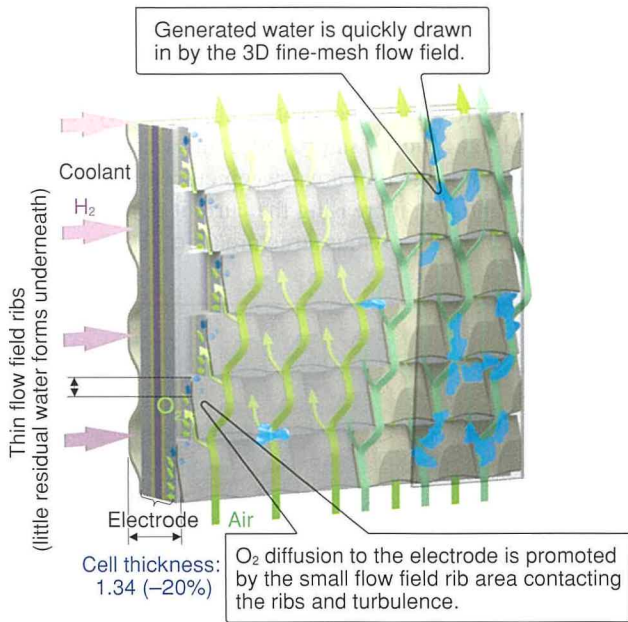
Fig. 5 New 3D Fine-Mesh Flow Field Structure
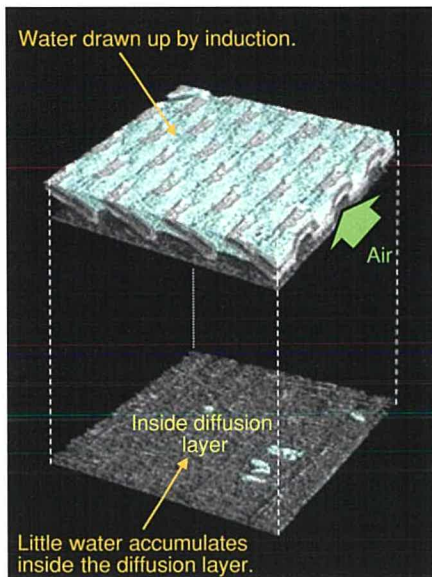
Fig. 6 State of Residual Water in 3D fine-Mesh Flow Field

In contrast, the H_2 flow field is channel-based and integrated with the coolant flow field at the back and front. This creates a 2-turn, 3-step cascade macrostructure in which the H_2 and air flow in counter directions on either side of the electrode. This structure uses the water generated at the air outlet by back diffusion to humidify the inlet H_2. The H_2 circulation pump then transports water vapor to the H_2 outlet and humidifies the flow field at the air inlet, which is susceptible to the drying action of the electrode. Therefore, this configuration enables self-humidification by circulating generated water within each cell. This flow field structure also ensures that more coolant flows

toward the air inlet, which is more susceptible to drying than at the air outlet, thereby restricting the evaporation of moisture from the electrode. As a result, the FC stack maintains the required high-temperature performance even without a humidifier (**Figs. 7** and **8**).
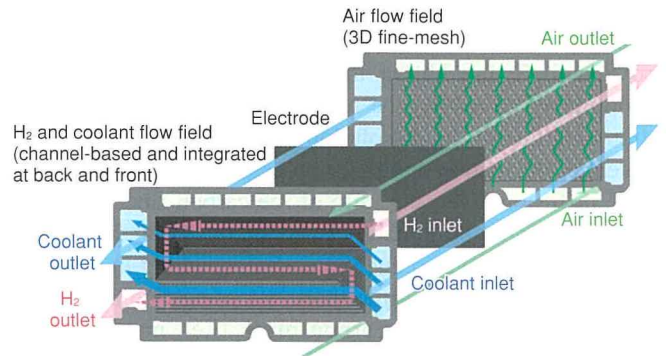
Fig. 7 New Cell Flow Field Structure
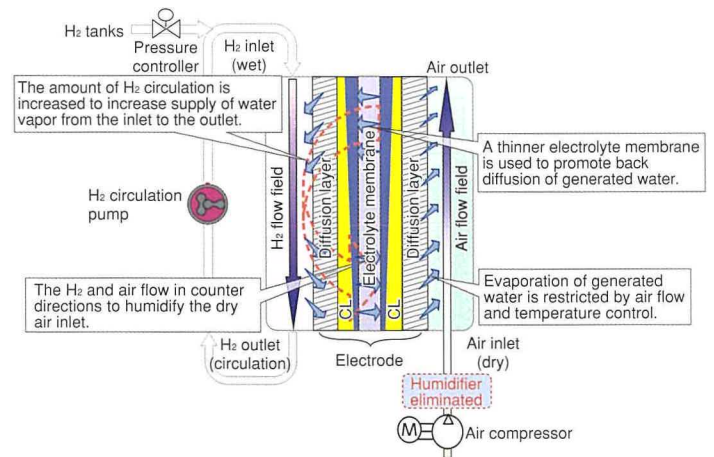
Fig. 8 Outline of Self-Humidification within Cell Surface

2.2 Innovative electrode

To enhance performance without a humidifier, the electrolyte membrane thickness was reduced by two-thirds, thereby promoting the generation of water by back diffusion and increasing the proton conductivity by a factor of at least 3. In addition, measures were also adopted to restrict chemical deterioration of the electrolyte membrane due to the formation of high concentrations of hydrogen peroxide and hydroxyl radicals, which are reaction by-products when the FC is operated under low-humidity conditions. These measures include the addition of a radical quencher into the electrode and the reduction of iron (Fe) ion contamination from auxiliary system parts. As a result, the required crossover lifetime was achieved.

In the CL, proton conductivity and gas diffusion performance was achieved by lowering the equivalent weight (EW) of the ionomers (i.e., by increasing the functional groups) and

optimizing the ratio of the ionomers. The activity of the catalyst was boosted by a factor of 1.8 by optimizing the Pt/cobalt (Co) alloy ratio and adopting an acid treatment. The carbon support was changed from a hollow to a solid type. This measure allowed the Pt catalyst to be supported on the carbon surface, reducing the O_2 diffusion resistance. It also increased the effective utilization rate of Pt, which promotes the reaction particularly under conditions of low humidity, by a factor of approximately 2. In addition, the Pt particle size and distribution were optimized to restrict the reduction in the size of the active reaction area due to the dissolution and particle growth of Pt in the potential fluctuation durability process.

In the diffusion layer, the ratio of the carbon fiber and binder in the carbon paper base material was optimized and the weight of the carbon paper was reduced by 45%, resulting in higher gas diffusion performance. Furthermore, adopting a thinner carbon paper and coarser grained carbon black (i.e., material with a larger pore diameter) in the micro porous layer (MPL) formed at the interface of the base material and CL reduced the water permeation pressure. This helped to improve the water removal performance and increased gas diffusion by a factor of 2 (**Figs. 9** and **10**).[3]
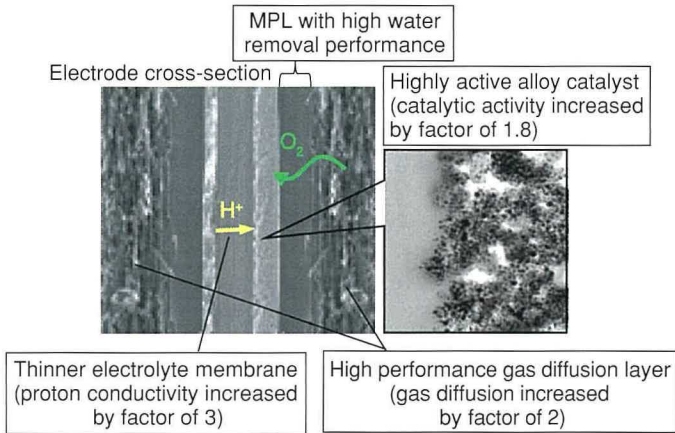
Fig. 9 Improvement of Physical Properties of Electrode
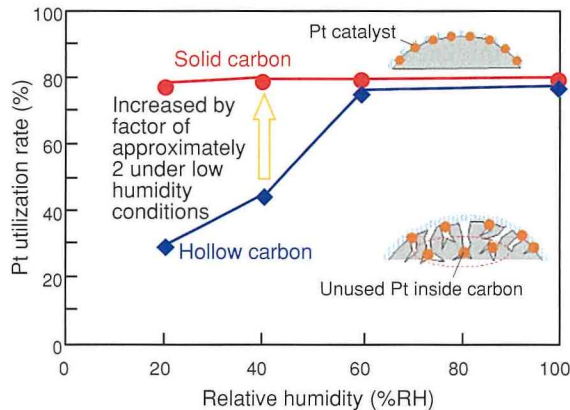
Fig. 10 Improvement of Utilization Rate of Pt in Catalyst

The innovative cell flow field structure and electrodes described above had the following effects: lower concentration overvoltage due to improved gas diffusion, lower resistance overvoltage due to improved proton conductivity, and lower active overvoltage due to improved catalytic activity. As a result, the maximum per unit area sweep current of the electrode improved substantially, increasing the current density by a factor of 2.4 compared to the previous structure (**Fig. 11**).
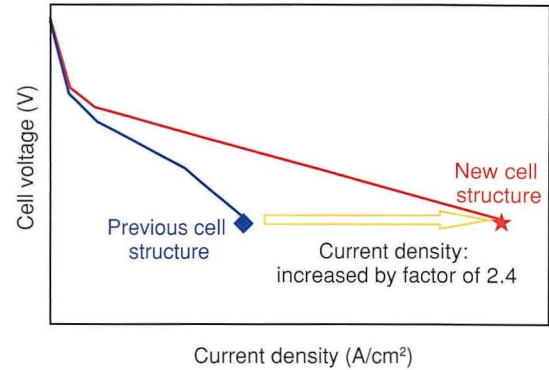
Fig. 11 Current-Voltage (I-V) Characteristics of New Cell Structure (Current Density)

3. Size and Weight Reduction of FC Stack

The maximum power of the new stack was increased by 27% from 90 to 114 kW (a per-cell increase of 36%). At the same time, the volume of the cells was reduced by 24% as a result of the higher current density (increased by a factor of 2.4) and the use of thinner cells (thickness reduced by 20%). Furthermore, changing the separator flow field material from stainless steel to titanium, which has a lower specific gravity, also reduced cell weight by 39%.

A new stack tightening structure was developed. Changing the cell layer configuration from a two-row to a single-row structure enabled the area of the tightening plates to be halved. The previous structure also used springs to achieve constant-pressure tightening. These springs were eliminated by adopting a constant-dimension tightening method using the internal cell spring properties. The stamped stack case was replaced by an aluminum casting and the number of tightening parts was reduced by incorporating measures to increase tightening strength in the case. As a result, the volume and weight of the case were reduced by 42% (from 64 to 37 L and 108 to 56 kg) (**Fig. 12**).
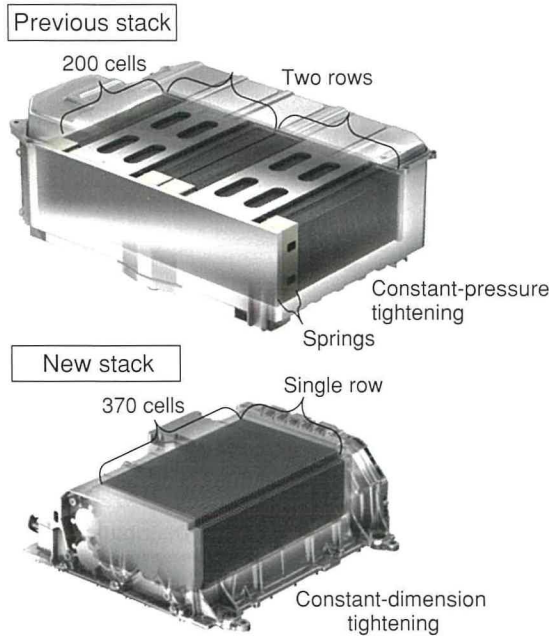
Fig. 12 FC Stack Tightening Structure

As a result of these measures, a high-performance, compact, and lightweight FC stack was developed with a power density of 3.1 kW/L and 2.0 kW/kg, more than twice that of the previous stack, enabling installation under the seats of a sedan (**Figs. 13** and **14**).
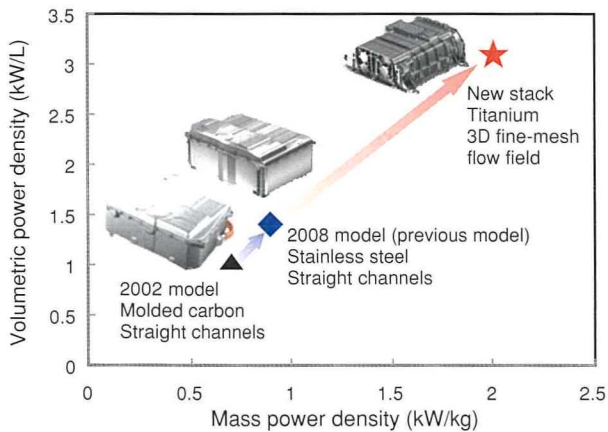
Fig. 13 FC Stack Volumetric and Mass Power Density
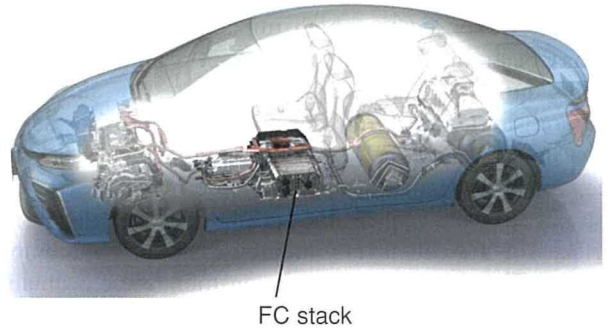
Fig. 14 Under-Floor Installation of New Stack

4. Ensuring the Reliability of the FC Stack

Due to its installation position under the floor of the vehicle, it was necessary to ensure the reliability of the new FC stack considering the following factors: (1) impacts such as collisions and road surface contact, (2) water resistance when driving on submerged roads and the like, and (3) corrosion resistance assuming use in regions susceptible to salt damage.

4.1 Measures to ensure impact resistance of FC stack

The new FC stack features 370 cells tightened together in layers. Gaskets are provided between each cell to seal the H_2, air, and coolant flows. From the standpoint of ensuring high-voltage and H_2 safety against impacts, it is necessary to prevent sealing defects occurring between the cells of the FC stack due to cell layer deviation.

The FC stack maintains its structure using the tightening force and the friction constraint force generated by the tightening friction between the cells. A sufficient friction constraint force must be ensured against impacts to prevent cell layer deviation. Therefore, experiments and simulations were carried out to identify the impact resistance of the friction constraint force of the FC stack (**Fig. 15**). The results found that the FC stack has sufficient impact resistance against impacts, and that the friction constraint force protects the stack against road surface contact and mild collisions.
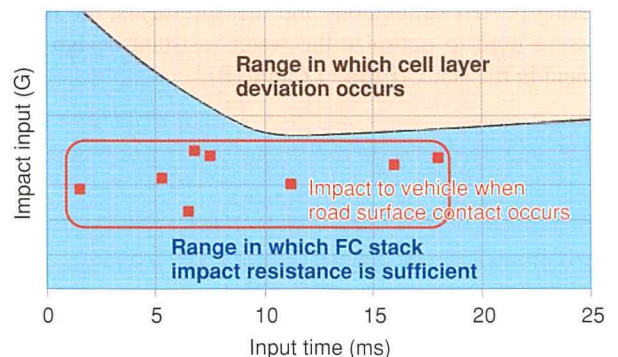
Fig. 15 Impact Resistance of FC Stack (Friction Constraint Force)

In addition, to prevent sealing defects between cells when the FC stack is exposed to a high impact force that exceeds the friction constraint force of the stack in a high-speed collision (such as during a legally required crash test or an ever higher speed collision), an external constraint structure was adopted to restrict the amount of cell layer deviation to below the required value. When an impact is applied to the FC stack, this external constraint structure reduces the shear force generated at the cell interfaces of the cell layers, thereby restricting the amount of deviation (**Fig. 16**). The external constraint force is obtained by contact with external constraints when the impact causes the stack layers to distort dynamically. To achieve the required reaction force, the development identified the deviation characteristics of the cell, and optimized the distance between the cells and external constraint, as well as the stiffness of the external constraints.

As a result, friction constraint force is used to prevent cell deviation when an impact occurs at normal speed, and external constraints are used to obtain the required reaction force when a high-speed impact occurs. These measures are effective against a wide range of impacts by restricting the amount of cell layer deviation to below the required value.
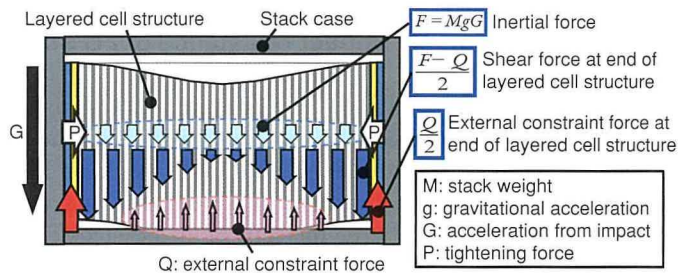
Fig. 16　Concept of FC Stack External Constraint Structure

4.2　Measures to ensure water resistance of FC stack

Because the FC stack is installed under the floor close to the ground, it must be resistant to water spray and submersion when the road is flooded.

Experiments and simulations were carried out to measure the required water pressure resistance when driving on a submerged road. A close correlation was achieved between computer aided engineering (CAE) simulations and measurements, the results of which were used to optimize the water-resistant design of each component in the stack (**Figs. 17** and **18**).
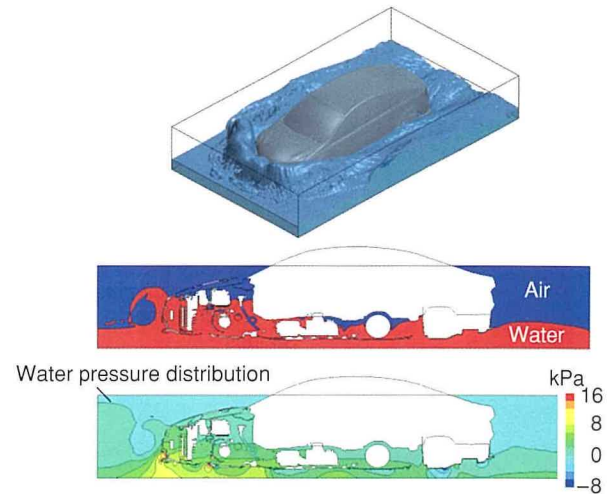
Fig. 17　CAE Results of Water Pressure Distribution when Driving on Submerged Road
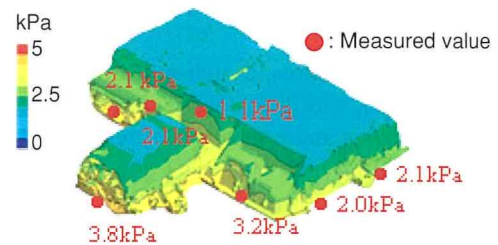
Fig. 18　Comparison between Measurements and CAE Simulations of FC Stack Water Pressure Distribution

4.3　Measures to ensure corrosion resistance of FC stack

The operating environment of the FC stack is disadvantageous compared to a conventional engine. For example, due to its low installation position, the FC stack is exposed to sprays of de-icing agents and water, as well as submersion on flooded roads. Furthermore, due to its low operating temperature, ice around the FC stack does not melt. This means that measures must be taken to ensure corrosion resistance.

Various anti-corrosion measures were applied to the new FC stack considering its corrosive usage environment. An alumite treatment was applied to the aluminum stack case, cationic electrodeposition was applied to the lower stack cover, and a Geomet coating was applied to the bolts. In addition, the structure of the FC stack was designed to restrict corrosion of the base material. Additionally, an ethylene-propylene-diene rubber (EPDM) was used for the sealing gaskets as a measure against the alkaline environment generated when the base material corrodes. These measures ensured the corrosion resistance performance of the FC stack installed under the floor (**Fig. 19**).[4]
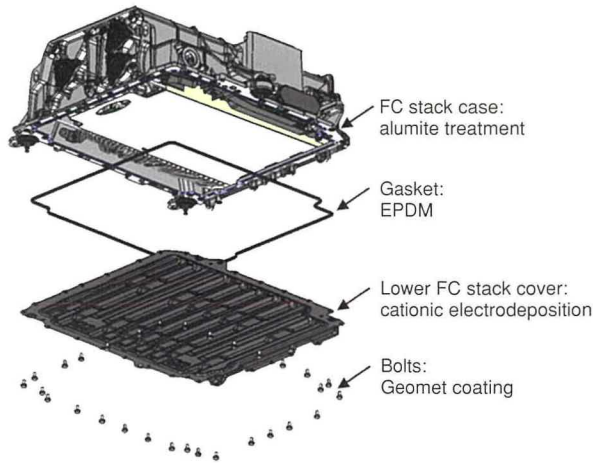
Fig. 19 Measures to Ensure Corrosion Resistance of FC Stack

5. Cost Reduction of FC Stack

The high cost of an FC stack is mainly due to the electrolyte membrane in the electrode, which is a special FC material, the Pt in the catalyst, and the Au plating separator surface treatment (to reduce contact resistance and provide corrosion resistance), which cannot be reduced by economies of scale through mass-production.

The development of the new FC stack successfully reduced the area of the electrode per unit power by 59%. This was accomplished by improving performance with the innovative cell flow field structure and electrodes (current density was increased by a factor of 2.4) and reducing the number of layered cells in the stack (from 400 to 370) by adopting an FC boost converter. Furthermore, the development also lowered the material cost of the electrode per unit area. This was accomplished by reducing the electrolyte membrane thickness by two-thirds to decrease the required amount of high-cost electrolyte polymer, and by reducing the amount of Pt by 72% by enhancing the activity of the catalyst and increasing the Pt utilization rate (**Fig. 20**).
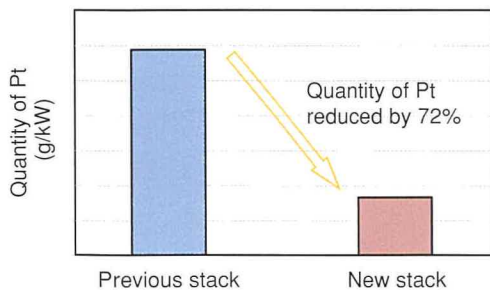
Fig. 20 Amount of Catalytic Pt Per Unit Power

In addition, the base material of the separator flow field was changed from stainless steel (SUS 316L) to corrosion-resistant titanium. This allowed the function of the surface treatment to be simplified to the reduction of contact resistance. As a result, the conventional Au plating treatment was replaced by a newly developed carbon nano-coating called Pi conjugated amorphous carbon (PAC). Eliminating the precious metal usage in the design enabled substantial cost reductions (**Photo 1**).
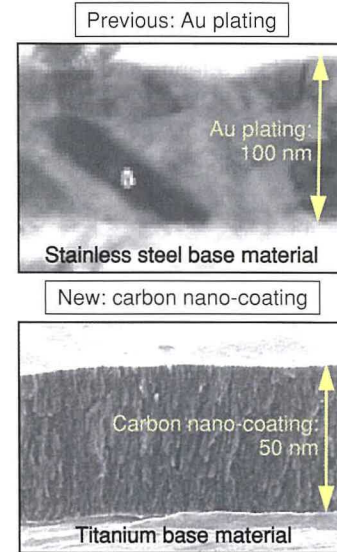
Photo 1 Separator Surface Treatment

As described above, simplifying the stack tightening structure by integrating the functions of the structure also reduced the number of tightening parts and helped to reduce cost.

6. Summary

The current density of the new FC stack was increased by a factor of 2.4 by adopting an innovative cell flow field structure (enabling more uniform power generation by improving gas diffusion and water removal through the use of a 3D fine-mesh flow field) and electrodes (enabling the promotion of electrochemical reactions by improving proton conductivity, gas diffusion, and catalytic activity). In addition, integrating the functions of the stack tightening structure reduced the size and weight of the stack, enabling a power density of 3.1 kW/L and 2.0 kW/kg, more than twice that of the conventional stack, and allowing the stack to be installed under the seats of a sedan. Furthermore, the durability of the electrodes was improved by a factor of 3 compared to the previous stack, and the reliability of the stack against impacts, water exposure, and corrosion was ensured. Finally, major cost reductions were achieved by reducing the amount of precious metals used (the amount of Pt in the catalyst was reduced by 72% and the Au surface treatment was eliminated) and by simplifying the stack tightening structure.

This development of a new high-performance and low-cost FC stack has enhanced the product appeal of FCVs and represents an important step toward the realization of a hydrogen-based society.

References

(1) M. Maeda et al. "Analysis of Water Distribution in a Fuel Cell Using X-Ray Computed Tomography." *Denso Technical Review* Vol. 13 No. 1 (2008) pp. 37-43.
(2) S. Hamada et al. "Performance Improvement of Polymer Electrolyte Fuel Cell with Porous Channel." *JSAE Annual Congress (Autumn)* 219-20115664 (2011).
(3) K. Tsubosaka et al. "Development of High Performance Fuel Cell Electrode for New FCV." *Proceedings of Conference of Japan Society of Mechanical Engineers* J0560201 (2015).
(4) T. Tonuma et al. "Development of Fuel Cell Stack for New FCV." *Proceedings of the JSAE Annual Congress (Autumn)* (2015) pp. 742-745.

Authors
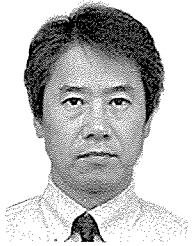
S. MIZUNO   **N. KONNO**   **K. TSUBOSAKA**

H. NISHIUMI   **H. KUBO**   **T. TONUMA**

The High-Pressure Hydrogen Storage System for the Mirai FCV

Masaaki Kondo[*1]
Akira Yamashita[*2]
Sogo Goto[*2]
Nobuyuki Ogami[*3]
Tomoyoshi Kobayashi[*3]
Hirokazu Otsubo[*3]

Abstract
This article describes the high-pressure hydrogen storage system developed for the Mirai fuel cell vehicle (FCV). This new storage system was designed with two different shaped tanks to hold the necessary quantity of hydrogen without sacrificing interior space in a sedan-type vehicle. As a weight reduction measure, the amount of carbon fiber was reduced by designing tanks with an innovative laminated carbon fiber reinforced plastic (CFRP) structure and bosses, resulting in class-leading lightness (weight effectiveness: 5.7 wt%). The storage system also features newly developed valves, pressure regulator, receptacle (hydrogen inlet), and piping, which enabled the vehicle to acquire certification under the newly established international standards for compressed hydrogen vehicle fuel devices. Since these standards involve exposing the tanks to a localized fire test, both drop and fire resistance requirements were satisfied without increasing the external volume of the tanks by combining the impact energy absorbing tank protector with a fire-resistant material. The storage system is also compatible with standards for communicating between FCVs and hydrogen refueling stations. As a result, a high filling efficiency was achieved while reducing the hydrogen refueling time to approximately 3 minutes, roughly the same level of convenience as a gasoline-powered vehicle.

Keywords: *hydrogen storage system, high-pressure hydrogen tanks, carbon fiber reinforced plastic (CFRP), carbon fiber, laminated structure, high-pressure valve, hydrogen refueling*

Special Feature

1. Introduction

Toyota Motor Corporation began development of fuel cell vehicles (FCVs) in 1992, and is currently engaged in various development initiatives with the aim of achieving widespread popularization. The Toyota FCHV-adv, which was launched in 2008, was more efficient than the 2005 model and adopted a hydrogen storage pressure of 70 MPa compared with the 35 MPa system of the 2005 model. As a result, the Toyota FCHV-adv achieved a cruising range in practical driving conditions of more than 500 km. Toyota subsequently developed a new high-pressure 70 MPa hydrogen storage system suitable for adoption in a sedan package. The developed system is substantially lighter and lower cost than the system adopted by the 2008 model.

2. System Configuration

Fig. 1 shows the installation layout of the developed high-pressure hydrogen tanks. The shapes of the newly developed high-pressure hydrogen tanks were optimized to fit under the seats of a sedan type vehicle. This configuration was designed to ensure both space for the vehicle occupants and the required hydrogen storage capacity.

High-pressure hydrogen tanks
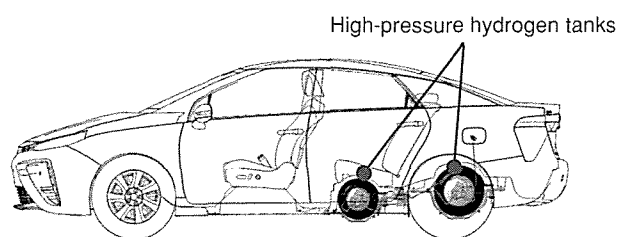
Fig. 1 Tank Installation Layout

*1 R&D and Engineering Management Div., Advanced R&D and Engineering Company
*2 Fuel Cell Products Development Div., Powertrain Company
*3 Fuel Cell Fundamental Development Div., Powertrain Company

Fig. 2 shows the basic outline of the high-pressure hydrogen storage system. **Table 1** lists the specifications of the high-pressure hydrogen tanks. High-pressure hydrogen is supplied from two tanks of different shapes. The hydrogen pressure is reduced in two stages by a high-pressure regulator and injector before reaching the fuel cell (FC) stack.
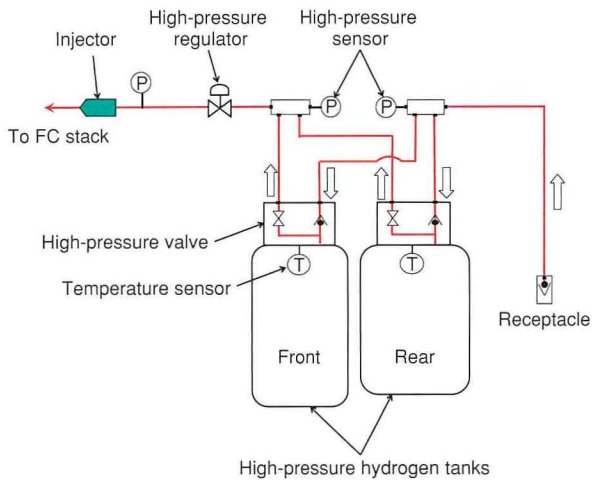
Fig. 2 Basic Outline of High-Pressure Hydrogen Storage System

Table 1 Main Specifications of High-Pressure Hydrogen Tanks

Nominal working pressure (MPa)	70
Type	4 (plastic liner)
Size (mm)	Front: diameter = 350 × length = 1,016 Rear: diameter = 436 × length = 748
Internal volume (L)	Front: 60.0, rear: 62.4
Weight (kg)	Front: 42.8, rear: 44.7 (The above figures do not include the hydrogen gas and valves.)
Hydrogen storage mass (kg)	Approx. 5.0
Regulatory and standard compliance	KHK S0128, SAE J2579, GTR No. 13, European regulations: EC Nos. 79 and 406

The two tanks are fixed under the floor by two band-shaped brackets (**Fig. 3**).
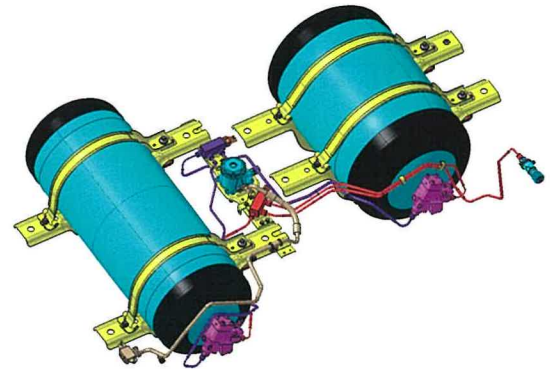
Fig. 3 Configuration of High-Pressure Hydrogen Storage System

3. High-Pressure Hydrogen Tank Weight Reduction

3.1 Improved CFRP lamination method

Since the high-pressure hydrogen tanks account for the highest proportion of the weight of the high-pressure hydrogen storage system, the design of the tanks was substantially revised. **Fig. 4** shows the structure of the high-pressure hydrogen tanks.
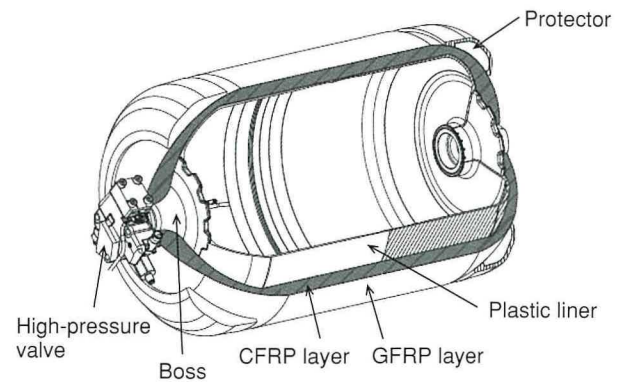
Fig. 4 Structure of High-Pressure Hydrogen Tanks

The high-pressure hydrogen tanks are composed of a plastic liner at the innermost layer that functions to seal in the hydrogen gas, surrounded by a strong carbon fiber reinforced plastic (CFRP) layer capable of withstanding high pressures. This is surrounded by a glass fiber reinforced plastic (GFRP) layer with high impact resistance, and a protector. Aluminum bosses are provided at both ends of the plastic liner for valve fitting. To reduce the weight of the tanks, this development lowered the CFRP content by improving the CFRP laminated structure. **Fig. 5** shows the normal basic lamination pattern of a high-pressure tank.
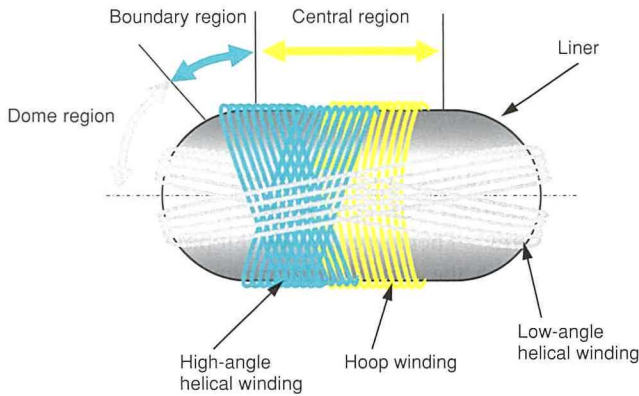
Fig. 5 Lamination Pattern of High-Pressure Hydrogen Tanks

Conventionally, a laminated high-pressure tank CFRP structure adopts a combination of the following three types of winding methods: hoop winding to strengthen the central region of the tank, low-angle helical winding to strengthen the dome regions (in the axial direction), and high-angle helical winding to reinforce the boundaries between these regions. By necessity, the high-angle helical winding required to strengthen the boundary regions is also wound over the central region. Since the high-angle helical winding is wound around the tank at an angle of approximately 70° with respect to the central axis, the efficiency of the reinforcement provided by this structure is reduced, as shown in **Fig. 6**.
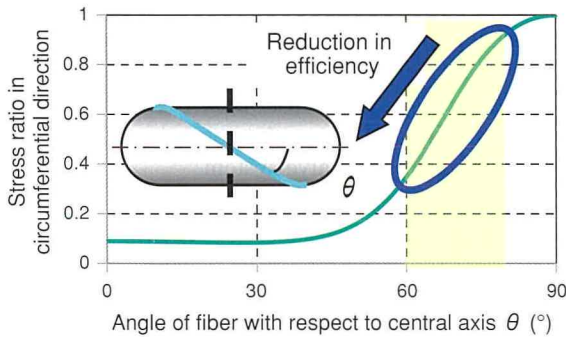
Fig. 6 Relationship between Fiber Angle and Strength Efficiency

Focusing on the ineffective high-angle helical winding at the central region of the tank, a lamination method was developed that strengthens the boundary regions without the use of high-angle helical winding. **Fig. 7** compares the conventional and new lamination methods.
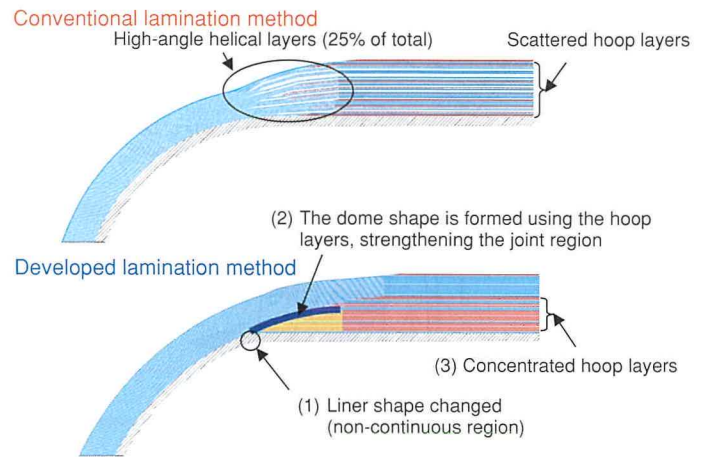
Fig. 7 Comparison of Conventional and New Lamination Methods

Specifically, the following three changes were made to the lamination method.

(1) The sectional shape of the liner was flattened to enable lamination by hoop winding at the boundary regions.
(2) The boundary regions were strengthened while forming the conventional liner shape by gradually retracting the end positions of the hoop winding.
(3) Hoop winding lamination was concentrated in the inner layers.

These changes had the following two effects. First, the high-angle helical winding, which accounted for approximately 25% of the total laminated structure, was eliminated. Second, hoop winding, which is a highly effective way of strengthening the central region of the tank, was concentrated in the inner layers of the laminated structure at which the generated stress is highest. This dual effect enabled an approximately 20% reduction in CFRP compared to the conventional lamination method.

3.2 Boss optimization

The shapes of the bosses were also optimized to help reduce the CFRP usage amount. The reaction force to the internal pressure acting on the CFRP opening is transferred by the bosses to the CFRP in the form of flange surface pressure. As a result, the surface pressure applied to the CFRP can be lowered by reducing the size of the opening (proportional to the valve diameter) and increasing the flange diameter. This enables less CFRP to be used in the helical layers. **Fig. 8** illustrates the action of surface pressure at the inner surface of the CFRP based on the differences between the previous and new boss shapes.

Special Feature
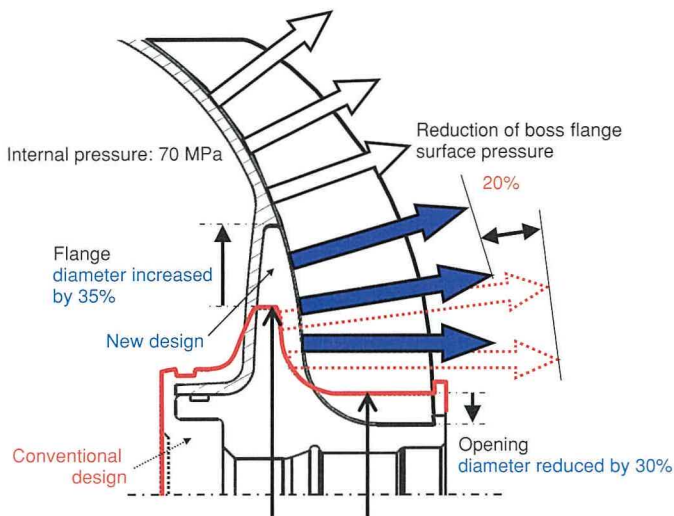
Fig. 8 Surface Pressure Applied to CFRP at Boss

By optimizing the shape of the bosses, the helical layers were reduced by approximately 5%.

Improving the laminated structure and optimizing the bosses in these ways substantially reduced the CFRP usage amount in the boundary regions (high-angle helical winding) and the dome regions (helical winding). Combined with other weight reduction items, these measures reduced the laminated proportion of the tanks by 40% compared to the conventional tanks. The weight effectiveness of the tanks was increased to 5.7 wt%, one of the highest levels in the world (as of 2015). **Fig. 9** compares the cross sections of tanks laminated by the conventional and newly developed methods.
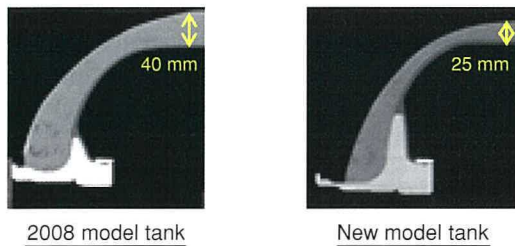
Fig. 9 Tank Cross Section Comparison with Conventional and New Lamination Methods

4. Cost/Size Reduction

4.1 Adoption of high-strength general-purpose carbon fiber

Reducing the number of tanks from four to two was not sufficient to achieve the cost target for the high-pressure hydrogen system. Therefore, the development examined the whole system with the aim of reducing material cost, lowering the number of parts, carrying over components from gasoline-powered vehicles, and so on. One particular cost driver in the system was the carbon fiber used for the tanks. The 2008 model adopted high-grade aviation carbon fiber, which is very expensive. Therefore, while considering the required characteristics of CFRP for Type 4 tanks, the development team worked with carbon fiber manufacturers to increase the strength of general-purpose carbon fiber. The resulting low-cost carbon fiber is almost as strong as high-grade material, while also retaining elasticity close to conventional general-purpose carbon fiber.

4.2 High-pressure valves

The development reduced the cost and size of other high-pressure components in addition to the tanks. Factoring in the risk of hydrogen embrittlement, high-pressure parts that come into contact with hydrogen tend to use aluminum alloy or stainless steel. Following the lead of the 2008 model, the high-pressure valve and high-pressure regulator bodies in the developed system were constructed of aluminum alloy, and stainless steel was adopted for all main components. The structure of the valve system was then revised to reduce the number of parts. **Fig. 10** shows the configuration of the newly developed and conventional valve system.
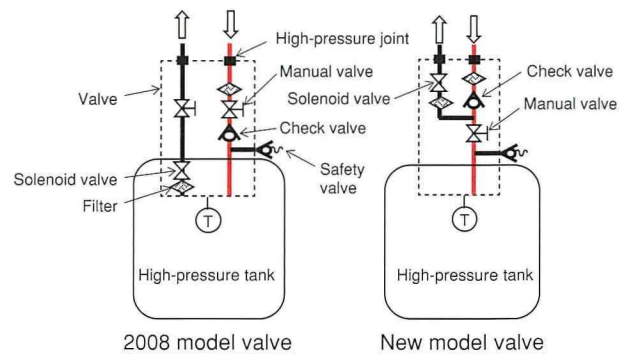
Fig. 10 Configuration of New and Conventional Valve Systems

The developed valve system features a simplified gas flow and a different solenoid valve layout. This solenoid valve is also smaller and has an improved internal structure. In addition, to ensure the durability of the sliding portions such as the check valve, the stainless steel sleeve used in the 2008 model was eliminated to reduce the number of parts and size of the valve system. **Fig. 11** compares the sliding portion of the check valves in the previous and newly developed solenoid valves.
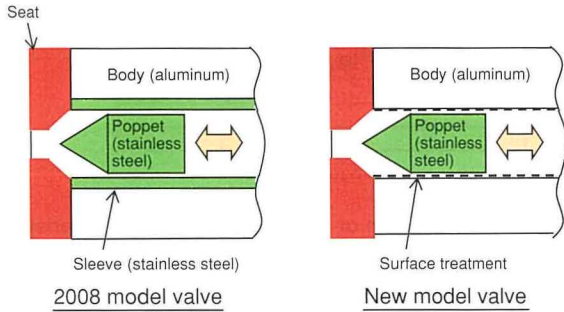
Fig. 11 Comparison of Valve Sliding Portions

Aluminum alloys are generally relatively soft. When used in combination with stainless steel, there is the concern that sliding may cause adhesion or generate foreign material. The 2008 model paired stainless steel surfaces with other stainless steel surfaces to restrict wear and the generation of foreign material. In contrast, this development studied the feasibility of replacing the stainless steel sleeve with a new surface treatment.

Fig. 12 shows an outline of the ball-on-disk wear test used for this study. A new tester was manufactured for wear tests in hydrogen. **Fig. 13** shows an outline of this tester. The ball side simulates the poppet and is made of stainless steel. In contrast, the disk side simulates the sliding surface of the valve body. Various materials and surface treatments were examined. The total sliding distance was set considering the durable lifetime of the valve. The test results found that an alumite surface treatment on the aluminum valve body achieved stable sliding characteristics in hydrogen.

Fig. 14 shows the average friction coefficient during the test with and without the alumite treatment and different materials used for the disk side. **Fig. 15** shows the wear generated on the surface.
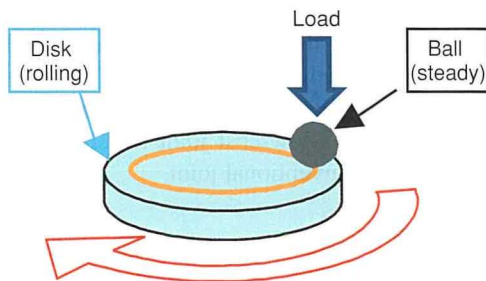
Fig. 12 Outline of Ball-on-Disk Wear Test
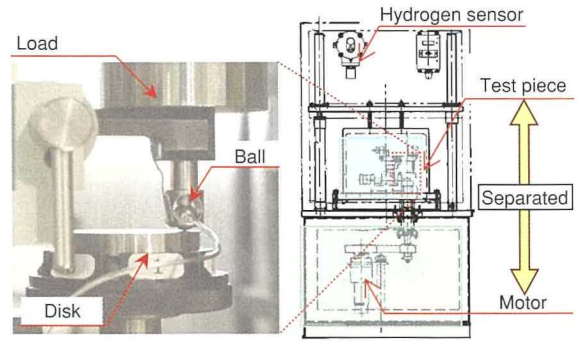
Fig. 13 Ball-on-Disk Wear Tester
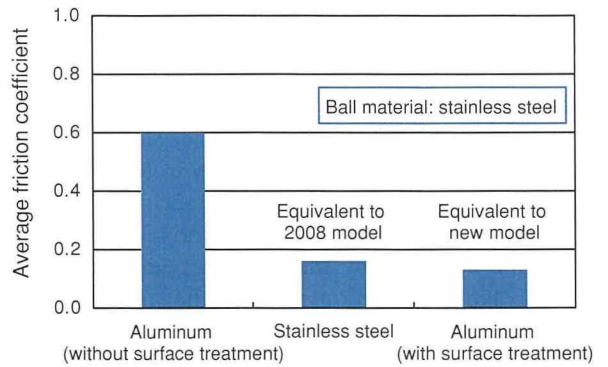
Fig. 14 Relationship between Disk Material, Surface Treatment, and Friction Coefficient
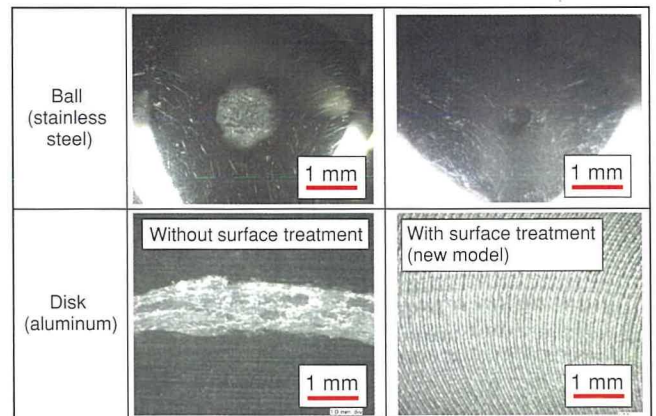
Fig. 15 Differences in Sliding Surface With and Without Surface Treatment

Figs. 14 and **15** show that the alumite surface treatment achieves stable sliding characteristics in hydrogen. These measures reduced the valve system weight by approximately 25% and the number of parts by 35%, thereby lowering both the size of cost of the system. **Fig. 16** shows the appearance of the new and conventional valves.
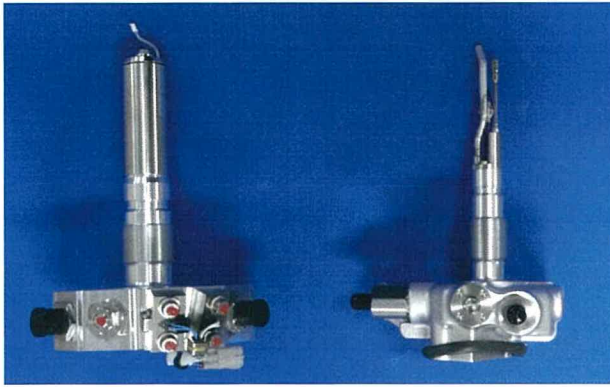
2008 model valve   New model valve

Fig. 16 Comparison of High-Pressure Valves

4.3 High-pressure regulator

The development studied the feasibility of reducing the cost of the high-pressure regulator by measures such as redesigning the sealing portion. The transient characteristics of the pressure control value achieved by the high-pressure regulator are an important aspect for controlling the injector installed downstream of the high-pressure regulator. If this transient pressure control value contains a large variation, this will cause large variations in the injection quantity and have an adverse effect on fuel efficiency. **Fig. 17** shows an outline of the pressure regulator structure.
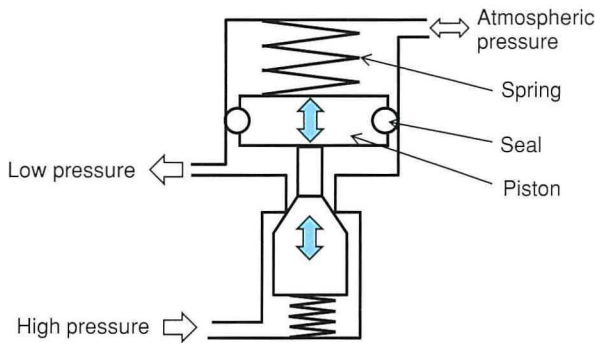
Fig. 17 Outline of Pressure Regulator Structure

The pressure regulator consists of parts such as a valve element on the high-pressure side, and a piston and spring on the low-pressure side. When fuel is supplied, the transient flow rate of the pressure regulator changes in synchronization with the operation of the downstream injector. Therefore, the piston, valve element, and the like move up and down by very small amounts. When this happens, instability in the pressure regulator (e.g., large changes in the friction coefficient of the piston sliding portion) causes variations in the pressure control characteristics. This development adopted lower cost materials for the piston sliding sealing portion and adjusted the shape of the sealing

materials to ensure stable sliding characteristics. The shape of the piston was also optimized. These measures achieved superior pressure control characteristics than the 2008 model at a lower cost. **Fig. 18** shows the changes and hysteresis of the pressure control value at different flow rates.
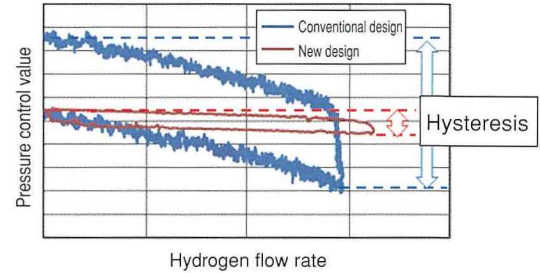
Fig. 18 Comparison of Pressure Control Characteristics

4.4 High-pressure joints

This development changed the high-pressure joints and sealing structure to reduce cost. The 2008 model used an O-ring sealing structure. However, since the temperature of the high-pressure joints drops to around -50°C when hydrogen gas is continuously consumed, this structure required the use of special high-cost materials. This development adopted a metal sealing structure and reduced the number of parts. **Fig. 19** shows the structure of a high-pressure joint.
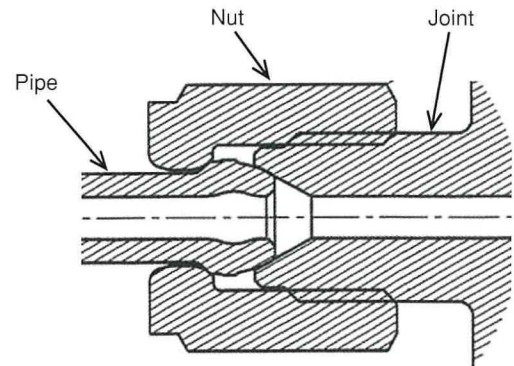
Fig. 19 Cross-Section of High-Pressure Joint

Stainless steel was adopted for both the pipe and joint material. However, the hardness of the stainless steel used was determined based on the required sealing performance. The new structure achieved the required reliability without the use of gaskets or other parts, resulting in a low-cost joint that can be assembled more quickly than the conventional joint.

4.5 High-pressure sensor

The high-pressure sensor is an enhanced version of a part adopted in an existing engine, adapted for use with high-pressure

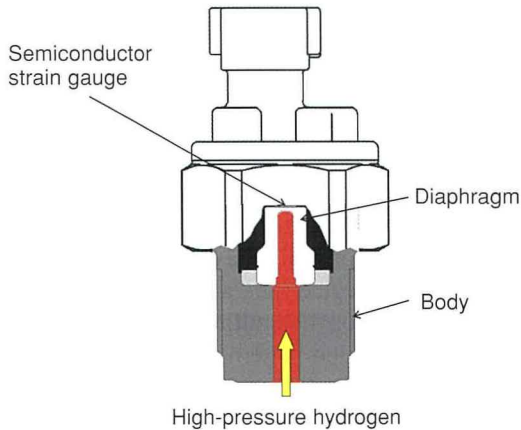hydrogen. **Fig. 20** shows a cross-section of the high-pressure sensor.

Fig. 20 High-Pressure Sensor

The high-pressure sensor is structured to detect minute deformations of the diaphragm under high pressure using the semiconductor strain gauge. It was found that, when this sensor is used for an extended period of time in hydrogen, small amounts of hydrogen form solid solutions with the diaphragm. This causes the diaphragm to deform and has an adverse effect on sensor accuracy. **Fig. 21** shows the measured results of diaphragm expansion and deformation due to hydrogen solid solution formation.
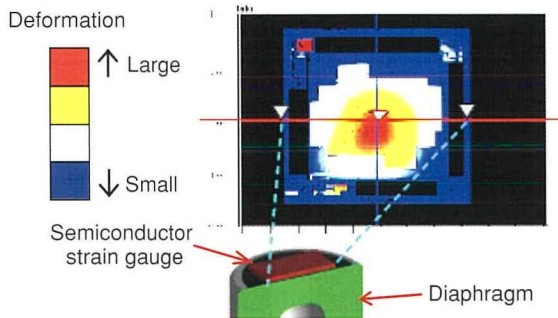
Fig. 21 Deformation of Diaphragm by Hydrogen Solid Solution Formation

Various proposals were examined to address this issue, such as changing the material or shape of the diaphragm. Eventually, the inner surface of the diaphragm was coated with a film to suppress hydrogen permeation. Conventional surface treatment technology was adopted for this film to minimize cost increases. This measure reduced the amount of hydrogen solid solution formation on the diaphragm by around 90%, and it was confirmed that sensor accuracy did not deteriorate even when used for an extended period of time in high-pressure hydrogen.

5. Improved Refueling Performance

In 2008, most hydrogen refueling stations compatible with pre-cooling used a hydrogen gas temperature of -20°C. At these stations, refueling took around 10 minutes. In addition, since these stations were not compatible with station/vehicle communication standards, a maximum state of charge (SOC) of around 90% of tank capacity could be achieved. More modern hydrogen refueling stations that comply with the SAE J2601 standard are compatible with pre-cooling down to -40°C. At these stations, the refueling time has been reduced to the equivalent amount of time required by a gasoline-powered vehicle. Since these stations are also compatible with the communication protocol, the achievable SOC is also higher. **Fig. 22** shows the configuration of the communication system and **Fig. 23** compares the refueling times and SOCs of the 2008 and new models (measured by Toyota under standard SAE conditions).
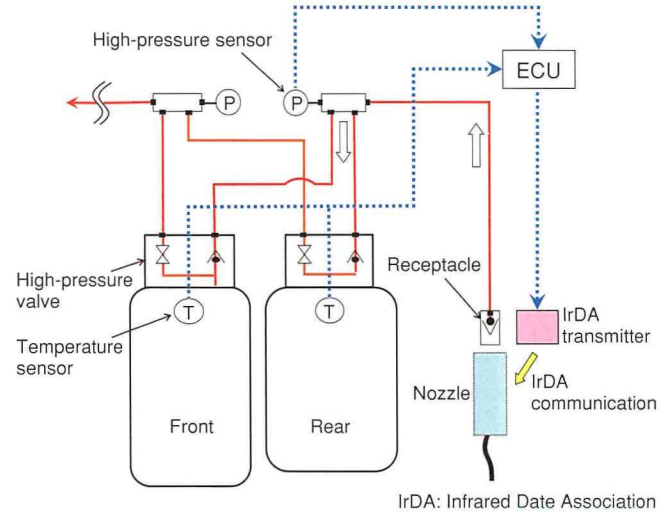
Fig. 22 Configuration of Communication System
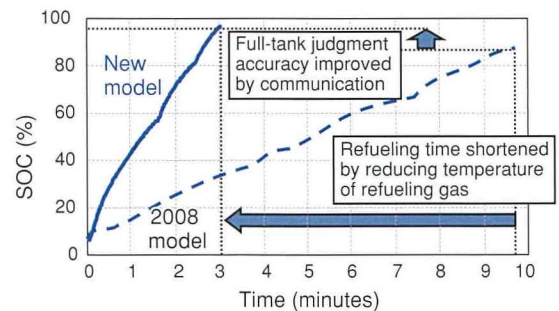
Fig. 23 Comparison of Hydrogen Refueling Times and SOCs

This development also examined ways of improving the full-tank judgment accuracy during communication to further enhance the SOC. In a system comprising multiple tanks of different shapes, the amount of temperature rise during refueling generally differs depending on the difference in pressure drop from the hydrogen inlet to the tank, as well as differences in the rate of heat dissipation. Previous studies have also found that a temperature distribution occurs inside the tank during refueling. Unlike a liquid fuel, a full tank of a gaseous fuel is usually judged by correcting the pressure during refueling using the temperature. Therefore, when large temperature differences occur between such tanks and inside the tanks, it is important to detect the average temperature as close as possible. The refueling paths to the tanks in the developed hydrogen storage system were designed to minimize the temperature difference between tanks. In addition, the spray direction of the refueling gas and the positions of the temperature sensors were adjusted to minimize the difference between the internal tank temperature distribution and the average temperature. These measures helped to achieve an SOC of at least 95%. **Fig. 24** shows the results of an experiment to identify the effects of the position of the internal tank temperature sensor position and gas spray direction on the SOC.
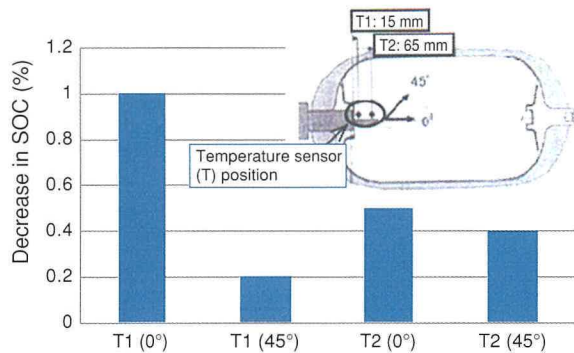
Fig. 24 Relationship of SOC with Gas Spray Direction and Temperature Sensor Position

6. Certification

For the component parts of the developed hydrogen storage system, this development aimed to achieve certification under the newly established global technical regulations (GTR) and the relevant European (EU) regulations (EC No. 79/2009 and EC No. 406/2010). The conventional high-pressure hydrogen tanks were type-certified under the Japanese standard KHK S0128, which was established in 2013 as a technical standard for compressed hydrogen vehicle fuel containers. However, the high-pressure hydrogen tanks and high-pressure valves used in the new FCV were the first such parts to be successfully certified in Japan under the more stringent test conditions described in the GTR. The three differences with the conventional test conditions are as follows: (1) continuous evaluation of resistance to chemical loads and physical impacts (drop resistance) after the application of a pressure cycle load, (2) evaluation under extreme temperatures as well as room temperature in the environmental temperature conditions of the pressure cycle test using hydrogen gas, and (3) in the bonfire test, the adoption of a flame application pattern on one side away from the thermally activated pressure relief device (i.e., a localized fire test pattern) in addition to the conventional engulfing fire over the entire tank. **Fig. 25** shows the evaluation pattern for condition (1) and **Fig. 26** shows photographs of condition (3) in progress.

It should be noted that condition (2) was applied to the whole hydrogen storage system including parts other than those specifically targeted by the test, using a vehicle cut body. **Fig. 27** shows the appearance of this test condition.
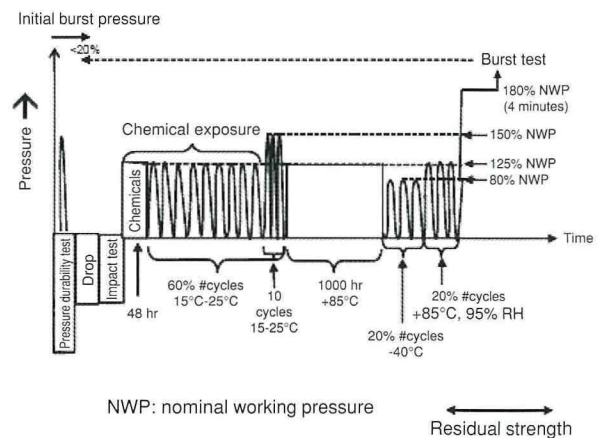

Fig. 25 Procedure of Hydrogen Gas Pressure Cycle Test

Fig. 26 Bonfire Test (Left: Localized Fire Test, Right: Engulfing Fire Test)

Fig. 27 External Appearance of Hydrogen Gas Pressure Cycle Test

In addition, to ensure compliance with the localized bonfire test requirements, fire-resistant material was incorporated into the conventional impact energy absorbing protector of the high-pressure hydrogen tanks. This satisfied the drop resistance and new fire resistance performance requirements without increasing the size of the tanks. **Fig. 28** shows the structure of the protector.
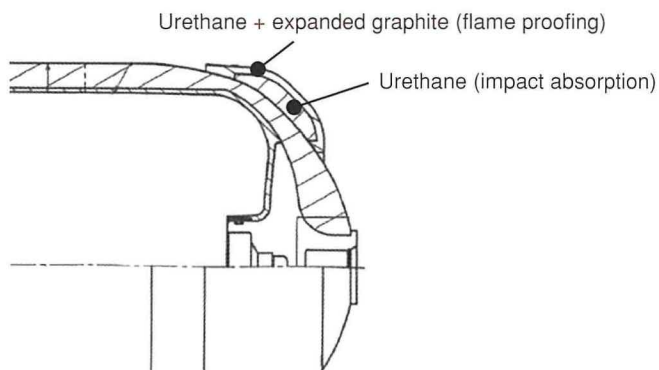

Urethane + expanded graphite (flame proofing)

Urethane (impact absorption)

Fig. 28 New Tank Protector

7. Conclusion

The high-pressure hydrogen storage system installed in the Mirai FCV incorporates newly developed component parts such as the tanks, valves, and regulator. As a result, this system ensures sufficient hydrogen storage capacity without sacrificing interior space. Weight reduction measures, including improvements to the laminated CFRP structure of the tanks helped to increase the weight effectiveness of the whole storage system by approximately 15% compared to the 2008 model. The adoption of a new low-cost and high-strength carbon fiber, the simplification of various high-pressure parts, and the carry-over

of other parts from conventional vehicles also helped to realize substantial cost reductions. Refueling performance was improved by ensuring compatibility with the SAE J2601 and J2799 standards for communication between the hydrogen refueling station and vehicle. As a result, a fueling time of approximately 3 minutes and a high SOC were achieved, thereby improving the usability of the vehicle. At the same time, the developed hydrogen storage system was certified under international guidelines for compressed hydrogen vehicle fuel containers and also achieved certification under the relevant EU regulations (EC No. 79/2009).

As the next step toward full-scale popularization of FCVs, technical development will be continued to further reduce the size and weight of the hydrogen storage system and advance the performance of the next-generation of FCVs.

References

(1) A. Yamashita et al. "Development of High-Pressure Hydrogen Valve System for FCHV." *Proceedings of the Society of Automotive Engineers of Japan* No. 24-10 (2010) pp. 13-16.
(2) M. Mizuno et al. "High-Pressure Hydrogen Tank for FCHV." *Proceedings of the Society of Automotive Engineers of Japan* No. 84-05 (2005) pp. 13-16.
(3) H. Mizuno et al. "Development of Fuel Cell Hybrid Vehicle with 70 MPa Hydrogen Tanks." *Journal of Society of Automotive Engineers of Japan* Vol. 62 No. 11 (2008) pp. 47-52.

Authors

M. KONDO   **A. YAMASHITA**   **S. GOTO**

N. OGAMI   **T. KOBAYASHI**   **H. OTSUBO**

Development of Fuel Cell System for New FC Bus

Tomohiro Ogawa*[1]
Kenji Umayahara*[1]
Yoshihiro Ikogi*[1]

Abstract

This article describes the fuel cell (FC) system adopted by the Sora, a new FC route bus developed after the Mirai FCV. Since an FC route bus has a greater frequency of high motor output than a conventional FCV, use of the FCV system in an FC bus results in larger electric potential fluctuations and causes a substantial reduction in power after a lifetime durability test. Therefore, for the Sora, the battery output rate was increased and a system and control adopted that reduces the electric potential fluctuations of the FC. This configuration and control enables the new FC bus to satisfy requirements for both durability and dynamic performance. Additionally, if sufficient power cannot be provided from the batteries due to a low state of charge (SOC) or the like, the system ensures the required dynamic performance by temporarily operating the FC at an operation point with a large potential fluctuation range to boost output. The durability of the FC system in the Sora, including this control, was verified in durability tests. These tests confirmed that the FC system achieved both the required durability and dynamic performance.

Keywords: *fuel cell (FC), FC system, HV system, electric potential fluctuation, power reduction, durability, power distribution*

1. Introduction

Fuel cells (FCs) are gaining attention as a promising means of helping to address environmental issues such as global warming and air pollution, which are becoming more and more serious. FCs generate no harmful emissions such as CO_2 and NOx, and are powered by hydrogen that can be produced from a wide range of energy sources, without becoming over-reliant on any particular country or region. To encourage the market acceptance of FCs and to help realize a hydrogen-based society, Toyota Motor Corporation has followed the development and launch of the Mirai fuel cell passenger vehicle (FCV) by developing a new FC bus called the Sora.

This article describes the configuration and controls of the FC system developed for this FC bus. This system was designed to satisfy requirements for both dynamic performance and durability, which are particular issues for a FC bus.

2. Outline of the Sora

2.1 Main specifications

Photo 1 shows an external view of the Sora, and **Table 1** compares the main specifications of this bus with the 2002 model that was certified by the Japanese Minister of Land, Infrastructure, Transport and Tourism (MLIT).[1]

Photo 1 The New Sora FC Bus

*[1] Fuel Cell Products Development Div., Powertrain Company

Compared to the 2002 model, the Sora features greater dynamic performance and substantially higher durability. It is also equipped with a high-capacity external power supply function that is capable of providing a substantial amount of power in the event of a natural disaster (provisionally calculated as equivalent to 4.5 days of power for an evacuation center, based on power consumption of approximately 50 kW/h per day).

Table 1 Specifications of the Sora

		Sora	2002 model FC bus
Vehicle	Length/width/height (mm)	10,525 2,490 3,350	10,515 2,490 3,360
	Occupant capacity	79	60
	External power supply system	Maximum power: 9 kW Power supply capacity: 235 kW	None
FC stack	Type	Polymer electrolyte	
	Power (kW)	114×2	90×2
Motor	Maximum power (kW)	113×2	80×2
	Maximum torque (N·m)	335×2	260×2
Traction battery	Type	Nickel-metal hydride	
High-pressure hydrogen tanks	Number of tanks	10	5
	Nominal working pressure (MPa)	70	35

2.2 FC system

Fig. 1 compares the system configurations of the Sora and Mirai. To ensure the required dynamic performance and durability, a second high-voltage battery was added to the Toyota Fuel Cell System (TFCS) developed for the FCV. Two systems incorporating this additional battery were then installed in the FC bus. These systems are electrically isolated. Each operates independently and the drive motors are connected mechanically through a gear. The power distribution was designed so that the power of the drive motors is the same. This design helps to enhance the durability of the FCs and auxiliary components.
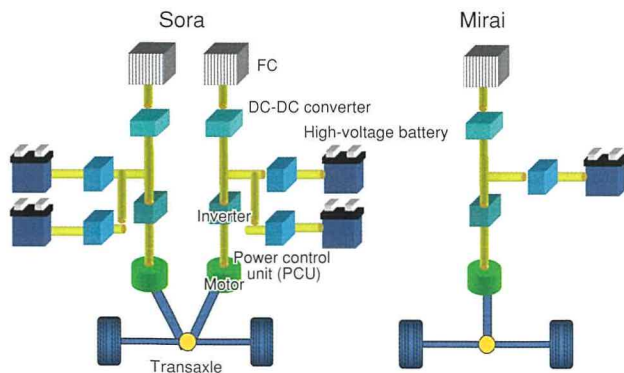
Fig. 1 System Configurations of the Sora and Mirai

3. Control to Enhance FC Durability

3.1 Outline

The durability of the FC stack adopted in the Sora was greatly enhanced compared to the stack adopted in the 2002 model. This was accomplished by developing a new system and control that restricts platinum (Pt) dissolution and the formation of large Pt particles, which are known to reduce the power of the FC stack.

3.2 Mechanism of power reduction in FC stack and issues of FC buses

The Pt used as a catalytic material in FCs tends to dissolve at high electric potentials and to precipitate at low electric potentials. Furthermore, at low electric potentials, the oxide film on the Pt surface is stripped away, facilitating Pt dissolution if the electric potential increases immediately afterward.[2][3]

When the electric potential changes repeatedly, successive dissolution and precipitation causes the Pt particle size to increase, lowering the effective catalyst surface area (**Fig. 2**). When the effective catalyst surface area is lowered, the reaction resistance increases, leading to a drop in power (**Fig. 3**).
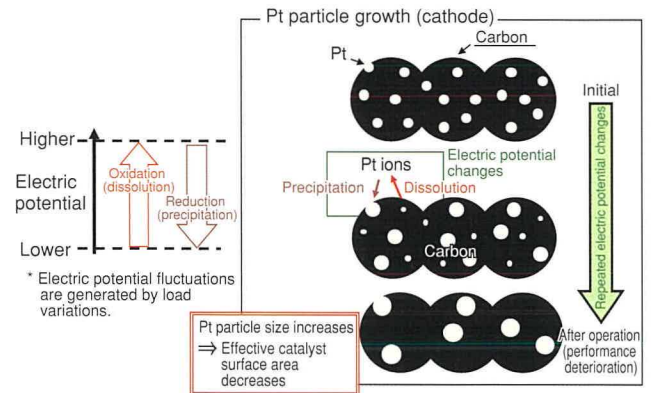
Fig. 2 Illustration of Power Reduction Mechanism
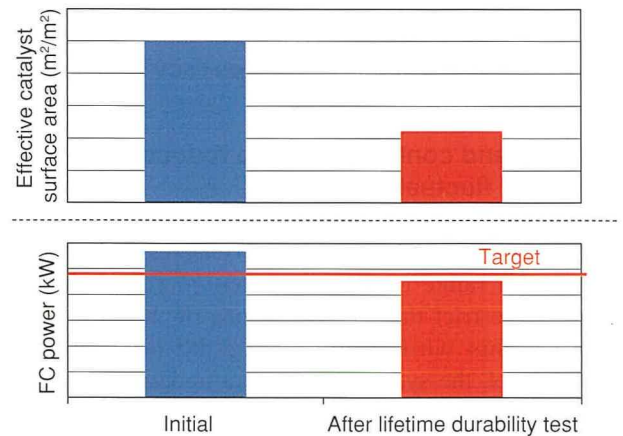
Fig. 3 Effective Catalyst Surface Area and FC Power after Lifetime Durability Test

When the system and control used in the Mirai were adopted in the Sora, the effective catalyst surface area fell dramatically after completing a lifetime durability test, leading to a substantial reduction in power.

The graph in **Fig. 4** shows the frequency of motor power in standard driving patterns for a passenger vehicle and a route bus. Compared to the FCV, the FC route bus has a higher frequency of high-power output. Consequently, to cover the output range of a bus, a larger voltage fluctuation range (i.e., the range of electric potential fluctuations) occurs in a bus than in an FCV (**Fig. 5**). As a result, the system is susceptible to much larger reductions in power.
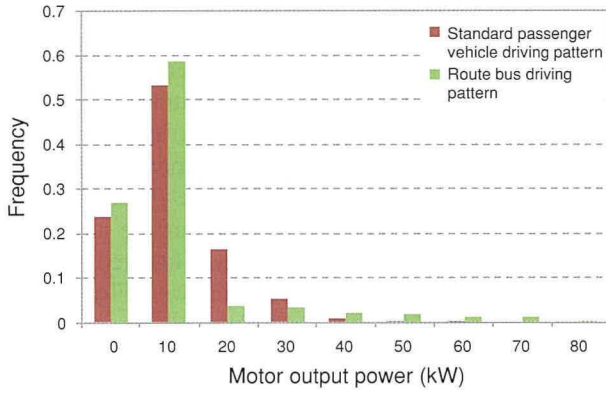
Fig. 4 Motor Power Frequency of FCV and FC Route Bus
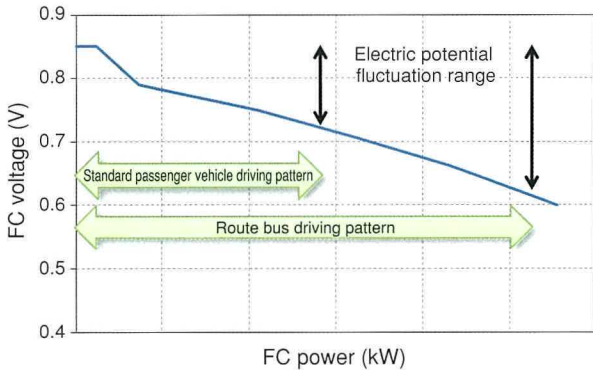
Fig. 5 Electric Potential Fluctuation Range of FCV and FC Route Bus

3.3 System and control design to reduce electric potential fluctuations

Fig. 6 shows the power-voltage (PV) characteristics of the FC. To reduce the range of electric potential fluctuations, it is necessary to restrict the load variations of the FC stack. To accomplish this while maintaining the minimum power generation level, the system in the Sora is designed so that the lower limit voltage (Vfmin) satisfies the power target after the durability test. This value is higher than that value adopted for the Mirai.

Motor power (P_{mot}) is supplied from the FC power (P_{fc}) and the power of the high-voltage batteries (P_{bat}), and is defined by the power balance equation shown below. (This equation omits the power consumption of the auxiliary equipment.)

$$P_{mot} = P_{fc} + P_{bat} \tag{1}$$

The following system design was required to achieve sufficient motor power up to the target FC maximum power (P_{fcmax}), which is determined from Vfmin.

$$P_{bat} \geq P_{mot} - P_{fcmaxt} \tag{2}$$

Fig. 7 shows the breakdown of the power of the FC and high-voltage batteries at the maximum motor power level of the Mirai and Sora. To obtain maximum motor power at P_{fcmax}, the Sora requires greater power from the high-voltage batteries than the Mirai. Therefore, maximum motor power is supplied in the Sora through two high-voltage batteries.
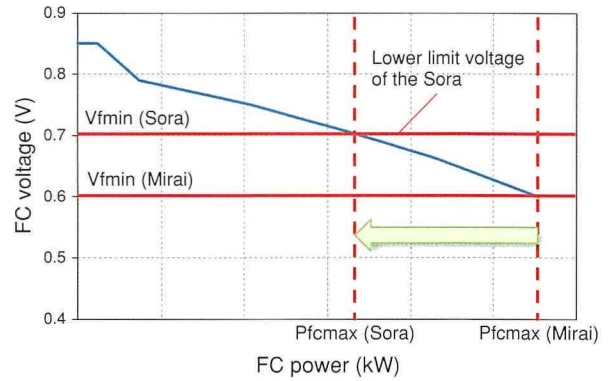
Fig. 6 Maximum Power of the Sora and Mirai
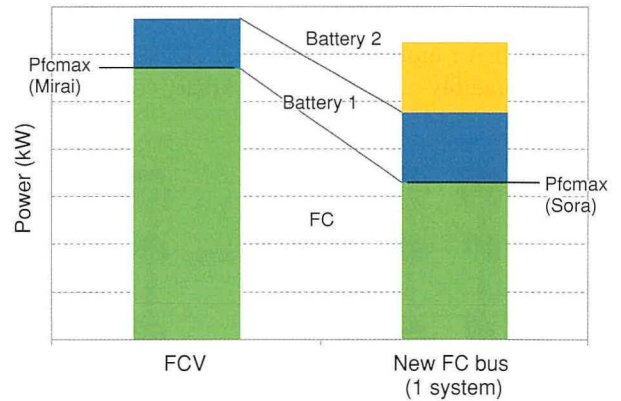
Fig. 7 Power Breakdown at Maximum Motor Power

3.4 Issues of system that secures power using high-voltage batteries

Supplying the power necessary for motor drive using the high-voltage batteries is an effective means of reducing FC load variations. However, if the bus is required to climb a long hill, the system may not be able to supply power from the high-voltage batteries if the state of charge (SOC) is too low or the battery temperature is too high, resulting in insufficient dynamic performance.

Therefore, if sufficient power cannot be obtained from the high-voltage batteries, the system secures the required dynamic performance by temporarily reducing the lower limit voltage and offsetting the reduction in power through the FC. **Fig. 8** shows an outline of this design. The FC power can be increased by raising the vehicle request power. However, when the lower limit voltage of the FC is reached, power is provided from the high-voltage batteries (**Fig. 8** (1)). If the vehicle request power is increased and maintained at a high value, output from the high-voltage batteries is used to offset the output at the lower limit voltage of the FC. In this case, the battery SOC falls (**Fig. 8** (2)). When the lower SOC limit is reached, durability is enhanced by temporarily reducing the voltage lower limit, increasing the FC power, and restricting the power of the high-voltage batteries (**Fig. 8** (3)). This design satisfies the power requirements of the bus.
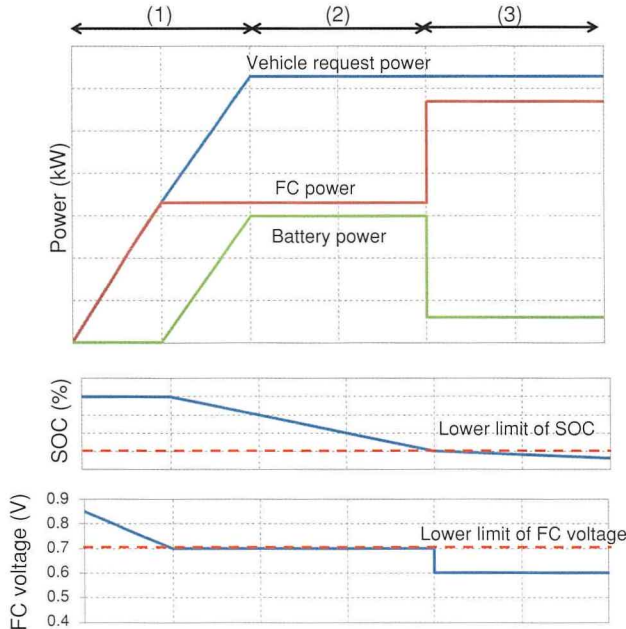
Fig. 8 Outline of Design to Secure Power Performance

3.5 Actual vehicle verification

Fig. 9 shows the acceleration data of the Sora in the route bus test pattern. The figure shows that the control supplies the vehicle request power from the high-voltage batteries and maintains the lower limit voltage to enhance durability.

Fig. 10 shows the temperature and SOC of the high-voltage batteries of the Sora in the route bus test pattern. In the route bus driving pattern, the temperature and SOC of the high-voltage batteries are within the range that allows the control to enhance durability by maintaining the lower limit voltage. As a result, this control satisfies the requirements for both FC durability and dynamic performance.
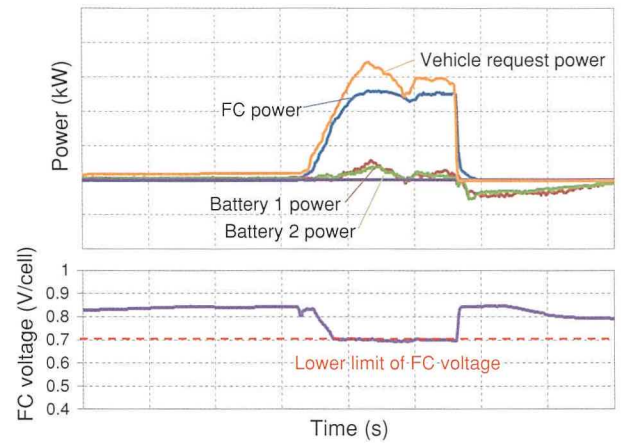
Fig. 9 Verification Results of FC Voltage Behavior during Acceleration
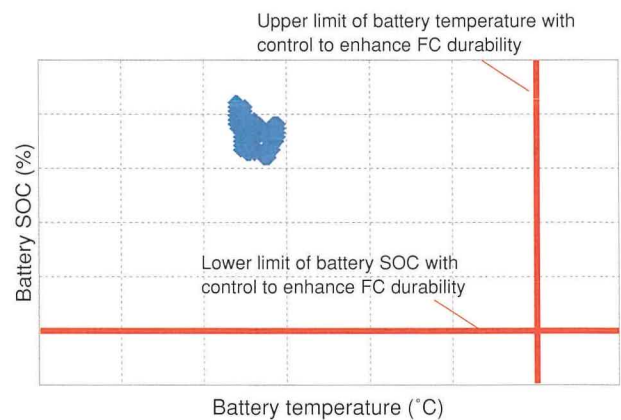
Fig. 10 Battery SOC and Temperature in Route Bus Driving Pattern

As described above, the developed control operates the FC system to reduce electric potential fluctuations. This helps to restrict the decrease in effective catalyst surface area, thereby satisfying the power reduction target after the lifetime durability test (**Fig. 11**).
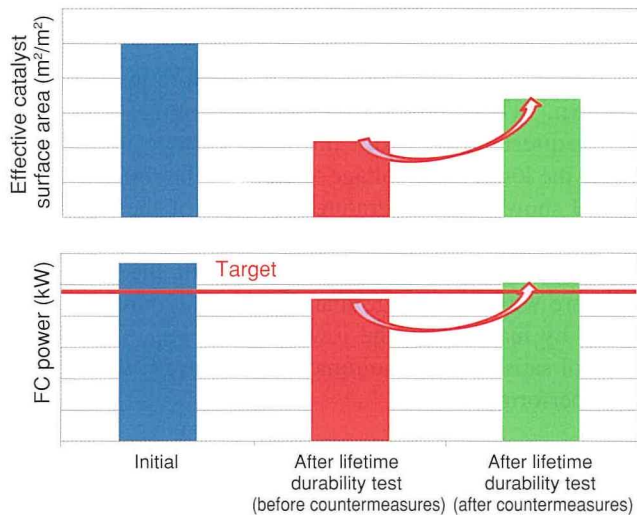
Fig. 11 Effectiveness Verification Results of Control to Enhance FC Durability

Finally, **Fig. 12** shows the data when climbing a long hill. When the SOC of the high-voltage batteries falls due to the long upward gradient, the system temporarily reduces the lower limit voltage of the FC, thereby increasing the FC power supply. This ensures that the motor power is sufficient and enables the bus to maintain speed up the hill.
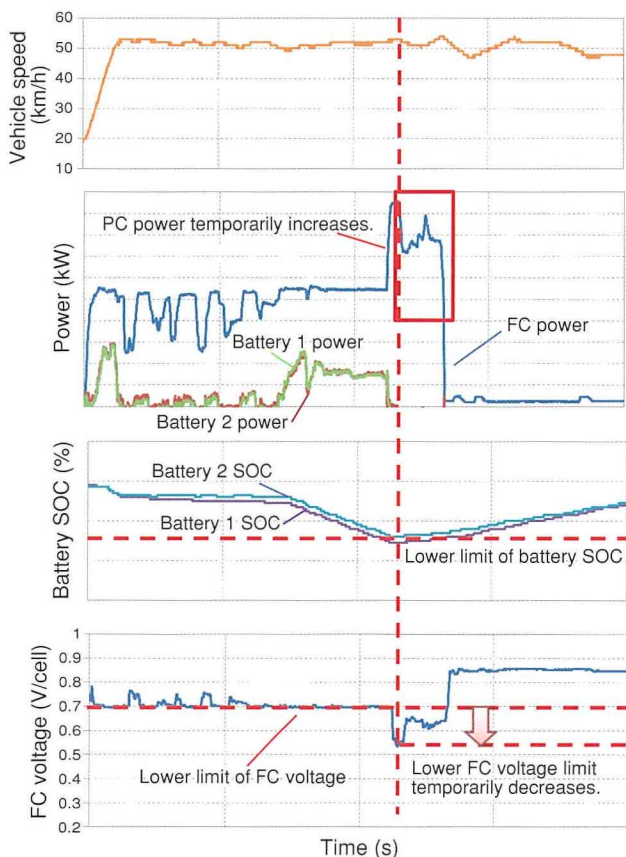

Fig. 12 Verification Results of Continuous Hill-Climbing Performance

4. Conclusions

Since an FC route bus has a greater frequency of high motor power output than an FCV, use of the FCV system in an FC bus generates larger electric potential fluctuations in the FC, resulting in a substantial reduction in power after a lifetime durability test. Therefore, for the Sora, the rate of battery power output was increased and a system and control was adopted that reduces the electric potential fluctuations of the FC. This configuration and control enable the Sora to satisfy requirements for both durability and dynamic performance.

References

(1) Y. Naganuma et al. "Development of Fuel Cell Hybrid Bus." *Proceedings of the JSAE Annual Congress (Spring)* (2003) p. 136.
(2) R. Darling, et al. "Kinetic Model of Platinum Dissolution in PEMFCs." *Journal of the Electrochemical Society* Vol. 150 (2003) A1523-1527.
(3) R. Darling et al. "Mathematical Model of Platinum Movement in PEM Fuel Cells." *Journal of the Electrochemical Society* Vol. 152 (2005) A242-247.

Note: this article is partly based on the following published technical paper.
T. Ogawa et al. "Development of the FC System for New Generation FC Bus." *Proceedings of the JSAE Annual Congress (Autumn)* (2018) p. 74.

Authors

T. OGAWA   **K. UMAYAHARA**   **Y. IKOGI**

Utilization of Production Line Information to Improve Productivity

Yuki Watanabe[*1]
Yuki Hayashi[*1]
Hiroaki Fujimura[*1]

Abstract

As the automotive industry faces a period of transformation, it is desirable to start up engine production lines smoothly and using a minimum of resources. However, it takes time for these lines to reach production targets. Utilizing information from engine machining lines, the causes of these production delays were identified as cutting tool replacement work, equipment malfunctions, and cutting tool abnormalities. This article outlines how these causes were identified and addressed by increasing the efficiency of cutting tool replacement work, managing signs of possible equipment malfunction, and establishing a system to identify the mechanism of cutting tool abnormalities. It also describes the results of these initiatives.

Keywords: *production line, IoT, causes of production delays, waveform monitoring, AI, neural net*

1. Background and Purpose

With the automotive industry entering a period of profound transformation and innovative electrification, autonomous driving, and connected technologies emerging at an increasingly rapid pace, the allocation of resources has become a key issue for automakers. In contrast, even as these technological innovations continue to evolve, conventional engines still play a central role in vehicle powertrains. Although the production lines for these engines must be started up using a minimum of resources, it remains a lengthy process and the required line operation is difficult to achieve within the target period. Therefore, a system capable of obtaining various items of information from production equipment (such as the state of work, details of abnormalities, current waveforms, and so on) has been constructed with the aim of rapidly identifying the causes of production delays and implementing countermeasures. This article outlines the development of a system that uses this information to identify these causes and implement countermeasures, and describes some results from the application of this system.

2. Developed Systems and Results of Introduction

2.1 Visualization of production status (enhanced production monitor)

First, to help identify the causes of production delays, this development enhanced the functions of the conventional production monitoring system to visualize the production status more clearly. Conventional production monitors indicate the status of production as a series of time-based events for individual items of equipment, such as "Operating," "Error," and "Stopped to replace cutting tool." However, these monitors are not able to fully determine why a production stoppage has occurred. Therefore, to clarify the causes of production stoppages, a system capable of obtaining detailed information about errors, the presence of work, and so on was constructed (**Fig. 1**). This system can identify whether production stopped because work was not transported in or because it was not transported out, thereby showing which piece of equipment was the cause of the line stoppage. Functions that show the stoppage time per error and total cutting tool replacement and quality confirmation time were also added. This monitoring system was then adopted and the causes of production stoppages were analyzed. The results found that production stoppages were mainly caused by delays in cutting tool replacement, equipment errors, and machining defects (**Fig. 2**). The countermeasures for each cause are described in the following sections.

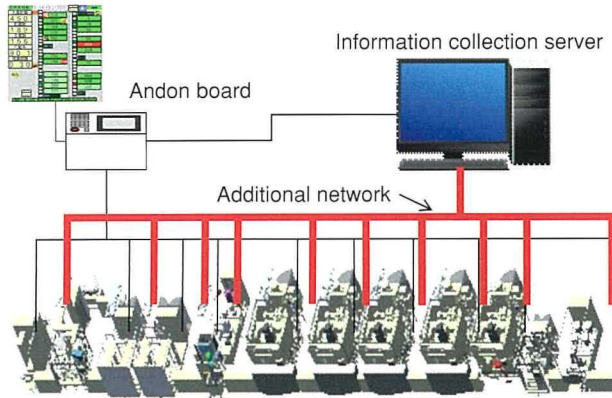[*1] Engine Production Engineering Div., Powertrain Company
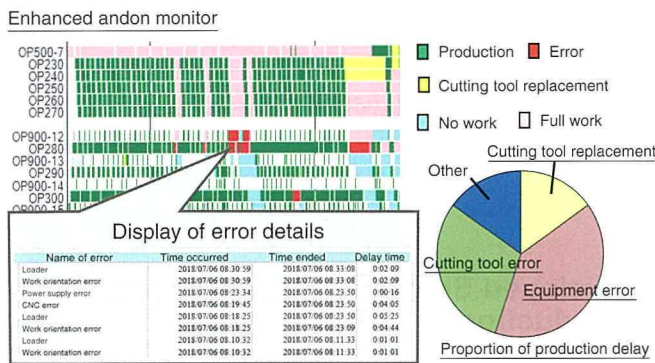
Fig. 1 Illustration of Information Collection

Fig. 2 Enhanced Production Monitor and Proportion of Production Delay Causes
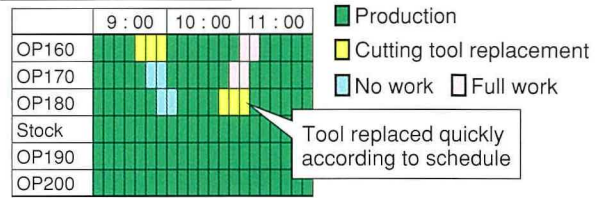
2.2 Cutting tool replacement work efficiency improvement (cutting tool replacement timing prediction system)

Cutting tool replacement delays are caused when the timing of replacement work overlaps. Although the work hours for cutting tool replacement and the like is estimated at the process planning stage to calculate the required number of staff, the tool replacement team cannot replace two different tools at the same time. This increases the duration of production stoppages (**Fig. 3**). Therefore, a cutting tool replacement timing prediction system was developed to identify the timing of simultaneous replacement work in advance. Since cutting tool replacement work occurs at fixed production volume intervals, the current production history of all equipment can be obtained to predict when replacement work will occur (**Fig. 4**). A screen was developed that shows the replacement times calculated for each tool, which can be confirmed as necessary (**Fig. 5**). This allows overlapping replacement work to be identified in advance so that the replacement team can make the necessary preparations. This system reduced the cutting tool replacement work by 80 minutes per shift.

As an incidental effect of this system, replacement work scheduled to take place during breaks can be brought forward,

enabling production to continue even when the replacement team is resting, thereby increasing the operational time of the production line.

Fig. 3 Increase in Equipment Stoppage Time when Cutting Tool Replacement Work Overlaps

Time occurred = (lifetime - current value) × cycle time

	Life time	Current value	Remaining	Cycle time (C/T)	Time occurred (Remaining × C/T)	
Cutting tool A	100	70	30	1 minute	In 30 minutes	
Cutting tool B	150	60	90	1 minute	In 90 minutes	Timing overlaps
Cutting tool C	200	185	15	2 minutes	In 30 minutes	

Fig. 4 Cutting Tool Replacement Time Calculation Method
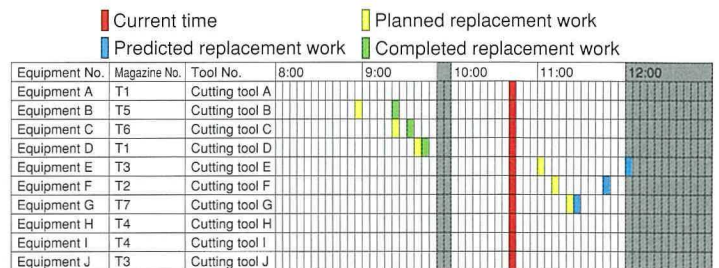
Fig. 5 Screen of Cutting Tool Replacement Prediction System

2.3 Equipment error reduction (equipment state monitor)

To reduce production stoppages caused by equipment errors, the causes of lengthy stoppages were categorized in detail and analyzed. Spindle and feed shaft seizures caused the longest production stoppages, followed by jig and motor issues (**Fig. 6**). When an equipment error occurs, the affected equipment must be disassembled, repaired, and re-assembled, before the accuracy of the repaired equipment is verified. Since this results in lengthy stoppages and affects the operation of the whole line, it is important to identify warning signs before the error occurs.

Although various efforts have been made to detect these warning signs at an early state, measurable data can only be obtained at irregular intervals, making it difficult to implement preventative measures. Therefore, an equipment state monitor was constructed to detect error warning signs by collecting and monitoring data at all times.

Data can be directly obtained from electrical parts such as motors. The developed system detects the spindle torque to monitor the occurrence of seizures or damage. During machining, torque trends are difficult to identify because the torque changes due to the degree of cutting tool friction, the hardness of the work, and so on. For this reason, this system monitors torque when no load is applied to the motor, that is, when machining is not being carried out and variations are low. This system also monitors the insulation resistance value to detect water intrusion into the motor and insulation deterioration. As a result, this system detects motor water intrusion using drops in insulation resistance, and prevents line stoppages due to motor malfunctions by replacing the motor when production is not in progress (**Fig. 7**).

In contrast, it is more difficult to collect data directly from mechanical parts such as jigs, clampers, and so on. Therefore, this system identifies the equipment state by monitoring alternative data. For example, to monitor the state of jigs, the system uses quality confirmation measurement results and detects jig tilting from surface position measurement data.

2.4 Cutting tool error reduction (cutting tool information link system)

Cutting tool breakage and other machining issues occur suddenly on production lines. If an issue occurs, the data collection location is determined and data collection started. However, the issue cannot be reproduced in simulations and the causes have to be estimated from the remaining defective work and broken cutting tool before a countermeasure can be applied. In this case, the presumed cause is often not the root cause, and the issue becomes a chronic long-term concern. Information about the production line, equipment, and cutting tool are all necessary to identify the mechanisms of such machining issues. Therefore, the conventional information collection system was enhanced to enable the collection of additional information on the cutting edge and setting (**Fig. 8**). A system was constructed to centrally collect the necessary information, such as data from the cutting edge inspection devices located in the tool re-grinding room (in which used tools are re-ground) and from the tool presetters to obtain the accuracy between the holder attached to the equipment and the cutting tool. In addition, when an issue occurs, to extract the target data from the huge quantities of available information, cutting tools, holders, and work are assigned individual IDs. Data can then be saved with links to those IDs (**Fig. 9**). This cutting tool information link system was used to identify the course of crankshaft oil hole drill damage, which had been a chronic machining issue (**Fig. 10**).
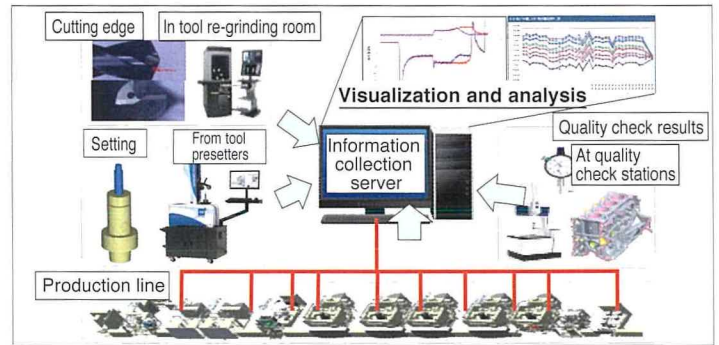

Fig. 6 Production Line Stoppage Times by Error Categories
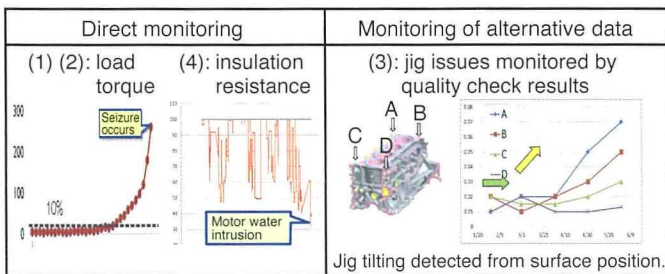
Fig. 7 Methods of Monitoring Error Warning Signs and Results

Fig. 8 Cutting Tool Information Collection System

Fig. 9 Outline of Cutting Tool Information Link System

Technical Papers/Technical Articles
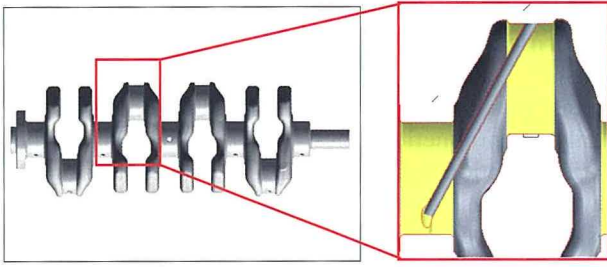
Fig. 10 Crankshaft Oil Hole

Fig. 12 Thinning Depth Check Method

Twenty crankshaft oil hole drills broke over the course of three months, which had a major impact on production. Two breakage modes were identified: one in which the first drill after cutting tool replacement broke (approximately 60%) and the other in which the drill broke before reaching its full lifetime (approximately 40%). This development studied each of these two modes.

(1) First tool breakage mode

The characteristics of breakage events were investigated using data linked to the occurrence of breaking and the cutting edge. Images of the cutting edge after re-grinding identified differences in thinning shapes (**Fig. 11**). If the thinning portion is too large, cutting tool stiffness decreases and leads to breakage. To confirm the correlation between the thinning shape and breakage, a verification evaluation was carried out to assess the breakage threshold value. It was found that breakage could be prevented by checking the thinning depth. Conventionally, the thinning depth was not checked during re-grinding. Therefore, the verification results were shared with the tool re-grind team members, who formulated a thinning depth check method and incorporated the results into the grinding process (**Fig. 12**). The first tool breakage mode has not re-occurred since this method was added to the check items after re-grinding (**Fig. 13**).

Fig. 13 Results after Implementation of Thinning Amount Check

(2) Breakage mode before reaching tool lifetime

The spindle torque was compared between normal and broken tools. The data showed an increase in spindle torque before breakage (**Fig. 14**). The timing of this torque increase was investigated and found to occur approximately 25 cycles before the breakage (**Fig. 15**). Assuming this increase to be a breakage warning sign, a torque waveform monitoring system was constructed to identify the phenomena occurring when the torque increases.

As it was necessary to identify the exact moment of torque increase, a threshold value was set to enable simple and clear judgment. However, it was realized that the waveform is not constant even under normal conditions, which means that a simple threshold value could not be used for judgment (**Fig. 16**). Therefore, machine learning was applied to judge the waveform. Although machine learning methodologies require large numbers of learning samples, this development adopted a neural net, which is capable of judging the waveforms without extracting feature quantities from the waveform. Learning was applied to all machining cycles over two-week periods to create a normal waveform model. Then, a monitoring system that detects errors in real-time was constructed by calculating the deviation between this model and each machining waveform over each cycle.

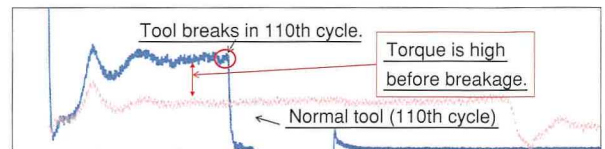Fig. 11 Observation Results of First Cutting Tool Breakage Mode

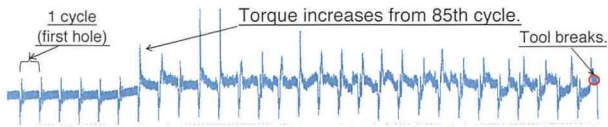Fig. 14 Comparison of Spindle Torque of Broken and Normal Tools

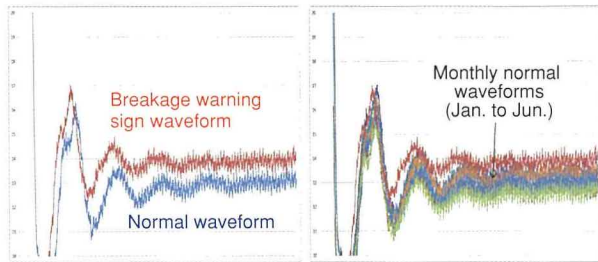Fig. 15 Timing of Change in Spindle Torque

Fig. 16 Variation between Waveform when Torque Increases and Normal Waveform

Monitoring using the neural net detected the increase in torque. When the drill cutting edge was examined after this torque increase was detected, the shoulder of the margin portion was found to be chipped (**Fig. 17**). A total of seven cases were detected, in all of which the same chipping phenomenon was identified (**Fig. 18**). This chipping is the eventual cause of cutting tool breakage, and the torque increase detection system was capable of detecting its warning signs.

Next, cutting tools with chipped margin portions were investigated with the tool re-grind team members to identify the cause of the chipping from photos after re-grinding and before equipment attachment. In one of the seven cases, manual honing of the cutting edge, which is carried out during re-grinding, was applied up to the margin portion (**Fig. 19**). Since this might be a cause of the chipping, a visual check was added after re-grinding to confirm that honing had not been applied to the margin portion. The other six cases are currently under investigation.

Fig. 17 Waveform and Cutting Edge when Torque Increase Detected

Spindle torque waveform	Cutting edge observation results

Fig. 18 Cutting Edge Observation Results when Torque Increase Detected

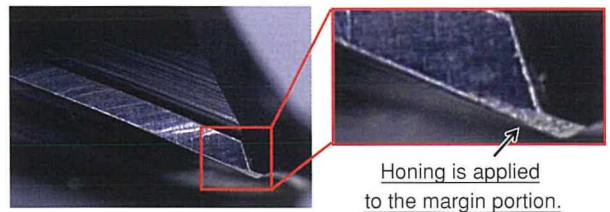Honing is applied to the margin portion.

Fig. 19 Observation Results of Chipped Cutting Tool after Re-Grinding

This system was applied to identify the cause of tool breakage by detecting torque increases in the crankshaft oil hole drilling process. As a result, tool breakages were stopped by replacing the tool after the detection of the torque increase. Subsequently, a trial was carried out to extend the tool lifetime until the torque increase timing. The trial results found that the current tool lifetime could be increased by four times without the occurrence of chipping. Additionally, when the grinding amount was

Technical Papers/Technical Articles

considered, it was still possible to extend the lifetime of the tool by two times without increasing the machining allowance during re-grinding (**Fig. 20**).

This process reduces tool lifetimes because of the frequency of breakage. This issue continues to be investigated since it was found that addressing the issue of tool chipping should enable substantial improvements in tool lifetimes. Cutting tool error mechanisms in other processes are also being investigated in similar ways and countermeasures are being adopted.

Authors

Y. WATANABE   **Y. HAYASHI**   **H. FUJIMURA**
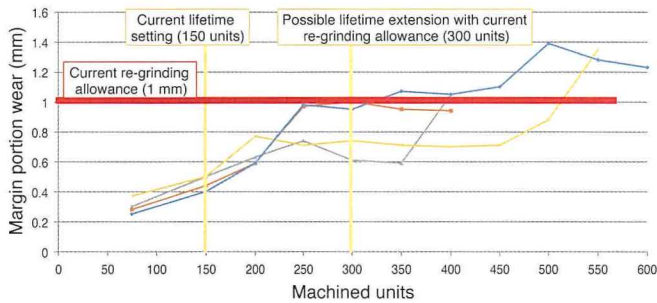
Fig. 20 Results of Lifetime Extension Trial

3. Adoption of Developed Systems

This development identified the causes of production line productivity issues to be delays in cutting tool replacement, equipment errors, and machining defects. The developed systems (the enhanced production monitor, cutting tool replacement timing prediction system, equipment state monitor, and cutting tool information link system) were confirmed to be effective ways of addressing these causes.

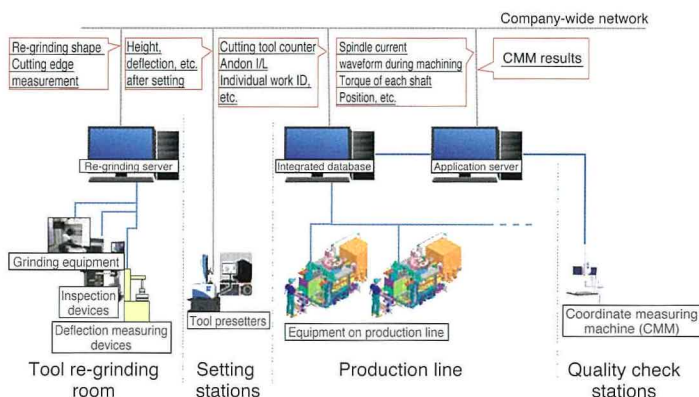These systems will be adopted on future production lines to help boost productivity on a global scale (**Fig. 21**).

Fig. 21 Outline of Standard Systems for Adoption

Factor Analysis of Engine Start Vibration Variations Using Artificial Intelligence

Kento Shimode[*1]
Keisuke Ishizaki[*1]
Masashi Komada[*1]

Abstract

Factor analysis of engine start vibration variations has been carried out by multivariate analysis or by analyzing phenomena based on vibration theory. However, with engine control unit (ECU) values related to excitation forces expanding massively, these methods have reached their useful limits. Therefore, this research focused on machine learning, which is capable of reproducing the complex relationship between multiple variables, and applied a decision tree that quantifies the contribution ratio of each factor. Subsequently, the validity of factor analysis using the developed model was verified.

Keywords: *engine start vibration, machine learning, random forest, variation factor analysis*

1. Introduction

Toyota Motor Corporation has announced its intention to help popularize electrified vehicles by 2030 through a range of initiatives to develop and adopt the relevant technologies. By that year, Toyota is planning to increase its annual global sales of electrified vehicles to at least 5.5 million units. With hybrid (HVs) and plug-in hybrid vehicles (PHVs) making up a significant portion of this figure, it will be necessary to further advance the technologies that enable cooperative control between motors and the engine. This article describes a technique for analyzing the factors responsible for vibration when the engine is started or stopped by this motor/engine cooperative control.

To achieve a target level for engine start/stop vibration, technologies have been developed to reduce in-cylinder pressure, which acts as an excitation force for this vibration, as well as to reduce the vibration sensitivity of the engine mounting system. However, the level of engine start vibration may vary, even with the same vehicle, and the maximum value of this variation range is a cause of stress for the vehicle occupants. One feasible countermeasure for reducing these variations is to control the initial crank angle at engine start to limit variations in engine in-cylinder pressure. However, since variations still occur even when the initial crank angle is kept at a constant value, it is necessary to identify the other factors.

Conventionally, this has been accomplished by multivariate analysis or by analyzing phenomena based on vibration theory. However, this analysis can be extremely difficult if the number of factors cannot be narrowed down or multicollinearity exists between the factors. Therefore, this research carried out factor analysis of engine start vibration using machine learning, which is a form of artificial intelligence (AI) capable of reproducing the complex relationships between multiple variables. A machine learning methodology was applied that can quantify the contribution ratios of factors. During analysis of transient vibration by machine learning, this research also reduced the computation load by converting vibration waveforms into feature quantities before input. In addition, this research confirmed the effects of factors extracted using an analytical model, and verified the validity of factor analysis using AI.

2. Mechanism of Engine Start Vibration and Conventional Technologies

Fig. 1 shows an outline of an HV system.[1] When the engine starts, the engine speed increases due to the drive torque generated by motor-generator 1 (MG1). Ignition then starts when the target engine speed is achieved. Engine start vibration occurs when the MG1 drive begins. Engine torque fluctuations (which are generated by the MG1 drive torque, the reaction forces generated by the compression and expansion of air in the cylinder, as well as the fuel pressure when ignition occurs) act as the excitation force for this vibration and are a transient phenomenon that increase and then decrease as the engine speed rises (**Fig. 2**).

*1 Advanced Vehicle Engineering Development Div., Advanced R&D and
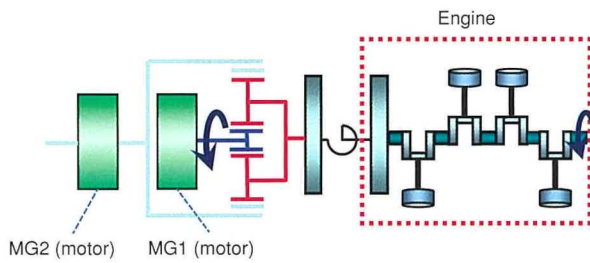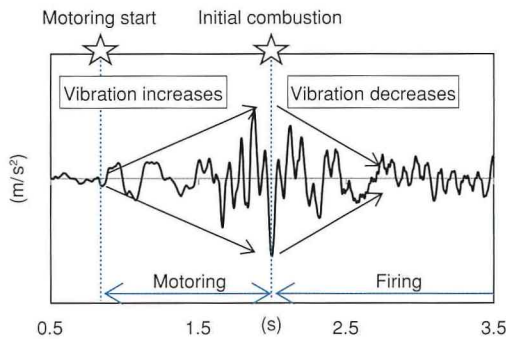Engineering Company

Fig. 1 Outline of HV System

MG2 (motor)   MG1 (motor)

Fig. 2 Floor Vibration when Engine Starts

As shown in **Fig. 3**, engine start vibration is generated by the transmission of excitation forces (i.e., engine torque fluctuations and motor drive torque) to the vehicle body via the engine mounts as well as via the transmission, driveshaft, and suspension.[2]
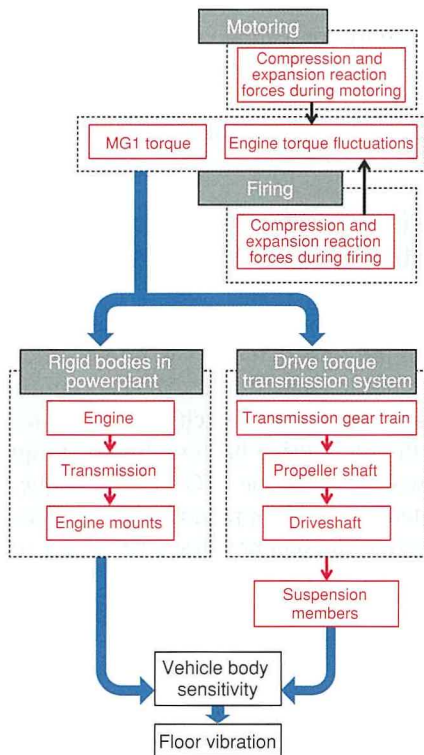

Fig. 3 Transmission Paths of Engine Start Vibration

As mentioned above, one conventional countermeasure for engine start vibration is to control the initial crank angle.[3] Of the excitation forces shown in **Fig. 3**, this countermeasure is capable of suppressing variations in the reaction forces generated by the compression and expansion of air during motoring caused by MG1. The reaction forces generated by the compression and expansion of air have a correlation with the initial crank angle when the engine starts. Therefore, variations in engine start vibration can be suppressed by stopping the crank angle within a certain range when the engine stops.

3. Factors of Engine Start Vibration Variations

Factors of engine start vibration variations include variations in the size of motor drive torque and engine in-cylinder pressure, variations in motor drive start and engine ignition timings, and variations in the backlash of gears and other components. As shown in **Fig. 4**, these factors can be categorized into B) control outputs (i.e., the size and timing of excitation forces, and the state of hardware) and C) undetermined factors (i.e., the backlash of gears and other components, and variations in combustion). Since the objective of this research is to carry out factor analysis of these variations, it is not possible to regard data measured under different scenarios as the same. Furthermore, since engine start vibration is a transient phenomenon, the relationship between factors over time is also important, which means that multiple items of data for possible factors must be measured simultaneously. Unfortunately, the physical values defined by categories B and C include some for which measurement technology does not exist and others that require large amounts of time to install the measuring instrumentation. However, since the control outputs of category B are determined by category A (i.e., the command values from the engine control unit (ECU)), it should be possible to extract factors related to control outputs by analyzing these ECU command values. Therefore, this research analyzed the values in the random access memory (RAM) of the ECU, which include the ECU command values, and extracted the variation factors. Here, the term "ECU RAM value" refers to the state observation values and control command values used for ECU control. Although variations in the backlash of gears and other components and combustion variations cannot be analyzed based on these ECU RAM values, this approach covers the factors related to variations in the size and timing of excitation forces as well as hardware state variations.
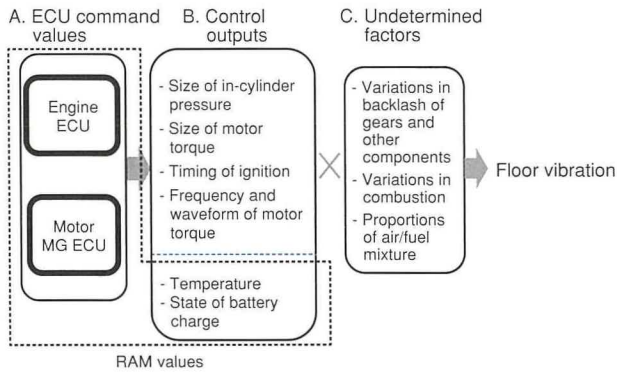
Fig. 4 Factors of Engine Start Vibration Variations

Fig. 5 shows the number of engine and motor RAM values for an HV. The engine electronic control unit (EFI ECU) contains approximately 30,000 and the motor ECU contains approximately 1,000. As the number of RAM values increases, analysis based on principles such as vibration theory, which involves formularizing the effect of each separate RAM value on vibration, has reached its useful limit. At the same time, multivariate analysis (such as linear regression methodologies and principal component analysis) also loses the capability to extract factors as the number of RAM values increases because cross-correlation becomes too complex.
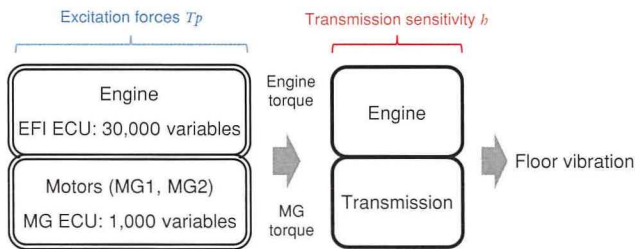
Fig. 5 Number of Control Variables in Hybrid System ECUs

4. Factor Analysis of Engine Start Vibration Variations Using Machine Learning

4.1 Selection of machine learning methodology

Since the objective of this research was to analyze ECU RAM values, a machine learning methodology capable of reproducing the interactions between data with strong multicollinearity was adopted. Machine learning includes supervised and unsupervised learning.[4] In supervised learning, pairs of data consisting of a user input and a desired output (called the supervisory signal) are used to create a function (i.e., a model) that generates the desired outputs from the inputs. In contrast, in unsupervised learning, only the input data is applied, without any output data. This research adopted supervised learning since an index (engine start vibration) exists to be used as the supervisory

signal.

Fig. 6 lists a number of supervised learning methodologies, organized along two axes: the expressiveness of the methodology and how simply it can identify the inputs that contribute to the model output. Highly expressive models are capable of more complex learning and class labeling (a term used to describe the decision making process). In supervised learning, expressiveness increases as the number of internal parameters of the model increases. However, as the model grows more complex, it becomes more difficult to identify the inputs that contribute to the model output. The purpose of the model used in this research was to analyze the RAM values contributing to variations in vibration. Therefore, the model must be capable of determining the inputs that contribute to the class label output. Therefore, of the methodologies capable of quantifying the contribution ratios of input variables, this research selected a highly expressive methodology called "random forest."[5] The random forest methodology combines an algorithm that uses a decision tree (the name is derived from the branch-like structure of the decision tree) with a majority decision algorithm. This decision tree carries out class labeling by making repeated judgments comparing the size of input variables and threshold values.
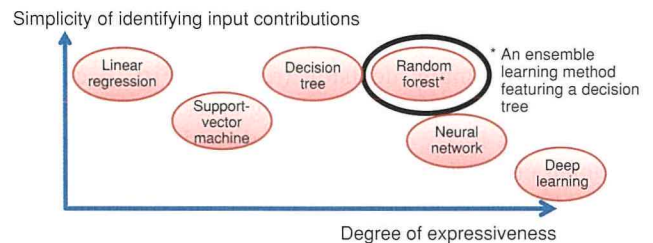

Fig. 6 Machine Learning Methodologies

The example shown in **Fig. 7** creates a class label that decides whether today's weather will be cold or not cold based on size judgments applied to two input variables: temperature and humidity. The model learns and determines the most appropriate input variables (temperature and humidity) and threshold values (certain numbers of degrees or percentages of humidity) for each size judgment to create the class label. The majority decision algorithm creates multiple decision trees from different items of learning data and makes a majority decision about the class labels generated by these decision trees.
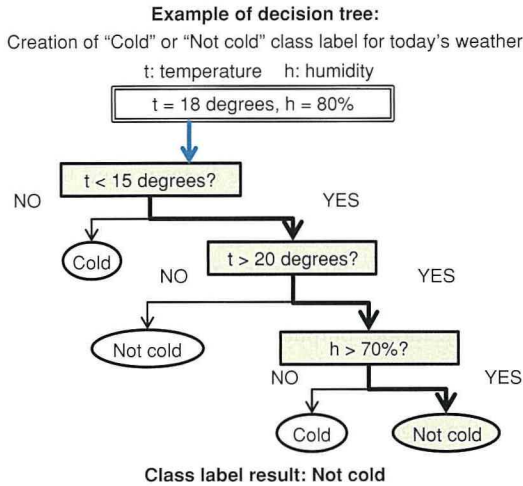
Technical Papers/Technical Articles

Example of decision tree:

Creation of "Cold" or "Not cold" class label for today's weather

t: temperature   h: humidity

t = 18 degrees, h = 80%

t < 15 degrees?

NO   YES

Cold   NO   t > 20 degrees?   YES

Not cold   h > 70%?

NO   YES

Cold   Not cold

Class label result: Not cold

Fig. 7 Outline of Decision Tree

Inputs

RAM 1	RAM 2	RAM 3	RAM 4	RAM 5	RAM 6	RAM 7	RAM 8	...	RAM X
0.12	0.47	0.33	0.52	0.28	0.72	0.81	0.39		0.03

○ : Vibration index

Decision tree 1   Decision tree 2   Decision tree N

1. RAM 3 > 0.2?   RAM 101 > 0.9?

NO   YES

9.5   2. RAM 5 > 0.3?   8   RAM 57 > 0.1?   9.5

7.5   M. RAM 10 > 0.5?   7   RAM 1 > 0.2?   8

8   7   9.5   7.5   7   7.5

Majority decision

Output | Vibration index: 7.5

Fig. 8 Outline of Class-Labeling Model Used in Research

Fig. 8 shows an outline of the class-labeling model used in this research. This model outputs a vibration index for a certain measurement scenario when X types of RAM values are inputted for that scenario. The model uses N decision trees (shown in **Fig. 7**) and each decision tree consists of size judgments involving a maximum number M of RAM values and threshold values. Each decision tree creates a class label for the vibration index based on size judgments using X types of RAM value inputs. For example, decision tree 1 in **Fig. 8** carries out repeated size judgments in descending order and decides that the vibration index is 7.5. In the same way, decision trees 2 to N also output class label results for the vibration index. Finally, a majority decision is applied to these class labels and the vibration index is outputted as a class label for the overall model.

The contribution ratio of each RAM value to the vibration index class label (i.e., the contribution ratio of that value to the variations in vibration) is calculated based on the number of times each RAM value appears in the size judgments of the multiple decision trees shown in **Fig. 8**.

In an identical fashion to a scenario with a single decision tree, the model learns and determines the most appropriate RAM values and threshold values for each size judgment in the N decision trees to create the class label. In contrast, the maximum number M of size judgments in each decision tree and the number of decision trees N used to make the majority decision must be set in advance.
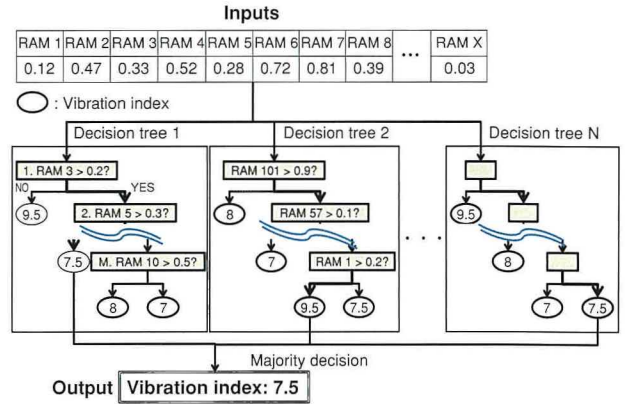
4.2 Maximum number of size judgments in each decision tree and number of decision trees used for majority decision

To make it easier to identify the inputs acting as factors for the class label and to prevent the model from becoming too complex, it is necessary to control two parameters: 1) the maximum number M of size judgments in each decision tree and 2) the number of decision trees N used to make the majority decision. After comparing scenarios with the maximum number of size judgments set to 4, 20, and 100, this research identified 20 as realizing the highest performance. In contrast, although performance increases as the number of trees used to make the majority decision also increases, it becomes more difficult to identify the inputs that contribute to model output. After comparing performance with an increasing number of decision trees, this research found that performance improvements became saturated when the number of decision trees was set to 30.

4.3 Increasing calculation process efficiency and reducing number of RAM values

In machine learning, the number of data measurement scenarios (N) is extremely important for generating a model with a high class-labeling capability. In ordinary multivariate analysis, N must be set to a value between three and ten times higher than the number of RAM values. It has been reported that machine learning requires an N value even higher than this. This research aimed to analyze around 750 types of RAM values that affect the excitation forces generated by the engine and motor. However, it would take roughly seven weeks to perform 7,500 test iterations (ten times the number of RAM values) following the current engine start vibration measurement process. However, the number of data items required to generate the machine learning model can be obtained in one week by making the measurement process more efficient, and by selecting the variables to be used by the machine learning methodology to reduce the number of RAM values.

The efficiency of the measurement process was improved by simplifying and automating time-consuming measurement steps. As a result, N was reduced to 1,000 (**Fig. 9**). The number of work hours required to obtain the data for each measurement scenario was reduced by (1) adopting integrated measurement to lower the number of measurement instruments, (2) grouping the measurement sequences together to lower the number of manual tasks, and (3) improving the data post-processing programs. As a result, the time required to carry out N=1,000 measurement processes of engine start vibration was reduced from 35 to 15 hours.
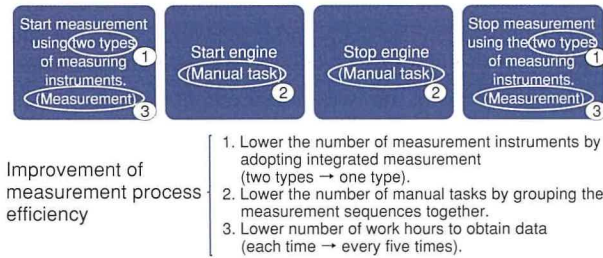
Fig. 9 Engine Start Vibration Measurement Process

The number of RAM values acting as the decision tree inputs was reduced by adopting the following four methods: (1) excluding RAM values with constant values, (2) excluding feature quantities that do not change in different measurement scenarios, (3) for combinations of feature quantities with a cross-correlation coefficient of 0.99 or higher, excluding all feature quantities other than the one with the highest level of controllability, and (4) excluding extremely outlying data based on the peakedness and distortion of the data distribution.

5. Results of Variation Factor Analysis

5.1 Measurement results of engine start vibration

Subjective evaluations of engine start vibration are not affected simply by the size of the vibration. Other factors include the speed at which the vibration is damped and the frequency of the vibration. Therefore, this research used the vibration dose value (VDV) shown in Equation 1 as the vibration index. This is a fourth power vibration dose method that considers the speed of vibration damping using a time integral and the effects of frequency using a frequency filter.[6]

$$VDV - 100 = \left\{ \int_0^T a_{wx}^4 \, dt + \int_0^T a_{wy}^4 \, dt + \int_0^T a_{wz}^4 \, dt \right\}^{¼} \tag{1}$$

where,

a_{wx}, a_{wy}, a_{wz}: acceleration time series data multiplied by the frequency filter[7]

The solid line in **Fig. 10** shows the engine start vibration measurement results after N iterations as a histogram, with VDV on the horizontal axis and the frequency of appearance on the vertical axis. The broken line in **Fig. 10** shows the normal distribution with the same mean value and standard deviation as this VDV distribution. In the normal distribution, the probability that the values exceed +3-sigma from the mean ($+3\sigma$) is 0.14%. However, according to the measurement results of this test (the solid line), $+3\sigma$ was exceeded approximately 10 out of 1,000 times, which is a larger variation than the normal distribution.
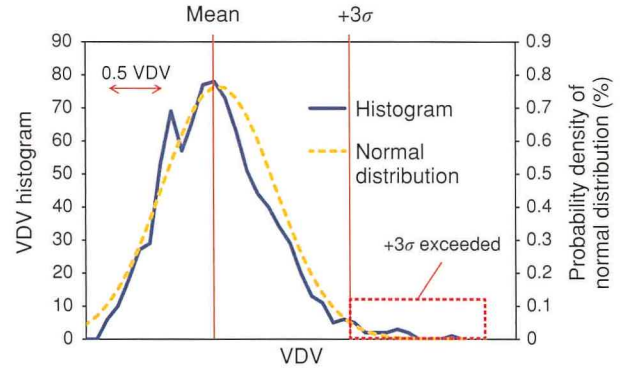
Fig. 10 Measurement Results of Engine Start Vibration

5.2 Results of factor analysis using machine learning

Table 1 shows the results expressing which of the constituent elements of the engine start vibration transmission paths have a relationship with the twenty highest-contributing RAM values. The results include RAM values such as the motor torque current control value, which were already recognized as having a relationship with vibration variations, as well as RAM values that had yet to be studied.

Table 1　Types of RAM Values Related to Engine Start Vibration Variations

Constituent elements of engine start vibration transmission paths	Number of relevant RAM values from those with the top twenty highest contribution ratios
Motor torque	13
In-cylinder pressure after initial combustion	5
Drive torque transmission system	2

5.3 Variation reduction methodology using extracted factors

Of the extracted RAM values, this research focused on RAM 1 and RAM 2, which are controllable but had yet to be studied. The time series changes in RAM 1 were compared in scenarios with high and low measured VDV index values. It was found that RAM 1 clearly decreased when the engine started, and that

the amount of this decrease varied between the scenarios with high and low measured VDV (**Fig. 11**).
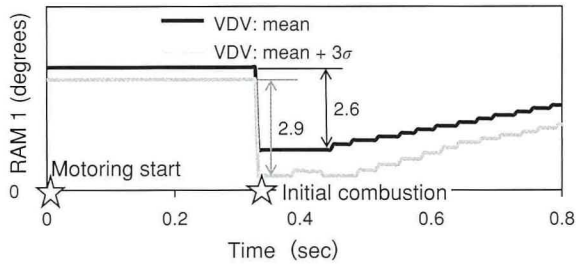

Fig 11 Relationship between RAM 1 and VDV

Fig. 12 illustrates the size of the VDV as shaded dots (the darker dots show higher VDV), with the initial RAM 2 value of each measurement scenario on the vertical axis, and the amount of decrease in RAM 1 in each measurement scenario on the horizontal axis. In these results, the measurement scenarios shown by the darker dots are those in which vibration exceeded +3σ from the mean VDV. These dots are grouped together in the area outlined in blue. Consequently, it should be possible to reduce the number of times that vibration exceeds +3σ by controlling the amount that RAM 1 decreases so that it falls outside this area. It should be noted that, although measurement scenarios in which VDV exceeded +3σ also exist outside this area, these indicate scenarios strongly affected by factors other than RAM 1 and 2.
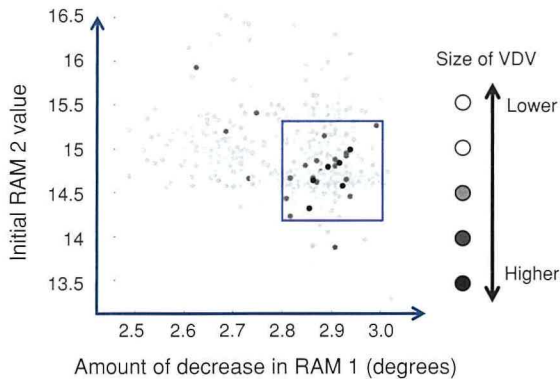
Fig. 12 VDV Distribution Organized by RAM 1 and RAM 2

The amount of decrease in RAM 1 affects vibration because the level of in-cylinder pressure (which is a vibration excitation force) changes in accordance with this RAM value. **Fig. 13** compares the time series changes in the air-fuel ratio at engine start when RAM 1 decreased by 2.9 and 2.6, respectively. When RAM 1 decreased by 2.6, the air-fuel ratio increased from 14.8 to 18.0. In contrast, when RAM 1 decreased by 2.9, the increase in the air-fuel ratio was delayed and only increased from 14.6 to 16.4.
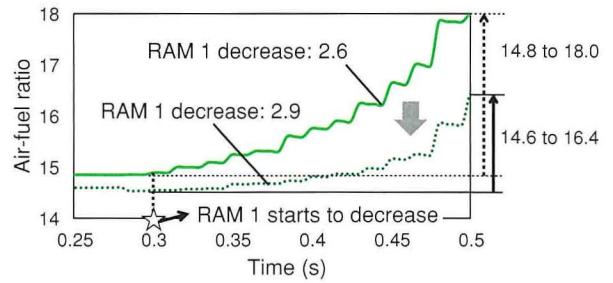
Fig. 13 Time Series Changes in Air-Fuel Ratio when Engine Starts

Fig. 14 shows the relationship between air-fuel ratio and in-cylinder pressure. The in-cylinder pressure at engine start was calculated and compared for each measurement scenario based on the air-fuel ratios in the two measurement scenarios illustrated in **Fig. 13**. When RAM 1 decreased by 2.6, the in-cylinder pressure ranged between 0.73 and 0.86 MPa. In contrast, when RAM 1 decreased by 2.9, the in-cylinder pressure ranged between 0.78 and 0.87 MPa. In this latter scenario, the in-cylinder pressure is higher and probably causes vibration to increase.
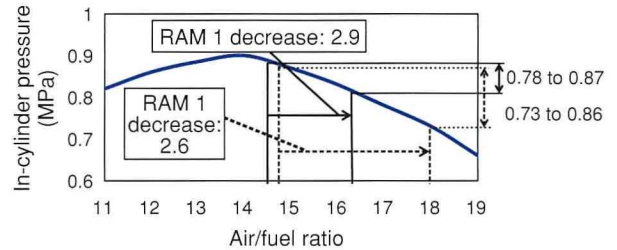
Fig. 14 Relationship between Air-Fuel Ratio and In-Cylinder Pressure[8]

5.4 Effect verification using analytical model

The effects of the factor extracted by machine learning (i.e., the amount of decrease in RAM 1) on vibration variations were verified using an analytical model. The engine torque fluctuations during firing were calculated from the in-cylinder pressure waveform in two measurement scenarios (RAM 1 decrease: 2.9 and 2.6). This waveform was calculated using a relational expression for in-cylinder pressure and engine torque fluctuations.[8] These engine torque fluctuations were inputted into the analytical model as vibration excitation force, the body vibration was calculated as a reaction to this force, and the level of the VDV index was compared with the two different RAM 1 decrease amounts. The analytical model was a spring-mass model consisting of a combined engine/HV system powerplant and a vehicle body as rigid elements, connected by springs simulating the engine mounting system. Engine torque fluctuations (the vibration excitation force) were inputted as torque in the powerplant roll direction. The results found that

engine start vibration was 36% lower in terms of VDV in the measurement scenario in which RAM 1 decreased by 2.6 compared to the measurement scenario in which RAM 1 decreased by 2.9. This demonstrates the effect that vibration exceeding $+3\sigma$ from the VDV mean decreased below the mean value. Therefore, it is possible to restrict the number of times that vibration exceeds $+3\sigma$ from the VDV mean by controlling the amount that RAM 1 decreases. This result verified the effect of the factors extracted in this factor analysis research on vibration variations.

6. Conclusion

Machine learning was used to analyze the contribution of multiple factors in factor analysis of engine start vibration variations in HVs. The random forest methodology was selected as an effective way of quantifying the vibration level and the contribution ratio of each factor. The analysis target was limited to engine and motor ECU signals related to vibration excitation force, and the methods of processing the large amount of sample data required for machine learning were improved to shorten the analysis time. As a result, this methodology extracted factors that had yet to be studied in this type of analysis. Furthermore, the effects of these factors on vibration variations were verified using an analytical model. It was confirmed that the random forest methodology effectively analyzed the many factors that cause transient phenomena to vary.

References

(1) Y. Jo et al. "Development to Improve Engine Starting Vibration in Hybrid Vehicle with Low Number of Cylinders." *Toyota Technical Review* Vol. 60 (2014) pp. 67-71.
(2) K. Watanabe et al. "Development of Engine Restart Vibration after Idling Stop Using Model Based Development Process." *Proceedings of the JSAE Annual Congress* No. 71-16 (2016) 20156333.
(3) M. Komada at al. "Noise and Vibration Reduction Technology in New Generation Hybrid Vehicle Development." *Proceedings of the Society of Automotive Engineers of Japan* No. 10-04 (2004) 20045298.
(4) Y. Hirai. *Introduction to Pattern Recognition* (in Japanese). Morikita Publishing Co., Ltd. Tokyo (2012) p.219.
(5) Research Institute of Systems Planning, Inc. Ed. *Introduction to Machine Learning Using Python* (in Japanese). Ohmsha, Ltd. Tokyo (2016) p. 248.
(6) *Mechanical Vibration and Shock – Evaluation of Human Exposure to Whole-Body Vibration - Part 1: General Requirements.* ISO 2631-1 (1997).
(7) *Mechanical Vibration and Shock – Evaluation of Human Exposure to Whole-Body Vibration - Part 2: Vibration in Buildings (1 Hz to 80 Hz).* ISO 2631-2 (2003).
(8) Society of Automotive Engineers of Japan Ed. *Automotive Engineering Handbook 1: Fundamentals and Theories* (in Japanese). Tokyo (2015) p. 556.
(9) Y. Ishikawa. *Essence of Gasoline Engine Design for Automobiles* (in Japanese). Sankaido. Tokyo (2002) p. 262.

Authors

K. SHIMODE   **K. ISHIZAKI**   **M. KOMADA**

Technical Papers/Technical Articles

Development of Solid Electrodeposition Method as an Environmentally Friendly Surface Treatment

Yuki Sato[*1]
Hirofumi Iisaka[*1]
Junya Murai[*1]

Abstract

Surface treatments such as plating and physical vapor deposition (PVD) are capable of satisfying various functional requirements at a reasonable cost, and are therefore indispensable parts of the vehicle manufacturing process. However, these treatments are not suitable for partial film formation, and have the fundamental issue of requiring a cumbersome masking step. Consequently, a stamping method capable of forming films only on necessary locations using electrodeposition was proposed based on the application of polymer solid electrolyte membranes used in fuel cells. To ensure rapid film formation using this method, electrode reactions and ion transfer phenomena were analyzed using electrochemical measurement methods, and structural analysis was applied to the electrolyte membrane. As a result, the oxidation reaction rate at the anode was identified as the rate-determining process. In addition, by improving the anode material, the developed method achieved the same film formation speed as electroplating.

Keywords: *solid electrodeposition method, environmentally friendly, patterning, plating, PVD, surface treatment, fuel cell, electrochemical measurement, ion transfer*

1. Introduction

Wet surface treatments such as electroplating and electroless plating are applied to base materials to satisfy various functional requirements such as rustproofing, corrosion resistance, sliding performance, wear resistance, bonding, and so on. For this reason, surface treatment technologies play an important role in vehicle manufacturing and are applied to a wide range of parts.[1] However, these treatments may have a high environmental impact due to the generation of large volumes of waste liquid containing harmful pollutants such as heavy metal ions, strong acids or alkalis, cyanic acid, chromic acid, and the like. In addition, with electrification and information technologies continuing to grow in importance, parts in these systems rely on patterning (i.e., partial film formation) to form wiring and electrodes. However, since plating requires the whole part to be immersed in a treatment bath, the fundamental issues of high-cost and cumbersome masking processes must be resolved.

These issues are being addressed by the development of a solid electrodeposition method, an innovative film formation process capable of forming films on only the necessary locations. **Fig. 1** shows the film formation principles of electroplating and solid electrodeposition. In the case of electroplating, the substrate

(i.e., the material on which the film is to be formed) is exposed to the plating liquid and connected to one electrode of a direct current (DC) power source. When power is applied, the metal ions that act as the film material are formed onto the surface of the substrate by a reduction reaction (i.e., an electrocrystallization process). In contrast, the proposed solid electrodeposition method uses a polymer solid electrolyte membrane to transfer metal ions onto the substrate surface. Other examples of electrocrystallization using solid electrolytes include a process that uses the ion exchange properties of polyamic acid as a precursor to form metal wiring on the surface of a polyimide film.[2] However, since the objective of this development was to form metallic films on a substrate rather than on a solid electrolyte membrane, it was decided to use a fluorinated solid electrolyte membrane, which has superior release performance. This material is mainly used for the membrane electrode assembly (MEA) of polymer electrolyte fuel cells, and it functions to transfer hydrogen ions (i.e., charge carriers) and to shut-out the hydrogen and oxygen gas materials used in the fuel cell. In addition, it also restricts the transfer of water generated at the cathode to the anode.[3] Focusing on these functions, this development considered whether the transfer of metal ions and restriction of water flow might be utilized in a electrocrystallization process to minimize the amount of the metal ion solution plating material as well as the amount of waste liquid generated in the substrate washing process.

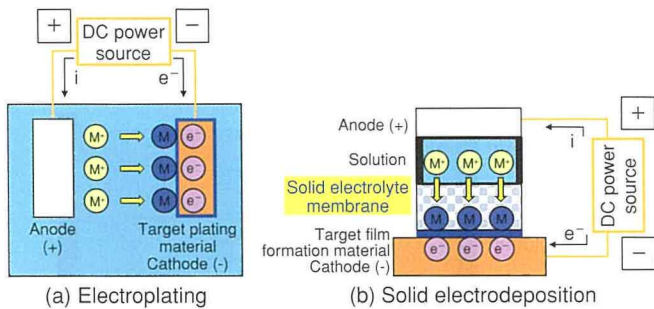*1 Material Engineering Div. No. 2, Advanced R&D and Engineering Company

(a) Electroplating   (b) Solid electrodeposition

Fig. 1 Principles of Film Formation Methods

Fig. 2 shows the provisionally calculated results for CO_2 emissions and the amount of waste liquid, assuming application to a wiring formation process on an electronic circuit board. It was calculated that replacing conventional electroplating with solid electrodeposition might reduce CO_2 emissions to approximately one-quarter and the amount of waste liquid to approximately one-thirtieth of the original levels. In addition, since solid electrodeposition does not require plating baths or other large-scale equipment, it might be possible to reduce the process footprint to approximately one-tenth of its original size.

(a) CO_2 emissions   (b) Waste liquid
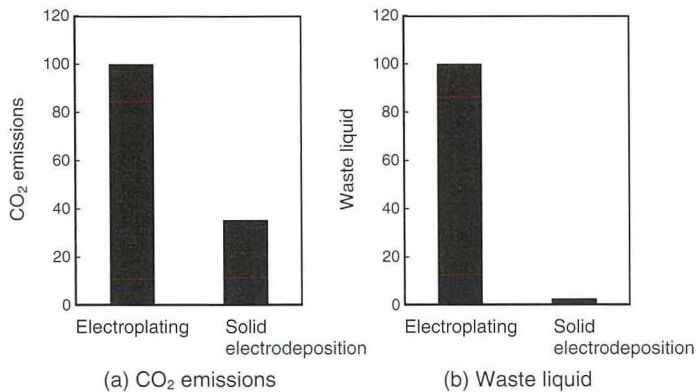
Fig. 2 Comparison of CO_2 Emissions and Waste Liquid (Provisional Calculations)

Another merit of a solid electrolyte membrane is its potential to enable patterning without masking. In solid electrodeposition, films are formed by pressing the solid electrolyte membrane onto the substrate like a stamp. Unlike conventional surface treatments, if the solid electrolyte membrane that contacts the substrate has the same shape as the target film, there is no need to apply a masking process to the substrate. This is a substantial advantage in terms of film formation cost and productivity. **Fig. 3** shows a potential example of solid electrodeposition application to an actual part, in this case the cooler used by the intelligent power module (IPM) of a third-generation hybrid vehicle (HV) inverter. The IPM uses semiconductors called power devices for DC/AC current conversion. These devices are soldered to the cooler to allow the transfer of current and heat.

To ensure the reliability of the soldered joints, an electroless film is formed on the surface of the direct bonded aluminum (DBA) substrate mounted on the cooler. Although the plating film is only required at the device joints to ensure soldering reliability, the plating film is actually formed over the whole surface of the cooler to avoid the application of a cumbersome and high-cost masking process. If the amount of this high-cost platinum-group metal plating is reduced, the increases in cost due to the addition of masking more than offsets any cost savings from reducing the plating film area in most cases. However, adopting solid electrodeposition for this process allows a film to be formed at the necessary locations only, without an additional masking step.
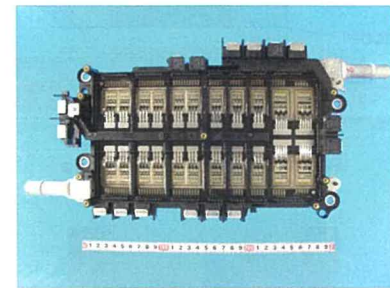
(a) IPM installed in third-generation HV inverter

Deposited film
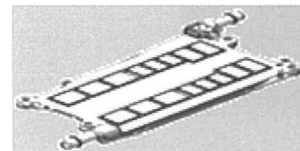
(b) Appearance of current cooler (whole-surface film formation)   (c) Appearance of cooler after solid electrodeposition (partial film formation)
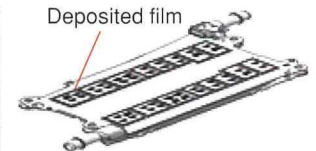
Fig. 3 Illustration of Potential Application of Solid Electrodeposition

To verify the concept of solid electrodeposition and identify potential technical issues, a copper (Cu) film formation experiment was carried out using a simple jig. **Fig. 4** shows an outline of the experiment. In the film formation experiment, a solid electrolyte membrane was placed in contact with a gold (Au) substrate. A titanium (Ti) electrode, which includes a porous anode and solution supply holes, was pressed down onto the membrane by a weight, and the metal ion film material was supplied by a syringe. The DC power source cathode was connected to the Ti block and the anode to the substrate. Power was then applied to deposit a metal film on the substrate. In the electrocrystallization process, the amount of metal deposition was proportional to the amount of current and time (following Faraday's laws of electrolysis), which can be analyzed in terms of current density and film formation speed. **Fig. 5** shows the external appearance of the Cu film formed by solid electrodeposition. Film formation tests were carried out under various current density conditions. The results found that normal Cu deposition did not occur at current densities of 20 mA/cm² or higher, and that the maximum film formation speed was 0.4

Technical Papers/Technical Articles

µm/minute.

Since this is an order of magnitude slower than conventional electroplating (approximately 2 µm/minute), it would be necessary to increase the film formation speed before this method can replace the conventional process. Therefore, basic studies were carried out into film formation speed.
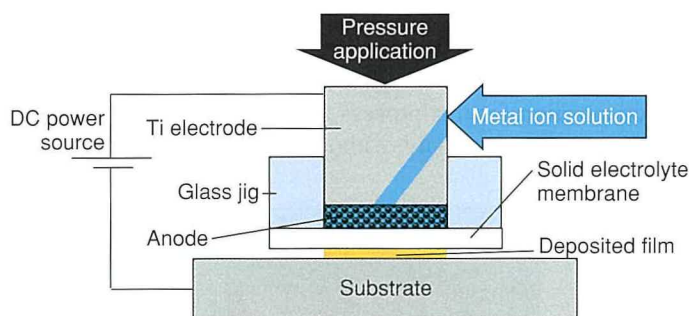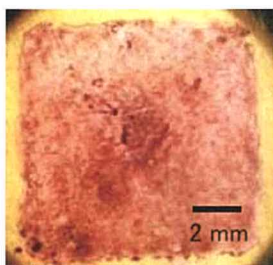

Fig. 4 Experimental Outline

Fig. 5 Cu Film Formed by Solid Electrodeposition

2. Basic Studies to Increase Film Formation Speed

2.1 Reaction and transfer mechanism model for solid electrodeposition

Fig. 6 shows the model used to simulate the cathode and anode reactions and metal ion transfer mechanism in solid electrodeposition. The deposition process consists of three elements: (1) a reduction reaction at the cathode (substrate) ($M^{n+} + ne^- \rightarrow M^0$), (2) metal ion transfer, and (3) an oxidation reaction at the anode (water oxidation: $H_2O \rightarrow 2H^+ + 1/2O_2 + 2e^-$, or metal oxidation: $M^0 \rightarrow M^{n+} + ne^-$). Normally, since the change in free energy ΔG in reactions (1) and (3) is positive, the reactions do not start spontaneously, and the reduction and deposition of metal ions occur only after the external DC power source is applied. However, if the voltage is increased to raise the current density and boost the film formation speed, the rates of reactions (1) and (3) or the rate of ion transfer in (2) cannot match this increase, and the resulting current density does not enable faster film formation. This is known as the maximum current density. Various verification experiments were then carried out to identify the rate-determining process for the film formation speed in solid electrodeposition.
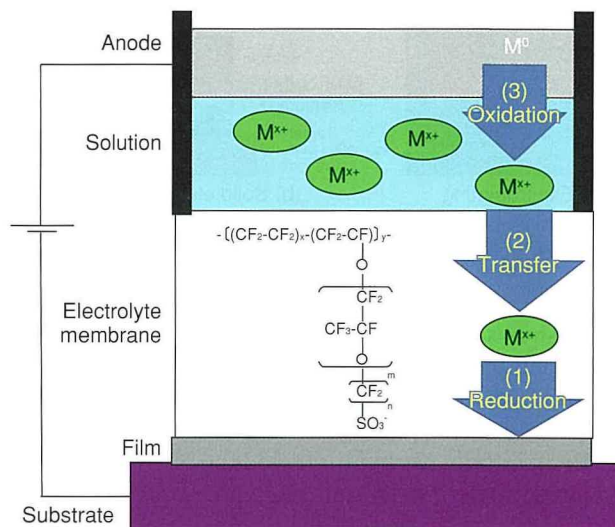
Fig. 6 Ion Transfer and Electrode Reaction Model

2.2 Analysis of reduction reaction at cathode

The metal ion reduction reactions in solid electrodeposition were analyzed in comparison with electroplating (no solid electrolyte membrane). Electrochemical impedance was selected as the analysis method.[4] Various solid electrolyte membranes were used: commercially available Nafion N117 and N115 films, as well as developed films A and B. Nafion is a typical fluorinated solid electrolyte membrane and consists of a main structure with C-F bonds and sulfonate group perfluoro side chains.[5] Developed film A has a different side chain structure to Nafion and developed film B has a higher sulfonate group content.

Fig. 7 shows the measurement system. Simulating the configuration of solid electrodeposition, the electrochemical cells were filled with a metal ion solution (1 mol/L $CuSO_4$), and an oxygen-free Cu plate was placed at the working electrode (WE) side. The solid electrolyte membrane was placed in contact with the Cu plate. On top of this configuration, a platinum (Pt) wire was connected as the counter electrode (CE) in addition to a reference electrode (RE) connected through a salt bridge. A potentio-galvanostat and function generator were used to perform the electrochemical measurement. In this analysis, the impedance was calculated from the voltage/current ratio measured when an alternating signal was applied. The impedance at each frequency was obtained by sweeping the voltage and current over a designated frequency range, and plotted on a graph with the real part on the horizontal axis and the imaginary part on the vertical axis. The resulting graph is called a Cole-Cole plot (**Fig. 8**) and is used to analyze electrochemical reactions. In this analysis, the DC potential was set to 0.05 V vs SSE, the potential amplitude was set to 10 mV,

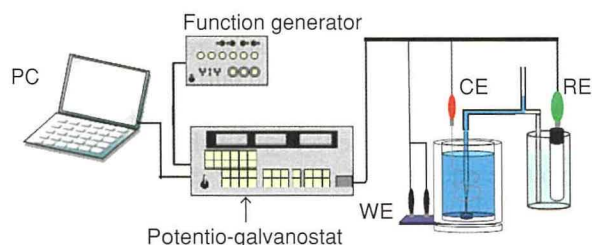and a 5-point logarithmic sweep per unit was carried out from 10 kHz to 10 mHz. The temperature was set to 25°C.

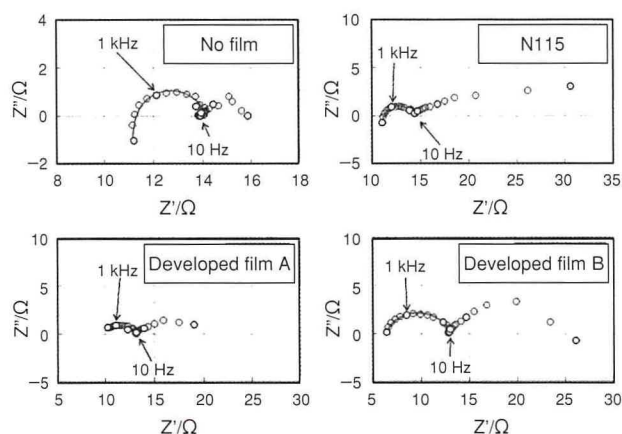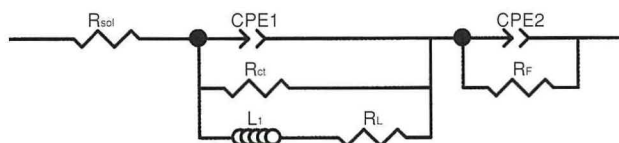
Fig. 7 Electrochemical Measurement System

Fig. 8 Cole-Cole Plot of Cu Film Formation

Each resistance component can be calculated by curve fitting the Cole-Cole plot to an equivalent circuit as shown in **Fig. 9**. For analysis, this study focused on the charge transfer resistance (R_{ct}), which corresponds to the ease of electron exchange.

R_{sol}: solution resistance R_{ct}: charge transfer resistance
CPE: constant phase element ⎱ Elements expressing capacitive
L_1: inductor R_L, R_F: resistors ⎰ and inductive semi-circles.

Fig. 9 Equivalent Circuit Diagram

Fig. 10 shows the charge transfer resistance of each solid electrolyte membrane in the Cu system. The charge transfer resistance of developed films A and B is lower than the conditions without a film (equivalent to electroplating), indicating that these films enabled more active reduction reactions than electroplating.
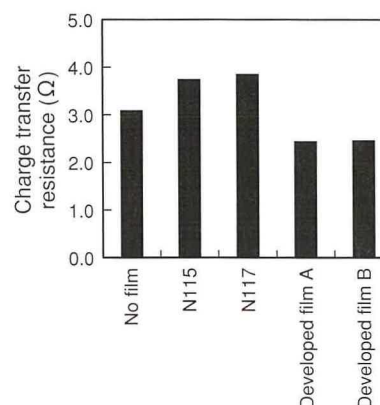
Fig. 10 Calculated Charge Transfer Resistance of Solid Electrolyte Membranes

2.3 Analysis of maximum metal ion transfer rate inside solid electrolyte membrane

In the solid electrodeposition process, metal ions from the solution on the anode side pass through the solid electrolyte membrane and reach the cathode. At the cathode, since the metal ions are consumed by reduction reactions that deposit the ions on the substrate surface, diffusion in accordance with the decrease in concentration creates supply from the anode side. When the current density is increased to boost the reduction rate, the transfer rate inside the solid electrolyte membrane cannot match the increase in current density. This may be the rate-determining process for the film formation speed.

Therefore, the maximum metal ion transfer rate inside the solid electrolyte membrane was analyzed. The experimental procedure was as follows. When a high-concentration solid electrolyte membrane is immersed in a metal ion solution, ion exchanges occur between the hydrogen ions in the membrane and the metal ions in the solution. As a result, virtually all of the positive ions in the solid electrolyte membrane are displaced by metal ions. Next, immersing the solid electrolyte membrane in a high-concentration acid solution causes virtually all the metal ions in the membrane to discharge into the acid solution. This analysis immersed each solid electrolyte membrane in ion-exchanged water for 24 hours, before subsequently immersing the membranes in a $CuSO_4$ aqueous solution (concentration: 1 mol/L) for a set duration. After the excess solution on the surface was removed, the membranes were immersed in a 30% sulfuric acid solution. The Cu ion concentration in that solution was then analyzed using an inductivity coupled plasma optical emission spectrometer (ICP-OES), and the amount of ions induced from the aqueous solution to the solid electrolyte membranes was measured.

Fig. 11 shows the relationship between the amount of ion induction and immersion time under normal temperature conditions using the Nafion N117 solid electrolyte membrane.
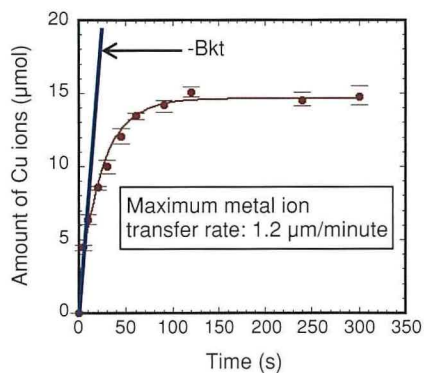
Fig. 11 Amount of Cu Ions in Nafion N117 Membrane (25°C)

To calculate the maximum metal ion transfer rate, the relationship between the amount of ion induction a(t) and immersion time t as shown in Equation 1 is used for curve fitting. Equation 2 is then derived from approximation by Maclaurin expansion.

$$a(t) = A + B \cdot e^{-kt} \tag{1}$$

$$a(t) = A + B - Bkt \tag{2}$$

where,

A and B: constants
k: rate constant (s^{-1})
t: immersion time (s)

-Bk is the initial immersion rate, and corresponds to the maximum metal ion transfer rate. This experiment calculated a value of 0.258×10^{-6} mol/cm^2/s, which translates to approximately 1.2 μm/minute after conversion to a film formation speed.

Fig. 12 shows the maximum metal ion transfer rate with developed film B, which has the lowest charge transfer resistance R_{ct}. The maximum metal ion transfer rate reached 3.9 μm/minute after the membrane type was changed.
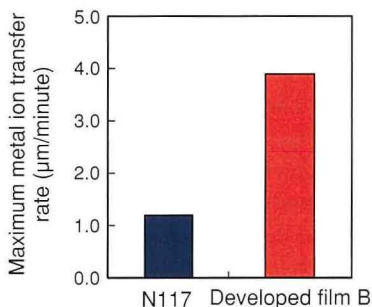
Fig. 12 Maximum Metal Ion Transfer Rate

2.4 Analysis of oxidation reaction at anode

To verify the effect of the reaction at the anode on the film formation speed, a film formation test was carried out using a conventional Pt/Ti anode (water oxidation reaction: $H_2O \rightarrow 2H^+ + 1/2O_2 + 2e^-$) and a Cu electrode used during electroplating (Cu dissolution reaction: $Cu \rightarrow Cu^{2+} + 2e^-$). The same test method as described in Section 1 was used. **Fig. 13** shows the relationship between voltage and current density for each anode material. The theoretical deposition start voltage of the Pt/Ti anode is approximately 0.9 V, compared to 0.0 V for the Cu anode. In addition, since the voltage required to reach a speed of 10 mA/cm^2 is approximately 2.0 V for the Pt/Ti anode and approximately 0.2 V for the Cu anode, the reactions with the Cu anode are more active than the Pt/Ti anode.
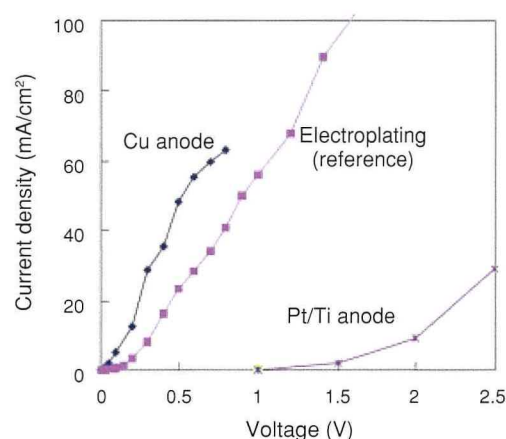
Fig. 13 Relationship between Voltage and Current Density with Different Anode Materials

This study also examined the specific surface area (SSA) of the anode material. Since reactions occur over the whole surface of the anode material in contact with the solution, the reaction rate has a close correlation with surface area. Therefore, the anode polarization was measured using anodes with different SSA values. The electrochemical cell described in Section 2.2 was used for the experimental system. **Fig. 14** shows the relationship between potential and current density. Since the surface area used here to calculate the current density assumes that the external shape of the anode is rectangular, the calculated values show the apparent current density. The foamed Cu and Cu mesh sheets, which have the largest SSA, obtained higher current densities at the same potential than sheet anodes (oxygen-free Cu sheets and Cu sheets containing phosphorous (P)). Particularly, the Cu mesh anode achieved the highest reaction activity at current densities up to 150 mA/cm^2 (equivalent to a film formation speed of 3 μm/minute).
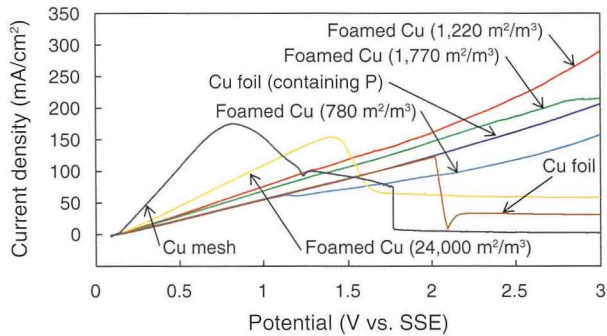
Fig. 14 Relationship between Potential and Current Density with Different Cu Anode Materials

3. Discussion and Verification Tests

The analysis results described above inferred that the rate-determining processes are the ion transfer in the solid electrolyte membrane for Cu film formation and the oxidation reactions at the anode. Unlike electroplating, since solid electrodeposition cannot apply mass transfer (convection) by agitation to ion transfer, it is important to increase the rate of diffusion in the solid electrolyte membrane. A specific method of achieving this is to use a solid electrolyte membrane with more developed ion channels (e.g., developed films A and B used in this study).

Fig. 15 shows the results of structural analysis of the solid electrolyte membrane by small angle X-ray scattering (SAXS). The periodic hydrophilic structure (d_1) that appears when the scattering vector q is close to 0.2 Å^{-1} was verified. It was confirmed that the hydrophilic portions of developed film B, which has a large maximum metal ion transfer rate, are more developed than the same portions in Nafion. However, as described above, since the maximum metal ion transfer rate of Nafion N117 is 1.2 µm/minute, it is more likely that the oxidation reaction at the anode is a more fundamental rate-determining process. In addition, it may be possible to achieve substantial increases in the film formation speed by replacing the conventional Pt/Ti anode with a more reactive Cu mesh anode to increase the reaction rate.

The countermeasures described above were verified in film formation tests that replaced the Nafion N117 solid electrolyte membrane with developed film B, and the Pt/Ti anode material with a Cu mesh anode. **Fig. 16** shows the relationship between voltage, current density, and film formation speed. The results found that the current density and film formation speed increased in accordance with the voltage, and that normal Cu film formation was achieved even at approximately 2.0 µm/minute. As shown in **Fig. 17**, this is virtually the same film formation speed as conventional electroplating. However, because the Cu mesh anode is consumed by the reaction, it requires regular replacement. Furthermore, adopting a solid electrolyte membrane with more developed ion channels and the higher film formation temperature conditions have an adverse effect on the durability of the solid electrolyte membrane. Therefore the impact of these countermeasures on cost must be assessed before application.
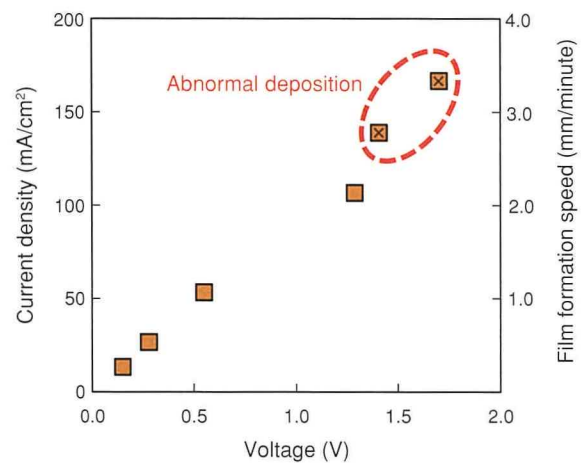

Fig. 16 Relationship between Voltage and Current Density (Film Formation Speed) (Cu Mesh, 60°C)

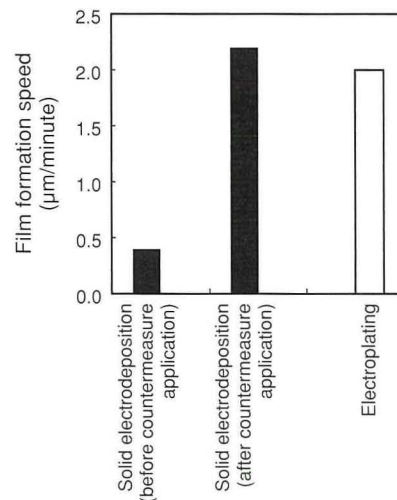Fig. 15 Results of Solid Electrolyte Membrane Analysis by SAXS

Fig. 17 Comparison of Film Formation Speed between Solid Electrodeposition and Electroplating

When solid electrodeposition was originally proposed, the application of a solid electrolyte membrane in which convection does not occur was regarded as a disadvantage for film formation speed. However, this study has demonstrated the high potential of the proposed method. Based on these results, it should be possible to realize a film formation method that is significantly more productive than conventional electroplating by further optimizing process conditions and developing a more suitable solid electrolyte membrane.

4. Conclusion

This article has described a solid electrodeposition method, which was proposed as a new surface treatment process using a solid electrolyte membrane, and the details of concept verification. After identifying a low film formation speed as one issue of the proposed method, the causes and possible countermeasures were analyzed. The following results were obtained.

1. Analysis results of the ion transfer rate and electrochemical measurement suggested that the ion transfer rate of the solid electrolyte membrane and the anode reaction rate were the main causes of the low film formation speed.
2. Applying a solid electrolyte membrane with more developed ion channels and changing the anode material (from a Pt/Ti sheet to Cu mesh) increased the film formation speed from approximately 0.4 μm to approximately 2.0 μm/minute, roughly the same as conventional electroplating.

References

(1) The Electroplating Research Society Ed. *Modern Plating Textbook* (in Japanese). The Nikkan Kogyo Shimbun. Tokyo (2011).
(2) K. Akamatsu et al. "Fabrication of Silver Patterns on Polyimide Films Based on Solid-Phase Electrochemical Constructive Lithography Using Ion-Exchangeable Precursor Layers." *Langumuir* Vol. 27 No. 19 (2011) pp. 11761-11766.
(3) T. Homma. "Polymer Electrolyte Fuel Cell" (in Japanese). *The Journal of the Institute of Electrical Engineers of Japan* Vol. 122 No. 1 (2002) pp. 29-32.
(4) I. Masayuki. *Laws of Electrochemical Impedance - Principles, Measurement, and Analysis -* (in Japanese). Maruzen Publishing Co., Ltd. Tokyo (2011).
(5) H. Yeager et al. "Perfluorinated Ionomer Membranes." *The ACS Symposium Series* (1982) pp. 1-6.

Authors

Y. SATO **H. IISAKA** **J. MURAI**

Research into Power Devices with Embedded Cooling

Yuji Fukuoka[*1]
Feng Zhou[*2]
Ercan M. Dede[*2]
Ki Wook Jung[*2]
Shailesh N. Joshi[*2]
Yanghe Liu[*2]

Abstract

Wide-bandgap (WBG) power devices are being developed for application in future generations of environmentally friendly vehicles. However, since the heat density of WBG power devices is approximately four times higher than conventional silicon devices, a new cooling structure is required. This research has proposed a cooling mechanism embedded in the device called a chip-scale cooler. This cooler, which contains minute lateral flow paths, was then fabricated and evaluated. Additionally, to further enhance cooling performance, a jet impingement cooler was designed through the application of topology optimization methodology. Simulations confirmed that this design achieved the targeted heat transfer coefficient of 184 kW/m²K.

Keywords: *cooler, power device, inverter, wide-bandgap, semiconductor process, jet impingement*

1. Introduction

With global warming caused by CO_2 emissions becoming an increasingly pressing issue, the Toyota group is responding by developing a wide range of environmentally friendly vehicles, including hybrid, fuel cell, and electric vehicles. All of these environmentally friendly vehicles adopt electrified powertrains that contain a power control unit (PCU, **Fig. 1**).
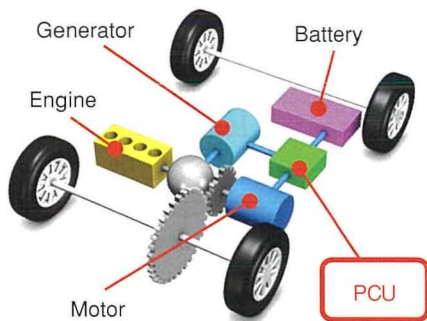
Fig. 1 Configuration of Hybrid Vehicle Powertrain

The PCU functions to control the power flow between the battery, motor, and generator, and contains a number of power devices to control current and voltage (**Fig. 2**). These power devices generate large amounts of heat and account for approximately 20% of the electrical loss in an electrified vehicle. Therefore, power modules are designed to transfer heat

efficiently from both sides using a layered structure in which power cards (consisting of power devices packaged together by a plastic molding) are stacked together with water-cooled cooling units.[1]

Although conventional power devices are generally fabricated from silicon (Si), the Toyota group is working on the development of wide-bandgap (WBG) power devices using next-generation semiconductor materials such as silicon carbide (SiC). When adopted in the PCU, SiC power devices have the potential to reduce conduction loss by approximately 60% compared to Si semiconductor devices. For this reason, the adoption of SiC power devices is regarded as a promising way to improve fuel efficiency and reduce the size of the PCU.[2]
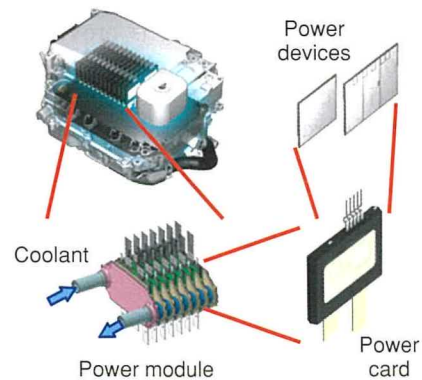

Fig. 2 Internal Structure of PCU

*1 EHV Electronics Design Div., Powertrain Company
*2 Toyota Research Institute of North America, Toyota Motor North America, Inc.

Since SiC power device chips can be made smaller than Si chips, it should be possible to develop compact power modules with a high power density. However, reducing the size of the chips has the effect of increasing the power density of the power devices. Specifically, the power density of SiC power devices is approximately 1 kW/cm^2, four times higher than the power density of current Si power devices, which is only 250 W/cm^2 (**Fig. 3**).[3] With conventional cooling structures reaching the feasible limits of performance, new cooling structures must be developed with substantially enhanced cooling performance.
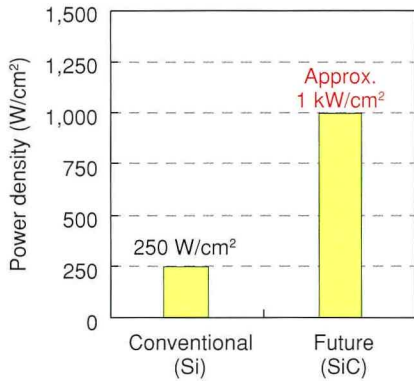
Fig. 3 Power Density of Power Devices

2. Application of Chip-Scale Cooler to Power Devices

This research proposed a chip-scale cooler as a new high-performance cooling structure. **Fig. 4** shows a conventional cooling structure and **Fig. 5** shows the proposed structure. In the conventional structure, the power devices are fixed between remote coolers. Heat discharged from the front and back surfaces of the power devices is diffused over a wide area using a copper block. The coolers are manufactured from aluminum, and the heat diffused by the copper block is dissipated to the coolant. A ceramic insulating plate is provided between the cooler and the copper block. The cooling area of the coolers is increased using fins consisting of thin corrugated aluminum plates. This configuration accelerates heat transfer to the coolant.
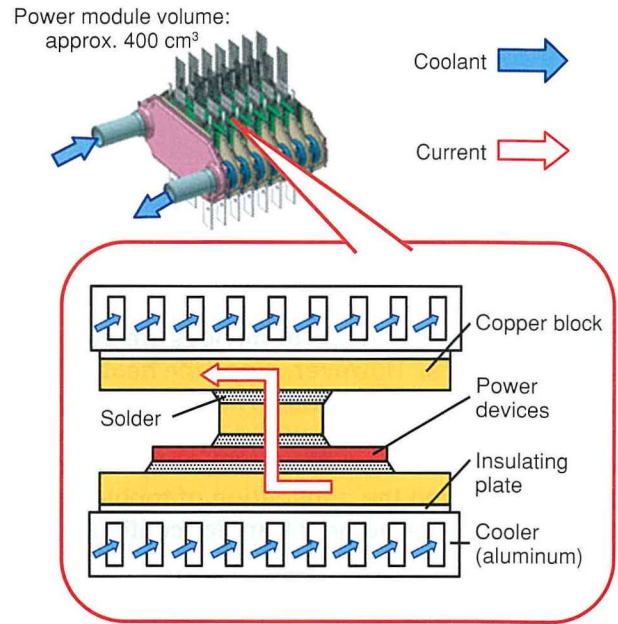
Fig. 4 Internal Structure of Conventional Cooler
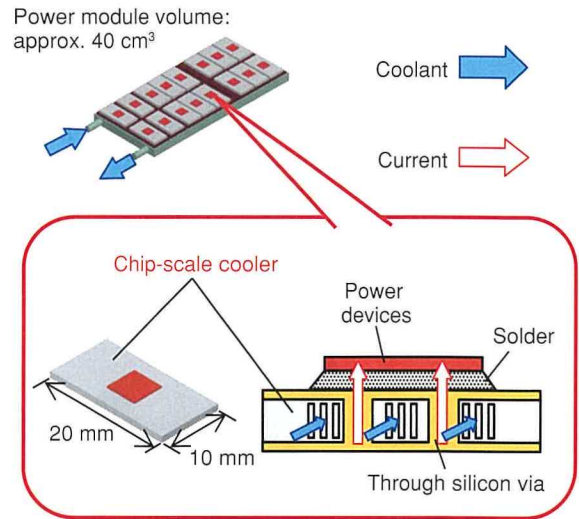
Fig. 5 Internal Structure of Chip-Scale Cooler

In contrast, the proposed chip-scale cooler structure consists of cooling paths positioned near the power devices with fewer intermediate thermal interface materials. High cooling performance can be achieved by creating these cooling paths on a microscopic scale to substantially increase the cooling area. Provisional calculations indicated that this structure can achieve a cooling area approximately five times as large as a conventional cooler. **Fig. 6** shows the correlation (simulation results) between the temperature of a power device with a power density of 1 kW/cm^2 and the heat transfer coefficient α (an index for cooling performance). From this graph, the necessary heat transfer coefficient α to maintain a WBG power device at or below an operating temperature of 175°C was estimated to be

130 kW/m²K or higher. This value was set as the cooling performance target. However, since the heat transfer coefficient of conventional cooling structures is only approximately 20 kW/m²K, substantial improvements in cooling performance were required.
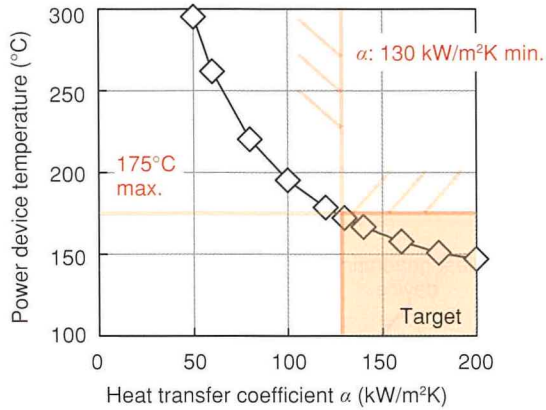

Fig. 6 Relationship between Heat Transfer Coefficient of Cooler and Power Device Temperature

Research into chip-scale coolers has focused on future high-frequency devices and 3D memory.[4][5] Previous research has also examined adopting this approach in lateral devices in which low currents flow horizontally on the device surface. However, since power devices that control large current flows tend to be vertical devices in which the current flows vertically, the current channels must be laid out within the cooling flow paths. As a result, the current channels and cooling flow paths must be electrically isolated.

The proposed structure consists of a separate cooling chip that is integrated with the devices by wafer bonding. Through silicon vias are formed in this structure to secure the current channels. Monocrystalline Si is used as the cooling chip material. This material has a high thermal conductivity and can ensure electrical isolation between the current channels and cooling flow paths using comparative resistance control technology developed for Si semiconductors. Microscopic cooling flow paths can then be formed using microfabrication techniques.

3. Prototyping of Cooler with Lateral Flow Paths

First, a prototype chip-scale cooler with lateral straight flow paths was fabricated to verify the feasibility of the proposed structure. **Fig. 7** shows the structure of this prototype. The cooler consists of two layers of thin Si chip wafers. The first layer includes a microscale straight cooling channel structure and manifold. The second includes the coolant inlet and outlet. The microscale channels are sealed by joining the first and second layers together by wafer bonding. Since the purpose of this prototype was only to evaluate the cooling capacity of the proposed structure, the through silicon vias were not fabricated.
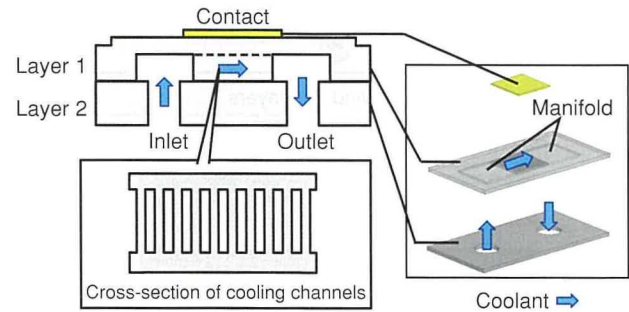

Fig. 7 Prototype of Cooler with Lateral Flow Paths

Fig. 8 shows the fabrication procedure. First, as shown in **Fig. 8**(a), the microscale channels and manifold are formed on the back surface of the first Si wafer layer. The microscale channels were formed using a plasma-based deep Si etching technique. The microscale channels have a width of 30 μm and a depth of 320 μm. On the second layer, the inlet and outlet holes for the coolant were formed using the same etching technique. After fabrication, the first and second Si wafer layers were bonded together. The wafer bonding methodology is as follows. The back surfaces of the Si were hydrophobized and provisionally welded together under a vacuum. Annealing was then applied in a nitrogen atmosphere at 1,100°C to achieve the bond by mutually diffusing Si atoms between the two layers. **Fig. 8**(b) shows an enlarged scanning electron microscopy (SEM) image of the connection interface. As the intersection is not visible on the SEM image, it was verified that the two Si wafers are completely bonded together. After wafer bonding, the titanium/nickel/gold (Ti/Ni/Au) contact was formed by applying vacuum deposition to the cooling surface of the first layer. Finally, the cooler as shown in **Fig. 8**(c) was fabricated by a separation technique referred to as dicing.
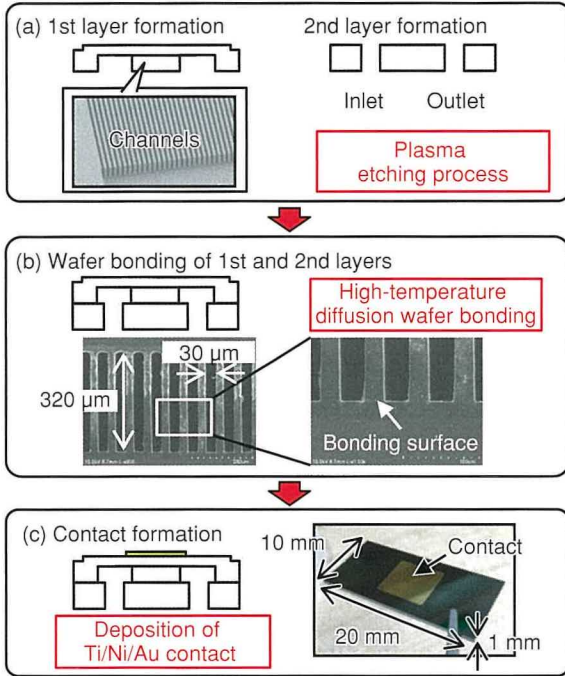
Fig. 8 Fabrication Method of Chip-Scale Cooler

Fig. 9 External Appearance of Evaluation Bench
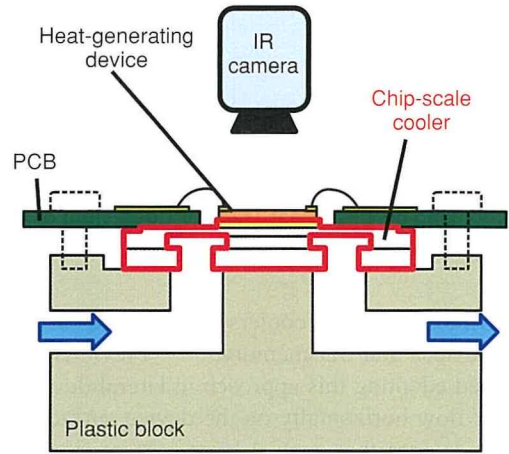
Fig. 10 Outline of Cross-Section of Evaluation Bench

4. Evaluation of Performance of Cooler with Lateral Flow Paths

A heat-generating device simulating a power device was used to evaluate the cooling performance of the proposed structure. This heat-generating device consisted of a platinum/gold (Pt/Au) resistor formed on the front surface and soldered to the fabricated Si chip-scale cooler. The wafer bonded Si chip-scale cooler with lateral flow paths was attached to the evaluation bench as shown in **Figs. 9** and **10**, and its cooling performance was evaluated. The heat-generating device was connected to the printed circuit board (PCB) by wire bonding, and voltage was applied to generate heat. The cooler was fixed between the PCB and plastic block and coolant was introduced. The cooling performance was evaluated by measuring the surface temperature of the heat-generating device using an infrared (IR) camera attached directly above the device, and by measuring the inlet and outlet coolant temperatures using thermocouples.

Heat transfer coefficient α is calculated by the following equation.

$$\alpha = Q / (T_{Dmax} - T_{Cin}) \qquad (1)$$

where,

      Q: power density
      T_{Dmax}: maximum device temperature
      T_{Cin}: coolant inlet temperature

Fig. 11 shows the results of device surface temperature measurement in the cooling performance evaluation. Coolant for HVs was used and the coolant inlet temperature was adjusted to 65°C. The circulating flow rate was set so that the standard pressure loss was not exceeded. The size of the device was 6 mm along each side, and power was applied to achieve a power density of 130 W/cm². The results showed that the device surface temperature distribution increased in the direction of coolant flow. The maximum temperature was 87.4°C on the downstream side of the coolant, and the measured heat transfer coefficient was 58 kW/m²K. This result was virtually consistent with the results of a thermal fluid simulation (54 kW/m²K) performed under the same conditions. However, the proposed cooler with lateral flow paths did not achieve the targeted heat transfer coefficient of 130 kW/m²K required by SiC power devices.
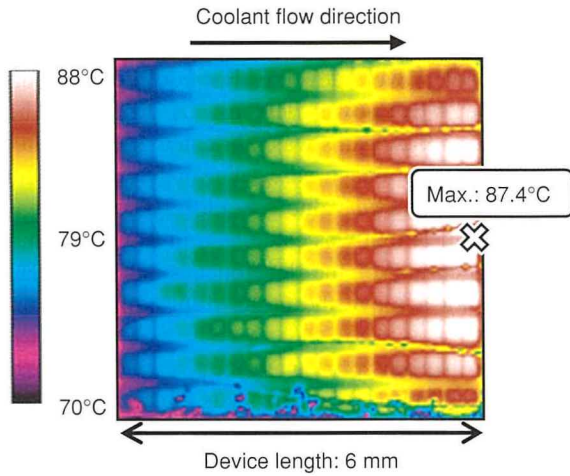
Fig. 11 Device Surface Temperature Distribution Measured by IR Camera

5. Design of Jet Impingement Cooler

To achieve higher cooling performance, a jet impingement chip cooler was designed. **Fig. 12**(a) illustrates that, in the case of a cooler with lateral flow paths, the coolant temperature increases as the cooler receives heat from the device because the coolant passes through long and thin cooling channels. As a result, the cooling performance worsens downstream of the coolant inlet. It is difficult to suppress this temperature rise by increasing the flow rate since this approach leads to an increase in pressure loss. As a result, the temperature difference within the device surface ΔT was 15.4°C, a very large value. Although this issue requires a design that creates uniform contact between the device surface and coolant, a jet impingement type of cooling structure, which flows coolant vertically and impinges on the heat-generation surface as shown in **Fig. 12**(b), was considered to be more effective than flowing coolant in the horizontal direction of the chip wafer.

Fig. 13 shows the cross-sectional structure of the jet impingement chip cooler. This structure differs from the lateral flow path structure by having three wafer chip layers and wafer bonding in two locations. The radial type channels shown in **Fig. 14** are formed on the back surface of the first layer. This was designed using a topology optimization methodology.[6] Topology optimization is a technique that uses repeated simulations to automatically calculate the topology (i.e., the structural features) capable of maximizing performance. In this research, it was used to automatically calculate the optimum flow path geometry for minimizing coolant pressure loss and maximizing the heat transfer coefficient while maintaining a uniform coolant surface temperature. The coolant impingement nozzles are formed on the second layer. After topology optimization, the design dimensions of each part were determined using thermal fluid simulations. As a result of these simulations, the nozzle diameter was set to 160 μm and the size

of one cell unit was set to 500 x 500 μm. With these dimensions, the target heat transfer coefficient α and pressure loss were achieved.
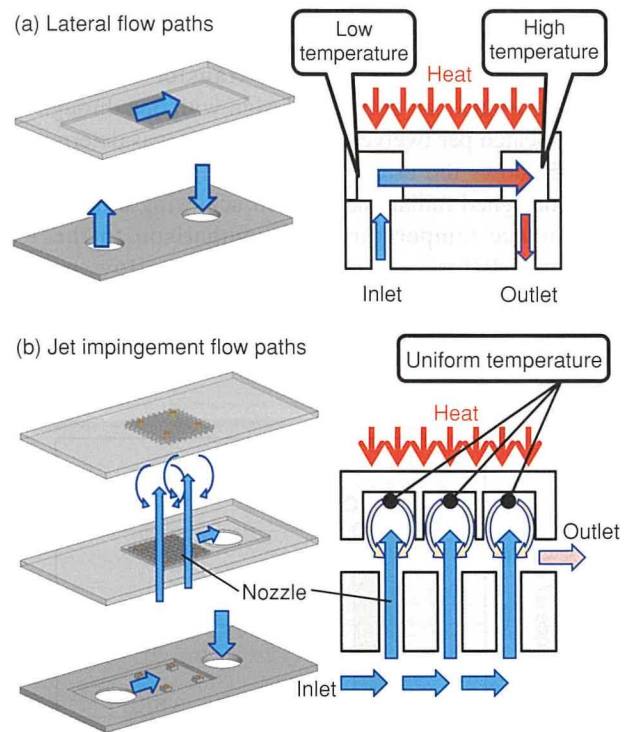

Fig. 12 Comparison of Lateral and Jet Impingement Flow Paths
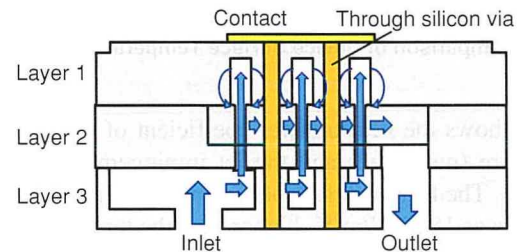

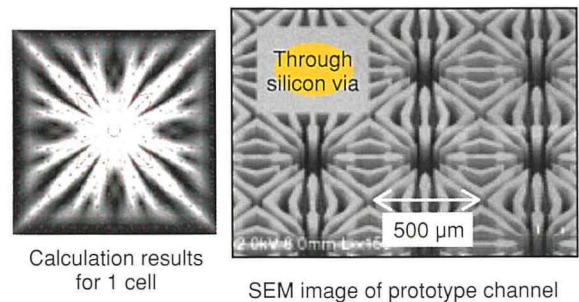**Fig. 13 Cross-Sectional Structure of Jet Impingement Cooler**

Fig. 14 Radial Type Cooling Channels Obtained by Topology Optimization Methodology

In addition, regions were provided in the microscale channel cells for through silicon vias as current channels. Although increasing the number of through silicon vias has the effect of lowering the electrical resistance, this is also likely to reduce the cooling performance since cooling channels cannot be located in those regions. Therefore, after studying the layout capable of achieving both the required heat transfer coefficient and electrical resistance, an optimum design with one through silicon via cell allocated per twelve nozzle unit cells was determined.

Fig. 15 shows the effect of the jet impingement cooler and specially designed radial channels on achieving a more uniform device surface temperature. In comparison to the 15.4°C temperature difference ΔT of the lateral flow paths, the simulation results showed that the temperature difference with the jet impingement structure was only 3.3°C, indicating uniform heat dissipation from the device.
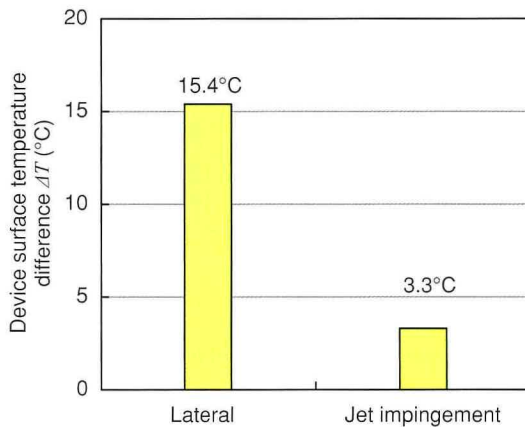
Fig. 15 Comparison of Device Surface Temperature Difference

Fig. 16 shows the heat transfer coefficient of the lateral flow path structure (measured) and the jet impingement chip cooler (simulated). The heat transfer coefficient of the jet impingement chip cooler was 184 kW/m²K, higher than the target performance of 130 kW/m²K.
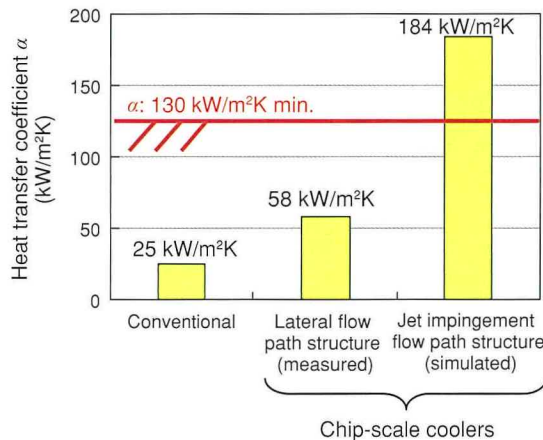
Fig. 16 Heat Transfer Coefficient of Cooler Structures

6. Summary and Future Plans

Chip-scale coolers were developed as cooling mechanisms for next-generation WBG power devices. A prototype chip-scale cooler with lateral flow paths was fabricated and evaluated. This structure achieved a measured heat transfer coefficient of 58 kW/m²K. This measured value was closely consistent with the value of 54 kW/m²K that was calculated in a simulation, thereby verifying the accuracy of the developed simulation. However, this value did not achieve the target minimum performance of 130 kW/m²K.

To achieve higher performance, a cooler with a jet impingement channel structure was designed. Topology optimization methodology was adopted to design the channel structure. A simulation calculated that the developed structure achieved a heat transfer coefficient of 184 kW/m²K while suppressing electrical resistance and coolant pressure loss.

An actual jet impingement chip cooler is currently being fabricated, and it is planned to confirm the consistency between measured results and the cooling performance calculated in the simulation.

Other issues for realizing chip-scale coolers include foreign matter blocking the microscale channels and reliability over extended periods of use. Once the target cooling performance has been achieved, it is intended to construct a test environment that simulates actual usage conditions, and to improve the developed cooler while evaluating its operational stability over the long term.

References

(1) Y. Sakamoto. "Assembly Technologies of Double-Sided Cooling Power Modules." *Denso Technical Review* Vol. 16 (2011) pp. 46-56.
(2) K. Hamada et al. "SiC-Emerging Power Device Technology for Next-Generation Electrically Powered Environmentally Friendly Vehicles." *IEEE Transactions on Electron Devices* Vol. 62 No.2 (2015) pp. 278-285.
(3) A. Bar-Cohen et al. "Near-Junction Microfluidic Cooling for Wide Bandgap Devices." *MRS Advances* Vol. 1 No. 2 (2016) pp.181-195.
(4) D. Altman et al. "Development of a Diamond Microfluidics-Based Intra-Chip Cooling Technology for GaN." *Proceedings of the 2015 InterPACK Conference* Paper No. IPACK2015-48179, V003T04A006.
(5) X. Zhang et al. "3D IC with Embedded Microfluidic Cooling Technology, Thermal Performance, and Electrical Implications." *Proceedings of the 2015 InterPACK Conference* Paper No. IPACK2015-48584, V003T10A008.
(6) E. Dede et al. "Scale Effects on Thermal-Fluid Performance of Optimized Hierarchical Structures." *Proceedings of the 8th ASME/JSME Thermal Engineering Joint Conference (AJTEC)* (2011).
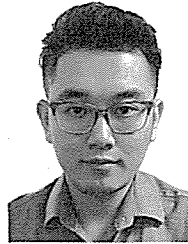
Authors

Y. FUKUOKA	F. ZHOU	E. DEDE
S. JOSHI	K. JUNG	Y. LIU

Technical Papers/Technical Articles

The 63rd Okochi Memorial Production Prize
Development of Highly Compact Painting Line with Substantially Lower CO$_2$ Emissions

Koki Hayashi*[1]   Wataru Murata*[1]   Tokio Endo*[1]   Tatsuya Iida*[1]

1. Introduction

The reduction of volatile organic compound (VOC) and carbon dioxide (CO$_2$) emissions is regarded as an increasingly important part of efforts to lower the amount of substances of concern (SOCs) discharged from manufacturing plants during the vehicle production process.

The environmental impact of this process is large due to the high number of individual steps required to manufacture a completed vehicle, including stamping, body welding, painting, and part assembly. Since painting consumes more energy and generates higher CO$_2$ emissions than any other step, reducing the energy consumption of this process is regarded as a particularly urgent issue (**Fig. 1**).
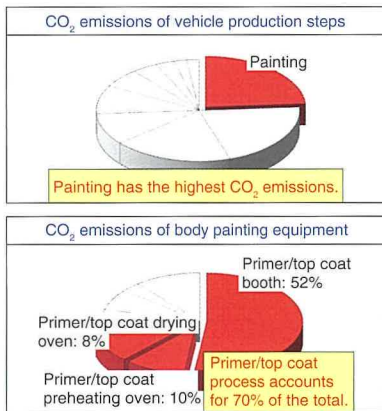
Fig. 1 CO$_2$ Emissions of Main Production Steps and Body Painting Equipment

In response, a highly innovative painting line was developed, which reduced the size of paint line equipment by 40%, CO$_2$ emissions from the line by 32%, installation time by 50%, and required investment by 30% by completely refining every part of the primer/top coat painting process.

2. Outline of Development

The key point for achieving this objective was the development of production technology capable of shortening the physical length of the process, lowering the equipment height, and reducing the size of auxiliary equipment (**Fig. 2**). A wide variety of measures were implemented, including reducing the space under the painting booth, creating a narrower booth air supply chamber, applying the concept of *jidoka* (automation with a human touch) to cleaning and interior painting processes, improving robot processing capabilities, optimizing the transfer pitch, decreasing the cross-sectional surface of the drying oven, making effective use of compact deodorization equipment, adopting an innovative booth air conditioner configuration, reducing installation times by half, and further enhancing the safety of engineering work. Reducing the size of the air supply chamber and space under the painting booth made the greatest contribution to reducing the size of the line. These measures resulted in a highly compact painting booth (**Fig. 3**) and helped to greatly lower CO$_2$ emissions (**Fig. 4**).
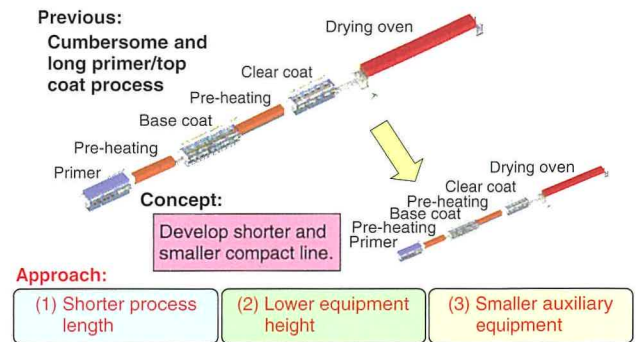

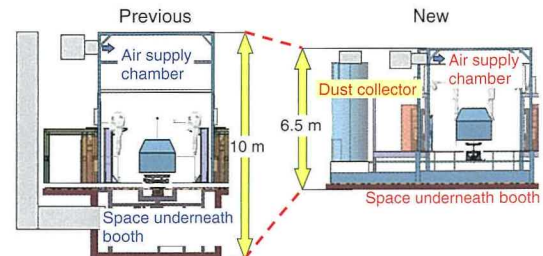**Fig. 2 Development Concept**

Fig. 3 Development of Compact Painting Booth

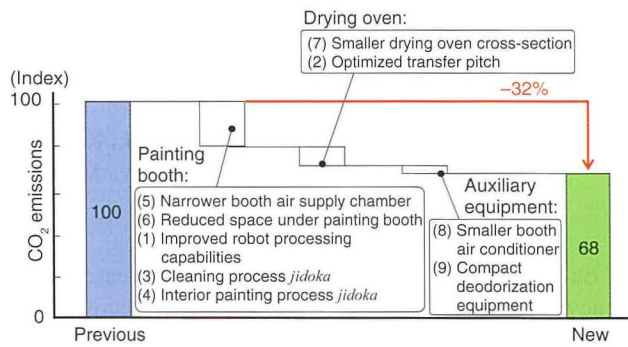*[1] MS Plastics & Surface Finishing Production Engineering Div., Mid-size Vehicle Company

Fig. 4 Reduction of CO₂ Emissions

Drying oven:
(7) Smaller drying oven cross-section
(2) Optimized transfer pitch

−32%

(Index)
CO$_2$ emissions

100

Previous

Painting booth:
(5) Narrower booth air supply chamber
(6) Reduced space under painting booth
(1) Improved robot processing capabilities
(3) Cleaning process *jidoka*
(4) Interior painting process *jidoka*

Auxiliary equipment:
(8) Smaller booth air conditioner
(9) Compact deodorization equipment

68

New

3. Conclusion

The developed painting technology was installed on the Prius production line at the Tsutsumi Plant. After verifying the lack of quality or equipment issues, this painting line is currently being rolled out globally in new plants and as part of projects to upgrade aging facilities.

The development of production engineering technology will continue to play a central role in achieving the Toyota Environmental Challenge 2050.

Technical Award News

2017 Energy Conservation Grand Prize (Minister Prize of Economic, Trade and Industry)
The Plug-In Hybrid System for the New Prius PHV

Shinji Ichikawa*1   Takashi Murata*2   Shigeki Kinomura*3
Michinobu Suzuki*4   Tatsuya Miyoshi*5

1. Introduction

This article outlines the plug-in hybrid system that was developed to enhance the product appeal of the new Prius PHV through world-leading environmental friendliness (power and fuel consumption) and substantially improved dynamic performance in EV mode. The developed plug-in hybrid system was awarded the Energy Conservation Grand Prize in recognition of its impressive environmental performance.

2. Main Characteristics

Fig. 1 shows the system configuration.
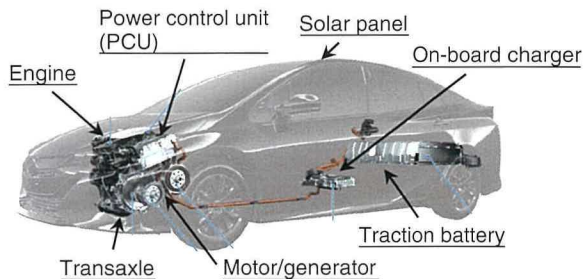
Fig. 1 Plug-In Hybrid System

The engine installed in the Prius PHV is the same 2ZR-FXE model adopted in the fourth-generation Prius and has a thermal efficiency of 40%.

The traction battery system plays a key role in increasing the power and range of the vehicle in EV mode. This was accomplished by increasing the number of cells to 95 (1.7 times higher than the previous model PHV) and raising the battery capacity to 8.8 kWh (approximately twice as high as the previous model). A new battery warm-up system was also adopted that helps to maintain an appropriate battery temperature under cold conditions, thereby ensuring EV mode performance.

A new dual motor drive system was adopted in which the transaxle uses the generator as a motor during EV mode. This approach substantially increases power in EV mode by supplementing the output of the motor with the generator.

The on-board charger was redesigned to increase charging efficiency from 89 to 95%, thereby helping to increase power consumption efficiency. This improvement was achieved by adopting low-loss power devices to reduce conduction loss and a new charging method to reduce switching loss. Direct current (DC) charging can also be selected in accordance with the charging requirements of the user.

A dedicated compact storage battery was adopted for the solar charging system to reduce system loss and enable highly efficient charging of the traction battery. While parked, solar power is generated and stored in the dedicated battery. This power is used to charge the traction battery once a certain storage threshold is reached. This increases the efficiency of the solar charging system and allows enough energy to be accumulated per day to drive the vehicle for up to 6.1 km in EV mode.

3. Conclusion

Table 1 shows the main specifications of the new Prius PHV.

Table 1 Main Specifications of the New Prius PHV

	New PHV model	Previous PHV model
EV mode range (JC08 test cycle) (km)	68.2	26.4
Maximum speed in EV mode (km/h)	135	100
Fuel efficiency (km/L)	37.2	31.6
Power consumption efficiency (km/kWh)	10.54	8.74

The developed PHV system increases the EV mode range and power of the new PHV by approximately 2.3 and approximately 1.8 times, respectively. As a result, according to data obtained from PHV field tests, the average EV mode coverage (i.e., the proportion of the total driving distance that can be driven in EV mode) of the new PHV is approximately 60%, twice as high as the previous model.

Since plug-in hybrid vehicles combine the fun-to-drive performance of electric vehicles with the fuel efficiency of hybrid vehicles, users can experience excellent environmental performance without anxiety about battery range. Promoting wider adoption of the new Prius PHV with its enhanced environmental performance should help to further lower the environmental impact of vehicles.

*1 Powertrain Product Planning Div., Powertrain Company
*2 EHV Battery Design Div., Powertrain Company
*3 EHV Electricity Converter Design Div., Powertrain Company
*4 Drivetrain-EHV Design Div. No. 1, Powertrain Company
*5 Electronics Control Engineering Div., Advanced R&D and Engineering Company

The JSAE Thesis Prize (68th JSAE Awards)

Research into Ride Comfort by Unsprung Negative Skyhook Damper Control Using In-Wheel Motors

Etsuo Katsuyama*1   Ayana Omae*1

1. Introduction

Vehicles equipped with in-wheel motors (IWMs) are capable of independently controlling the driving force at each wheel. For this reason, IWMs are regarded as a highly promising technology from the standpoint of enhancing vehicle dynamics. However, the increase in unsprung mass has an adverse effect on vibration in the 4 to 8 Hz range, which is often regarded as uncomfortable by vehicle occupants. Therefore, this research examined a method of reducing this vibration using driving force control by IWMs. As a result, it was discovered that vibration in this range could be damped effectively by a control using unsprung vertical vibration information.

2. Outline of Technology

2.1 Unsprung negative skyhook damper control method

Skyhook control is a widely adopted conventional control method. Despite being a highly effective method that uses simple control laws, its effectiveness is limited to the range around the sprung resonance frequency of 1 to 2 Hz. Furthermore, in the 4 to 8 Hz range, skyhook control is either ineffective, or has even a slight adverse effect due to the control lag that occurs.

After analysis, the force component proportional to the vertical velocity of the unsprung mass was identified as the cause of this adverse effect. Therefore, to counter this effect, a control method was proposed that reduces vibration in the 4 to 8 Hz range by applying a negative force proportional to the vertical velocity of the unsprung mass. The vertical acceleration of the vehicle body in response to road surface inputs was calculated using the simple vehicle model shown in **Fig. 1**. As a result, it was confirmed that the proposed control is extremely effective in the targeted frequency range (**Fig. 2**).
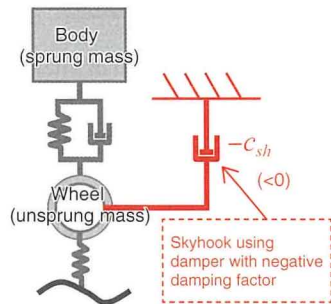
Fig. 1 Simple Vehicle Model

This control was named the negative skyhook damper control since it functions as an unsprung skyhook using a damper with a negative damping factor.

2.2 Application to vehicle equipped with IWMs

Effective utilization of the vertical suspension reaction force components generated from the IWMs enables the vertical forces
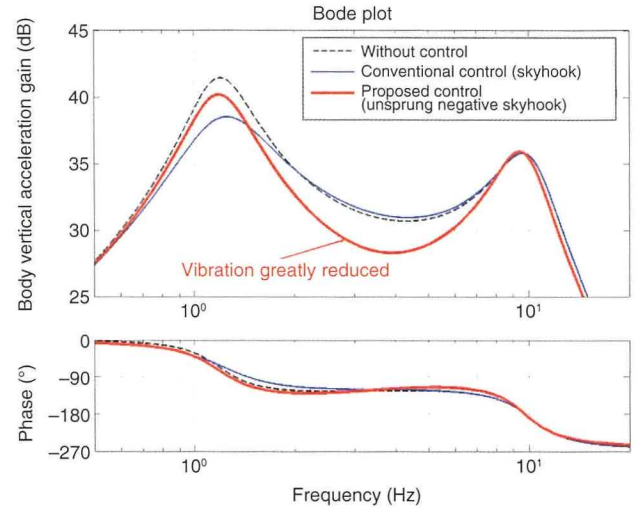
Fig. 2 Vertical Acceleration of Vehicle Body Due to Road Surface Irregularities

acting on the vehicle body to be freely controlled by driving force distribution. The driving force control values at each wheel (F_{xfl}, F_{xfr}, F_{xrl}, and F_{xrr}), which enable this control to be applied to the roll, pitch, and vertical motions of the vehicle without disturbing the speed or trajectory of the vehicle, are derived as shown in Equation (1).

$$\begin{bmatrix} F_{xfl} \\ F_{xfr} \\ F_{xrl} \\ F_{xrr} \end{bmatrix} \approx -\frac{2c_{sh}}{tan\theta_r} \begin{bmatrix} -\{v_p + (1-e)\,v_q + ev_z\} \\ -\{-v_p + (1-e)\,v_q + ev_z\} \\ v_p + (1-e)\,v_q + ev_z \\ -v_p + (1-e)\,v_q + ev_z \end{bmatrix} \quad (1)$$

In this equation, c_{sh} is the damping factor of the control, θ_r is the inclination angle of the driving force at the rear wheels, v_p and v_q are the lateral and longitudinal difference in the unsprung vertical velocity, v_z is the average unsprung vertical velocity, and e is the weighting function of the pitch and vertical controls.

These values were applied to a vehicle equipped with IWMs at each wheel, and it was confirmed that vibration was reduced in the target frequency range in both simulations and in an actual vehicle.

3. Conclusion

This article proposed a control method that effectively damps vibration in frequency ranges that are uncomfortable for vehicle occupants. This effect was achieved by driving force control using IWMs without adding suspension control devices.

*1 Advanced Chassis Development Div., Advanced R&D and Engineering Company

Technical Award News

New Laser-Clad Valve Seat Technology Enabling High-Speed Combustion and Global Production

Hironori Aoyama[1]   Natsuki Sugiyama[1]   Kohei Yanaka[2]
Yuki Kamo[3]   Tadashi Oshima[4]

1. Introduction

The development of vehicle engines with substantially higher fuel efficiency is an important part of measures for achieving a sustainable society. At the same time, engines also require a high level of dynamic performance to ensure an enjoyable driving experience. To meet these difficult requirements, Toyota Motor Corporation has developed a series of next-generation engines based on the concept of high-speed combustion to achieve world-leading levels of thermal efficiency and specific power.

2. Development Aims

High-speed combustion helps to reduce cooling and pumping losses by expanding the exhaust gas recirculation (EGR) limit. This concept can also boost power at high engine loads that cannot utilize EGR by enhancing knocking resistance. To achieve high-speed combustion, it is necessary to increase the intensity of turbulence inside the combustion chambers. An effective way of accomplishing this in a gasoline engine is to generate tumble flows. However, the formation of tumble flows tends to reduce the intake airflow, creating a trade-off relationship that is difficult to overcome.

To enable the formation of intense tumble flows while simultaneously reducing intake resistance, this development took on the challenge of designing an innovative intake port shape featuring laser-clad valve seats (LCVS) that were originally adopted in race car engines (**Fig. 1**). In addition, the following objectives were also established as part of the decision to adopt LCVS in these globally strategic engines: (1) the development of highly durable LCVS usable in environments around the world, including regions adopting bioethanol as a renewable resource, and (2) the development of a globalized and large-scale production system.

Fig. 1 Cross-Section of Intake Port Featuring LCVS

3. World-Leading Highly Efficient Intake Port Design

The surface against which the cylinder head valve rests when the valve is closed is called the valve seat. The function of the valve seat is to ensure the wear resistance of this surface. Conventional valve seats are sintered steel rings that are molded in advance and press-fitted. However, it is difficult to reduce the size of these parts since a certain thickness is required to hold the seats in place. This constraint forces the design of curved intake port shapes that inhibit the efficient intake of gas into the combustion chamber (**Fig. 2**).
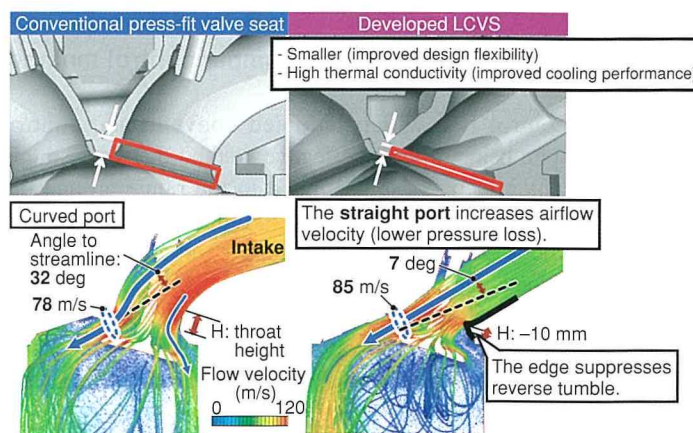
Fig. 2 Comparison of Intake Port Structures and Streamlines

In response to these issues, a technology was adopted that directly clads wear-resistant copper alloy powder onto the aluminum cylinder head using laser cladding. This technology enables the size of the valve seat to be reduced and allows the design of straight intake ports that efficiently draw the intake air into the combustion chamber while maintaining a high flow velocity. In addition, the airflow can be separated by an edge at the throat portion located at the bottom surface of the port, thereby helping to suppress reverse tumble. This innovative intake port design helps to achieve world-leading intake efficiency, including a tumble ratio of 2.9 and a flow coefficient of 0.49 (**Fig. 3**).

4. Development of LCVS Technology

4.1 Valve seat material compatible with wide range of fuels

The alloy used for LCVS must be durable under the high temperature and pressure environment created by high-speed

[1] Production Engineering Development Div., Powertrain Company
[2] Raw Material Development Div. No. 2, Powertrain Company
[3] Material Engineering Div. No. 1, Advanced R&D and Engineering Company
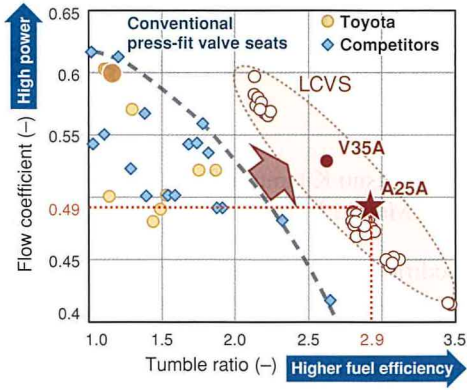[4] Toyota Central R&D Labs., Inc.

Fig. 3 Comparison of Intake Port Performance

combustion. At the same time, it must also be durable under the highly corrosive environment created by fuels with a high ethanol content. This material must also adhere closely to the aluminum base material and have the necessary machinability for forming the part shape. To satisfy these diverse requirements, a composite microstructure was designed in which hard wear-resistant grains are dispersed in a copper (Cu) alloy. The phenomenon of liquid immiscibility was utilized to create a uniform dispersion of the hard grains during laser cladding, which functions as a rapid melting and solidification process.

Molybdenum (Mo), which increases the active iron (Fe) content in the liquid phase, was added to the peritectic Cu-Fe alloy to create the immiscible two-liquid phase region (L1+L2) (**Fig. 4**). This phenomenon enabled the development of a new five-element Cu-Fe-Mo-Ni-Si alloy featuring hard wear-resistant grains dispersed in a heat-resistant Cu matrix. This alloy satisfies the characteristic requirements of the new LCVS.
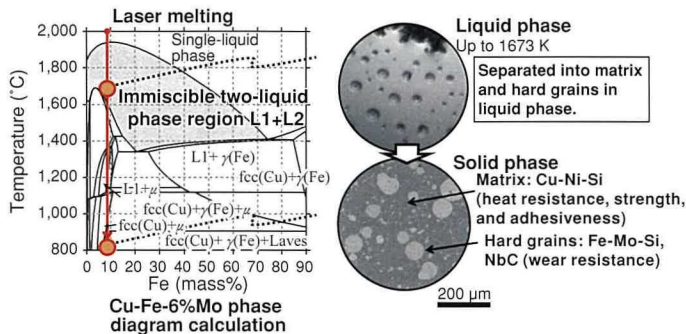
Fig. 4 LCVS Microstructure and Alloy Design

4.2 Technology for large-scale production

Since LCVS are formed by directly cladding a high-melting point Cu alloy onto a low-melting point aluminum base material, the cladding layer is susceptible to dilution by the base material. Production issues such as the difficulty of controlling this phenomenon had restricted laser cladding to low-volume production in a small number of plants within Japan.

The conventional LCVS process maintained a constant cladding point by fixing the complex optical system that generates the laser beam and the alloy powder supply nozzle, and by moving the parts being processed. This approach increases the size of the equipment required to clad large parts. Therefore, the new cladding method adopts a highly efficient diode laser with a compact optical system. A new angled forming technique was also developed with a coaxial nozzle to integrate the delivery of the laser beam, powder, and shielding gas. Under this approach, the cladding can be applied by rotating the laser beam with respect to the cylinder head (**Fig. 5**), thereby reducing energy consumption to less than one-fifth and the machine footprint to less than one-third of the conventional process, while also enabling large-scale production.
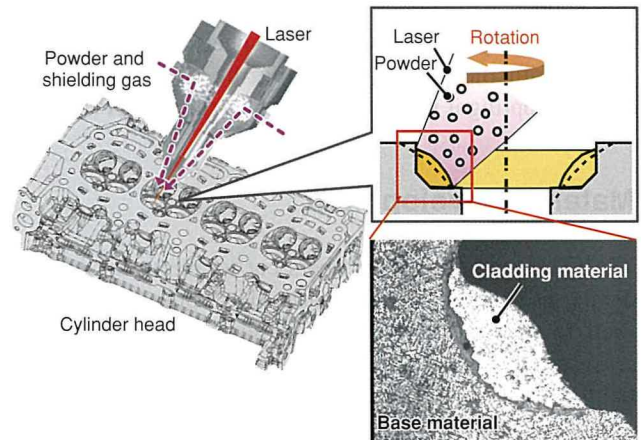
Fig. 5 Outline of New Cladding Process and Appearance after Cladding

5. Conclusion

The development of a highly reliable new alloy compatible with renewable bioethanol resources and a highly efficient and robust new manufacturing method has enabled the adoption of LCVS technology in a wide range of regions around the world. Taking advantage of this technology, intake port shapes have been designed that dramatically speed up combustion, thereby making a major contribution to the development of engines with a world-leading thermal efficiency in excess of 40% and a specific power of 60 kW/L.

Starting in 2017, this technology has been installed in Toyota's next-generation series of engines and will be adopted throughout the world with the aim of helping to realize a sustainable society.

Technical Award News

Mass Production Development of Vehicle Shell Inner Parts Applying Sheet Molding Compounds

Hiroshi Urayama[*1]   Tatsuo Kitamura[*2]   Yoshiyuki Adachi[*3]
Yoshihiro Iwano[*4]   Motoki Baba[*5]

1. Background and Purpose

Reducing the weight of mass-production vehicles is critically important for curbing CO_2 emissions. Carbon fiber reinforced plastic (CFRP) is a resinous material with a higher specific strength and specific stiffness than materials such as steel and aluminum, and is regarded as having extensive potential applications. This development focused on low-cost and potentially highly productive carbon-sheet molding compounds (C-SMC) with the aim of achieving the world's lightest rear hatch and adopting it in a plug-in hybrid vehicle (PHV).

2. Material Development

C-SMC consists of carbon fibers cut to a constant length and randomly distributed in a resin paste. Heat press forming is then applied to this paste to produce thermosetting CFRP. To increase productivity, the hardening time of the C-SMC was restricted to two minutes, significantly shorter than for conventional materials (**Fig. 1**). This development also reduced the amount of polymerization-inhibitor, identified the appropriate mold temperature range, and adjusted the hardener. These measures enabled the development of a quick-hardening material that satisfies the requirements for both hardening time and performance.
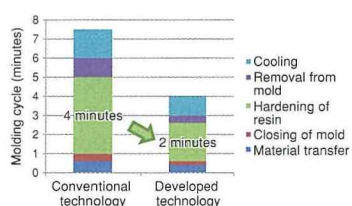
Fig. 1 Productivity Comparison
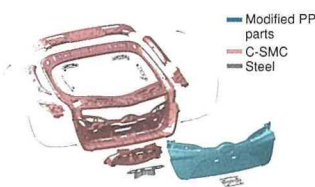
Fig. 2 Component Parts of Rear Hatch

3. Part Structural Design

The rear hatch is structured without steel reinforcing members. The inner frame is manufactured from C-SMC and the outer panel uses modified polypropylene (PP, **Fig. 2**). To ensure the same strength and stiffness as a conventional metallic rear hatch, a CFRP closed section frame was adopted and combined with resin reinforcing panels. High door stiffness was achieved by applying a structural adhesive to bond the CFRP parts and creating a continuous join. An integrated inner frame was formed, thereby reducing the number of parts from the five components used in the conventional frame. This approach lowered both weight and cost, and resulted in an extremely light rear hatch.

4. Production Engineering Development

The conventional technology requires a labor-intensive production process containing a high proportion of manual work. Substantial improvements in productivity were achieved by adopting automation throughout. **Fig. 3** shows an outline of the production process. The materials are cut to the shape of the parts using an ultrasonic cutter (1). In the heat press forming step (2), robots are used to transfer the materials to the mold and remove the products after forming. In the drilling step (4), an end mill is used to form several types of holes. In part assembly (5), handling equipment is used to transfer the products for adhesive coating, as well as to set and remove the products from jigs.
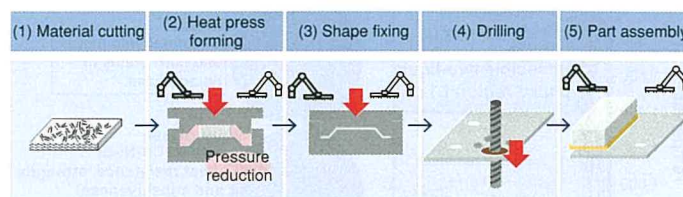

Fig. 3 Assembly Process of CFRP Rear Hatch Inner

5. Conclusion

By adopting an innovative three-in-one approach factoring in the materials, manufacturing process, and structure, the world's lightest plastic rear hatch was developed with a monthly production capacity of 5,000 units. The developed rear hatch is approximately 40% lighter than an aluminum rear hatch with the same design. This development may be considered the first step toward the adoption of C-SMC as a multi-purpose automotive material, as demonstrated by its subsequent application to the inner door panels and inner trunk lid panel of a luxury coupe.

[*1] Material Engineering Div. No. 1, Advanced R&D and Engineering Company
[*2] MS Plastics & Surface Finishing Production Engineering Div., Mid-size Vehicle Company
[*3] BR Compact SUV Productization Dept., Mid-size Vehicle Company
[*4] Prototype Production Div., Advanced R&D and Engineering Company
[*5] Toyota Daihatsu Engineering & Manufacturing Co., Ltd.

Development of Highly Fuel Efficient and High Power Engine Adopting New Combustion Concept

Masashi Hakariya[1]   Tadashi Toda[2]   Mitsuto Sakai[3]
Takahiro Kawashima[4]   Kunihiko Sakata[5]

1. Introduction

Internal combustion engines with substantially higher fuel efficiency and cleaner emissions are an essential part of efforts to help realize a sustainable society by addressing future energy-related and environmental issues. At the same time, these engines must also have high power performance to ensure a fun-to-drive experience that exceeds user expectations. Toyota Motor Corporation has developed a new 2.5-liter gasoline engine to satisfy both of these requirements.

2. Development Aims

This engine was developed with the objective of further advancing high-speed combustion technologies for conventional engines. Specific development aims included achieving a maximum thermal efficiency of 40%, equivalent to the latest engines used in hybrid vehicles (HVs), as well as top-class power performance of 60 kW/L (**Fig. 1**). In addition, as a base engine developed to facilitate future development and ensure productivity, performance was further enhanced to maximize the potential of various technologies adopted in the engine (**Fig. 2**).

Fig. 1 Trends and Targets for Specific Power and Thermal Efficiency

Fig. 2 Main Technologies

3. Details of Technology

Thermal efficiency and power performance are generally regarded as having a trade-off relationship. To achieve the high targets set for both of these items, it is necessary create in-cylinder flows capable of generating stable combustion, while ensuring high knocking resistance and carrying out heavy exhaust gas recirculation (EGR). A long stroke design was adopted as the basic engine structure to enable the realization of high-flow, high-tumble intake ports capable of satisfying the conflicting requirements for turbulence and flow rate. The intake and exhaust valve layout was optimized and laser-clad valve seats adopted on the intake side, a significant step for a mass-produced engine. These measures enabled a port design that greatly improves the performance trade-off line of conventional ports. Specifications were selected to achieve the performance targets of this engine (**Figs. 3** and **4**).

Fig. 3 Details of Intake Port
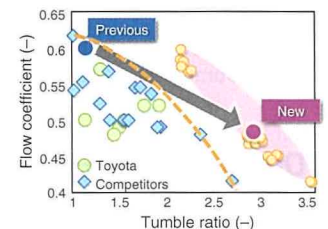
Fig. 4 Intake Port Performance

Technical Award News

In addition, the stratified cavity on the top of the piston was eliminated as shown in **Fig. 5** to maintain the in-cylinder turbulence intensity in the compression stroke even under the higher compression ratio.
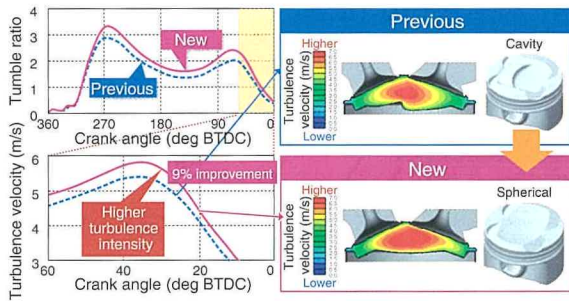

Fig. 5 Comparison of Piston Top Shape and Turbulence Intensity

To enable a thorough redesign of the cooling structure and system, and to suppress deterioration in knocking resistance due to the higher compression ratio, a motor-driven water pump was adopted that can control the coolant flow rate regardless of the engine speed. In consideration of power consumption and to reduce the size of the pump, the pressure loss of the cooling paths and overall system was reduced, and efficient cooling performance improvements were adopted. Specific measures included creating a cylinder head structure that concentrates the flow of coolant between the exhaust valves, which are susceptible to temperature increase, and reducing the sectional area of the water jacket core by 20%. As a result, the coefficient of heat transfer was increased by 20% with around half the flow rate of the previous engine (**Fig. 6**). Knocking resistance was substantially improved from low engine speeds, further advancing the high-speed combustion concept.
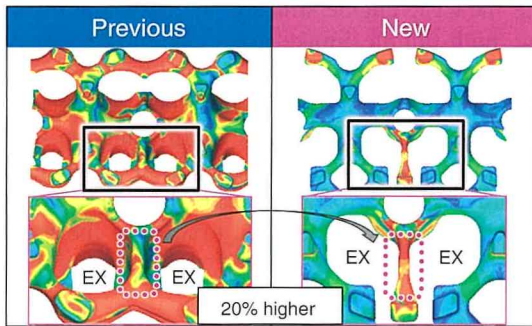
Fig. 6 Water Jacket Structure and Coefficient of Heat Transfer Comparison

4. Development Results

Compared to the previous engine, by advancing the high-speed combustion concept and adopting new technologies, substantial improvements were achieved in engine performance across all engine operating regions, from low to high engine speeds. As a result, the new engine achieved a maximum power of 151 kW (specific power: 60 kW/L) (**Fig. 7**). Fuel efficiency was enhanced by improving thermal efficiency over a wide operation range. A maximum thermal efficiency of 40% was achieved in the conventional vehicle engine and 41% in the HV engine (**Fig. 8**).
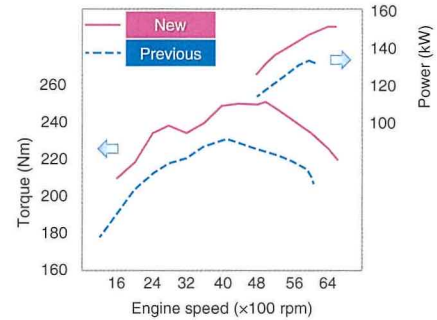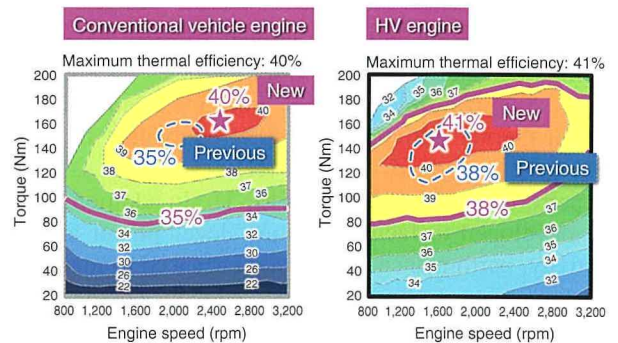

Fig. 7 Engine Power and Torque Curves

Fig. 8 Comparison of Thermal Efficiency Maps

5. Conclusion

This engine achieved world-leading maximum thermal efficiency and power performance by adopting a full range of the latest technologies as described in this article, reflecting its status as a key next-generation engine of Toyota.

Starting with this engine, Toyota plans to launch a series of engines incorporating high-speed combustion technologies and other key concepts of the Toyota New Global Architecture (TNGA) to meet the wide-ranging needs of different regions and users.

Best Poster Paper Presentation Award at 2017 Annual Congress of Society of Automotive Engineers of Japan, Inc.
Research into Power Transfer Analysis Methodology for Dynamic Wireless Charging

Masato Maemura[*1]   Kimitoshi Tsuji[*2]   Tomokiyo Suzuki[*1]
Tsuyoshi Nakamura[*3]   Yasunao Yoshizaki[*4]   Kensuke Kamichi[*5]

1. Introduction

Three main issues must be addressed before electrified vehicles gain widespread market acceptance, namely battery range, the difficulty and length of time required for charging, and high vehicle cost. Development is under way to resolve these issues, primarily to increase battery capacity and enhance rapid charging capabilities. This article describes a different approach to popularizing electrified vehicles through dynamic wireless charging, which aims to reduce the amount of energy stored on-board the vehicle by supplying power as the vehicle is driven.

The following sections introduce an analysis methodology using a concept called one-dimensional computer aided engineering (1D CAE), in which the essential nature of the analysis target is identified and rendered in a simple and easy-to-understand manner. This methodology was applied to wireless power supply using magnetic fields generated by current passing through coils.

2. Outline of Developed Technology

Fig. 1 shows an outline of this system. The system was examined based on the magnetic resonance coupling method discussed in the SAE J2954 standard, and featuring 85 kHz power sources, capacitors for magnetic resonance coupling, wireless power transfer coils, a rectifier (for AC to DC conversion) once the power is received, and the electrical load of the vehicle.

The process for creating the analysis model and the results are as follows.

1. Modeling of the geometry of the power transfer (primary) and receiving (secondary) coils
2. Acquisition of the movement distance by electromagnetic analysis, and the relational expression of the coupling coefficient (**Fig. 2**)
3. Modeling of the electromagnetic circuit for power transfer
4. Modeling of the moving vehicle for calculating energy consumption
5. Modeling of the dynamic wireless charging system (**Figs. 3** and **4**)

Steps 1 and 2 were carried out by three-dimensional electromagnetic analysis using finite elements, and steps 3 to 5 were carried out using 1D CAE.

It should be noted that, considering utilization in model-based development (MBD), the model used in this study was expressed using a standardized language called Very High Speed Integrated Circuit Hardware Description Language - Analog Mixed Signal (VHDL-AMS). This language allowed the creation of a versatile model to facilitate future scalability.
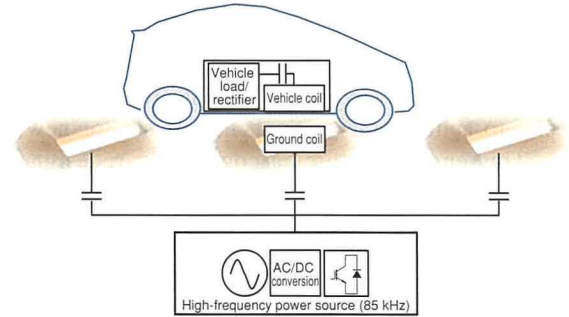

Fig. 1 Outline of Dynamic Wireless Charging System
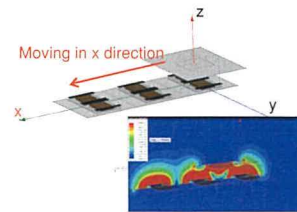

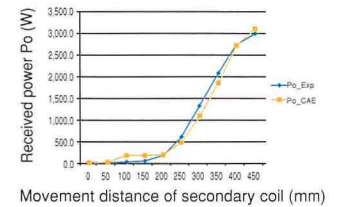Fig. 2 Coil Movement and Magnetic Field Analysis

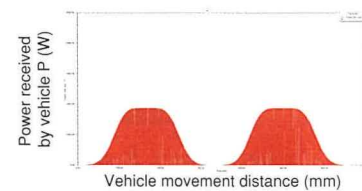Fig. 3 Results of Comparison (Analysis vs. Experiment)

Fig. 4 Power Received during Coil Movement (Passing over Two Ground Coils)

3. Conclusion

This article has described an analysis methodology capable of continuously calculating system behavior from the infrastructure (i.e., the magnetic field source) to the energy consumption of the moving vehicle. By distilling the components of the system into a 1D model, the interactions between these components can be discussed based on the properties of the electromagnetic circuit, which are the main design elements of a wireless power transfer circuit. This model should be applicable to future research into the effects of movement on equivalent inductance, control methodologies for maximizing efficiency, and the like. Development of this system is currently ongoing.

[*1] S-Frontier Div., Frontier Research Center
[*2] Advanced Project Promotion Div., Advanced R&D and Engineering Company
[*3] R&D and Engineering Management Div., Advanced R&D and Engineering Company
[*4] Electronics Control System Development Div., Advanced R&D and Engineering Company
[*5] Powertrain Product Planning Div., Powertrain Company

Technical Award News

New Combustion and Powertrain Control Concepts for Achieving both Fun-to-Drive Dynamic Performance and Better Fuel Economy

Takashi Yoshida[*1]   Taketo Nagasaki[*1]   Tsuyoshi Takahashi[*2]
Shigeru Itabashi[*1]   Masaaki Yamaguchi[*1]   Eiji Murase[*3]

1. Introduction

Vehicle engines with better fuel economy that comply with emissions regulations around the world are an important part of measures to improve energy security and respond to global-scale environmental changes. A new 2.5-liter engine was developed following the Toyota New Global Architecture (TNGA) design philosophy to achieve the difficult targets set for new vehicle models. This engine features a completely redesigned basic structure to comply with the SULEV30 and Euro 6c emissions regulations, and achieves a thermal efficiency of 40% and specific power of at least 60 kW/L, leading figures for a mass-produced engine.

2. Combustion Concept

The TNGA engine series shares the same fast combustion concept. The intensity of turbulence inside the combustion chamber has a strong correlation with combustion speed. A turbulence intensity target was set to achieve a thermal efficiency of 40%. Turbulence intensity can be predicted accurately using representative parameters from the engine specifications and physical indices. Highly efficient combustion that achieves the targets for high thermal efficiency and specific power, which have a strong trade-off relationship, was realized by redesigning the basic structure of the engine using this design methodology and by adopting the refinements shown in **Fig. 1**. Better catalyst warm-up performance and a lower particle number (PN) were also achieved by changing the catalyst warm up strategy.
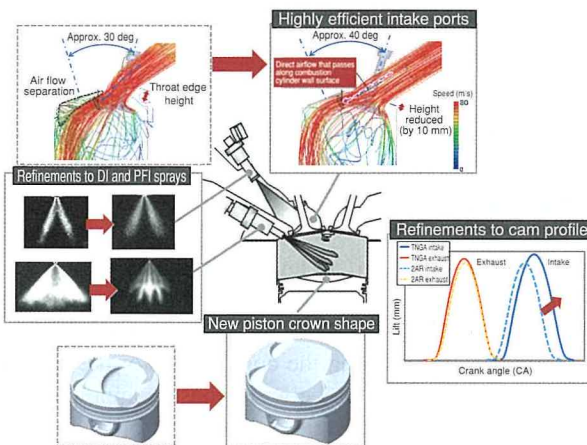
Fig. 1 TNGA Engine Refinements

3. Results of Engine Experiments

Fig. 2 shows the results of the combustion confirmation tests. By achieving the targeted turbulence intensity, it was confirmed that combustion speed increased substantially compared to the previous engine. Fast combustion also suppressed combustion fluctuations, reduced knocking, and advanced the 50% heat release rate timing (CA50). The resulting increase in performance offset the reduction in volumetric efficiency that accompanies the higher tumble ratio.
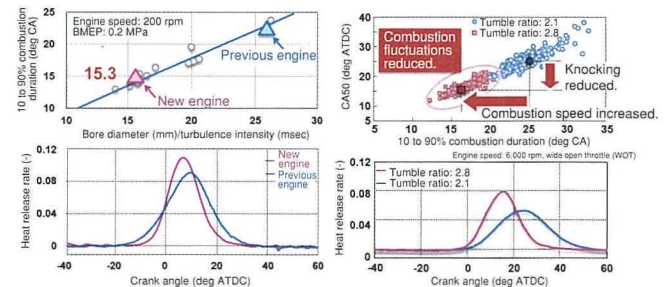

Fig. 2 Results of Combustion Confirmation Tests at Partial load (Left) and Full Load (Right)

4. Conclusions

- A maximum thermal efficiency of 40% and a specific power of 60 kW/L were achieved by redesigning the basic structure of the engine based on the fast combustion concept.
- Compliance with the SULEV30 and Euro 6c regulations was achieved by changing the catalyst warm up strategy and redesigning the direct injection (DI) and port fuel injection (PFI) sprays.
- Full load acceleration performance and fun-to-drive dynamic performance were achieved by setting driving performance targets even for everyday driving scenarios.
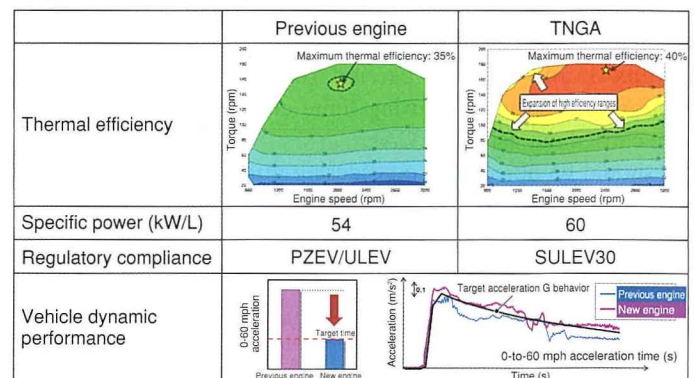

Fig. 3 Summary of Engine and Vehicle Performance Aspects

[*1] Electric Powertrain System Development Div. No. 3, Powertrain Company
[*2] Electric Powertrain System Development Div. No. 2, Powertrain Company
[*3] Powertrain Product Planning Div., Powertrain Company

Analysis of CVT Belt Noise Mechanism by Measuring Vibration Source

Jiro Hayashi[*1]   Tadashi Morimoto[*2]   Yasunori Takeda[*3]   Yuichi Miwa[*2]

1. Introduction

Reducing belt noise has been a long-term issue in the development of quieter continuously variable transmissions (CVTs). However, since the generation mechanism of this noise was not fully understood, countermeasures have mainly focused on improving the transmission case through trial and error rather than addressing the source of the noise in the variator. With the aim of improving CVT performance and identifying ways of reducing development times and cost by front-loading the noise performance development process, this research analyzed the CVT belt noise mechanism, developed a variator sub-assembly evaluation technique capable of reproducing the vibration mode contributing to belt noise, and validated the accuracy of CAE prediction.

2. Details of Research

Previous research identified the following CVT belt noise generation mechanism. When the CVT belt engages the sheave, force is generated that causes the sheave to vibrate. This vibration is then transmitted to the shaft and case, causing noise to radiate outward. However, the vibration modes of the sheave and shaft, which make a high contribution to the noise, have not been identified (**Fig. 1**). In response, this research developed technology to measure microscopic vibrations of the variator during actual operation (**Fig. 2**). For axial direction vibration, it was possible to isolate and detect sheave vibration by reducing the stiffness of the sensor holder to damp high-frequency vibration transmitted from the case to the sensor. However, for rotation direction vibration, it is difficult to detect the target rotational fluctuations using an equipment-based torque meter

Fig. 1 CVT Belt Noise Generation Mechanism Hypothesis

*1 Measurement & Instrumentation Engineering Div., Powertrain Company
*2 Powertrain Development Digital Innovation Div., Powertrain Company
*3 Drivetrain-EHV Design Div. No. 3, Powertrain Company

because these rotational fluctuations are microscopic and are damped before reaching the torque meter. This research detected these rotational fluctuations as torque fluctuations by installing a torque meter on the shaft nearest the sheave.

(a) Axial direction
vibration measurement
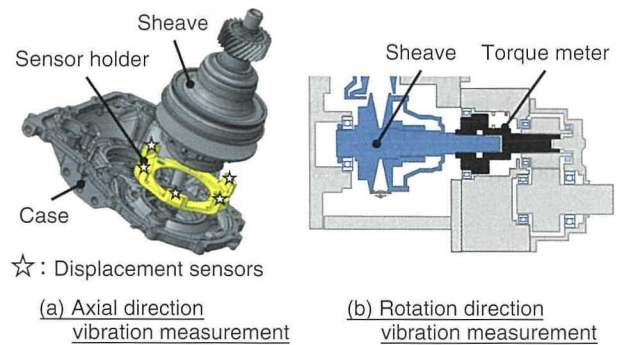
(b) Rotation direction
vibration measurement

Fig. 2 Developed Sheave Vibration Measurement System

The developed measurement technology was used to analyze the vibration mode that makes a high contribution to CVT belt noise. Sheave axial direction vibration associated with the shaft bending mode was identified for the first time as the main factor of CVT belt noise (**Fig. 3**).
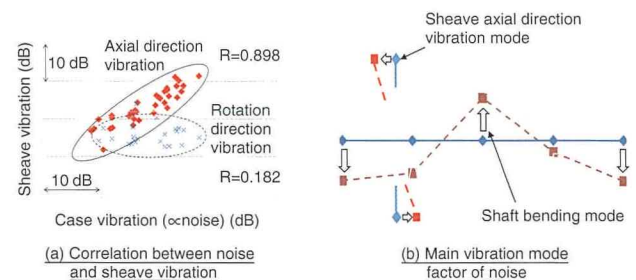

(a) Correlation between noise
and sheave vibration

(b) Main vibration mode
factor of noise

Fig. 3 Sheave Vibration Mode Analysis Results

3. Conclusion

This research identified the CVT belt noise mechanism, thereby enabling design studies to help reduce noise. Based on the identified mechanism, this research also established an evaluation technique for the variator sub-assembly capable of reproducing the shaft bending mode, and confirmed that the vibration mode predicted using CAE closely matches the actually measured vibration mode. The developed technologies are being applied to accelerate front-loading of the development process.

Improved Prediction Methodology for Tooth Root Strain in Transmission

Toshiaki Tsuda[*1] Takanori Nukata[*1] Miho Horiuchi[*1]
Tomoyuki Hirota[*2] Tetsuya Yamaguchi[*2] Mitsuharu Sekiyama[*2]

1. Introduction

Simulation technologies are used in transmission development to ensure reliability and reduce weight. When calculating the fatigue strength of gears, it is important to accurately predict the deformation (i.e., the misalignment) of the gear support system as this has a large influence on tooth contact.

This research enabled the accurate prediction of misalignment and tooth root strain (**Fig. 1**) by improving the modeling of bearings and other components within the gear support system.

Fig. 1 Tooth Root Strain Generation Mechanism

2. Construction of Analytical Model

Experiments have found that bearings, bolts, and gears have a major influence on misalignment. However, the influence of these components has conventionally been analyzed using simple models due to the complexity of the modeling required to examine this influence with precision. This study aimed to accurately simulate misalignment and predict tooth root strain by precisely reproducing the load transfer of these mechanical elements. First, as shown in **Fig. 2**, models were constructed that simulate the detailed shapes and contact states between parts. Incorporating these models into an overall transmission model increased the scale of computation, either preventing calculation or increasing the calculation time above acceptable limits. These issues were resolved by adopting a sub-modeling methodology.
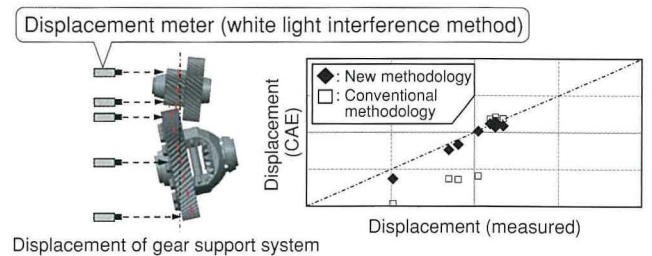

Fig. 2 Detailed Model Construction

3. Confirmation of Analytical Model Validity

The validity of the new methodology was confirmed by measuring the displacement and tooth root strain of the gear support system in an actual transmission, and then comparing these values with the analytical results (**Figs. 3** and **4**). The comparison results demonstrated greater prediction accuracy, thereby confirming the validity of the new methodology.

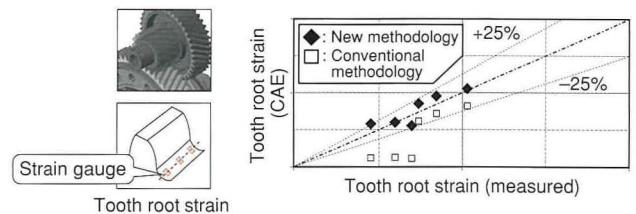**Fig. 3 Comparison of Gear Support System Displacement**

**Fig. 4 Comparison of Tooth Root Strain**

4. Conclusion

This research enabled the highly precise prediction of tooth root strain. It is planned to use this new methodology to help reduce transmission weight.
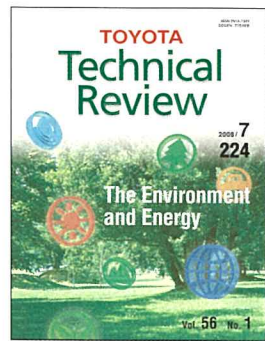
*1 Powertrain Development Digital Innovation Div., Powertrain Company
*2 Measurement Instrumentation & Digital Development Innovation Div., Powertrain Company
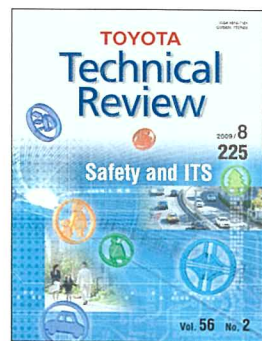
TOYOTA Technical Review

Back Number Index
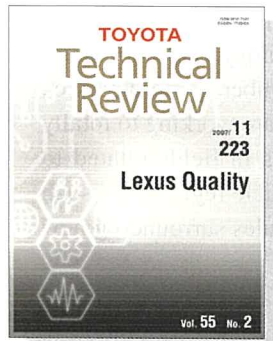
Vol. 55 No. 2 (2007)
Special Feature: Lexus Quality

Vol. 56 No. 1 (2008)
Special Feature:
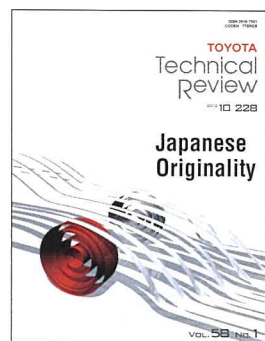The Environment and Energy

Vol. 56 No. 2 (2009)
Special Feature: Satety and ITS

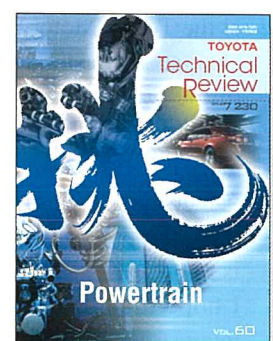**Vol. 57 No. 1** (2010)
Special Feature: Prius

Vol. 57 No. 2 (2011)
Special Feature:
Next-Generation Electric Storage
and its Applications

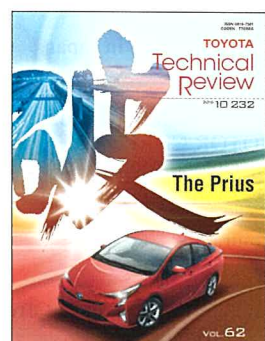**Vol. 58 No. 1** (2012)
Special Feature:
Japanese Originality

Vol. 59 (2013)
Special Feature:
Production Engineering
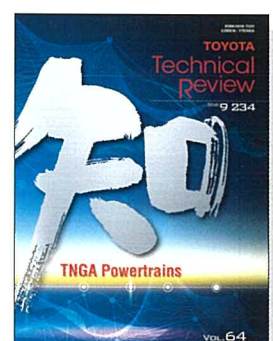
Vol. 60 (2014)
Special Feature: Powertrain

Vol. 61 (2015)
Special Feature 1: The Mirai FCV
Special Feature 2: ITS and
Advanced Driving Support Systems

Vol. 62 (2016)
Special Feature: The Prius

Vol. 63 (2017)
Challenging and Innovative
Technological Development

Vol. 64 (2018)
Special Feature:
TNGA Powertrains

¥2,800 (tax not included)

Thank you for reading the *Toyota Technical Review*. It is my pleasure to present Volume 65, which is the 235th edition of the *Toyota Technical Review* since its publication began.

The special feature of this edition covers the battery technologies of the future, with a particular emphasis on fuel cells and storage batteries. As always, I would like to extend my sincere gratitude to the authors and everyone that worked to assemble the articles for their cooperation during this incredibly busy time.

Starting a few years ago, people began to describe the automotive industry as having entered a once-in-a-century period of profound transformation. Some of the largest information technology (IT) companies in the world, led by Google, Amazon, Facebook, and Apple (GAFA), as well as a number of startups, i.e., venture businesses equipped with ultra-cutting-edge technologies, have broken into and are working to totally redraw the map of the global automotive business. Competition between companies in fields related to battery development is growing fiercer as countries introduce increasingly stringent vehicle regulations, such as the Zero Emission Vehicle (ZEV) program initiated by California and the range of rules surrounding new energy vehicles (NEVs) in China.

Toyota Motor Corporation regards this situation as a life-or-death fight for survival, rather than just a question of winning or losing in the market. To this end, Toyota is working to reinvent itself as a mobility company.

This year, 2019, also marked the end of the Heisei era in Japan (1989 to 2019), and the beginning of the Reiwa era. I looked back at the *Toyota Technical Reviews* that were published at the end of the previous era, Showa (1926 to 1989). I found an article describing the EV-30, an electric vehicle that Toyota first exhibited at the Tokyo Motor Show in 1987. The EV-30 had a top speed of 43 km/h and a range of 165 km on a single charge. Interestingly, it was equipped with zinc-bromine batteries. The EV-30 was the first electric vehicle in the world to adopt a power control unit (PCU) featuring an integrated inverter, charger, and DC-DC converter. At the end of the Heisei era, Toyota announced that it would make many patents related to vehicle electrification available free of charge. The PCUs in these patents have their origins in the one developed for the EV-30.

As the publisher of the *Toyota Technical Review*, my role is to create a useful, informative, and interesting publication. I hope that you will continue to read these articles with interest.

(Publisher: Yonemura)

Total Lunar Eclipse at Tsuki Elementary School

A total lunar eclipse occurs when the moon is completely hidden by the Earth's shadow.
This photograph was taken on January 31, 2018, from the grounds of the abandoned Tsuki
Elementary School (in the Tsuki district of Toei, Aichi Prefecture).
Munehiro Hirano, member of the Okumikawa Stargazing and Appreciation Society